

Ultrafast Field Dynamics in Laser Ion Acceleration

vorgelegt von
Dipl.-Phys. Florian Abicht
geb. in München

von der Fakultät II - Mathematik und Naturwissenschaften
der Technischen Universität Berlin
zur Erlangung des akademischen Grades

Doktor der Naturwissenschaften
– Dr. rer. nat. –

genehmigte Dissertation

Promotionsausschuss:

Vorsitzender: Prof. Dr. Knorr
Berichter: Prof. Dr. Sandner
Prof. Dr. Schreiber

Tag der wissenschaftlichen Aussprache: 13.07.2015

Berlin 2015
D 83

À Hélène

List of Publications

- F. Abicht, J. Bränzel, G. Priebe, C. Koschitzki, A. A. Andreev, P. V. Nickles, W. Sandner, and M. Schnürer, “Tracing ultrafast dynamics of strong fields at plasma-vacuum interfaces with longitudinal proton probing”, *Applied Physics Letters* **105**, 034101 (2014).
- F. Abicht, R. Prasad, M. Borghesi, G. Priebe, J. Bränzel, A. Andreev, P. V. Nickles, M. Schnürer, S. Jequier, G. Revet, V. Tikhonchuk, and S. Ter-Avetisyan, “Energetic beams of negative and neutral hydrogen from intense laser plasma interaction”, *Applied Physics Letters* **103**, 253501 (2013).
- M. Schnürer, F. Abicht, R. Prasad, M. Borghesi, G. Priebe, J. Bränzel, A. Andreev, P. V. Nickles, S. Jequier, V. Tikhonchuk, and S. Ter-Avetisyan, “Charge steering of laser plasma accelerated fast ions in a liquid spray - creation of MeV negative ion and neutral atom beams”, *Physics of Plasmas* **20**, 113105 (2013).
- M. Schnürer, A. A. Andreev, F. Abicht, J. Bränzel, C. Koschitzki, K. Y. Platonov, G. Priebe, and W. Sandner, “The beat in laser-accelerated ion beams”, *Physics of Plasmas* **20**, 103102 (2013).
- R. Prasad, F. Abicht, M. Borghesi, J. Bränzel, P. V. Nickles, G. Priebe, M. Schnürer, and S. Ter-Avetisyan, “Thomson spectrometer-microchannel plate assembly calibration for MeV-range positive and negative ions, and neutral atoms”, *Review of Scientific Instruments* **84**, 053302 (2013).
- A. Zigler, S. Eisenman, M. Botton, E. Nahum, E. Schleifer, A. Baspaly, I. Pomerantz, F. Abicht, J. Bränzel, G. Priebe, S. Steinke, A. Andreev, M. Schnürer, W. Sandner, D. Gordon, P. Sprangle, and K. W. D. Ledingham, “Enhanced proton acceleration by an ultrashort laser interaction with structured dynamic plasma targets”, *Physical Review Letters* **110**, 215004 (2013).
- S. Steinke, P. Hilz, M. Schnürer, G. Priebe, J. Bränzel, F. Abicht, D. Kiefer, C. Kreuzer, T. Ostermayr, J. Schreiber, A. A. Andreev, T. P. Yu, A. Pukhov, and W. Sandner, “Stable laser-ion acceleration in the light sail regime”, *Physical Review Special Topics-accelerators and Beams* **16**, 011303 (2013).

- F. Abicht, R. Prasad, G. Priebe, J. Bränzel, L. Ehentraut, A. Andreev, P. V. Nickles, M. Schnürer, V. Tikhonchuk, and S. Ter-Avetisyan, “Energetic negative ion and neutral atom beam generation at passage of laser accelerated high energy positive ions through a liquid spray”, *SPIE Proceedings* **8779**, 87790M (2013).
- F. Abicht, M. Schnürer, J. Bränzel, G. Priebe, A. A. Andreev, C. Koschitzki, S. Steinke, T. Toncian, O. Willi, and W. Sandner, “Coaction of strong electrical fields in laser irradiated thin foils and its relation to field dynamics at the plasma-vacuum interface”, *SPIE Proceedings* **8779**, 87790V (2013).
- S. Gross, M. Esselborn, F. Abicht, M. Wirth, A. Fix, and A. Minikin, “Airborne high spectral resolution lidar observation of pollution aerosol during EUCAARI-LONGREX”, *Atmospheric Chemistry and Physics* **13**, 2435–2444 (2013).
- E. Schleifer, E. Nahum, S. Eisenmann, M. Botton, A. Baspaly, I. Pomerantz, F. Abicht, J. Bränzel, G. Priebe, S. Steinke, A. Andreev, M. Schnürer, W. Sandner, D. Gordon, P. Sprangle, K. D. Ledingham, and A. Zigler, “Microstructured snow targets for high energy quasi-monoenergetic proton acceleration”, *SPIE Proceedings* **8779**, 87791M (2013).
- R. Prasad, M. Borghesi, F. Abicht, P. V. Nickles, H. Stiel, M. Schnürer, and S. Ter-Avetisyan, “Ethanol (C₂H₅OH) spray of sub-micron droplets for laser driven negative ion source”, *Review of Scientific Instruments* **83**, 083301 (2012).

Contents

Introduction	1
I Basics	5
1 Intense and Ultra-short Laser Pulses with High Temporal Contrast	7
1.1 Mathematical Description	7
1.1.1 Propagation of a Laser Pulse in Vacuum	7
1.1.2 Interaction of Light with Matter	10
1.2 Generation of Ultra-short Pulses	13
1.3 Chirped Pulse Amplification	19
1.4 Contrast Enhancement	20
1.5 Gaussian Optics and the Focussing of a Laser Pulse	25
2 Laser System	29
2.1 Specifications	29
2.2 Synchronization and Focus Alignment	31
3 Laser Plasma Interactions	35
3.1 Interaction of a Laser Pulse with a Single Electron	35
3.2 Ponderomotive Force	40
3.3 Laser Generated Solid Density Plasmas	42
3.4 Debye Length	44
3.5 The Plasma Frequency	46
3.6 The Dielectric Plasma Medium	47
4 Laser-driven Ion Acceleration	49
4.1 Absorption Mechanisms	49
4.2 Acceleration by Electric Charge Separation Fields	50
4.3 Magnetic Field Generation Mechanisms	54
II Characterization of Laser Accelerated Proton Beams	57
5 The Thomson Slit Spectrometer	59

5.1	Setup	59
5.2	Multi-Channel Plate	61
5.3	Ion Traces	62
5.4	Data Analysis	63
5.5	Angle and Energy Resolution	69
6	The Beat in Ion Acceleration	77
6.1	Experimental Setup	77
6.2	Experimental Results	78
6.3	Simulation Results	81
6.4	Model Results	86
6.5	Discussion	86
III	Proton Imaging	91
7	Principle of Proton Imaging	93
7.1	Imaging with Laser-driven Proton Beams	93
7.2	Principal Experimental Setup	94
7.3	Probing Configurations	95
8	Streak Deflectometry	99
8.1	Principle of Streak Deflectometry	99
8.2	Lateral Displacement Setup	101
8.3	Measurements and Data Analysis	102
8.4	Results and Discussion	106
8.5	Time Resolution	110
9	Energy Redistribution Effects in Proton Beams by Probing Strong Fields at Plasma Vacuum Interfaces	113
9.1	Conception	113
9.2	Experimental Setup	114
9.3	Experimental Results	116
9.3.1	Variation of the Target Distance	116
9.3.2	Variation of the Lateral Focus Position	119
9.3.3	Variation of the Irradiation Geometry	121
9.4	Theoretical Description	123
9.4.1	Analytical Field Description of Moving Ion Fronts	123
9.4.2	Numerical Method	129
9.4.3	Surface Potential Model	130
9.4.4	Proton Energy Redistribution	131
9.5	Modeling of the Experiments and Discussion	133
9.5.1	Redistribution Effects due to Expanding Ion Fronts	133
9.5.2	Special Redistribution Effects	144

10 Electromagnetic Fields initiated on Ultra-thin Foils with High-contrast Laser Pulses	151
10.1 Experimental Setup	151
10.2 Experimental Results	154
10.2.1 Field Effects due to Ultra-short Laser Pulses	154
10.2.2 Field Effects due to Picosecond Laser Pulses	163
10.3 Theoretical Description	167
10.3.1 Model A - Ultra-short Fields on Ultra-thin Foils	167
10.3.2 Model B - The Electric Field of an Expanding Proton Front .	173
10.3.3 Model C - Analytic Description of Magnetic Fields on Thin Foil Targets	174
10.4 Modeling of the Experiments and Particle Simulations	175
10.4.1 Simulation Concept	175
10.4.2 Field Effects due to Ultra-short Laser Pulses	177
10.4.3 Field Effects due to Picosecond Laser Pulses	191
Summary	195
IV Appendix	201
A Basics	203
A.1 Slowly Varying Envelope Approximation	203
A.2 Dispersion Parameters	204
A.3 Group Delay Dispersion	206
A.4 Change of the Pulse Shape in Dispersive Media	207
A.5 Wavelength Dependence of the Dispersion Coefficients	209
A.6 Birefringence	209
A.7 Nonlinear Optical Processes	210
A.8 Energy Sensitive Proton Detection	212
B Specifics	215
B.1 Source Properties of the Probing Proton Beam	215
B.2 Redistribution Effects due to Exponentially Decaying Fields	218
B.3 Magnetic Field Components of the Permanent Magnet	222
B.4 Energy Modulations in Laser Accelerated Ion Beams - Analytical Description	223
List of Abbreviations	227

Bibliography	229
Acknowledgments	245

Introduction

Fast ions have a decisive impact on basic science, technological development and application in bio-medical areas. The term fast in this context covers several per cent of the speed of light up to the ultra-relativistic range. For instance, fast ions are used as an experimental tool to explore the nuclear synthesis of heavy elements, which is often ranked among the top ten questions of fundamental physics [1]. Devices and facilities for fast ion production have been progressing since the 1930s [2] and have reached a high level of development. Ions are accelerated in electrical fields to high velocities, whereby the maximum field gradient determines the length of the acceleration unit. In ionized matter, or plasma, these gradients can be substantially higher than those of vacuum-solid interfaces in acceleration cavities. Therefore, the use of plasma is predestined for the development of more compact devices. However, efficient and controlled acceleration in plasma involves complex physics and is a continually advancing area of scientific research, which this thesis will attempt to explore further.

Lasers can create plasmas with high particle densities that constitute a state of high energy density. In order to use this effect for the efficient acceleration of ions a certain structure of the plasma is required. In simple terms, a kind of charge separation and field rectification within plasma dynamics is necessary for a directed acceleration. This was discovered at the turn of the millennium through experiments with powerful short-pulse lasers. This finding, along with the enormous progress made in ultra-short pulse and high power laser technology, has boosted research in particle acceleration with laser-driven plasmas. Today, ion beams with maximum particle energies of 83 MeV/amu (1 GeV carbon ions) can be generated through the application of improved ion acceleration mechanisms [3].

Compared to conventional radio frequency (RF) wave based ion accelerators (hundreds of GeV) these particle energies are still low. However, laser-induced ion beams exhibit special properties.

The acceleration time of a laser-driven ion beam is ultra-short, typically of the order of picoseconds. At the same time, the acceleration gradients are of the order of MV/ μm and are therefore extremely high when compared to conventional accelerators (tens of MV/m). The effective source size of the laser-induced ion emission is extremely small with a typical extension of several micrometres. In addition laser-driven ion beams are divergent, exhibit a very low transversal and longitudi-

nal emittance [4] and can provide a wide spectral bandwidth. Due to these specific and unique attributes, laser-driven ion beams offer a potential for use in future applications. Several applications are discussed intensively and various experiments have already been started. Among them are such topics as, proton imaging and deflectometry [5–8], the production of warm dense matter (WDM) [9, 10], ion fast ignition in laser-driven nuclear fusion [11, 12], injectors for the conventional accelerators [13–15], sources for ion cancer therapy [16–21], production of short-lived radioisotopes [22, 23] for positron emission tomography (PET) [24], implantation of ions into materials [25–27].

Regarding these unique applications, laser-driven ion sources inherently have significant benefits. However, the ion beam parameters that are available today are far from sufficient for some of the previously mentioned applications. In fact, there are a variety of issues that have to be addressed. These include the conversion efficiency from laser energy into the ion beam, the still low particle energies, the angular and spectral control of the ion beam, and the stability of the acceleration process itself. In principle, a laser-driven ion accelerator will be competitive in applications if the vision of *ion steering with light* can be realized, and thus beam transport and beam manipulation of ions can be small and economical in size. The actual laser-induced ion acceleration is an extremely complex process. It highly depends on the applied laser and target parameters and involves a series of physical phenomena, which occur at different stages of the interaction. For typical laser-matter interactions, these stages can be classified into the ionization of the target, the formation of an initial pre-plasma, the absorption of the laser energy followed by the acceleration of electrons, the plasma evolution determined by the laser and collective plasma fields, and finally the propagation of the ions during and after the acceleration process. Due to the complexity of these linked and rapidly evolving processes, a direct and precise determination of all plasma parameters is simply not possible. Therefore, the identification and description of the dominant acceleration mechanism may prove difficult.

In order to create ion-beams with the desired properties, better understanding and control of the laser-induced ion acceleration process is necessary. Therefore, it is crucial to obtain further insight into the complex laser-plasma interactions, the associated strong fields, and the evolving plasma kinematics. Efforts are being made to develop diagnostic tools that can measure particular features of the accelerated ion beam and properties of the induced plasma. At the same time, theoretical models are needed that describe the acceleration process and allow the calculation of specific ion beam properties. Generally, such models start from laser parameters and include phenomenological assumptions with limited applicability range. The comparison between the calculated quantities and the experimentally observed properties allows for an indirect identification and characterization of the acceleration mechanism. Particularly in light of the upcoming new laser facilities [1] with petawatt pulse-power scaling, investigation and methodological approaches with measurement, simulation and analytical modeling are important.

This work primarily focuses on the investigation of strong accelerating fields which are initiated on thin and ultra-thin foils with ultra-high ($\sim 10^{18} - 10^{20}$ W/cm²) intensity and ultra-high contrast ($10^9 - 10^{11}$) laser pulses. For this purpose several common diagnostic methods were developed further and adapted to the experimental conditions. These methods allowed the direct probing of the transient electromagnetic field structure and the determination of properties of the laser-driven proton beam. In addition, several theoretical models were tested regarding their ability to explain the experimental observations.

- Chapter 1 provides the general mathematical description of a laser pulse, and describes its propagation in vacuum and interaction with a dielectric medium. In addition, it gives an overview of the physical concepts and their technical implementations, that allow for the generation of intense and ultra-short laser pulses with high temporal contrast.
- Chapter 2 introduces the relevant parameters of the two high power laser systems of the Max-Born-Institute (MBI) which were used for the experiments. In addition the laser pulse synchronization and focus alignment is explained.
- Chapter 3 describes the interaction of a laser pulse with a single electron and introduces the basics of laser-plasma physics.
- Chapter 4 introduces several absorption mechanisms which are relevant for laser-plasma interactions at relativistic intensities. In addition the ion acceleration by electric charge-separation fields and several mechanisms for the generation of magnetic fields are presented.
- Chapter 5 introduces a modified version of the Thomson spectrometer, the so called *Thomson slit spectrometer*, which enables the determination of the angle and energy dependent proton distribution. In order to visualize the distribution in an orthogonal coordinate system a numerical coordinate transformation method was developed and described in detail.
- Chapter 6 describes a newly observed property of a laser-driven ion source, which has been observed for the first time [28]. Modulations in the proton energy spectrum become detectable if intense femtosecond laser pulses with very high temporal contrast ($\sim 10^{10} - 10^{11}$) are used for target normal sheath acceleration of ions.
- Chapter 7 explains the principle of proton imaging and introduces two imaging geometries, the so called *transverse* and *longitudinal configuration*. These configurations can be used to probe different components of the laser-induced fields. In addition, several definitions and new terms are introduced in order

to facilitate the explanations of the following chapters. Finally, several energy sensitive detection methods for ions are discussed, providing time resolution in imaging experiments.

- Chapter 8 introduces the *proton streak deflectometry* method which allows for the continuous recording of transient fields on a picosecond time scale. First an explanation of the basic principle is presented. Then, a further development of the method is proposed, which can be used to investigate different parts of an extended field distribution in consecutive shots.
- Chapter 9 deals with energy redistribution effects in proton beams while transversing the strong electric fields created at plasma vacuum interfaces on laser irradiated thin foils. The consistency of different models and simulation is investigated and conclusions on field dynamics are drawn.
- Chapter 10 investigates the field dynamics initiated on ultra-thin foils (30 – 50 nm) if femtosecond and picosecond laser pulses with high temporal contrast are used. As a diagnostic tool, the method of proton streak deflectometry is applied in two different probing configurations. The combination of two configurations provides additional and complementary information about the investigated field distribution. Different theoretical models are presented, which can describe particular aspects of the laser-induced electromagnetic fields. Based on the respective model, the calculation of these fields is explained with respect to the applied laser and target parameters. In addition, the temporal evolution and spatial distribution of particular field components are visualized. The proposed analytical field descriptions are used to reproduce particular features of the experimental results by means of three-dimensional particle simulations. The field effects resulting from ultra-short laser pulses can be emulated in both probing configurations with the help of different analytical models. These models can explain different features of the observed streak deflections and can describe different properties of the field and thus allow for a more comprehensive and complementary explanation of the experimental observations.

Part I

Basics

1 Intense and Ultra-short Laser Pulses with High Temporal Contrast

This chapter gives an overview of the physical concepts and their technical implementations, that allow for the generation of intense and ultra-short laser pulses with high temporal contrast. Within this thesis the SI system will be the primary unit system used to describe physical quantities if not stated otherwise.

1.1 Mathematical Description

In this section the general mathematical description of a laser pulse is introduced. First, the pulse propagation in vacuum is presented, then the propagation within a dielectric medium and nonlinear effects are discussed.

1.1.1 Propagation of a Laser Pulse in Vacuum

As electromagnetic waves, laser pulses have to fulfill the Maxwell Equations. The wave equation for the electric field takes in vacuum the form

$$\Delta \mathbf{E}(\mathbf{x}, t) - \epsilon_0 \mu_0 \frac{\partial \mathbf{E}(\mathbf{x}, t)}{\partial t} = 0 \quad \text{with} \quad c = \sqrt{\frac{1}{\epsilon_0 \mu_0}}. \quad (1.1)$$

Using the ansatz

$$\mathbf{E}(\mathbf{x}, t) = \int d^3k \int d\omega (\mathbf{E}(\mathbf{k}, \omega) \exp[i(\mathbf{k} \cdot \mathbf{x} - \omega t)]), \quad (1.2)$$

whereby $\mathbf{E}(\mathbf{k}, \omega)$ is the fourier transform in space and time, \mathbf{k} the wave vector and ω the angular frequency, the general solution is given by

$$\mathbf{E}(\mathbf{x}, t) = \int d^3k (\mathbf{E}_0(\mathbf{k}) \exp[i(\mathbf{k} \cdot \mathbf{x} - \omega t)] + \mathbf{E}_0(\mathbf{k}) \exp[-i(\mathbf{k} \cdot \mathbf{x} - \omega t)]). \quad (1.3)$$

In the case of linear polarization a scalar representation of the field is sufficient. Neglecting the spatial dependence of the electric field, a short laser pulse can be described in the time and frequency domain using the expressions

$$E(t) = \mathcal{F}^{-1}[\tilde{E}(\omega)] = \frac{1}{2\pi} \int_{-\infty}^{\infty} \tilde{E}(\omega) e^{i\omega t} d\omega, \quad (1.4)$$

$$\tilde{E}(\omega) = \mathcal{F}[E(t)] = \int_{-\infty}^{\infty} E(t) e^{-i\omega t} dt. \quad (1.5)$$

Since the electric field is an observable and can be measured its value is real and the relation

$$\tilde{E}(\omega) = \tilde{E}^*(-\omega) \quad (1.6)$$

applies in the frequency domain. Here (*) indicates the complex conjugate function. The last equation signifies that already the positive part of the function $\tilde{E}(\omega)$ contains the complete information of the pulse. The complex electric field $\tilde{E}(\omega)$ in the frequency domain can be expressed by means of the real amplitude $\tilde{\mathcal{E}}(\omega)$ and the so called spectral phase $\tilde{\phi}(\omega)$

$$\tilde{E}(\omega) = \tilde{\mathcal{E}}(\omega) e^{i\tilde{\phi}(\omega)}. \quad (1.7)$$

The definition of the reduced field functions $\tilde{E}^+(\omega)$ and $\tilde{E}^-(\omega)$, whereby

$$\tilde{E}^+(\omega) = \begin{cases} \tilde{E}(\omega), & \text{if } \omega > 0, \\ \tilde{E}(\omega)/2, & \text{if } \omega = 0, \\ 0, & \text{if } \omega < 0, \end{cases} \quad \tilde{E}^-(\omega) = \begin{cases} 0, & \text{if } \omega > 0, \\ \tilde{E}(\omega)/2, & \text{if } \omega = 0, \\ \tilde{E}(\omega), & \text{if } \omega < 0 \end{cases} \quad (1.8)$$

allows the electric field in the frequency domain to be written as $\tilde{E}(\omega) = \tilde{E}^+(\omega) + \tilde{E}^-(\omega)$. With respect to the fourier transformation, it is advantageous to describe the reduced field function $\tilde{E}^+(\omega)$ by means of the real amplitude $\tilde{\mathcal{E}}^+(\omega)$ and the phase $\tilde{\phi}^+(\omega)$, whereby

$$\tilde{E}^+(\omega) = \tilde{\mathcal{E}}^+(\omega) e^{i\tilde{\phi}^+(\omega)}. \quad (1.9)$$

A comparison between Equation 1.6 and Equation 1.7 yields $\tilde{\phi}(\omega) = \tilde{\phi}^+(\omega)$ and

$$\tilde{\mathcal{E}}^+(\omega) = \begin{cases} \tilde{\mathcal{E}}(\omega), & \text{if } \omega > 0, \\ \tilde{\mathcal{E}}(\omega)/2, & \text{if } \omega = 0, \\ 0, & \text{if } \omega < 0. \end{cases} \quad (1.10)$$

The Fourier transform of $\tilde{E}^+(\omega)$ in the time domain describes the electric field $E^+(t)$ as a complex quantity which can be represented by the real amplitude $\mathcal{E}^+(t)$ and the phase $\phi^+(t)$ by means of the equation

$$E^+(t) = \mathcal{E}^+(t) e^{i\phi^+(t)}. \quad (1.11)$$

Using Equation 1.6 and 1.8 the electric field $E(t)$ can be described as twice the real part of the reduced field function

$$E(t) = 2 \operatorname{Re} \{ E^+(t) \} = (E^+(t) + E^{+*}(t)) = 2\mathcal{E}^+(t) \cos(\phi^+(t)). \quad (1.12)$$

In addition the electric field $E(t)$ can be expressed by the real amplitude $\mathcal{E}(t)$ and the instantaneous phase $\phi(t)$ by means of the equation

$$E(t) = \frac{1}{2}\mathcal{E}(t)e^{i\phi(t)} + \frac{1}{2}\mathcal{E}(t)e^{-i\phi(t)} = \mathcal{E}(t) \cos(\phi(t)). \quad (1.13)$$

A comparison of the last two equations yields $\mathcal{E}(t) = 2\mathcal{E}^+(t)$ and $\phi(t) = \phi^+(t)$. On condition that the amplitude of the envelope function changes slowly in time in relation to the carrier wave, the so called slowly varying envelope approximation (SVEA) is applicable, as proposed in the appendix (A.1). In this case the electric field $E(t)$ can be expressed by means of the complex field amplitude $\hat{\mathcal{E}}(t)$ using the equation

$$E(t) = \frac{1}{2} \left(\hat{\mathcal{E}}(t)e^{i\psi(t)} + \hat{\mathcal{E}}(t)^*e^{-i\psi(t)} \right), \quad (1.14)$$

whereby $\psi(t) = \omega_0 t$ and $\hat{\mathcal{E}}(t) = \mathcal{E}(t)e^{i\varphi(t)}$. The instantaneous phase $\phi(t)$ can be written as the sum of the fast varying phase $\psi(t)$ and the slowly varying temporal phase $\varphi(t)$ using the formula

$$\phi(t) = \psi(t) + \varphi(t) = \omega_0 t + \varphi(t). \quad (1.15)$$

Therefore, the electric field function can be expressed as $E(t) = \mathcal{E}(t) \cos(\omega_0 t + \varphi(t))$. The instantaneous angular frequency is defined as

$$\omega(t) = \frac{d\phi(t)}{dt} = \omega_0 + \frac{d\varphi(t)}{dt}. \quad (1.16)$$

If the instantaneous angular frequency changes in time, the frequency modulated pulse is called chirped. If the frequency increases with the pulse duration the pulse is called up-/positive-chirped. In the opposite case the pulse is named down-/negative-chirped. By expressing the temporal phase $\varphi(t)$ or the spectral phase $\tilde{\phi}(\omega)$ in a Taylor expansion the modulation state of a pulse can be described by means of several dispersion parameters as proposed in Section A.2 of the appendix. The intensity of a light pulse in vacuum is defined by

$$I(t) = \epsilon_0 n c \frac{1}{T} \int_{t-T/2}^{t+T/2} E^2(t') dt'. \quad (1.17)$$

If the SVEA is valid Expression 1.17 can be simplified

$$I(t) = \frac{1}{2}\epsilon_0 n c \mathcal{E}^2(t) = 2\epsilon_0 n c E^+(t)E^-(t) = \frac{1}{2}\epsilon_0 n c \hat{\mathcal{E}}(t)\hat{\mathcal{E}}^*(t). \quad (1.18)$$

In experiments usually the peak intensity $I_0(t)$ is used to characterize the laser pulse

$$I_0(t) = \frac{1}{2}\epsilon_0 n c \mathcal{E}_0^2. \quad (1.19)$$

Conventionally, the unit is given in W/cm². However, Equations 1.18 and 1.19 apply only for linear polarization. In the circular case the formulas are to be multiplied by the factor of two, whereby the field amplitude (\mathcal{E}_0 , $\mathcal{E}(t)$) does not change.

The pulse duration τ_p is defined as the full width at half maximum (FWHM) of the intensity profile and the spectral width is denoted by $\Delta\omega_p$. Since the spectral and temporal properties of the electric field are coupled via the Fourier transformation, τ_p and $\Delta\omega_p$ are not independent. Both quantities are connected by the time-bandwidth product (uncertainty principle) which has a lower bound

$$\Delta\omega_p \tau_p \geq 2\pi c_B, \quad (1.20)$$

whereby c_B depends on the pulse shape and is 0.441 for a Gaussian pulse.

1.1.2 Interaction of Light with Matter

If an electromagnetic wave propagates through a medium the bound and free charges will react on the fields. This reaction of atoms and molecules is described by the polarization density \mathbf{P} which is related to the electric displacement field

$$\mathbf{D} = \epsilon_0 \mathbf{E} + \mathbf{P}. \quad (1.21)$$

In connection with the Maxwell Equations [29] this leads to the wave equation in matter

$$\left(\nabla^2 - \frac{1}{c^2} \frac{\partial^2}{\partial t^2} \right) \mathbf{E}(\mathbf{x}, t) = \mu_0 \frac{\partial^2}{\partial t^2} \mathbf{P}(\mathbf{x}, t), \quad (1.22)$$

where c is the speed of light in vacuum and μ_0 the permeability of free space. This fundamental equation in optics describes the influence of matter on the electric field as well as the response of matter on the field. External charges, currents and magnetic effects are not included in the equation since their influence is negligible in optical media.

Linear Pulse Propagation in a Dispersive Medium

The propagation of an ultra-short laser pulse within an optical medium is characterized by dispersion. The specific material constants of the medium and the central frequency of the laser pulse determine the dispersion of the system. If the

dispersion is known, the widening of the pulse duration while propagating through the medium can be calculated. Due to the Fourier transformation a laser pulse is composed of several spectral components. Since the refractive index $n = n(\lambda)$ is a function of the wavelength in a dispersive medium each spectral component propagates with a different velocity. This leads to a change of the temporal pulse shape.

In linear optics the interaction between light and matter is described by a linear dependency between the electric field \mathbf{E} and the induced polarization \mathbf{P} . If the medium is homogeneous and isotrop, the polarization can be written as $\mathbf{P} = \epsilon_0 \chi^{(1)} \mathbf{E}$. Substituting this into Equation 1.22 in combination with a Fourier transformation leads to the Helmholtz equation

$$\left(\nabla^2 - \frac{\omega^2}{c^2} \tilde{\epsilon}(\omega) \right) \tilde{\mathbf{E}}(\mathbf{x}, \omega) = 0. \quad (1.23)$$

If the pulse propagates in positive z-direction and has only one polarization component the solution of the Helmholtz equation is given by

$$\tilde{E}(z, \omega) = \tilde{E}(0, \omega) \exp(-ik(\omega)z), \quad (1.24)$$

with the dispersion relation

$$k^2(\omega) = \frac{\omega^2}{c^2} \tilde{\epsilon}(\omega) = \frac{\omega^2}{c^2} (1 + \chi^{(1)}(\omega)) = \frac{\omega^2}{c^2} n^2(\omega). \quad (1.25)$$

The equation contains both absorption and dispersion which are connected via the Kramers-Kronig-relation. In the following the absorption is neglected. The electric field is given by $E(t, z) = \mathcal{F}^{-1}[\tilde{E}(z, \omega)]$. While propagating through the dispersive medium the pulse gains the additional phase $\tilde{\phi}_z(\omega) = k(\omega)z$. Using a Taylor expansion the additional phase can be expressed as

$$\tilde{\phi}_z = \sum_{n=0}^{\infty} \frac{\tilde{\phi}_z^{(n)}}{n!} (\omega - \omega_0)^n, \quad \tilde{\phi}_z^{(n)} = \left. \frac{d^n}{d\omega^n} \tilde{\phi}_z(\omega) \right|_{\omega=\omega_0}, \quad (1.26)$$

$$\tilde{\phi}_z = \tilde{\phi}_z^{(0)} + \tilde{\phi}_z^{(1)}(\omega - \omega_0) + \frac{\tilde{\phi}_z^{(2)}}{2}(\omega - \omega_0)^2 + \frac{\tilde{\phi}_z^{(3)}}{6}(\omega - \omega_0)^3 + \dots, \quad (1.27)$$

whereby a comparison with $\tilde{\phi}_z(\omega) = k(\omega)z$ yields

$$k(\omega)z = k^{(0)}z + k^{(1)}z \cdot (\omega - \omega_0) + \frac{k^{(2)}z}{2} \cdot (\omega - \omega_0)^2 + \dots, \quad (1.28)$$

with $k^{(n)} = d^n k(\omega) / d\omega^n|_{\omega_0}$. This signifies that the phase of the pulse is shifted by $t_\phi = k^{(0)}z / \omega_0 = z / v_{\phi(\omega_0)}$, whereby $v_{\phi(\omega_0)}$ denotes the phase velocity in the medium. In contrast the envelope of the pulse is retarded by $t_g = k^{(1)}z = \tilde{\phi}_z^{(1)} = z / v_g$ with the group velocity v_g . The coefficient $k^{(2)}$ is called group velocity dispersion (GVD).

The dispersion relation (1.25) connects the refractive index $n(\omega)$ with the additional phase $\tilde{\phi}_z(\omega)$ and the following equations are valid:

$$\begin{aligned} \tilde{\phi}_z(\omega) &= \frac{z}{c} \omega n(\omega), & \frac{d\tilde{\phi}_z}{d\omega} &= \frac{z}{c} \left(n(\omega) + \omega \frac{dn}{d\omega} \right), \\ \frac{d^2\tilde{\phi}_z}{d\omega^2} &= \frac{z}{c} \left(2 \frac{dn}{d\omega} + \omega \frac{d^2n}{d\omega^2} \right), & \frac{d^3\tilde{\phi}_z}{d\omega^3} &= \frac{z}{c} \left(3 \frac{d^2n}{d\omega^2} + \omega \frac{d^3n}{d\omega^3} \right). \end{aligned} \quad (1.29)$$

The dispersion of a medium can either be described by the frequency dependency of the refractive index $n(\omega)$ or by its dependence on wavelength $n(\lambda)$. The dependence of the dispersion coefficients $\tilde{\phi}_z^{(n)}$ and $k^{(n)}$ on wavelength is described in Section A.5 of the appendix.

A considerable effect in linear optics which appears in nonisotropic media is called birefringence and is presented in Section A.6 of the appendix.

Nonlinear Optics

The linear description is only valid if the intensity of the incident light pulse is low. For high intensity laser pulses the electric field amplitude E cannot be neglected in relation to the local fields of the atoms or molecules, respectively. The properties of the medium change in a nonlinear way and higher orders of the electric field have to be considered in the equation of the induced polarization \mathbf{P} . As a consequence, a variety of nonlinear optical processes can take place.

The following part is based partly on the description of reference [30]. For the sake of simplicity and in order to focus on the essential features of nonlinear optical behavior, material dispersion, inhomogeneity, and anisotropy are neglected. In this case the induced polarization \mathbf{P} can be expressed in a Taylor expansion

$$\mathbf{P} = \epsilon_0 \left(\chi^{(1)} E + \chi^{(2)} E^2 + \chi^{(3)} E^3 + \dots \right). \quad (1.30)$$

In a more general treatment the vector form of \mathbf{E} and \mathbf{P} has to be taken into account. In this case the local susceptibilities $\chi^{(i)}$ are tensors of the order $(i + 1)$. In addition, the nonlocal response of the medium has to be considered.

For convenience the polarization density is expressed as the sum of a linear $P_L = \epsilon_0 \chi^{(1)} E$ and a nonlinear part $P_{NL} = \epsilon_0 (\chi^{(2)} E^2 + \chi^{(3)} E^3 + \dots)$. Using the relations $c_{n_0} = c/n_0$, $n_0^2 = 1 + \chi^{(1)}$ and $c = 1/(\mu_0 \epsilon_0)^{1/2}$ the fundamental wave Equation 1.22 can be rewritten as

$$\nabla^2 E - \frac{1}{c_{n_0}^2} \frac{\partial^2 E}{\partial t^2} = -S, \quad (1.31)$$

$$S = -\mu_0 \frac{\partial^2 P_{NL}}{\partial t^2}. \quad (1.32)$$

Because P_{NL} and therefore S are nonlinear functions of E , Equation 1.32 is a nonlinear partial differential equation in E .

Two approximate approaches exist to solve the nonlinear wave equation. The first approach is a coupled-wave theory. In this connection the nonlinear wave equation is the basis for the derivation of linear coupled differential equations that govern the interacting waves. The second is an iterative approach and is known as the Born approximation. Here, $S(E)$ is a function of the electric field E and is regarded as a source that radiates itself in a linear medium of refractive index n . Let us suppose that the field E_0 is incident on a nonlinear medium which is confined to some volume. This field creates the radiation source $S = S(E_0)$ that radiates the field E_1 . Due to E_1 the corresponding radiation source $S(E_1)$ is created, radiating the field E_2 , and so on. The first step of this iterative solution is known as the first Born approximation. The second step leads to the second Born approximation and so on.

If the light intensity is sufficiently weak the nonlinearity is relatively small and the first Born approximation is valid. In this case the light propagation through the nonlinear medium can be regarded as a process in which the incident light is scattered by the medium [30]. In a first step the nonlinear polarization density P_{NL} and the radiation source $S(E_0)$ can be determined depending on E_0 . Using the theory of diffraction, the scattered field E_1 can be determined by means of the radiation source in a second step. In this connection, spherical waves are associated with different source points in the medium.

A variety of effects used in femtosecond optics can be explained on the basis of the first Born approximation. A selection of nonlinear optical processes which are of interest for the generation of ultra-short and intense laser pulses with high temporal contrast is proposed in the appendix (A.7). These are the second-harmonic generation (SHG), the AC Kerr effect and the self-phase modulation (SPMD).

1.2 Generation of Ultra-short Pulses

Femtosecond laser pulses can be generated by different kinds of lasers, like solid-state lasers, fiber-lasers or dye-lasers, respectively. Of these, solid-state lasers are most suitable for the generation of high intensity laser pulses. The presented experiments were conducted by means of titanium-sapphire (Ti:sapphire) laser systems which will be presented in more detail in Chapter 2. In this section the principle of mode-locking which is the key mechanism for the generation of ultrashort pulses will be discussed in theory. Afterwards, its practical implementation in a Ti:sapphire oscillator in the form of Kerr-lens mode-locking (KLM) will be explained.

Principle of Mode-locking

A laser can oscillate with many different frequencies that are equally separated and called longitudinal modes. Normally, these modes oscillate independently and are called free-running modes. In this case the intensity of the emitted laser radiation is

constant in time and the mode of operation is described as continuous wave (CW). If the bandwidth of the laser transition is big enough multiple modes of the laser cavity resonator can be excited at once. The use of external means allows the modes to be coupled and locked together. This way the generation of ultrashort laser pulses is possible.

Considering the laser cavity as an ideal cavity resonator, the Maxwell-equations require that the boundary conditions of the electromagnetic field are satisfied at the boundary surface. This leads to standing waves with an electric field amplitude vanishing on the surface of the reflecting mirrors. In this connection each standing wave represents a possible mode of the cavity resonator. In the case of a Fabry-Perot-cavity the condition for a standing wave is satisfied if the optical path $n \cdot L$ of the laser cavity resonator equals to a multiple of half the wavelength λ_m and can be written in the form

$$m \cdot \frac{\lambda_m}{2} = n \cdot L. \quad (1.33)$$

Here m indicates a single mode and n denotes the effective refraction index of the transversal mode in the resonator. The corresponding angular frequency is given by $m(c\pi/nL)$. In first order, the angular frequency separation ω_s between two modes is given by

$$\omega_s = \frac{c_n \pi}{L}, \quad (1.34)$$

whereby $c_n = c/n$. In the following it is assumed that the $q = 0$ mode coincides with the central frequency of the atomic lineshape. In this case the frequency of mode q is given by

$$\omega_q = \omega_0 + q\omega_s, \quad q = 0, \pm 1, \pm 2, \dots \quad (1.35)$$

Within the resonator the electric field of the longitudinal mode q is a standing wave which can be expressed as the difference of two counter-propagating waves with equal amplitudes

$$\begin{aligned} E_q(z, t) &= E_q^l(z, t) - E_q^r(z, t) \\ &= \mathcal{E}_q \cos(\omega_q t + \varphi_q - k_q z) - \mathcal{E}_q \cos(\omega_q t + \varphi_q + k_q z) \\ &= 2\mathcal{E}_q \cdot \sin(k_q z) \cdot \sin(\omega_q t + \varphi_q), \end{aligned} \quad (1.36)$$

where \mathcal{E}_q denotes the real amplitude, $k_q = \omega_q/c_n$ the wavevektor and φ_q phase constant of the q 'th mode.

If the amplification bandwidth exceeds the frequency separation multiple modes can oscillate at the same time in the laser cavity resonator, providing that the lasing threshold is reached. The total electric laser field is given by the superposition of

M single modes within the amplification bandwidth and can be expressed as the sum of all left ($E^l(z, t)$) and right ($E^r(z, t)$) propagating waves

$$E(z, t) = \sum_q E_q(z, t) = \sum_q E_q^l(z, t) + \sum_q E_q^r(z, t) = E^l(z, t) + E^r(z, t), \quad (1.37)$$

whereby the sum goes from $q = -(M - 1)/2$ to $q = (M - 1)/2$.

In CW operation the longitudinal modes of the oscillator vary in amplitude \mathcal{E}_q and the phase constants φ_q are statistically independent. Therefore, the mean total intensity can be written as the sum of the single mode intensities

$$\bar{I}_{\text{cw}} = \sum_q I_q = \sum_q \overline{E_q(t)^2} = \sum_q |\mathcal{E}_q|^2. \quad (1.38)$$

If the phase relation between single modes is fixed (mode coupling), the situation is totally different and Equation 1.38 is not valid any more.

In order to describe the process of mode locking in a qualitative way the amplitudes $\mathcal{E}_q = \mathcal{E}_0$ and the phase constants $\varphi_q = \varphi_0$ are assumed to be constant in time and identical for all modes. In addition the case without dispersion is discussed, implying that the longitudinal mode difference $\Delta\omega_q = \omega_q - \omega_{q-1} = \omega_s$ is constant as well. The reduced field function of the left propagating part of mode q can be described by

$$E_q^{l,+}(t) = \frac{\mathcal{E}_q}{2} \exp[i(\omega_q t - k_q z + \varphi_q)] = \frac{\hat{\mathcal{E}}_q}{2} \exp[i(\omega_q t - k_q z)], \quad (1.39)$$

whereby the complex amplitudes $\hat{\mathcal{E}}_q$ contain the phase of the mode. The sum of all contributing modes is given by

$$E^{l,+}(z, t) = \sum_q \frac{\hat{\mathcal{E}}_q}{2} \exp[i(\omega_q t - k_q z)]. \quad (1.40)$$

Using Equation 1.35 the complex field can be expressed as

$$E^{l,+}(z, t) = \frac{1}{2} \hat{\mathcal{E}} \left(t - \frac{z}{c_n} \right) \exp[i(\omega_0 t - k_0 z)], \quad (1.41)$$

with the complex field amplitude

$$\hat{\mathcal{E}}(t) = \sum_q \hat{\mathcal{E}}_q \exp[iq\omega_s t]. \quad (1.42)$$

Assuming a total number of M modes with $q = 0, \pm 1, \pm 2, \dots, \pm S$ and $M = 2S + 1$ and considering that the complex coefficients are all equal $\hat{\mathcal{E}}_q = \mathcal{E}_q \exp(i\varphi_q) = \mathcal{E}_0 \exp(i\varphi_0) = \hat{\mathcal{E}}_0$, the complex amplitude $\hat{\mathcal{E}}(t)$ can be expressed as

$$\hat{\mathcal{E}}(t) = \hat{\mathcal{E}}_0 \sum_{q=-S}^S \exp[iq\omega_s t] = \hat{\mathcal{E}}_0 \sum_{q=-S}^S x^q = \hat{\mathcal{E}}_0 \frac{x^{S+1} - x^{-S}}{x - 1} = \hat{\mathcal{E}}_0 \frac{x^{S+\frac{1}{2}} - x^{-S-\frac{1}{2}}}{x^{\frac{1}{2}} - x^{-\frac{1}{2}}}, \quad (1.43)$$

whereby $x = \exp[i\omega_s t]$. Using Euler's formula, $\hat{\mathcal{E}}(t)$ can be cast in the form

$$\hat{\mathcal{E}}(t) = \hat{\mathcal{E}}_0 \frac{\sin\left(\frac{1}{2}M\omega_s t\right)}{\sin\left(\frac{1}{2}\omega_s t\right)}. \quad (1.44)$$

Substituting this expression in Equation 1.41 and using $k_s = \omega_s/c_n$ yields the reduced electric field function for the left propagating part of the modes

$$E^{l,+}(z, t) = \frac{1}{2}\hat{\mathcal{E}}_0 \frac{\sin\left[\frac{1}{2}M(\omega_s t - k_s z)\right]}{\sin\left[\frac{1}{2}(\omega_s t - k_s z)\right]} \exp[i(\omega_0 t - k_0 z)]. \quad (1.45)$$

The right propagating part can be evaluated in the same manner and the total electric field is obtained by means of Equations 1.12 and 1.37

$$E(z, t) = \mathcal{E}_0 \cdot \left(\frac{\sin\left[\frac{1}{2}M(\omega_s t - k_s z)\right]}{\sin\left[\frac{1}{2}(\omega_s t - k_s z)\right]} \cdot \cos(\varphi_0 + \omega_0 t - k_0 z) - \frac{\sin\left[\frac{1}{2}M(\omega_s t + k_s z)\right]}{\sin\left[\frac{1}{2}(\omega_s t + k_s z)\right]} \cdot \cos(\varphi_0 + \omega_0 t + k_0 z) \right). \quad (1.46)$$

Thus the electric field of M coupled modes consists of two plane waves with the center frequency ω_0 propagating in opposite directions with envelope functions having a periodicity equal to the roundtrip time T_R in the laser cavity resonator

$$T_R = \frac{2\pi}{\omega_s} = \frac{2Ln}{c}. \quad (1.47)$$

Figure 1.1 shows the spatial dependence of a series of $M = 7$ mode-locked standing waves at different points in time. Here, the central angular frequency is $\omega_0 = 20 \cdot (c\pi/nL)$, $n = 1$, $L = 1$ m and $q \in [-3, 3]$. In the lower parts of the charts the electric field amplitude of the single contributing modes are shown in different colors. Above, the resulting total electric field (Formula 1.46) is depicted. Because of the constant phase relation between the single modes, they can interfere constructively at some points in space and due to the fact that each mode oscillates with a slightly different angular frequency ω_q the maximum of the interference moves in space.

Since the time difference T_R of two pulses is equal to the round trip time within the laser cavity (Equation 1.47) the oscillation characteristics of a mode-locked laser can be described as a circulating pulse within the laser cavity moving with the velocity $c_n = c/n$. If one of the cavity mirrors is partially transmitting, the laser radiation is emitted in form of short pulses. In this case one of the wave packets $E^l(z, t)$ or $E^r(z, t)$ is transmitted at $z = 0$ or $z = L$. At $z = 0$ the intensity of the emitted pulse $I(t)$ (neglecting the dispersion of the mirror) is given by

$$I(t) = |(E^l(z = 0, t))|^2 = T_M \mathcal{E}_0^2 \cdot \frac{\sin^2\left[\frac{1}{2}M(\omega_s t)\right]}{\sin^2\left[\frac{1}{2}(\omega_s t)\right]} \cdot \cos^2(\varphi_0 + \omega_0 t) \quad (1.48)$$

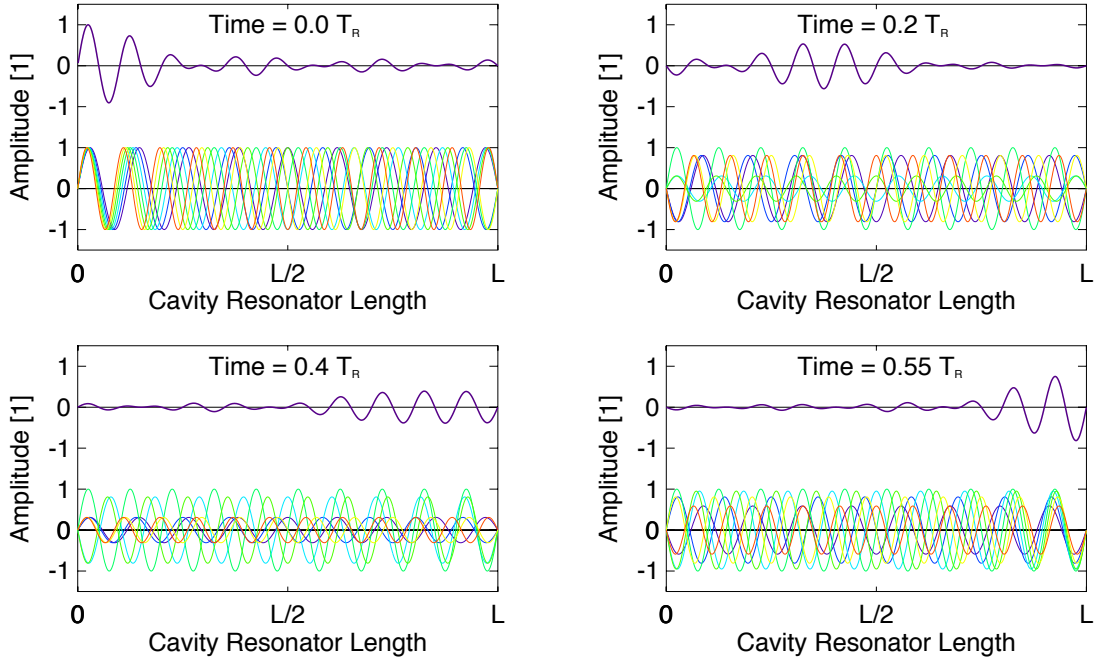


Figure 1.1: Electric field amplitude of an idealized mode-locked laser pulse within the laser cavity resonator at different moments in time. The lower curves show the contributing single modes, the upper curves represent their superpositions

where T_M stands for the transmittance of the mirror. The intensity of a CW-laser is lower in comparison to a mode-locked laser. In CW-operation, the mean intensity is given by Equation 1.38 with the proportionality

$$I_{cw} \propto M |\mathcal{E}_0|^2. \quad (1.49)$$

The maximum intensity of a mode locked laser $I_{ml, \max}$ is given by

$$I_{ml, \max} \propto M^2 |\mathcal{E}_0|^2. \quad (1.50)$$

The Titanium Sapphire Oscillator

The active medium of a Ti:sapphire oscillator [31] is a crystal consisting of Al_2O_3 doped with Ti_2O_3 molecules. A small part of the Al^{3+} ions is replaced by Ti^{3+} ions which are responsible for the laser transition. The absorption and emission spectrum of a Ti:sapphire crystal is shown in Figure 1.2.A.

The active medium absorbs in the wavelength range of 400 to 660 nm and the emission bandwidth ranges from 600 to 1070 nm with a maximum intensity at about 800nm. Since the absorption and emission spectra overlap in a small region, laser emission is only possible over 660 nm.

The pulse repetition frequency of a Ti:sapphire oscillator is usually around 70 to

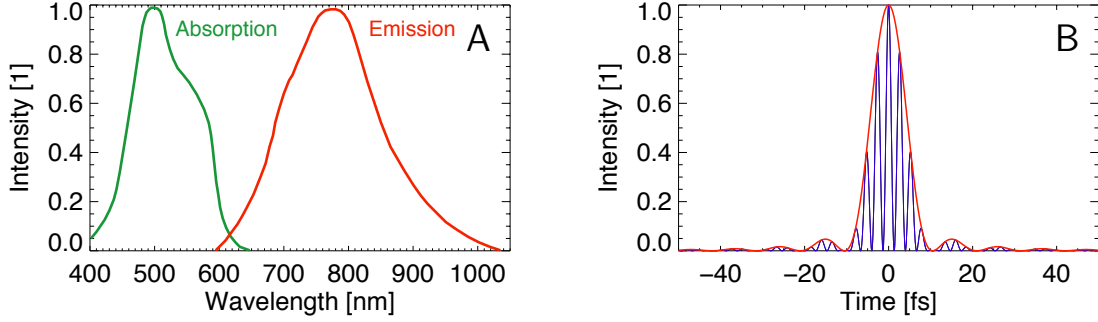


Figure 1.2: **A** - Absorption and emission spectrum of a Ti:sapphire crystal. **B** - Intensity of an idealized mode-coupled Ti:sapphire laser pulse.

90 MHz. Figure 1.2 shows the idealized intensity of an mode-coupled laser pulse using Equation 1.48 with a repetition frequency of 80 MHz and a bandwidth of 700 to 900 nm. In this case more than one million modes are coupled resulting in a femtosecond laser pulse with a FWHM lower than 10 fs.

In reality not every simplification used in the derivation of Equation 1.46 and 1.48 is valid. The functional dependence of a real mode-coupled pulse is more complex and additional parameters have to be taken into account. Nevertheless Equation 1.48 can explain the principal connection between the pulse length and the amount of coupled modes. The more modes are involved the smaller is the width of the envelope function. This dependence can be expressed in a more general way by

$$\Delta\nu\Delta\tau \geq K, \quad (1.51)$$

where $\Delta\tau$ denotes the FWHM of the pulse in time and K is a constant which depends on the pulse shape. In the case of a Gaussian pulse K accounts to $4 \ln(2)$. If the longitudinal modes are coupled, their phase difference $\Delta\varphi_m(t) = \Delta\varphi$ and thus the instantaneous angular frequency (Equations 1.16 and A.12) is constant in time. In this case the pulse is called unchirped and the " \geq " - sign in Relation 1.51 can be replaced by an "=" - sign. This means that the pulse is bandwidth-limited (Fourier transform-limited). This is the shortest pulse which can be generated with a given spectral width.

The pulse duration $\Delta\tau$ as a function of the wavelength is then given by the equation

$$\Delta\tau = K \frac{\lambda_0^2}{\Delta\lambda c}, \quad (1.52)$$

whereby λ_0 is the central wavelength, $\Delta\lambda$ the FWHM of the wavelength and c is the speed of light in vacuum.

The transmission of the laser light through the optical components in the Ti:sapphire oscillator leads to a group velocity dispersion. In order to avoid a chirp of the pulse and thus an increase of the temporal pulse width an integrated prism compressor

is used for compensation.

In principle there are active and passive ways to couple the phases within the laser cavity and to achieve a mode-locked operation of the oscillator.

Active mode-coupling can be realized by the use of an acousto-optic Modulator (AOM). In this case a control loop monitors the current repetition rate of the laser and continuously tunes the frequency of the AOM. This way the coupling of the resonator modes is initiated and maintained.

Kerr-lens Mode-locking

The most convenient way of passive mode-coupling is the so called Kerr-lens mode-locking (KLM) [32, 33]. In this connection an absorber medium in combination with a small aperture is implemented in the cavity. Within the absorber medium the Kerr-lens effect takes place which reduces the beam waist for intensive light pulses. Since the aperture is positioned in the focus of the Kerr-lens, the CW light is blocked and mode-coupling is achieved by the interplay of both components.

The Kerr-lens effect is basically the focussing of an intense laser field. If the electric field amplitude E is big enough, the refractive index n gets intensity dependent within the Kerr medium.

Within the oscillator the pump beam is focused on the Ti:sapphire crystal. Since the intensity of the pump beam is higher in the center than at the edges of the crystal, also the intensity of the emitted light is higher in the center. This intensity gradient leads to a distortion of the wave front and thus to self-focussing of the laser beam. Because the focussing effect is higher for higher intensities, the configuration of the resonator causes the formation of stable pulses from random intensity fluctuations.

1.3 Chirped Pulse Amplification

In order to amplify laser pulses to intensities many times higher than those of the laser oscillator, the so called chirped pulse amplification (CPA) technique is used [34]. The active laser medium of the amplifier chain consists of nonlinear crystals which are excited by external pump laser until a population inversion is reached. The pulse of the laser oscillator is linearly chirped by means of different propagation distances of its spectral components. This temporally stretched oscillator pulse is then used as a seed pulse in the amplification chain. This allows for the amplification of the pulse to saturation while a low peak power is maintained at the same time. After amplification a compressor restores the original short pulse width. This way a damage of the optical components is circumvented.

1.4 Contrast Enhancement

The contrast $C(t)$ of a laser pulse is defined by the ratio between the peak intensity $I(t_0)$ of the main pulse and the intensity $I(t)$ at a given time t [35]:

$$C(t) = \frac{I(t_0)}{I(t)}. \quad (1.53)$$

Figure 1.3 shows a schematic of the temporal intensity distribution of a typical multi-terawatt laser pulse. Its temporal evolution is governed by several processes during the amplification of the pulse.

The local intensity peaks that occur later than the main pulse are called post-pulses. These are normally generated by inner reflections on mirrors. If the coating of a mirror is somehow damaged and its reflection coefficient diminished, the main pulse is partially transmitted and reflected on the rear surface of the substrate. Due to the additional optical length $l \cdot d$ the pulse is retarded by $t = (l \cdot d)/c$.

The temporal intensity pedestal before the main pulse consists of different contributions. One part is caused by the so called amplified spontaneous emission (ASE). Its temporal occurrence is limited by the fluorescence lifetime $\tau_{12} = 1/A_{12}$ of the amplification medium, which has a value of $5 \mu\text{s}$ for titanium sapphire [35]. The ASE has a typical contrast of $10^6 - 10^{11}$ and a duration of few nanoseconds.

The occurrence of pre-pulses on the nanosecond-scale can be explained by the difference of the repetition rate of the oscillator and the amplification chain. The repetition frequency of the oscillator is determined by the length of the laser cavity

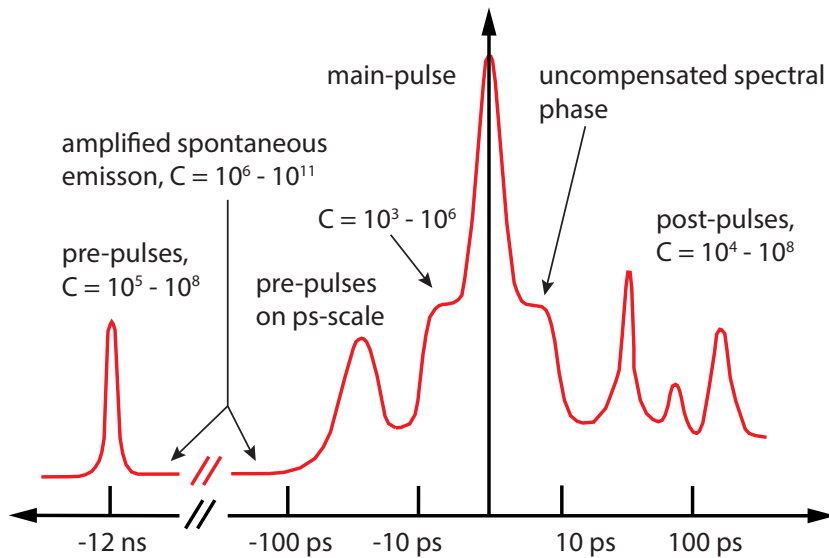


Figure 1.3: Typical temporal intensity distribution of a multi-terawatt laser pulse.

(Equation 1.47). A typical Ti:sapphire-oscillator operates at around 80 MHz which corresponds to temporal pulse distance of 12.5 ns. In order to reduce the frequency to 10 Hz which is typically the operating frequency of the amplifier system, optical switches (Pockels-cells) are used. These cells make use of an electro-optical effect which rotates the polarization plane of the incident light. A subsequent polarization filter then blocks or transmits the laser pulse depending on the applied voltage. Since the transmittance of the filter is $\geq 0.1\%$ in reverse-biasing, pre-pulses of this kind are not entirely suppressed before the amplification chain.

Similarly a pre-pulse can be generated by the leakage of a regenerative amplifier if it is employed in the laser system. In this connection the laser pulse is amplified in several round trips before it gets transmitted to the subsequent amplifiers by means of a Pockels-cell and a polarization dependent mirror. Typically, the pre-pulse is situated ~ 10 ns before the main pulse and has a typical contrast of $\sim 10^5$.

In addition pre-pulses on the picosecond-scale can be generated due to unwanted reflections in the regenerative amplifier. Since the surface of the Pockels-cell is not antireflection coated and perpendicular to the optical path the main pulse is subjected to unwanted reflections.

Besides, pre-pulses on the picosecond-scale with a broad range of contrasts and durations can be transformed from post-pulses at similar absolute delay values due to the nonlinearity of CPA-systems [36].

A slow decrease of the picosecond contrast to the ASE level indicates the existence of higher orders of the spectral phase, which are not entirely compensated in the compressor.

In principle the temporal contrast of high intensity laser pulses can be classified into two regimes. On the nanosecond-scale the contrast is defined by the ratio between the peak intensity of the main pulse and the intensity of the preceding ASE. The contrast ratio on the picosecond-scale is normally reduced due to one or several pre-pulses with intensities higher than the ASE-level or by the existence of uncompensated higher orders of the spectral phase $\Phi(\omega)$.

If the intensity of the pedestal reaches values of $10^{10} - 10^{13}$ W/cm² a pre-plasma can be generated depending on the temporal length and the kind of the illuminated material (c.f. Section 3.3).

In order to circumvent a significant influence of ionization by ASE or pre-pulses the contrast has to be better than 10^6 when intensities of approximately 10^{19} W/cm² are reached. Because of the hydrodynamic expansion of the pre-plasma the main pulse cannot interact with a steep electron density gradient and the underlying physics of the laser-plasma interaction is fundamentally changed.

For this reason a high temporal contrast is indispensable for several mechanisms. These are for example the generation of high harmonics on solids [37] or the radiation pressure acceleration (RPA) of ultra-thin foils [38].

One way to enhance the contrast is to minimize the creation of ASE or the generation of pre-pulses in the first place. This is normally achieved by a sophisticated setup of the amplification chain, but also the temporal shaping of the pulse can

influence the contrast ratio. An other way of contrast enhancement consists in the suppression of all light preceding the main pulse. Therefore, a temporal switch with a small response time is needed. Conventionally ultra-fast Pockels-cells are used in this context, but their efficiency is limited by their rise time which is in the range of hundreds of picoseconds.

Essentially, every realization of a temporal switch which operates on a femtosecond time scale is governed by a nonlinear optical process. If the process of contrast enhancement depends on the intensity $I(t)$, it can be described by means of a filter function $f(I(t))$. The filtered intensity $I_f(t) = f(I(t))$ can be expressed by a Taylor expansion

$$f(I(t)) = \sum_n c_n \cdot I^n(t) \tag{1.54}$$

whereby nonlinear filter processes are indicated by the appearance of coefficients $c_n \neq 0$ ($n > 1$). The contrast enhancement ΔC can be defined as the ratio of the contrast of the filtered laser pulse C_f and the contrast C of the initial laser pulse

$$\Delta C = \frac{C_f}{C} = \frac{I_f(t_0)/I_f(t)}{I(t_0)/I(t)} = \frac{I(t)}{f(I(t))} \cdot \frac{f(I(t_0))}{I(t_0)}. \tag{1.55}$$

Obviously, a contrast enhancement is not possible if the filter function is linear $f(I(t)) = c_1 \cdot I(t)$ and gets more and more efficient the higher the order of the nonlinear optical process.

In order for the change to happen very fast a high order nonlinearity is desirable. It means that a small change in intensity can make the desired effect go from negligible to dominant. A usual setup for contrast enhancement consists of a focussing and a collimating element. The nonlinear optical component is usually placed in the convergent beam on a linear stage. By moving the component closer or further towards the focus the intensity trigger can be set to the up-flank of the pulse.

In the following the plasma mirror and the cross-polarized wave (XPW) generation process are presented, as two examples for contrast enhancement that are applied at the MBI.

Plasma Mirror

The functional principle of a plasma mirror consists in the abrupt rise of the reflectivity of a material as soon as an intensity threshold of the incident light is reached. For that purpose the laser pulse is slightly focused on a dielectric surface. If the illumination parameters of the incident pulse and the target material are chosen in a way that the reflectivity is small, most part of the ASE and the pre-pulses are transmitted. If the focussing of the pulse is adjusted correctly the intensity threshold for plasma creation is reached in the moment the rising edge of the main pulse arrives at the surface. Instantly an overcritical plasma is generated on the

time scale of femtoseconds. Since the laser pulse cannot penetrate into the plasma further than the skin depth, the light gets reflected on the plasma surface. By means of a plasma mirror the contrast can be increased by more than two orders of magnitude [39]. The use of two dielectric substrates and the staged plasma creation on both surfaces can increase the contrast even further. This setup is called double plasma mirror and leads to a contrast enhancement of four orders of magnitude [40, 41].

Cross-polarized wave generation

The so called cross-polarized wave (XPW) generation process can be described as a self-induced nonlinear intensity dependent rotation of the polarization state. Figure 1.4 illustrates the basic idea of how this process can be used for contrast enhancement.

A linearly polarized laser pulse impinges on a polarizer (\parallel). The transmitted wave is called fundamental wave (FW) and is polarized in (\parallel)-direction. It has the initial amplitude A_0 and the angular frequency ω^\parallel . The focussing of the FW into an nonlinear medium initiates the XPW process which can be classified in the group of frequency degenerate (four wave mixing [42])

$$\omega_{out}^\perp = \omega^\parallel + \omega^\parallel - \omega^\parallel. \tag{1.56}$$

As a result of this process a linearly polarized wave (XPW) with the amplitude B and the angular frequency ω_{out}^\perp is generated. It has the same frequency as the FW, but a perpendicularly oriented polarization (\perp). A second polarizer (\perp) is used for the separation of the XPW and the FW. The process occurs in media with

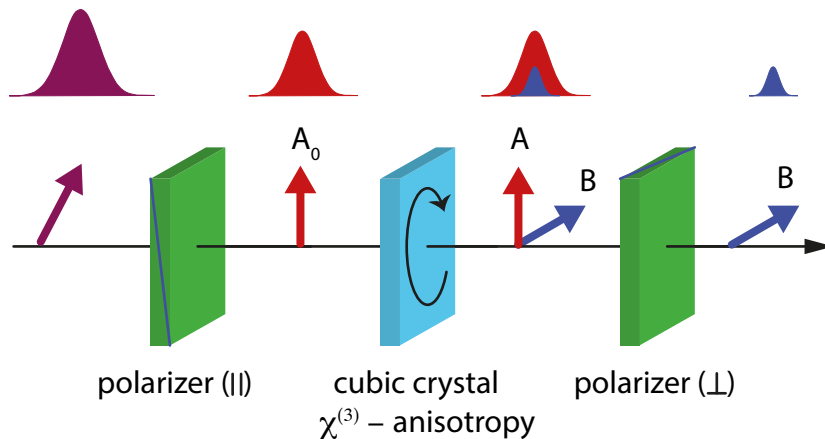


Figure 1.4: Basic concept of using the XPW generation process for contrast enhancement.

anisotropy of third order nonlinearity that is an anisotropy of the $\chi^{(3)}$ tensor

$$\sigma = \frac{\chi_{xxxx}^{(3)} - (\chi_{xxyy}^{(3)} + 2\chi_{xyyx}^{(3)})}{\chi_{xxxx}^{(3)}} \neq 0. \quad (1.57)$$

A cubic crystal provides this prerequisite and is isotropic in respect to linear properties at the same time. Therefore, birefringence cannot occur and phase and group velocities of both waves, the XPW and the FW, are identical. This leads to ideal phase and group velocity matching within the crystal and thus results in a very high efficiency η of the XPW generation process.

The self-phase modulation of the component A polarized in the direction of the FW and the generation of the XPW with amplitude B can be described [43] on condition $|B| \ll |A|$ by the equations

$$\frac{dA}{dz} = i\gamma_{\parallel} |A|^2 A, \quad \frac{dB}{dz} = i\gamma_{\perp} |A|^2 A, \quad (1.58)$$

whereby $\gamma_{\parallel} = \gamma_0[1 - (\sigma/2)\sin(2\beta)]$, $\gamma_{\perp} = -(\sigma/4)\sin(4\beta)$, $\gamma_0 = (6\pi/\lambda m)\chi_{xxxx}^{(3)}$ and $\beta = m\pi/4$ (m an odd number) [43, 44]. With the initial conditions $B(0) = 0$ and $A(0) = A_0$ (A_0 real), the solution to the systems of Equations 1.58 is given by

$$A = A_0 \exp(i\gamma_{\parallel} A_0^2 L), \quad (1.59)$$

$$B = A_0 (\gamma_{\perp}/\gamma_{\parallel}) [\exp(i\gamma_{\parallel} A_0^2 L) - 1]. \quad (1.60)$$

where L is the length of the nonlinear media. The efficiency of the XPW process is defined as the ratio between the intensity of the XPW I_{out} at the output of the nonlinear medium and the input intensity I_{in} of the FW

$$\eta = \frac{I_{out}}{I_{in}} = \frac{|B(L)|^2}{|A_0|^2} = 4\left(\frac{\gamma_{\perp}}{\gamma_{\parallel}}\right)^2 \sin^2(\gamma_{\parallel} |A|^2 L/2). \quad (1.61)$$

If self-phase modulation is small $\gamma_{\parallel} |A|^2 L \leq 1$ the expression for η can be simplified

$$\eta = (\gamma_{\perp})^2 |A|^4 L^2 \propto \gamma_{\perp}^2 I_{in}^2 L^2. \quad (1.62)$$

The integration of the XPW generation process within the amplification chains of the high intensity laser systems at MBI leads to a contrast enhancement $\Delta C = 10^4$ and is described in detail in reference [45].

1.5 Gaussian Optics and the Focussing of a Laser Pulse

After amplification and compression of the laser pulse, the intensity can be increased further by focussing the beam with parabolic mirrors. In this case the minimum laser focus and the maximum intensity is only limited by diffraction. The fundamental transversal mode within a laser cavity constitutes a Gaussian beam. Therefore, the Gaussian optics is predestined to model the propagation of a laser beam [30].

For a time-harmonic wave of frequency, the Maxwell's equations (wave equation) take the form of the Helmholtz equation (Formula 1.23). In free space it can be expressed by

$$(\Delta + k^2) E(x, y, z) = 0, \quad (1.63)$$

where $E(x, y, z)$ is the complex field amplitude for any polarization component of the electric field vector and $k = n\omega/c$. Under the assumption, that the "principal" propagation direction is along the z-axis, the complex field amplitude can be written as product of a fast and slowly varying part in z-direction

$$E(x, y, z) = \psi(x, y, z)e^{-ikz}, \quad (1.64)$$

where $\psi(x, y, z)$ describes the transverse profile and its slow variation in propagation direction. Substituting this expression into the Helmholtz equation yields

$$\nabla^2 \psi - 2ik \frac{\partial \psi}{\partial z} = 0. \quad (1.65)$$

In order to find a solution for paraxial waves, the so called "Paraxial approximation" in wave analysis can be applied

$$\left| \frac{\partial^2 \psi}{\partial z^2} \right| \ll 2k \left| \frac{\partial \psi}{\partial z} \right|, \quad \left| \frac{\partial^2 \psi}{\partial z^2} \right| \ll \left| \frac{\partial^2 \psi}{\partial x^2} \right|, \quad \left| \frac{\partial^2 \psi}{\partial z^2} \right| \ll \left| \frac{\partial^2 \psi}{\partial y^2} \right|. \quad (1.66)$$

This means that the variation of the field amplitude in propagation direction is both, slow on the scale of λ and slow on the scale of transverse extent of the wave. Therefore, the longitudinal component $\partial^2 \psi / \partial z^2$ can be neglected and the Helmholtz equation can be written in the form of the so called *paraxial wave equation*

$$\left(\nabla_{\perp}^2 - 2ik \frac{\partial}{\partial z} \right) \psi(x, y, z) = 0, \quad (1.67)$$

where $\nabla_{\perp}^2 = \partial^2 / \partial x^2 + \partial^2 / \partial y^2$. Under the assumption that the solution has cylindrical symmetry, the paraxial wave equation can be written in the form

$$\frac{1}{r} \frac{\partial}{\partial r} \left(r \frac{\partial \psi}{\partial r} \right) \nabla^2 \psi - 2ik \frac{\partial \psi}{\partial z} = 0, \quad (1.68)$$

with $r^2 = x^2 + y^2$. In this case the solution given by the fundamental (lowest-order TEM₀₀) Gaussian mode ψ_0 and the complete expression for the fundamental Gaussian beam can be expressed by

$$\begin{aligned} E(x, y, z) &= E_0 \psi_0(x, y, z) \exp(-ikz) \\ &= E_0 \frac{w_0}{w(z)} \exp\left(-\frac{r^2}{w^2(z)}\right) \exp\left(-i\frac{kr^2}{2R(z)}\right) \exp[-i(kz - \phi(z))]. \end{aligned} \quad (1.69)$$

The beam waist w_0 (or minimum spot size radius) is connected to the Rayleigh range z_0 by the equation

$$z_0 = \frac{\pi}{\lambda} w_0^2. \quad (1.70)$$

Therefore, it determines the spot size radius $w(z)$, the radius of curvature $R(z)$ and the Guoy phase shift $\phi(z)$ of the Gaussian beam

$$w(z) = w_0 \sqrt{1 + \left(\frac{z}{z_0}\right)^2}, \quad (1.71)$$

$$R(z) = z \left[1 + \left(\frac{z_0}{z}\right)^2\right], \quad (1.72)$$

$$\phi(z) = \arctan\left(\frac{z}{z_0}\right), \quad (1.73)$$

depending on the position z (cf. Figure 1.5.A). Due to Equation 1.70 also the intensity

$$I(r, z) = |E(r, z)|^2 = I_0 \left(\frac{w_0}{w(z)}\right)^2 e^{-\frac{2r^2}{w(z)^2}} \quad (1.74)$$

is connected to the Rayleigh range z_0 [29, 30]. The power of the laser beam

$$P = \int_0^\infty I(\tilde{r}, z) 2\pi\tilde{r} d\tilde{r} = \frac{1}{2} I_0 (\pi w_0^2) \quad (1.75)$$

is connected with the integral of the intensity over a transversal plane at position z . Similarly, the power $P(r)$ passing through a circle of radius r in the transverse plane at position z is can be defined by

$$P_r(r) = \int_0^r I(\tilde{r}, z) 2\pi\tilde{r} d\tilde{r} \quad (1.76)$$

and the ratio q between the encircled power and the total power can be expressed by

$$q = \frac{P_r}{P} = \int_0^r I(\tilde{r}, z) 2\pi\tilde{r} d\tilde{r} = 1 - e^{-\frac{2r^2}{w(z)^2}}. \quad (1.77)$$

For a Gaussian distribution, the intensity drops down to $1/e^2$ of its maximum value for $r = w(z)$. In this case the ratio q is approximately 86%. At the position $r = r_{\text{HM,I}}(z)$, with

$$r_{\text{HM,I}}(z) = \sqrt{0.5\ln(2)} \cdot w(z), \quad (1.78)$$

the intensity (Equation 1.74) is at half of its maximum value in the transverse plane at position z . Therefore, the FWHM of the intensity is defined by

$$d_{\text{HM,I}}(z) = 2 \cdot r_{\text{HM,I}}(z) = 2 \cdot \sqrt{0.5\ln(2)} \cdot w(z). \quad (1.79)$$

For a circle with radius $r = r_{\text{HM,I}}(z)$ the fraction of the power q which is transmitted through this circle is 50%. Naturally, this value can be reduced further due to aberrations and deviations from the Gaussian profile.

The focussing of an aberration free Gaussian beam using an ideal parabolic mirror is limited by the laws of Gaussian optics, i.e. the diffraction of the beam. Using a parabolic mirror with the focal length f , a beam with waist size w_0 can be focused on an area with the new beam waist

$$w'_0 = \frac{w_0}{\sqrt{1 + \left(\frac{z_0}{f}\right)^2}}. \quad (1.80)$$

If the beam is collimated, i.e. if the Rayleigh length of the incident beam is much longer than the focal length of the parabolic mirror, the equation can be approximated by

$$w'_0 \approx \frac{\lambda}{\pi w_0} f = \theta_0 f, \quad (1.81)$$

where θ_0 is the half opening angle of the focussed beam. In this case w'_0 is the smallest possible waist size. Since the beam diameter $D \approx 2w_0$ determines the

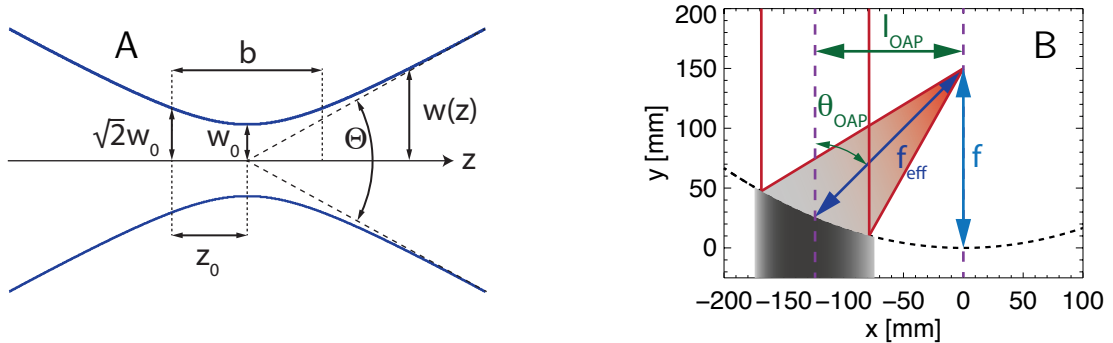


Figure 1.5: **A** - Dependence of the spot size radius $w(z)$ of a Gaussian beam on the position z . **B** - Parameters of an off-axis parabolic mirror.

aperture of the parabolic mirror, the characterization of the mirror by the f-number

$$k_f = \frac{f}{D} \approx \frac{f}{2w_0} \quad (1.82)$$

is reasonable. This allows for a simple estimation of the smallest possible waist size

$$w'_0 = \frac{2\lambda}{\pi} F_A = \frac{2\lambda}{\pi} \frac{f}{D}. \quad (1.83)$$

In order to separate the focus position from the incident beam, a segment of a paraboloid can be applied, as illustrated in Figure 1.5.B. If the optical axis of the incident beam does not coincide with the parallel axis of paraboloid the focus point has the distance l_{OAP} to optical axis. This distance is referred to as off-axis-distance and determines the off-axis-angle θ_{OAP} by the equation

$$l_{\text{OAP}} = 2f \tan\left(\frac{\theta_{\text{OAP}}}{2}\right). \quad (1.84)$$

The effective focal length f_{eff} is connected to the off-axis-angle θ_{OAP} by the equation

$$f_{\text{eff}} = \frac{2f}{1 + \cos(\theta_{\text{OAP}})}. \quad (1.85)$$

2 Laser System

All presented experiments of this thesis were conducted with the high field laser (HFL) system at the Max-Born-Institute (MBI). The system allows for pump-probe experiments at intensities $\geq 5 \cdot 10^{19} \text{ W/cm}^2$. This chapter gives a short overview of the laser system and explicates the synchronization and focus alignment of two laser beams in the experiment.

2.1 Specifications

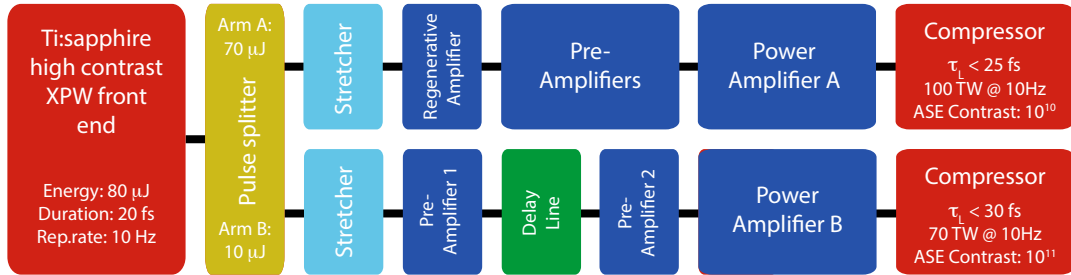


Figure 2.1: Schematic setup of the multi TW laser system at the MBI. Laser arm A is illustrated by the upper amplification chain and laser arm B by the lower one.

Figure 2.1 is schematic of the multi TW laser system at the MBI. It consists of two separate Ti:sapphire amplifier chains which are optically synchronized and seeded with a XPW-frontend. Due to the different architecture of these chains, laser pulses with different pulse duration and temporal contrast are generated.

The upper amplification chain is called *laser arm A* and provides a pulse power of 100 TW within a pulse duration τ_L of 25 fs (FWHM of intensity). It is a commercial system from Amplitude TechnologyVR and is based on a regenerative amplifier inclusive spectral steering. Its laser contrast, i.e. the ASE background level, has a value between 10^9 and 10^{10} . *Laser arm B* is illustrated by the lower amplification chain. It is designed and constructed at MBI and consists only of multi-pass amplifier sections. It delivers pulses with 30 fs duration and a power of 70 TW. Its ASE background level is between 10^{10} and 10^{11} .

High Temporal Contrast Front End

As described in Section 1.4 the temporal contrast of a high power laser system is highly important for experiments on laser ion acceleration. The main source of ASE in high power Ti:sapphire laser systems is usually the front-end. Since the main amplification is achieved with the first amplifier, this stage is most important for the final contrast ratio. The low energy level of the oscillator, losses in the stretcher and implementations for the correction of the spectral phase can lead to a low signal-to-noise ratio and the high amplification factor ($\sim 10^6 - 10^7$) limits the bandwidth.

Conventionally, fast Pockels-cells were installed after the first amplifier to reduce the nanosecond ASE pedestal. Depending on the pump conditions of the Ti:sapphire crystal and the timing of the Pockels-cells a laser contrast in the range of $10^7 - 10^8$ could be realized with laser arm B in this case [8].

For the presented experiments a novel high temporal contrast front end was developed [45] and implemented in the high-power laser system at the MBI. The system is based on negatively and positively chirped pulse amplification (NPCPA) and the XPW generation process (cf. Section 1.4). The XPW generation takes place in a single CaF₂ [011] crystal arrangement and has an efficiency η of 7%. The generated pulses have a bandwidth of 80 nm, a stability of 6% and are applied to seed both laser arms. Figure 2.2.A shows several measurements with a third order cross correlator. The different colors illustrate the final contrast of laser arm A and laser arm B with and without the application of the novel high temporal contrast frontend.

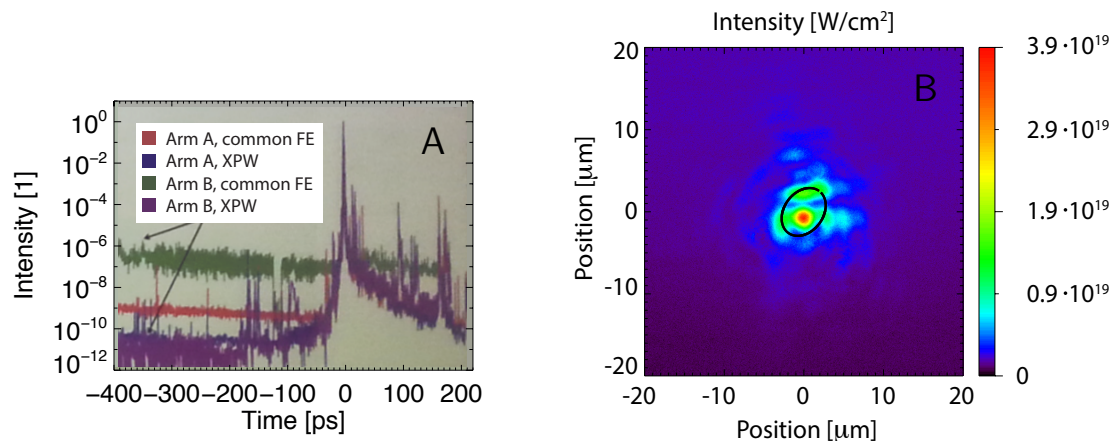


Figure 2.2: **A** - Contrast of laser arm A and laser arm B with and without the implementation of the novel high temporal contrast frontend. **B** - Typical focal spot in experiments due to the focussing of the laser beam with an off-axis parabolic mirror ($f/1.5$).

Laser Focussing and Intensity Calculations

To circumvent a damaging of optical components the high energy laser pulse is extended to a beam diameter of approximately 70 mm before compression. The resulting ultra-short pulse is guided in a vacuum beam-line to the experimental chamber. Here, an off-axis parabolic mirror (f/1.5) with a focal length of 15 mm is applied to focus the beam to a focal spot of a few micrometer (cf. Section 1.5). Figure 2.2.B shows the typical intensity distribution of the focused laser pulse. The diffraction rings are partially caused by imaging the focus with an additional lens. However, without flattening the beam front which is distorted after propagating through the amplification chain [46], an ideal focussing of the laser pulse is impossible. Since the application of a deformable mirror was not possible for the presented experiments some of the side maxima may be due to this effect.

The intensity values were calculated with respect to the available pulse power after compression and transmission through the beam-line. For the calculation of averaged intensity values the following procedure was applied. First a two-dimensional Gaussian distribution was fitted to the measured intensity distribution. As a result the following parameters were obtained. The off-set value, the position of the calculated maximum, the rotation-angle of the distribution and two beam waists $w_{0,a}$ and $w_{0,b}$ along the rotated axes.

The black curve in Figure 2.2.B borders the area where the intensity of the fitted distribution is above $1/e$ of the calculated maximum (cf. Section 1.5). The half-axes of this rotated ellipse correspond to the values $w_{0,a}/\sqrt{2}$ and $w_{0,b}/\sqrt{2}$, respectively, whereby $w_{0,a}$ and $w_{0,b}$ denote the beam waists of the rotated one-dimensional Gaussian distributions. This area could be used to calculate the mean intensity of the measured distribution.

Similarly, an ellipse with the half-axes $\sqrt{0.5 \ln(2)} \cdot w_{0,a}$ and $\sqrt{0.5 \ln(2)} \cdot w_{0,b}$ (cf. Equation 1.78) could be applied. In this case the ellipse borders the area where the intensity of the fitted distribution is greater than half of the calculated maximum value. If not stated otherwise, this definition is used for all calculated intensity values in this thesis. In the presented case the measured distribution has a FWHM of about $2.5 \mu\text{m} - 3.0 \mu\text{m}$.

2.2 Synchronization and Focus Alignment

Due to the common front-end both laser arms are intrinsically synchronized to each other. However, to allow for an equal pulse propagation length from the oscillator to the experimental chamber, a delay line of approximately 25 m was implemented in laser arm B. For the fine tuning of both laser pulses an additional optical delay stage was placed in the experimental chamber. Using a second-order autocorrelator, a jitter of several femtoseconds between both pulses could be measured at this position.

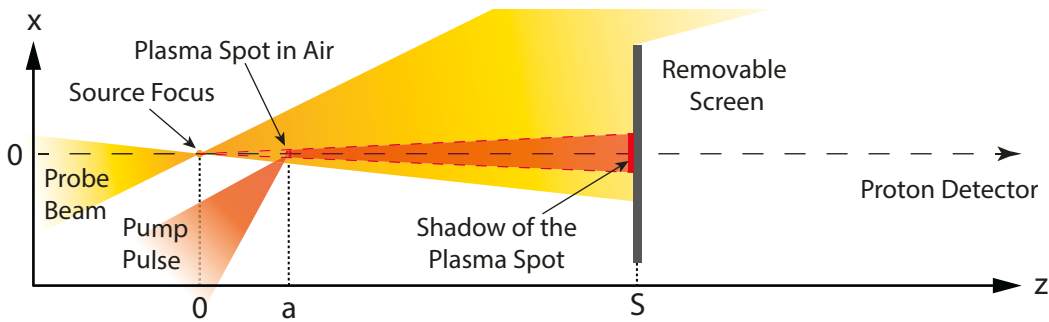


Figure 2.3: Setup for the synchronization of the laser pulses and the alignment of the laser foci applying the plasma shadowgraphy method.

To calibrate the delay stage in the experimental chamber in 10 Hz operation mode, the plasma shadowgraphy method was applied. Both laser arms were focused inside the experimental chamber as illustrated by Figure 2.3.

One laser was used as a probe. Its focus point was placed at a defined and fixed position in space. This position was used in following proton imaging experiments as the source point of the probing proton beam. Behind the source focus (in z -direction), the laser light of the probe beam is divergent. It was used to illuminate the surface of a removable screen, which was placed before the entrance slit of an energy sensitive proton detector. The direction to the center of this detector was marked by a target point on the screen, as shown in Figure 2.4.A. Thus, the position of the source focus and the target point on the screen defined the central axis in z -direction for all experiments.

The focus of the pump laser was positioned at a defined distance in z -direction to the source focus and its intensity was increased until the laser radiation generated a plasma in air. Due to the local increase of the electron density, the created plasma acted like a concave lens. The probe beam was influenced by this lens and a shadow of the plasma spot became visible at the removable screen.

Figure 2.4.B shows a photograph of this shadow, whereby a charge-coupled device (CCD) camera was used, which is sensitive to infra red (IR) radiation. By means of the optical delay stage the creation of the plasma at the pump focus can be varied in time with respect for the arrival time of the probing laser light at the point $z=a$. The position of the stage at which the probe beam is barely distorted corresponds to the time when both pulses are overlapping in the plasma at $z=a$. The plasma lifetime is of the order of nanoseconds and thus relatively long compared to the laser pulse duration. Therefore, the position where the plasma is generated can be found easily, which is an advantage over conventional correlation devices.

For comparison, the temporal observation window of Cross-correlators or streak cameras is much smaller, of the order of a few picoseconds. The accuracy of the

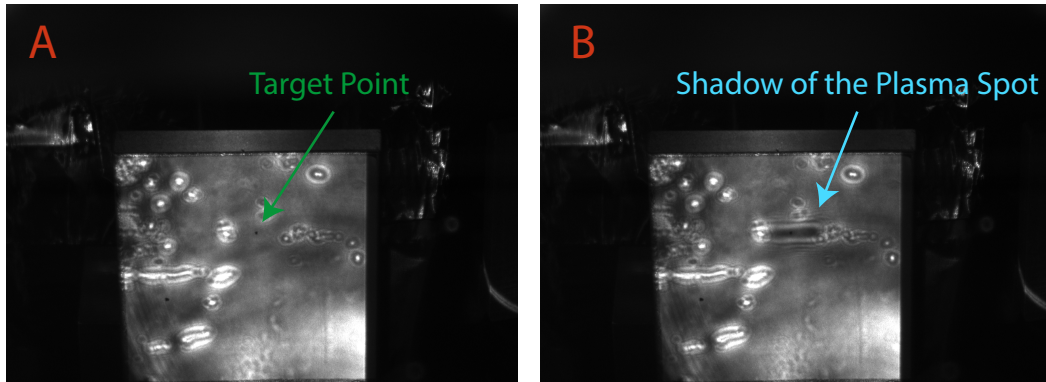


Figure 2.4: Photograph of the removable screen for the pulse synchronization and the alignment of the laser foci. **A** - Illuminated screen with marked target point. **B** - Shadow of the plasma spot on the illuminated screen.

presented method is approximately 1 ps which was more than sufficient for the conducted experiments.

As explicated, an overlap between the two laser foci is not necessary for the synchronization. This situation was used to align the pump focus with respect to the defined central axis. The distance between the foci was usually set to 5 – 10 mm and the distance between the source focus and the removable screen was 450 mm. The alignment of the plasma shadow to the target point could be realized with an accuracy of approximately 2 mm. Thus, the pump focus could be positioned on the central axis with a radial accuracy of approximately 25 μm .

3 Laser Plasma Interactions

This chapter describes the interaction of a laser pulse with a single electron and introduces the basic physics of laser-plasma interactions, which is relevant for this thesis.

3.1 Interaction of a Laser Pulse with a Single Electron

The motion of a charged particle within an electromagnetic field in vacuum is given by the Lorentz equation [47]

$$\frac{d\mathbf{p}}{dt} = \frac{d(\gamma m \mathbf{v})}{dt} = -q(\mathbf{E} + \mathbf{v} \times \mathbf{B}), \quad (3.1)$$

$$\frac{d(\gamma mc)}{dt} = -q(\mathbf{v} \cdot \mathbf{E}). \quad (3.2)$$

The Normalized Vector Potential

In the non-relativistic regime ($\gamma \approx 1$) the $\mathbf{v} \times \mathbf{B}$ -term is negligible. Assuming a linearly polarized plane wave with the amplitude E_0 and the angular frequency ω_L , a single electron oscillates in the field with a maximum displacement (y_{\max}) and a maximum velocity (v_{\max}) of

$$y_{\max} = \frac{eE_0}{m_e \omega_L^2}, \quad v_{\max} = \frac{eE_0}{m_e \omega_L}. \quad (3.3)$$

Using the maximum velocity of Formula 3.3 the dimensionless normalized vector potential a_0 is defined by

$$a_0 = \frac{v_{\max}}{c} = \frac{eE_0}{m_e \omega_L c}. \quad (3.4)$$

The relation with the intensity can be derived using Equations 1.19 and 3.4

$$I_0 = \frac{a_0^2}{\lambda^2} \cdot \frac{\epsilon_0 m_e^2 c^5}{2e^2} (2\pi)^2 \approx \frac{a_0^2}{\lambda^2} \cdot 1.37 \cdot 10^{18} \text{ W/cm}^2 \cdot \mu\text{m}^2. \quad (3.5)$$

In the relativistic regime ($\gamma \gg 1$), Equation 3.3 is not valid anymore and the equation of motion 3.1 has to be treated fully relativistically. In this case, the normalized vector potential a_0 shows values greater than one, corresponding to an intensity of $> 10^{18} \text{ W/cm}^2 \cdot \mu\text{m}^2$.

Relativistic Electron Motion in the Laser Field

This section describes the motion of a single electron in the presence of a focused laser pulse. It partly follows the description given in reference [47]. First, the discussion is simplified and the laser field is described as a plane electromagnetic wave. Subsequently, the influence of a temporal and spatial dependent field amplitude will be taken into account.

An elliptical polarized wave propagating in x-direction can be expressed by the vector potential

$$\mathbf{A} = \left(0, \delta A_0 \cos(\Phi), (1 - \delta^2)^{\frac{1}{2}} A_0 \sin(\Phi), \right) \quad (3.6)$$

where $\Phi = \omega t - kx$ is the phase of the wave and A_0 the amplitude of the vector potential. The polarization parameter δ has a value of $\{\pm 1, 0\}$ for linear polarization and $\{\pm 1/\sqrt{2}\}$ for circular polarization. The relation between the momentum \mathbf{p} of the electron and the gamma factor γ is given by

$$\gamma = \left(1 + \frac{\mathbf{p}^2}{m^2 c^2} \right)^{\frac{1}{2}} \quad (3.7)$$

and the functional dependency between the momentum \mathbf{p} and the velocity \mathbf{v} of the electron can be expressed as

$$\mathbf{p} = \gamma m \mathbf{v}. \quad (3.8)$$

The fields \mathbf{E} and \mathbf{B} are connected with the vector potential by the following relations

$$\mathbf{E} = -\frac{\partial \mathbf{A}}{\partial t} = \left(0, -\frac{\partial A_y}{\partial t}, -\frac{\partial A_z}{\partial t} \right), \quad (3.9)$$

$$\mathbf{B} = \nabla \times \mathbf{A} = \left(0, -\frac{\partial A_z}{\partial x}, +\frac{\partial A_y}{\partial x} \right). \quad (3.10)$$

Substitution of Equation 3.6 yields a relation between the field amplitudes \mathbf{E} and \mathbf{B} with the amplitude of the vector potential A_0 .

$$E_0 = \omega A_0, \quad B_0 = k A_0. \quad (3.11)$$

Using Equations 3.4 and 3.11 the normalized vector potential takes the form

$$A_0 = \frac{m_e c}{e} a_0. \quad (3.12)$$

In the following, vector quantities which are directed parallel to the propagation axis (x-axis) of the electromagnetic wave are denoted with \perp and those perpendicular to this axis with \parallel . Based on Formula 3.10 the vector product $\mathbf{v} \times \mathbf{B}$ can be expressed as

$$\mathbf{v} \times \mathbf{B} = \left(v_y \frac{\partial A_y}{\partial x} + v_z \frac{\partial A_z}{\partial x}, -v_x \frac{\partial A_y}{\partial x}, -v_x \frac{\partial A_z}{\partial x} \right). \quad (3.13)$$

Substituting this into the Lorentz Equation 3.1 results in a relation of the perpendicular component of the momentum

$$\frac{d\mathbf{p}_\perp}{dt} = e \left(\frac{\partial \mathbf{A}}{\partial t} + v_x \frac{\partial \mathbf{A}}{\partial x} \right). \quad (3.14)$$

Integration of Equation 3.14 yields

$$\mathbf{p}_\perp = e\mathbf{A} + \mathbf{p}_{\perp 0}, \quad (3.15)$$

whereby the constant of motion $\mathbf{p}_{\perp 0}$ denotes the initial component of the momentum perpendicular to the x-axis. The difference between the derivative of the parallel component of the momentum (Equation 3.1) and the energy Equation 3.2 leads to the equation

$$\frac{dp_x}{dt} - \frac{d(\gamma m_e c)}{dt} = -ev_y \left(\frac{\partial A_y}{\partial t} + \frac{\partial A_y}{\partial x} \right) - ev_x \left(\frac{\partial A_z}{\partial t} + \frac{\partial A_z}{\partial x} \right). \quad (3.16)$$

Since the electromagnetic wave is a function of $\omega x - kt$, the right side of Equation 3.16 is zero and an integration leads to

$$\gamma - \frac{p_x}{m_e c} = \alpha, \quad (3.17)$$

where the constant of motion α is not determined yet. A conversion of Equation 3.7 yields $\gamma^2 - p_x^2/(m_e c)^2 - p_\perp^2/(m_e c)^2 = 1$. With that, Equation 3.17 leads to a relation between the parallel and perpendicular components of the momentum

$$\frac{p_x}{m_e c} = \frac{1 - \alpha^2 + (p_\perp/m_e c)^2}{2\alpha}. \quad (3.18)$$

This is the Lorentz covariant equation of motion of a single electron in a plane electromagnetic wave [48]. The solution of this equation is obtained by integration and allows for the determination of the constants of motion $\mathbf{p}_{\perp 0}$ and α . The following simplifications are introduced with the use of Equation 3.17

$$\frac{d\Phi}{dt} = \frac{\partial \Phi}{\partial t} + \frac{p_x}{\gamma m_e} \frac{\partial \Phi}{\partial x} = \frac{\omega \alpha}{\gamma}, \quad (3.19)$$

$$\mathbf{p} = \gamma m_e \frac{d\mathbf{r}}{dt} = \gamma m_e \frac{d\Phi}{dt} \frac{d\mathbf{r}}{d\Phi} = \omega m_e \alpha \frac{d\mathbf{r}}{d\Phi}. \quad (3.20)$$

Laboratory Frame

If the electron is at rest before the interaction it follows that $\mathbf{p}_{\perp 0} = 0$, $p_{x0} = 0$ and $\gamma = 1$. With Equation 3.18 this leads to $\alpha = 1$ and on the basis of Equations 3.12, 3.15 and 3.18 the following relations for the momentum of the electron can be deduced

$$p_x = m_e c \frac{a_0^2}{4} [1 + (2\delta^2 - 1) \cos(2\Phi)], \quad (3.21)$$

$$p_y = m_e c a_0 \delta \cos(\Phi), \quad (3.22)$$

$$p_z = m_e c a_0 (1 - \delta^2)^{\frac{1}{2}} \sin(\Phi). \quad (3.23)$$

By means of Equation 3.20 the trajectory of the electron in the Laboratory Frame can be derived

$$x = \frac{c a_0^2}{\omega 4} \left[\Phi + \frac{(2\delta^2 - 1)}{2} \sin(2\Phi) \right], \quad (3.24)$$

$$y = \frac{c}{\omega} a_0 \delta \sin(\Phi), \quad (3.25)$$

$$z = -\frac{c}{\omega} a_0 (1 - \delta^2)^{\frac{1}{2}} \cos(\Phi). \quad (3.26)$$

Equation 3.23 shows that the electron momentum in x-direction exhibits a constant component which is superposed by a component oscillating with twice the laser frequency. The meaning of this component becomes clear by changing of the frame of reference. Averaging over the fast varying phase Φ , results in a mean momentum or a mean drift velocity, respectively

$$\overline{p_x} = m_e c \frac{a_0^2}{4}, \quad \overline{v_x} = c \cdot \frac{\overline{p_x}}{\overline{\gamma}} = c \cdot \frac{a_0^2}{4 + a_0^2}. \quad (3.27)$$

Average Rest Frame

The frame which moves with the velocity $\overline{v_x}$ in x-direction with respect to the laboratory frame is called average rest frame. In this frame the mean momentum of the electron in x-direction $\overline{p_x}$ is zero. Averaging Equation 3.18 over a laser cycle with $\overline{p_x} = 0$ gives

$$\alpha = \left(1 + \frac{a_0^2}{2} \right)^{\frac{1}{2}} \equiv \gamma_0. \quad (3.28)$$

Substituting this back in Equation 3.18 leads to the following set of Equations:

$$p_x = m_e c \frac{a_0^2}{4\gamma_0} (2\delta^2 - 1) \cos(2\Phi), \quad x = \frac{c a_0^2}{\omega 4\gamma_0} \frac{1}{2} (2\delta^2 - 1) \sin(2\Phi), \quad (3.29)$$

$$p_y = m_e c a_0 \delta \cos(\Phi), \quad y = \frac{c a_0}{\omega \gamma_0} \delta \sin(\Phi), \quad (3.30)$$

$$p_z = m_e c a_0 (1 - \delta^2)^{\frac{1}{2}} \sin(\Phi), \quad z = -\frac{c a_0}{\omega \gamma_0} (1 - \delta^2)^{\frac{1}{2}} \cos(\Phi). \quad (3.31)$$

Figure 3.1 illustrates the electron trajectory in the average rest frame for different polarizations, with a normalized vector potential of $a_0 = 2$ and an angular frequency of $\omega = 2.35 \cdot 10^{15}$ 1/s. For a plane wave with linear polarization in z-direction ($\delta = 1$), the electron motion takes place in the x-z-plane and resembles a figure of eight. For circular ($\delta = 1/\sqrt{2}$) polarization, the component which oscillates with 2Φ disappears. Therefore, the electron movement is restricted to the y-z-plane and the motion is circular with a radius of $a_0/(\sqrt{2}\gamma_0)$.

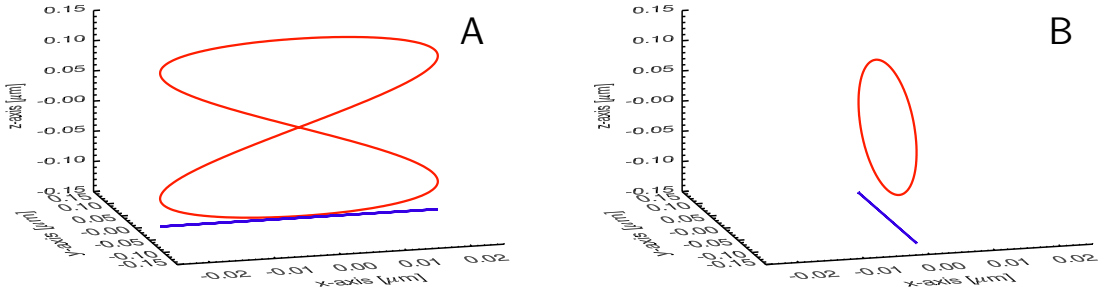


Figure 3.1: Trajectory of an electron in the field of a plane electromagnetic wave in the average rest frame. The normalized vector potential is $a_0 = 2$ and the angular frequency $\omega = 2.35 \cdot 10^{15}$ 1/s. **A** - Linear polarization ($\delta = 1$). **B** - Circular polarization ($\delta = 1/\sqrt{2}$).

Finite Pulse Duration

So far, the finite pulse duration of a laser pulse has not been considered in the derivation of the electron movement. Mathematically, the temporal distribution of a laser pulse can be described by the product of the amplitude of the vector potential A_0 with a time dependent envelope function $f(x, t)$: $A_0 \rightarrow A_0 f(x, t)$. Therefore, the vector potential has the form

$$\mathbf{A} = \left(0, \delta A_0 f(x, t) \cos(\Phi), (1 - \delta^2)^{\frac{1}{2}} A_0 f(x, t) \sin(\Phi) \right). \quad (3.32)$$

For instance the envelope $f(x, t)$ can be represented by a Gaussian function

$$f(x, t) = \exp\left(-\frac{(\omega t - kx)^2}{2\omega^2\sigma_t^2}\right) = \exp\left(-\frac{\Phi^2}{2\omega^2\sigma_t^2}\right), \quad (3.33)$$

with the temporal width σ_t . In principle, the equation of motion cannot be solved analytically any more. If the SVEA is applicable, the factor a_0 in Equations 3.21 to 3.23 can directly be substituted by $a_0 f(x, t)$ and the trajectory of the electron can be evaluated numerically. Figure 3.2 shows the electron motion in the laboratory frame under the influence of a Gaussian pulse with a temporal width of $\sigma_t = 5$ fs and different polarizations. The normalized vector potential a_0 is 2 and the angular frequency ω has a value of $2.35 \cdot 10^{15}$ 1/s. Since the transverse momentum is a

constant of motion, the net energy gain of the electron is zero for both polarizations. The electron comes back to rest as soon as the laser pulse is gone. In addition, it is only displaced in propagation direction of the pulse.

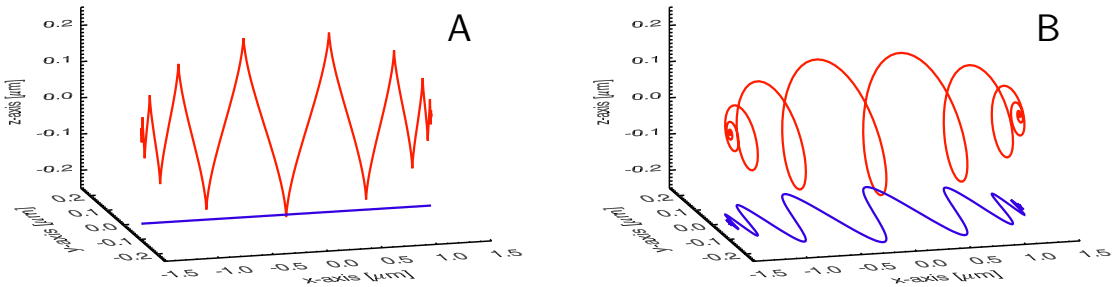


Figure 3.2: Trajectory of an electron in the laboratory frame under the influence of a Gaussian pulse with a temporal width of $\sigma_t = 5$ fs. The normalized vector potential is $a_0 = 2$ and the angular frequency $\omega = 2.35 \cdot 10^{15}$ 1/s. **A** - Linear polarization ($\delta = 1$). **B** - Circular polarization ($\delta = 1/\sqrt{2}$)

3.2 Ponderomotive Force

Taking into account the spatial dependency of the electromagnetic field distribution within a real laser pulse, the situation differs. Let's consider an electron being at rest and located in the center of a laser focus. Furthermore, the electric field vector is assumed to be zero at the beginning. In the first half of the laser cycle, the electron is accelerated predominantly in the direction of the electric field vector and leaves the center of the focal region. Outside the center, the laser field is weaker. Therefore, the electron does not completely come back to rest when the field reverses in the second half cycle of the laser period. The electron is subjected to the so called ponderomotive force. In the non relativistic regime this net force points in opposite direction of the gradient of the electric field amplitude and pushes the electrons out of regions of high intensity.

For the derivation of the ponderomotive force, two timescales must be separated [49]. The fast motion of the particle is on the time scale of the laser period $2\pi/\omega$ and the slow motion is described by the ponderomotive force. The latter one depends on the spatial distribution of the electromagnetic field amplitude and the slow time dependence of the laser field envelope. The real electric field of a laser pulse can be written as

$$\mathbf{E}(\mathbf{r}, t) = \frac{1}{2} \left(\hat{\mathbf{E}}(\mathbf{r}, t)e^{i\omega t} + \hat{\mathbf{E}}^*(\mathbf{r}, t)e^{-i\omega t} \right). \quad (3.34)$$

It can be assumed that the field amplitude $\hat{\mathbf{E}}$ contains the factor $e^{-i\mathbf{k}\cdot\mathbf{r}}$ and describes the laser field envelope, having a slow time dependence in comparison to the laser

frequency. For this reason and because of Equation $\nabla \times \mathbf{E} = -\partial \mathbf{B} / \partial t$ the complex magnetic field can be expressed as

$$\hat{\mathbf{B}}(\mathbf{r}, t) = \frac{i}{\omega} \nabla \times \hat{\mathbf{E}}(\mathbf{r}, t). \quad (3.35)$$

Expressed in a Taylor expansion the field amplitude $\hat{\mathbf{E}}$ has the form

$$\hat{\mathbf{E}}(\mathbf{r}, t) = \epsilon \hat{\mathbf{E}}(\mathbf{r}_0, t) + \epsilon^2 ((\mathbf{r} - \mathbf{r}_0) \cdot \nabla) \hat{\mathbf{E}}(\mathbf{r}, t) \Big|_{\mathbf{r}=\mathbf{r}_0} + \dots \quad (3.36)$$

whereby the smallness parameter $\epsilon = 1$ is used. Using perturbation theory the Lorentz equation

$$m\ddot{\mathbf{r}} = \cdot e [\mathbf{E}(\mathbf{r}, t) + \mathbf{v} \times \mathbf{B}(\mathbf{r}, t)] \quad (3.37)$$

can be written in terms of the power of ϵ by means of $\mathbf{r} = \epsilon \mathbf{r}_1 + \epsilon^2 \mathbf{r}_2 + \dots$ and Equations 3.35 and 3.36

$$m (\epsilon \ddot{\mathbf{r}}_1 + \epsilon^2 \ddot{\mathbf{r}}_2) = e \left[\epsilon \cdot \frac{1}{2} \left(\hat{\mathbf{E}}(\mathbf{r}_0, t) e^{i\omega t} + \text{c.c.} \right) + \epsilon^2 (\Delta \mathbf{r}_1 \cdot \nabla) \frac{1}{2} \left(\hat{\mathbf{E}}(\mathbf{r}_0, t) e^{i\omega t} + \text{c.c.} \right) \right] \quad (3.38)$$

$$+ (\epsilon \dot{\mathbf{r}}_1) \times \frac{1}{2} \left((i/\omega) \nabla \times \epsilon \left(\hat{\mathbf{E}}(\mathbf{r}_0, t) e^{i\omega t} - \text{c.c.} \right) \right) \Big]. \quad (3.39)$$

In the last equation and for the rest of this section the ∇ -operator is supposed to act on \mathbf{r}_0 for notational convenience. In first order the motion of the particle is determined by the fast oscillating component of the electric field at the position \mathbf{r}_0

$$m\ddot{\mathbf{r}}_1 = \frac{1}{2} \left(\hat{\mathbf{E}}(\mathbf{r}_0, t) e^{i\omega t} + \hat{\mathbf{E}}^*(\mathbf{r}_0, t) e^{-i\omega t} \right). \quad (3.40)$$

Neglecting the slow time dependence of $\hat{\mathbf{E}}(\mathbf{r}_0, t)$, the corresponding velocity and position are given by

$$\dot{\mathbf{r}}_1 = -\frac{ie}{2m\omega} \left(\hat{\mathbf{E}}(\mathbf{r}_0, t) e^{i\omega t} - \hat{\mathbf{E}}^*(\mathbf{r}_0, t) e^{-i\omega t} \right), \quad (3.41)$$

$$\Delta \mathbf{r}_1 = -\frac{e}{2m\omega^2} \left(\hat{\mathbf{E}}(\mathbf{r}_0, t) e^{i\omega t} + \hat{\mathbf{E}}^*(\mathbf{r}_0, t) e^{-i\omega t} \right). \quad (3.42)$$

In the next higher order the Lorentz equation has the form

$$m\ddot{\mathbf{r}}_2 = \frac{e}{2} \left[(\Delta \mathbf{r}_1 \cdot \nabla) \left(\hat{\mathbf{E}}(\mathbf{r}_0, t) e^{i\omega t} + \text{c.c.} \right) + \dot{\mathbf{r}}_1 \times \left((i/\omega) \nabla \times \left(\hat{\mathbf{E}}(\mathbf{r}_0, t) e^{i\omega t} - \text{c.c.} \right) \right) \right]. \quad (3.43)$$

Substituting of Equation 3.41 and 3.42 leads to

$$m\ddot{\mathbf{r}}_2 = \frac{e}{2} \left[-\frac{e}{2m\omega^2} \left(\hat{\mathbf{E}} e^{i\omega t} + \hat{\mathbf{E}}^* e^{-i\omega t} \right) \cdot \nabla \left(\hat{\mathbf{E}} e^{i\omega t} + \hat{\mathbf{E}}^* e^{-i\omega t} \right) \right] \quad (3.44)$$

$$+ \frac{e}{2m\omega^2} \left(-i \hat{\mathbf{E}} e^{i\omega t} + i \hat{\mathbf{E}}^* e^{-i\omega t} \right) \times \nabla \times \left(i \hat{\mathbf{E}} e^{i\omega t} - i \hat{\mathbf{E}}^* e^{-i\omega t} \right) \Big] \quad (3.45)$$

$$= \frac{e^2}{4m\omega^2} \left[\hat{\mathbf{E}} \cdot \nabla \hat{\mathbf{E}}^* + \hat{\mathbf{E}} \times \nabla \times \hat{\mathbf{E}}^* + \text{c.c.} + \Omega_{2\omega} \right], \quad (3.46)$$

whereby $\Omega_{2\omega}$ collects all terms $\sim e^{\pm i2\omega t}$. Upon averaging over a laser cycle, all terms of $\Omega_{2\omega}$ disappear and by means of the identity

$$\mathbf{A} \times \nabla \times \mathbf{B} + \mathbf{B} \times \nabla \times \mathbf{A} + \mathbf{A} \cdot \nabla \mathbf{B} + \mathbf{B} \cdot \nabla \mathbf{A} = \nabla \mathbf{A} \cdot \mathbf{B} \quad (3.47)$$

the expression for the nonrelativistic ponderomotive force is obtained

$$\mathbf{F}_{\text{p,nr}} = m\bar{\mathbf{r}}_2 = -\frac{e^2}{4m\omega^2} \nabla \left| \hat{\mathbf{E}}(\mathbf{r}_0, t) \right|^2. \quad (3.48)$$

In this connection, the position \mathbf{r}_0 in $\hat{\mathbf{E}}(\mathbf{r}_0, t)$ refers to the so called oscillation center. The fully relativistic derivation of the force delivers an additional factor $1/\bar{\gamma}$ [50]

$$\mathbf{F}_{\text{p}} = -\frac{e^2}{4m\bar{\gamma}\omega^2} \nabla \left| \hat{\mathbf{E}}(\mathbf{r}_0, t) \right|^2, \quad (3.49)$$

whereby $\bar{\gamma}$ can be regarded as the cycle averaged mass increase of an electron

$$\bar{\gamma} = \sqrt{1 + \frac{a_0^2}{2}}. \quad (3.50)$$

By means of Equation 3.4 the ponderomotive force can be derived from the ponderomotive potential, which is defined by

$$\Phi_{\text{p}} := mc^2 \cdot \left(\sqrt{1 + a_0^2} - 1 \right). \quad (3.51)$$

3.3 Laser Generated Solid Density Plasmas

If a laser pulse impinges on matter, atoms are ionized and cleared away as soon as the damage threshold of the material is reached. A plasma is only generated if the intensity of the pulse is high enough. The damage thresholds of media can vary over several orders of magnitude and depend on the band gap E_g of the respective material. Since the energy of a single near infrared photon $E_p = \hbar\omega \approx 1.3\text{eV}$ is much lower than binding energy of electrons in atoms, linear absorption of the laser light is not the dominant process of plasma generation.

Nevertheless, high intensity laser pulses can efficiently generate solid density plasmas by means of nonlinear excitation mechanisms, like nonlinear photo ionization or collisional ionization [51].

Concerning the nonlinear photo ionization, a distinction must be drawn between multiphoton ionization, tunnelling ionization and barrier suppression ionization. At moderate intensities an electron can absorb multiple photons at once. In this case multiphoton ionization is the dominant process. At higher intensities, when the electric potential of the laser pulse is of the order of the coulomb potential,

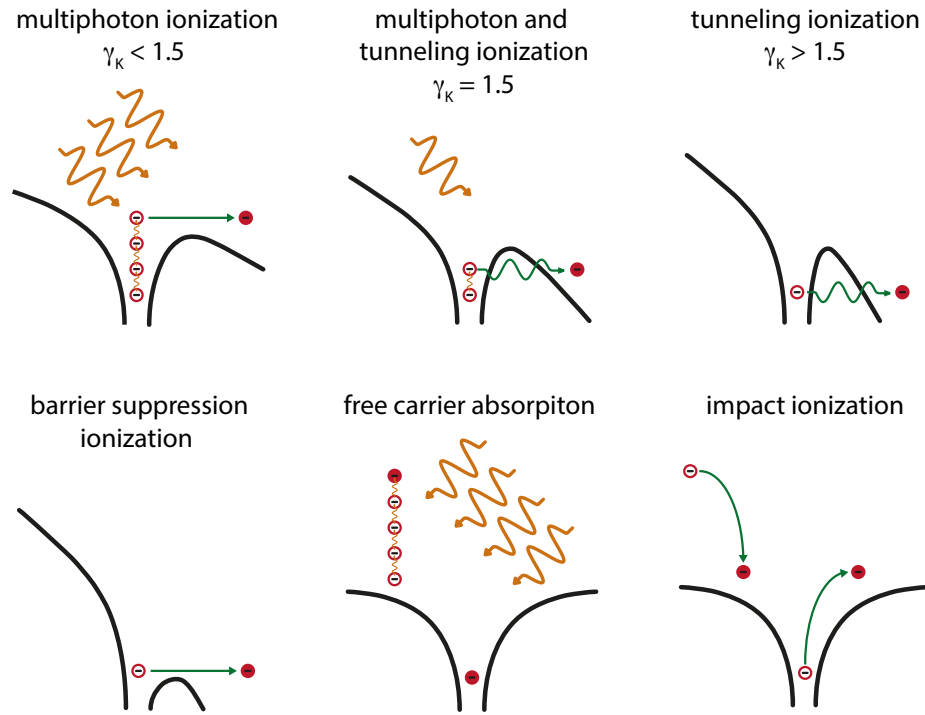


Figure 3.3: Nonlinear ionization processes during the interaction of high intensity laser pulses with solids

electrons can tunnel through the barrier and tunnel ionization becomes relevant. By means of the so called Keldysh parameter γ_K [52] the ionization regime of a laser can be determined quantitatively

$$\gamma_K = \frac{\omega}{e} \sqrt{\frac{m_e c n \epsilon_0 E_g}{I}}, \quad (3.52)$$

whereby m_e is the mass and e the charge of an electron. The refractive index of the medium is denoted by n . Here, ω and I are the frequency and intensity of the laser pulse. When the Keldysh parameter γ_K is smaller (larger) than 1.5, photo ionization is a tunnelling (multiphoton) process. Around a Keldysh parameter γ_K of 1.5 a combination of both processes takes place. At 800 nm the refractive index of aluminum is $n = 2.8$ and the first ionization energy accounts to $E_g = 5.98$ eV. The intensity at which the Keldysh parameter γ_K is 1.5 is given by

$$I_{Al} = 6 \cdot 10^{13} \text{ W/cm}^2. \quad (3.53)$$

At very high intensities the electron can even be freed by suppression of the barrier below the binding potential. This process is known as barrier suppression ionization (BSI) and is dominant for typical laser intensities of the order of $1 \cdot 10^{19} \text{ W/cm}^2$ [47].

The real ionization dynamics of solid targets is naturally more complicated, because the barrier suppression is influenced by free ions and electrons. In addition, impact ionization can take place in the presence of free electrons. Because free electrons can gain kinetic energy in the laser field (free carrier absorption), they can ionize bound electrons by collisions (impact ionization). If the mean free time between two collisions is less than the pulse duration, the excited electrons can also gain enough energy to contribute to this avalanche ionization process [47, 53]. Figure 3.3 illustrates the proposed ionization mechanisms of this section.

3.4 Debye Length

In order to quantitatively investigate the shielding of electric fields within a plasma, a test charge is assumed to be in the origin of a coordinate system. Assuming spherical symmetry, the Poisson equation of a hydrogen plasma [54] is given by

$$\nabla^2\Phi = \frac{1}{r^2} \frac{d}{dr} \left(r^2 \frac{d\Phi}{dr} \right) = -\rho/\epsilon_0 = \underbrace{-\frac{q\delta(r)}{\epsilon_0}}_1 + e \underbrace{\frac{n_e - n_i}{\epsilon_0}}_2, \quad (3.54)$$

whereby $\delta(r)$ is the dirac-delta function, e the elementary charge and n_i and n_e are the ion and electron density, respectively. The charge density ρ is composed of two terms. The first term (1) describes the charge density of a test charge in vacuum and the second term (2) accounts for the charge density distribution in the plasma. In the classical case, the electron distribution is given by the Boltzmann distribution and depends on the potential energy $q\Phi$

$$dN \sim \exp\left(-\frac{m_e/2v^2 - e\Phi(r)}{k_B T_e}\right) dx^3 dv^3. \quad (3.55)$$

Integration over the velocity dependent part of the distribution function yields an expression of the electron density in the space domain

$$n_e = \frac{dN}{dx^3} = n_{e,0} \cdot \exp\left(\frac{e\Phi}{k_B T_e}\right), \quad (3.56)$$

whereby k_B denotes the Boltzmann constant and $n_{e,0}$ the mean concentration of electrons. Assuming that the plasma is ideal ($e\Phi/k_B T_e \ll 1$) and that the plasma approximation is valid ($n_{e,0} = n_{i,0}$), the exponential function can be expressed in a first order Taylor polynomial and the effective charge density of the right term (2) in Equation 3.54 can be written as

$$e(n_e - n_i) = en_{e,0} \cdot \exp\left(\frac{e\Phi}{k_B T_e}\right) - en_{e,0} \quad (3.57)$$

$$\approx en_{e,0} \left(1 + \frac{e\Phi}{k_B T_e} - 1\right) = n_{e,0} \frac{e^2\Phi}{k_B T_e}. \quad (3.58)$$

Substituting this ansatz in the Poisson Equation 3.54 a solution is can be found

$$\Phi(r) = -\frac{e}{4\pi\epsilon_0 r} \exp\left(-\frac{r}{\lambda_D}\right). \quad (3.59)$$

Here, λ_D denotes the Debye length which is defined by

$$\lambda_D = \sqrt{\frac{\epsilon_0 k_B T_e}{n_{e,0} e^2}}. \quad (3.60)$$

Figure 3.4 compares the trend of the Coulomb potential in vacuum and in a plasma with a Debye length $\lambda_D = 1 \mu\text{m}$. For $r \ll \lambda_D$ the exponential function in Equa-

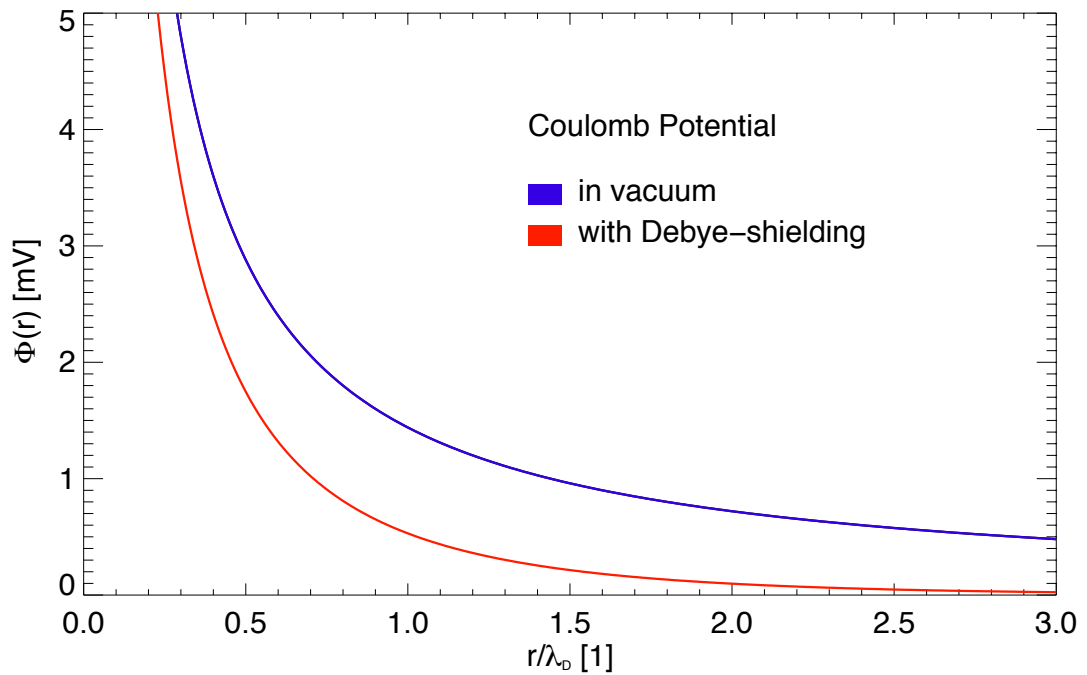


Figure 3.4: Coulomb potential of a single point charge in vacuum or in plasma (with Debye shielding, $\lambda_D = 1 \mu\text{m}$).

tion 3.59 is in good approximation around 1 and the potential is close to the Coulomb potential in vacuum. At the characteristic length $r = \lambda_D$ the electrostatic potential drops down by a value of around $1/e$. Since the potential decays exponentially, which is much faster than the $1/r$ -decay in vacuum, the potential of a test charge is shielded by the surrounding plasma for distances greater than the Debye length ($r \gg \lambda_D$).

3.5 The Plasma Frequency

A periodical oscillation of the charge density within a plasma is called plasma oscillation. In order to describe the oscillations of electrons within a cold plasma, the thermal motion of the particles and the pressure gradient force are not taken into account. Furthermore, the ions are regarded as immobile in relation to the electrons and serve as a stationary charge neutralizing background. Thus the ion density $n_i = n_0$ is constant. The electron density $n_e(\mathbf{r}, t)$ is expressed by means of a small perturbation $n'_e(\mathbf{r}, t)$ [55]

$$n_e(\mathbf{r}, t) = n_0 + n'_e(\mathbf{r}, t), \quad (3.61)$$

whereby $|n'_e| \ll n_0$. For simplicity, a hydrogen plasma is assumed. Therefore, the charge density is given by

$$\rho(\mathbf{r}, t) = -e [n_0 + n'_e(\mathbf{r}, t)] + en_0 \quad (3.62)$$

and the Poisson equation can be written as

$$\Delta\Phi(\mathbf{r}, t) = \nabla \cdot \mathbf{E}(\mathbf{r}, t) = \frac{\rho(\mathbf{r}, t)}{\epsilon_0} = -\frac{e}{\epsilon_0} n'_e(\mathbf{r}, t). \quad (3.63)$$

Similarly, the induced electric field $\mathbf{E}(\mathbf{r}, t)$ and the average electron velocity $\mathbf{v}_e(\mathbf{r}, t)$ are assumed to be first order perturbations. Using Equations 3.61 and 3.62 the continuity equation can be linearized

$$\frac{\partial\rho(\mathbf{r}, t)}{\partial t} + \nabla \cdot \mathbf{j}(\mathbf{r}, t) = 0 \Rightarrow \frac{\partial n'_e(\mathbf{r}, t)}{\partial t} + n_0 \nabla \cdot \mathbf{v}_e(\mathbf{r}, t) = 0. \quad (3.64)$$

Newtons second law describes the kinetic response of the particles to the force of the induced electric field $\mathbf{E}(\mathbf{r}, t)$ and takes the form

$$\frac{\partial\mathbf{v}_e(\mathbf{r}, t)}{\partial t} = -\frac{e}{m_e} \mathbf{E}(\mathbf{r}, t). \quad (3.65)$$

Combining Equations 3.63, 3.64 and 3.65 leads to the differential equation of a harmonic oscillator

$$\frac{\partial^2 n'_e(\mathbf{r}, t)}{\partial t^2} + \omega_p^2 n'_e(\mathbf{r}, t) = 0, \quad (3.66)$$

whereby the natural frequency

$$\omega_p = \sqrt{\frac{n_0 e^2}{m_e \epsilon_0}} \quad (3.67)$$

is called (nonrelativistic) electron plasma frequency. The fully relativistic derivation [56] of the plasma frequency delivers the additional factor $\sqrt{1/\bar{\gamma}}$ (Equation 3.50)

$$\omega_{p,rel} = \sqrt{\frac{n_0 e^2}{m_e \bar{\gamma} \epsilon_0}}. \quad (3.68)$$

3.6 The Dielectric Plasma Medium

A plasma can be described as a dielectric medium with a scalar permittivity ϵ . For simplicity it is assumed that the ions are stationary and serve as a charge neutralizing background. If the charge density ρ_e and the electron current density \mathbf{j}_e are defined by

$$\rho_e = -en_e + qn_0, \quad \mathbf{j}_e = -en_e\mathbf{v}_e, \quad (3.69)$$

the plasma can be described by the equations in vacuum. Here, n_e denotes the electron density and n_0 is the constant ion density. In the unmagnetized case, the equations that include the sources are given by

$$\nabla \cdot \mathbf{E} = \frac{\rho_e}{\epsilon_0}, \quad \nabla \times \mathbf{B} - \frac{1}{c^2} \frac{\partial}{\partial t} \mathbf{E} = \mu_0 \mathbf{j}_e. \quad (3.70)$$

For an dielectric medium without external sources these equations correspond to

$$\nabla \cdot (\epsilon \mathbf{E}) = 0, \quad \nabla \times \mathbf{B} - \frac{1}{c^2} \frac{\partial}{\partial t} (\epsilon \mathbf{E}) = 0. \quad (3.71)$$

The other equations are identical in a dielectric medium and in vacuum.

As described in the previous section, electrons at distances beyond λ_D can be regarded as free. If an electromagnetic wave impinges on the plasma, the motion of these electrons is governed by the electric field amplitude of the incident light. Their deflection \mathbf{s}_e can be described by the differential equation of a driven and damped oscillator [54, 57]

$$\frac{\partial^2 \mathbf{s}_e(\mathbf{r}, t)}{\partial t^2} + \nu_e \frac{\partial \mathbf{s}_e(\mathbf{r}, t)}{\partial t} = -\frac{e}{m_e} \mathbf{E}(\mathbf{r}, t), \quad (3.72)$$

where ν_e is the electron collision frequency and m_e is the electron mass. Substituting the electron current density of Equation 3.69 in Equation 3.72 yields

$$\frac{\partial \mathbf{j}_e(\mathbf{r}, t)}{\partial t} + \nu_e \mathbf{j}_e(\mathbf{r}, t) = \epsilon_0 \omega_p^2 \mathbf{E}(\mathbf{r}, t). \quad (3.73)$$

The Fourier transform of this differential equation with the substitution $\frac{\partial}{\partial t} \rightarrow -i\omega$ results in the algebraic equation

$$-i\omega \mathbf{j}_e(\mathbf{r}, \omega) + \nu_e \mathbf{j}_e(\mathbf{r}, \omega) = \epsilon_0 \omega_p^2 \mathbf{E}(\mathbf{r}, \omega) \quad (3.74)$$

which can be solved for the electron current density in the frequency domain

$$\mathbf{j}_e(\mathbf{r}, \omega) = \frac{\epsilon_0 \omega_p^2}{\nu_e - i\omega} \mathbf{E}(\mathbf{r}, \omega) = \sigma_E(\omega) \mathbf{E}(\mathbf{r}, \omega), \quad (3.75)$$

whereby $\sigma_E(\omega)$ denotes the electrical conductivity. Substituting $\mathbf{j}_e(\mathbf{r}, \omega)$ into Equation 3.70 and comparing the Fourier transforms of Equations 3.70 and 3.71 yields the dielectric function of the plasma medium

$$\epsilon = 1 + \frac{i\epsilon_0}{\omega} \sigma_E = 1 - \frac{\omega_p^2}{\omega^2 + i\nu_e\omega}. \quad (3.76)$$

Using this expression of the permittivity ϵ , the validity of the left side of Equation 3.71 can be shown [54], which proves that a plasma can be treated as a dielectric medium. Assuming high frequencies and a collisionless plasma the dielectric function $\epsilon(\omega)$ is real. In this case the refractive index $n = \sqrt{\epsilon}$ of a plasma

$$n = \sqrt{1 - \frac{\omega_p^2}{\omega^2}} \quad (3.77)$$

depends only on the plasma frequency ω_p or on the electron density n_e , respectively. If the angular frequency of the incident light is smaller than the plasma frequency ($\omega < \omega_p$), the refractive index becomes imaginary. In this case the electromagnetic wave is partially reflected or absorbed and the plasma is called over-critical (over-dense). In the opposite case ($\omega > \omega_p$) the refractive index is real and the electromagnetic wave can propagate within a so called under-critical (under-dense) plasma.

The critical electron density n_c indicates the transition between an under- and over-dense plasma and is defined by the condition $\omega = \omega_p$. For a laser wave length of $\lambda = 800$ nm the corresponding critical electron density is given by

$$n_c = \frac{\epsilon_0 m_e \omega^2}{e^2} = 1.7 \cdot 10^{21} \text{ cm}^{-3}. \quad (3.78)$$

4 Laser-driven Ion Acceleration

Compared to vacuum, the motion of a particle in plasma is not exclusively determined by the direct action of the laser pulse (cf. Section 3.1). On the contrary, the particle motion is governed by collective fields, which are created due to the ionization of the target by the laser pulse. In addition, the laser pulse itself is modified by nonlinearities in the generated plasma medium.

Due to their higher charge-to-mass ratio electrons are accelerated first by the laser pulse, while the heavier ions respond slower. The displacement of the electrons leads to the formation of quasi-static charge-separation fields, which vary on a relatively slow time scale compared to the electron dynamics.

In addition, quasi-static magnetic fields are created by the laser-induced electron currents. The proton and ion acceleration takes place on a longer time scale due to the action of these collective plasma fields [47].

The ion acceleration mechanism which is both used and investigated in this thesis is based on the generation of electric charge-separation fields. Its basic principle will be presented in this chapter. Besides this, a number of alternative acceleration mechanisms exist, which are not described in detail here. A good summary can be found in review articles [58, 59]. Moreover, this chapter introduces several absorption mechanisms which are relevant for laser-plasma interactions at relativistic intensities and, in addition, several mechanisms for the generation of magnetic fields are presented.

4.1 Absorption Mechanisms

Since the laser pulse interacts primarily with electrons, the absorption of laser light in plasmas has an important impact on the generation of the collective plasma fields that govern the ion acceleration. The laser energy absorption to plasma electrons and waves is a highly complex process and depends on a variety of laser and plasma parameters. For this reason, only the absorption mechanisms relevant for laser-driven ion acceleration are briefly introduced. A detailed description can be found in several reviews [60–62].

In case of initially solid targets, the laser light absorption is most efficient at the critical surface, i.e. where the electron density n_e equals the critical density $n_c \approx$

$1.7 \cdot 10^{21} \text{ 1/cm}^3$ (Equation 3.78). The laser pulse can be absorbed due to several mechanisms:

- In the initial stage, i.e. for lower intensities ($I_L \lambda_L^2 \sim 10^{12} - 10^{17} \text{ W}\mu\text{m}^2\text{cm}^{-2}$) and steep plasma gradients ($L = n_e/(dn_e/dx) < 1 \mu\text{m}$), the absorption is dominated by **resonant absorption** and **inverse bremsstrahlung** [60]. The resonant absorption can still be important for higher intensities, i.e. for the absorption of the main pulse, if the plasma scale length L_{cr} at the critical density is of the order of the laser-wavelength or larger and the obliquely incident laser light is polarized parallel to the plane of incidence.
- **Vacuum heating** or **Brunel absorption** [63, 64] is gaining increasing importance for the main pulse absorption if the plasma gradient is sharp and the laser p-polarized.
- **$\mathbf{J} \times \mathbf{B}$ heating** [65] is connected with the oscillating component of the ponderomotive force (Sections 3.1 and 3.2). This absorption mechanism becomes important for lower plasma gradients and relativistic intensities. In the case of high-density plasmas with sharp gradients, its effectivity decreases [60].

Finally, it should be mentioned that the laser absorption can be considerably increased due to multi-dimensional effects, such as the bending or rippling of the plasma surface [66]. In addition, certain absorption mechanisms which are absent in the one-dimensional case will gain importance. For instance the resonant absorption in the case of s-polarization or normal incidence.

4.2 Acceleration by Electric Charge Separation Fields

Many experiments on laser-driven ion-acceleration have shown a characteristic quasi-thermal distribution of the ion energy with a cut-off at some energy $\epsilon_{i,\text{max}}$. Based on the plasma expansion into vacuum [67–72] a variety of theoretical models [73–77] were developed, which can describe the generation of these features.

The principle process is similar for all models and is illustrated in Figure 4.1. A laser pulse irradiates the surface of a foil. Typically a pre-plasma is generated due to ASE or the existence of a pre-pulse (cf. Section 1.4). Depending on the dominant absorption mechanism the energy of the main pulse is absorbed in the laser-plasma interaction and transferred into hot electrons (A). Some of the accelerated electrons penetrate through the target and leave the foil on its rear side (B). The resulting positive charge of the foil forces some electrons to turn around and reenter the target. This leads to the formation of a strong charge-separation field between the electrons and the foil surface. The atoms in the vicinity of the target surface are ionized and accelerated within the strong electric field (C). The ions

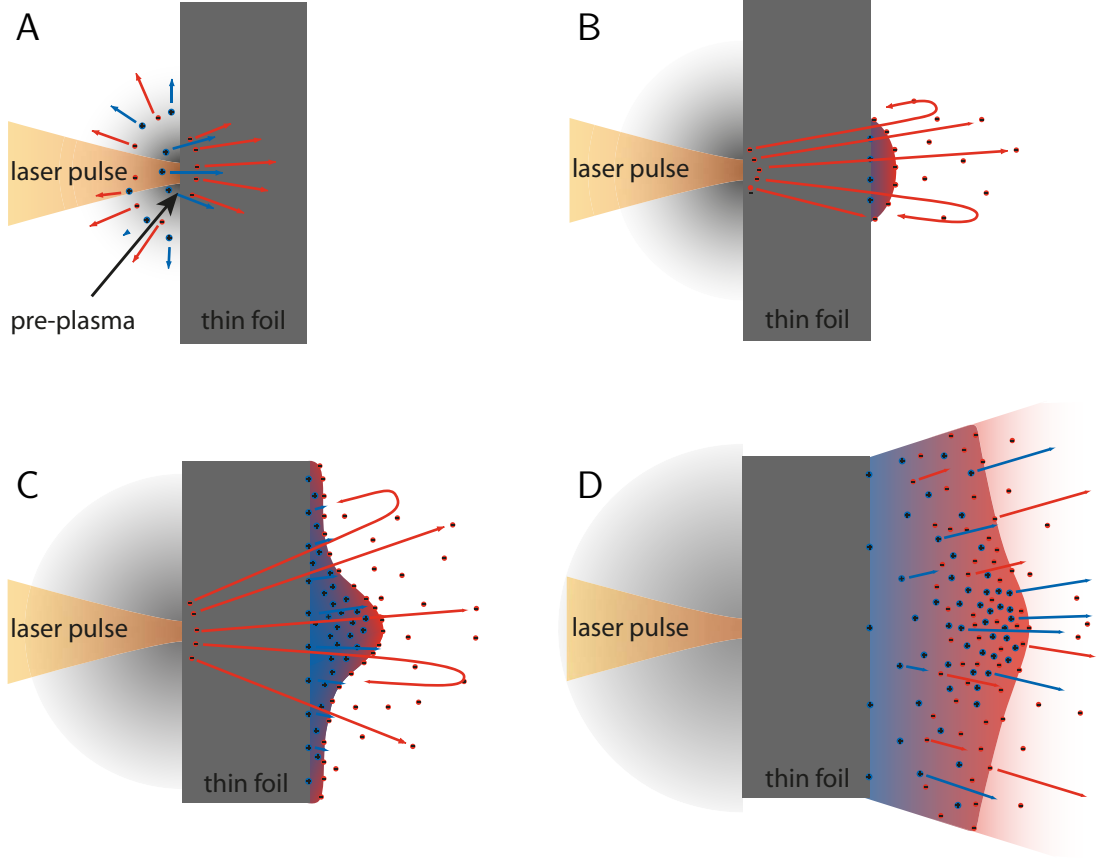


Figure 4.1: Acceleration by electric charge-separation fields at the rear side of a thin foil. **A** - Ionization and pre-plasma creation by the weak precursor of the main laser pulse (ASE or pre-pulse). **B** - Interaction of the main pulse with pre-plasma. Absorption of laser energy and acceleration of hot electrons. **C** - Formation of a charge-separation field. Ionization and acceleration of ions. **D** - Ion expansion into vacuum

expand into vacuum, following the electrons and the field declines (D).

In most of the models the ions are assumed to be initially cold, forming a sharp boundary with vacuum. In contrast the electrons have a Boltzmann-like density distribution

$$n_e = n_{e,0} \exp\left(\frac{e\Phi}{k_B T_e}\right) \quad (4.1)$$

depending on the electrostatic potential Φ , whereby e is the elementary charge and k_B the Boltzmann constant. The hot electron density and temperature are denoted by n_e and T_e , respectively. In one-dimensional models the electric field is obtained by integrating the Poisson equation

$$\epsilon_0 \Delta \Phi = e(n_e - Zn_i), \quad (4.2)$$

whereby Z_i denotes the charge number and n_i is the ion density. Conventionally, the maximum ion energy $\epsilon_{i,\max}$ is proportional to the temperature of hot electrons T_e , however the proportionality factor depends on the details of the respective model.

Target Normal Sheath Acceleration

In the case of the target normal sheath acceleration (TNSA) model, the plasma is assumed to be neutral, with exception of a small region close to the expanding front. A violation of the charge neutrality is only allowed in an area with an extension of the order of the Debye length λ_D (Equation 3.60). In this case the initial electric sheath field is given by

$$E_{\text{sheath},0} = \sqrt{\frac{2}{e_N} \frac{T_e}{e \lambda_D}} = \left(\frac{8\pi}{e_m} n_e T_e \right)^{1/2}, \quad (4.3)$$

whereby e_m is Euler's number.

Ion Expansion into Vacuum

The model suggested by Patrick Mora [73] is presented in more detail, since it will be used in Chapter 9 and 10 to describe the experimental observations. It describes the isothermal plasma expansion into vacuum and explains the ion acceleration as the result of charge separation. In between a positively and a preceding negatively charged region an electric field is created which peaks at a definite position. Since the accelerated ions accumulate at this position, an ion front is generated which propagates with increasing velocity. In this isothermal description the plasma is described with one electron temperature T_e and does not cool down while expanding. For this reason, the model intrinsically overestimates the velocity of the ion front, which has been shown experimentally [78, 79]. An adiabatic model is proposed in [74, 80].

In the isothermal model, the initial situation is a quasi-neutral plasma ($n_e = Z_i n_i$) which occupies the half-space $z < 0$ and begins to expand into vacuum. Here, Z_i denotes the charge number and n_i is the ion density. The ions are initially cold and the electrons have a Boltzmann-like density distribution depending on the electrostatic potential Φ , as described by Equation 4.1. In this one-dimensional model the electric field is obtained by integrating the Poisson equation (Equation 4.2). In addition, the equations of continuity and motion are necessary to describe the

temporal and spatial evolution of the expansion

$$\left(\frac{\partial}{\partial t} + v_i \frac{\partial}{\partial z}\right) n_i = -n_i \frac{\partial v_i}{\partial z}, \quad (4.4)$$

$$\left(\frac{\partial}{\partial t} + v_i \frac{\partial}{\partial z}\right) v_i = -\frac{Ze}{m_i} \frac{\partial \Phi}{\partial z}. \quad (4.5)$$

Using a Lagrangian code, Equations 4.1 to 4.5 can be solved and the time dependent electric field at the ion front can be calculated numerically. As a good approximation the analytic expression

$$E_f \simeq \frac{2\mathcal{E}_c}{\sqrt{2e_m + \omega_{pi}^2 t^2}}, \quad \mathcal{E}_c = \sqrt{\frac{n_{e,0} k_B T_e}{\epsilon_0}} \quad (4.6)$$

is provided [73], where e_m is the base of the natural logarithm and ω_{pi} the ion plasma frequency

$$\omega_{pi} = \sqrt{\frac{n_{e,0} Z e^2}{m_i \epsilon_0}}. \quad (4.7)$$

Using Formula 4.6 the velocity of the ion front v_{front} and its positions z_{front} can be obtained by integration of Equation 4.5

$$v_{\text{front}} \simeq 2c_s \ln\left(\tau + \sqrt{\tau^2 + 1}\right), \quad (4.8)$$

$$z_{\text{front}} \simeq 2\sqrt{2e_m} \lambda_{D0} \left(\left(\tau \ln\left(\tau + \sqrt{\tau^2 + 1}\right) + \sqrt{\tau^2 + 1} \right) + 1 \right), \quad (4.9)$$

where the normalized time τ is defined by

$$\tau = \frac{\omega_{pi} t}{2e_m}. \quad (4.10)$$

The ion acoustic velocity c_s is defined by

$$c_s = \frac{Z_i k_B T_e}{m_i} \quad (4.11)$$

and the initial Debye length $\lambda_{D,0}$ is given by the relation

$$\lambda_{D,0} := \sqrt{\frac{\epsilon_0 k_B T_e}{n_{e,0} e^2}}. \quad (4.12)$$

The local Debye length depends on the evolution of the electron density and is defined by

$$\lambda_D = \lambda_{D,0} \sqrt{\frac{n_{e,0}}{n_e}}. \quad (4.13)$$

According to reference [73] the following equation is valid at the position of the ion front

$$(\partial \ln n_e / \partial z)_{\text{front}} = -\frac{e E_{\text{front}}}{k_B T_e} \simeq 2 / (c_s t). \quad (4.14)$$

Using Equation 4.1 and 4.13, the temporal dependence of the Debye length at the ion front can be approximated by

$$\lambda_{D,\text{front}}(t) \simeq \frac{c_s t}{\sqrt{2}} = \frac{\lambda_{D,0} \omega_{pi} t}{\sqrt{2}}. \quad (4.15)$$

4.3 Magnetic Field Generation Mechanisms

In laser-plasma interactions quasi-stationary magnetic fields can arise from electron transport in the vicinity of the focal spot. In the absence of one-dimensional symmetry, the accelerated electrons can return along a different path and create a current loop which leads to the generation of a magnetic field. In short-pulse interactions, a distinction is made between different mechanisms [47], such as radial thermal transport, DC currents in steep density gradients, or fast electron currents. The last two mechanisms will act primarily at early times ($t < \tau_L$) in the overdense (solid) region. In contrast, the thermoelectric magnetic field generation occurs on a hydrodynamic timescale and persists much longer than the laser-plasma interaction.

Thermoelectric Magnetic Field Generation

In the case of the thermoelectric magnetic field generation, the electron temperature and the density gradients are not parallel, as illustrated in Figure 4.2.A. This leads to the electromagnetic source term [81]

$$\frac{\partial \mathbf{B}}{\partial t} = \frac{\nabla T_e \times \nabla n_e}{e n_e}. \quad (4.16)$$

Under the assumption that the density gradient points predominately in the direction of the target normal, the magnitude of the field can be estimated [82] by

$$B \sim 2 \cdot \left(\frac{\tau_L}{\text{ps}} \right) \left(\frac{k_B T_e}{\text{keV}} \right) \left(\frac{L_{\perp}}{\mu\text{m}} \right)^{-1} \left(\frac{L_{\parallel}}{\mu\text{m}} \right)^{-1} [\text{MGauss}], \quad (4.17)$$

whereby τ_L is the laser pulse duration, T_e the electron temperature and L_{\parallel} and L_{\perp} the temperature and density scale length, respectively. This mechanism is well known and has been observed in various experiments [82–84].

Magnetic Fields due to DC Ponderomotive Currents

Another possibility for the generation of a magnetic field are DC currents in steep density gradients, which are driven by temporal variations in the ponderomotive force [85–87]. As discussed in Section 3.2 electrons are pushed away from the laser focus due the gradient of the time-averaged laser intensity, i.e. the ponderomotive force. In the adiabatic limit, i.e. for a constant laser intensity, the electron current is eventually stopped by the electric field of the induced charge separation [47]. This leads to a local electron density depletion for a time period of approximately the laser pulse duration. If the ponderomotive force \mathbf{F}_p (Equation 3.49) increases in time, the electron push is never entirely balanced and some electrons will gain the velocity

$$\mathbf{v}_p \propto m_e^{-1} \mathbf{F}_p \sim \nabla E_L^2. \quad (4.18)$$

In this case a net DC ponderomotive current $\mathbf{J}_p = en_e \mathbf{v}_p \sim n_e \nabla I_L$ is induced, whereby I_L is the intensity of the laser pulse. The application of Ampère’s law provides an estimation of the distribution of the field

$$\nabla \mathbf{B} \sim \nabla \times \mathbf{J}_p \sim \nabla n_e \times \nabla I_L. \quad (4.19)$$

Therefore, a magnetic field distribution in the sense of Figure 4.2.A is generated if a radial laser intensity profile is incident on a steep density gradient.

Magnetic Fields due to Fast Electron Currents

Independent of ponderomotive effects, fast electron currents can be generated as a consequence of the laser energy absorption (Section 4.1) to plasma electrons. Depending on the relevant absorption mechanism, fast electron currents can either be

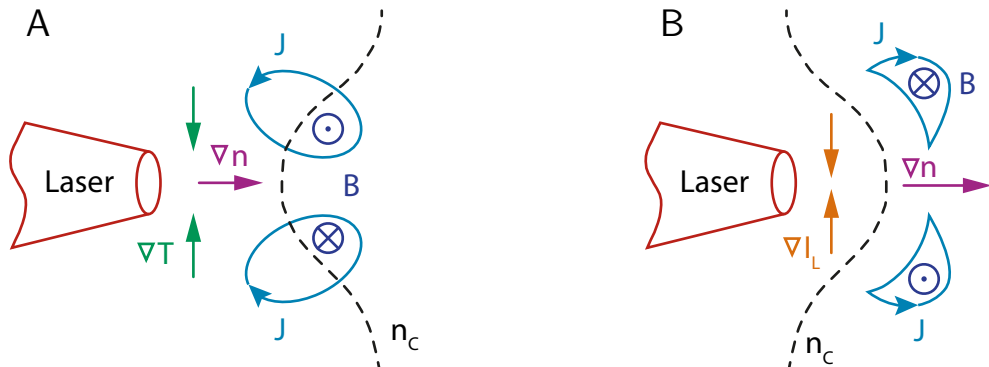


Figure 4.2: Geometry of magnetic field generation mechanisms. **A** - Thermoelectric magnetic field ($\nabla T \times \nabla n_e$). **B** - Ponderomotively generated magnetic field ($\nabla n_e \times \nabla I_L$)

directed into the target [88, 89] or along the target surface [90–92]. For intensities above 10^{18} W/cm² the electron flux $n_{\text{eh}}v_{\text{h}}$ can be significant, but will eventually be compensated by a cold return current [47].

In addition magnetic fields may arise by the recirculation of electrons at the plasma boundary [93, 94], Weibel-like instabilities [95] and the filamentation of the expanding current sheet [96].

Part II

Characterization of Laser Accelerated Proton Beams

5 The Thomson Slit Spectrometer

In this chapter a modified version of the Thomson spectrometer, the so called *Thomson slit spectrometer* is introduced [97]. This spectrometer type allows for the determination of the angle dependent proton energy distribution $\tilde{\rho}(\beta, \epsilon)$. For the retrieval of $\tilde{\rho}(\beta, \epsilon)$ a numerical processing of the recorded proton density distribution on the detector plane $\rho(x, y)$ is required. For this purpose a new numerical method for the coordinate transformation from $\rho(x, y)$ to $\tilde{\rho}(\beta, \epsilon)$ is developed and described in detail. In addition, the energy resolution of the spectrometer is determined and compared to the resolution of a conventional Thomson spectrometer.

5.1 Setup

The setup (Figure 5.1) is comparable to a conventional Thomson spectrometer [8], however the use of a thin slit instead of a pinhole allows additional information to be gathered about the anisotropy of the proton beam in one dimension. The small width of the slit in y-direction ($s_y \approx 100 - 200 \mu\text{m}$) restricts the divergent proton beam to the x-z-plane. Its length in x-direction $s_x \approx 10 \text{ mm}$ determines the maximum opening angle $\alpha = 2 \cdot \text{atan}(s_x / (2 \cdot L_1))$ and thus the detectable angle interval. Behind the slit the ions propagate mainly in z-direction and have only a comparable small velocity component v_x in x-direction. After the distance L_2 the particles reach the center of a combination of electric and magnetic field plates. The combined field is static and mainly directed in x-direction. Due to the field component B_x the ions are deflected in y-direction. After the additional propagation length L_3 a particle detector is located with a spatial resolution in the x-y-plane. In first approximation the ions reach the position

$$y \approx \frac{QB_x l L_3}{m_i v_z} \quad (5.1)$$

on the detector, whereby Q is the charge of the ion, m_i its mass and v_z its velocity component in z-direction [98]. The effective extension of the electric and magnetic field is denoted by l . The distances L_1 , L_2 and L_3 are defined in Figure 5.1. The

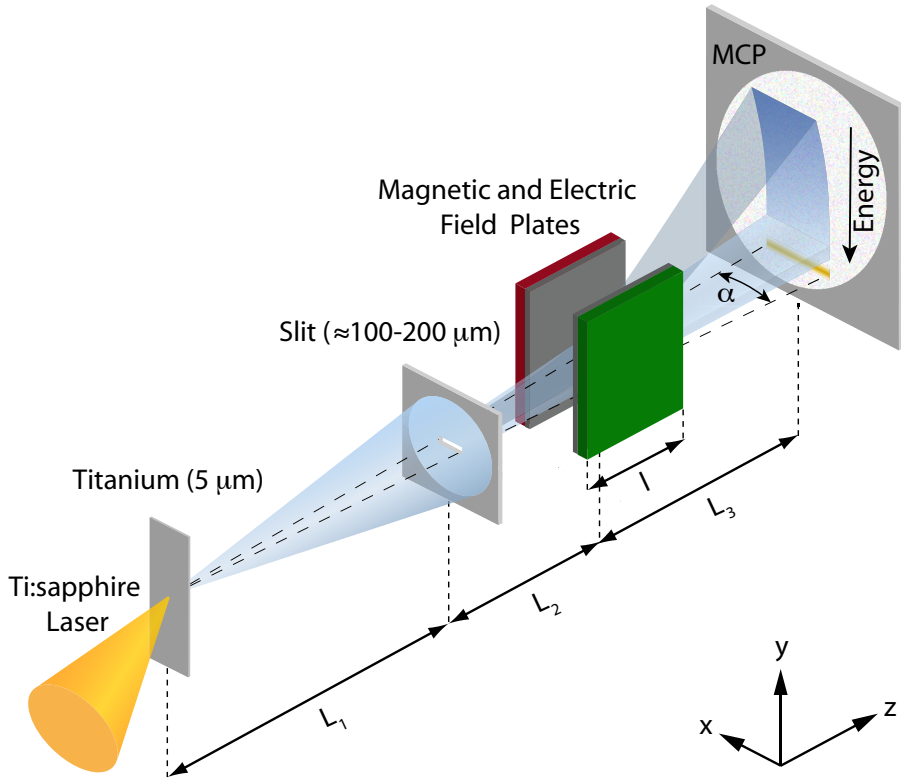


Figure 5.1: Implementation of a Thomson slit spectrometer in an experimental setup for laser-driven ion acceleration

electric field E_x causes an additional deflection x of the ions in x-direction. In first approximation this deflection can be described by neglecting the initial velocity component v_x and the slope propagation path through the magnet

$$x \approx \frac{QE_x l L_3}{m_i v_z^2} = \frac{C}{2\epsilon}, \quad (5.2)$$

where C is a constant and ϵ_i the kinetic energy of the ion. Substituting Equation 5.1 into 5.2 yields the parabolic function

$$x = \frac{m_i E_x}{QB_x^2 l L_3} \cdot y^2 = D y^2 \quad (5.3)$$

which describes the parabolic deflection curve on the detector in first approximation.

The point of impact of a single ion on the detector in x-direction depends on its initial ejection angle $\beta = \text{atan}(v_x/v_z) \leq \alpha/2$ with $|\beta| \leq \alpha/2$ and the electric field deflection x and is given by

$$\tilde{x} = \left(L_1 + L_2 - \frac{l}{2} \right) \tan(\beta) + x. \quad (5.4)$$

5.2 Multi-Channel Plate

As a detector a multi-channel plate (MCP) coupled with a phosphor screen camera was used. The MCP consists of a two-dimensional array of ultra-small diameter glass capillaries. These channels are fused together and sliced in the shape of a thin disc. Figure 5.2.A shows the section along the surface normal of the disc and

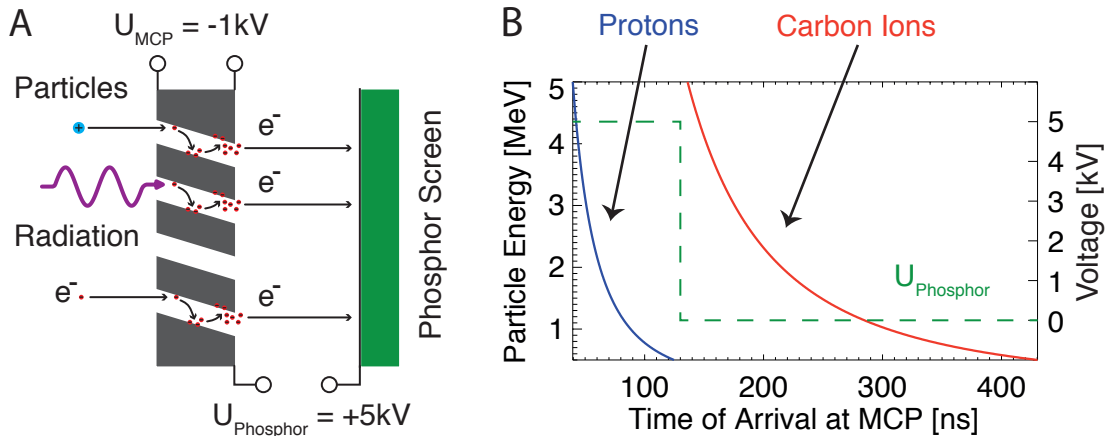


Figure 5.2: **A** - Operating principle of a MCP. **B** - Time of arrival of protons and carbon ions on the MCP depending on their energy. Here, a distance of 1220 mm between the ion source and the detector is assumed.

illustrates the operating principle. The inside walls of the channels are processed to have a specified resistance. Thus each channel forms an independent secondary electron multiplier. All channels are orientated in the so called bias angle ($\sim 8^\circ$) which is formed by the channel axis and the axis perpendicular to the plate surface. For this reason, all entering particles or x-rays impinge on the channel wall and lead to the emission of secondary electrons. These electrons are accelerated by an electric field due to the voltage $U_{MCP} = -1\text{ kV}$, which is applied across the end faces of the MCP. Travelling along parabolic trajectories they strike the opposite wall. In this way further secondary electrons are produced. This process is repeated several times along the channel. Finally a large number of electrons is released from the output side and accelerated towards the phosphor screen due to the applied voltage $U_{Phosphor} = 5\text{ kV}$. The light emitting phosphor screen is then photographed by a cooled CCD camera with a resolution of 512×768 pixel. The used imaging MCP (Hamamatsu, Type F1942-04) has an active area of 77 mm in diameter. The channel diameter is $25\ \mu\text{m}$ and the open area ratio is 60%. The imaging quality of an MCP was verified with laser accelerated proton beams and projection imaging of test objects and the energy dependent ion sensitivity was calibrated [99].

5.3 Ion Traces

Figure 5.3 is a photograph of the phosphor screen emission and shows a typical example of parabolic-shaped ion traces on the MCP. The traces are caused by the record of a laser-driven ion beam with a Thomson slit spectrometer. The

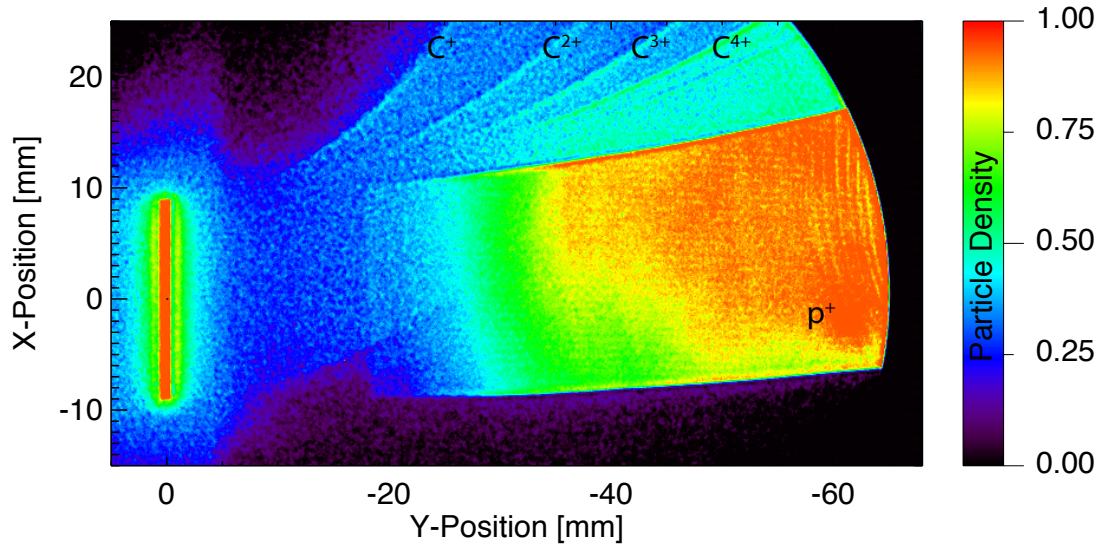


Figure 5.3: Recording of a laser-driven ion beam with a Thomson slit spectrometer. Photograph of the phosphor screen emission coupled with the MCP (camera view).

traces represent different ion species, protons and positively charged carbon ions. Due to the slit extension s_x , the traces partly overlay each other, but are clearly distinguishable. The width of the deflected traces c_x in x-direction is given in first approximation by the magnified projection of the slit on the detector screen

$$c_x = (L_1 + L_2 + L_3) \cdot 2 \cdot \tan\left(\frac{\alpha}{2}\right). \quad (5.5)$$

The ions were accelerated by irradiating a $5 \mu\text{m}$ thick titanium foil with a Ti:sapphire laser pulse at an intensity of $I_L \approx 1 \cdot 10^{19} \text{ W/cm}^2$. Protons and carbon ions originate from a contamination layer consisting of hydrocarbon and water [100, 101]. For some of the presented experiments in this work the detection of a pure proton signal without the contribution of other ion species was crucial. Figure 5.2.B shows the time of arrival of protons and carbon ions on the MCP as a function of their energy. The green dashed line represents the applied voltage U_{Phosphor} between the MCP and the phosphor screen in connection with the arrival time of the particles. By switching off the voltage 130 ns after the laser-plasma interaction an exclusive proton signal with energies above 0.5 MeV could be detected.

5.4 Data Analysis

A precise study of Image 5.3 reveals that the parabolic shape of the proton trace is not identical at its lower and higher edge and that the width c_x of the trace changes in y -direction. These characteristics can be explained by the specific magnetic field distribution of the permanent magnet. To investigate a proton beam with the opening angle α , a U-shaped magnet with a gap width of 4 cm was used. This relatively high distance of the field plates leads to a considerable inhomogeneity of the magnetic field components. In order to account for their influence on the ion deflection, the components B_x , B_y and B_z were measured with a spatial step width of 2.5 mm in x - and y -direction and 1 mm in z -direction. In addition 3D-field maps were computed for each field component by the interpolation of the measured data to a $[1 \times 1 \times 1]$ mm grid. Figure 5.4 shows these field components in the x - z -plane of the magnet at the position $y = 0$, which corresponds to the position of the slit center in y -direction (cf. Figure 5.1).

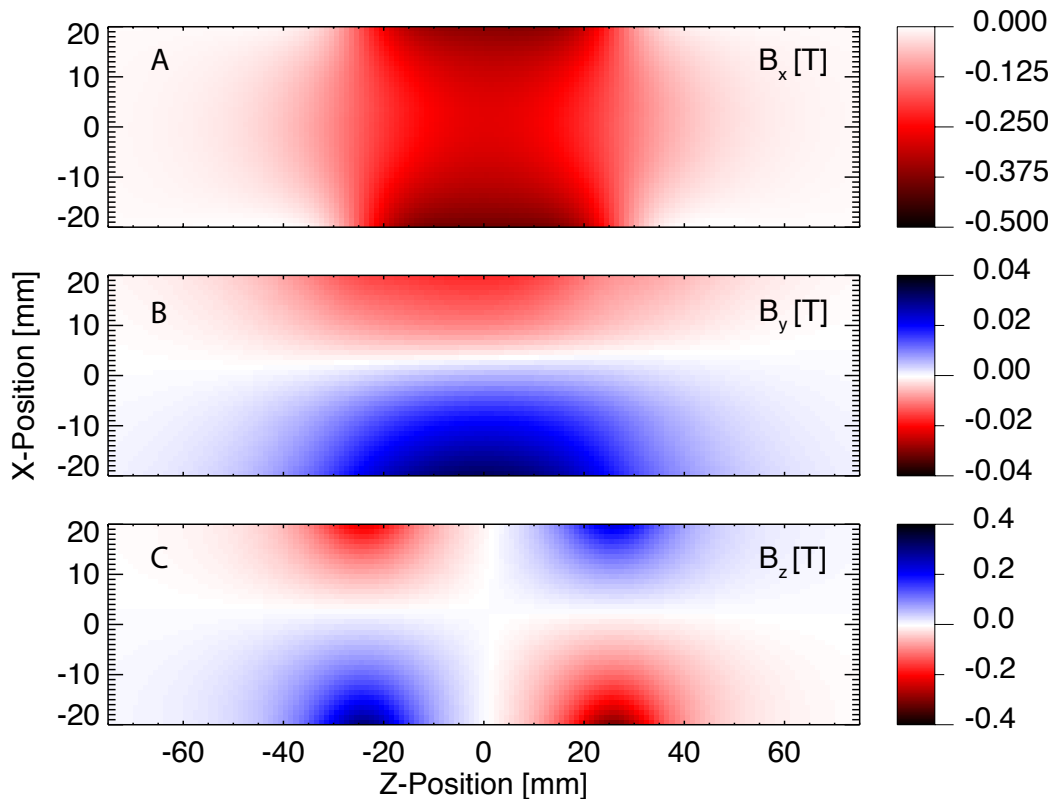


Figure 5.4: Magnetic field components in the x - z -plane of the permanent magnet at the position $y = 0$. The positions $x = 0$ and $y = 0$ correspond to the center of the slit, whereas $z = 0$ is the middle of the magnet in z -direction. **A** - B_x , **B** - B_y , **C** - B_z .

The magnetic field distribution in the y - z -plane at the position $x = 0$ (slit center in x -direction) is depicted in Figure B.7 in the appendix.

As illustrated the amplitude of each magnetic field component strongly varies in x -direction. Therefore, the influence of the magnetic field on the particle trajectory differs for ions which have the same energy but a different initial ejection angle β . The trajectory of each particle is governed by the Lorentz force. Therefore, the B_y and B_z components of the magnetic field become relevant if their amplitudes are sufficiently strong and if the particle exhibits a velocity component which is perpendicular to one or both of these field components.

Depending on β the ejected particle has a velocity component in x -direction and due to the main field component B_x the particle gains a velocity component in y -direction during its propagation through the field. As visible in Figure 5.4 and B.7 the field component B_z show values of the order of B_x . In addition the effective field extension in z -direction is relatively large ($l \approx 10$ cm). Therefore, their influence of the secondary field components B_y and B_z on the particle deflection should be taken into account.

The electric field caused by one of the two electric field plates can be described by the equation

$$\mathbf{E} = -\nabla \cdot \left(\frac{\sigma}{4\pi\epsilon_0} \int_{-a/2}^{a/2} \int_{-b/2}^{b/2} \frac{1}{\sqrt{(x-x_0)^2 + (y-y_0-y')^2 + (z-z_0-z')^2}} dy' dz' \right), \quad (5.6)$$

where the integral and gradient can be calculated analytically. The extensions of the field plates in y - and z -direction are given by $a = 5$ cm and $b = 5$ cm and the values x_0 , y_0 and z_0 determine the position of the field plates in space. The surface charge σ can be calculated by means of the applied voltage ($U \approx 7$ kV) and the gap width $d_g = 4$ cm between the two field plates. Due to Formula 5.6 the electric field vector has a spatial dependence and is not only directed in x -direction. Because the gap width d_g is comparable to the extensions of the field plates a, b the anisotropy of the field even appears for two parallel field plates. Therefore, the influence of the electric boundary fields on the particle deflection should be considered.

Since equations 5.1 to 5.4 account only for the x -components of the electric and magnetic fields, they provide a relatively inaccurate coordinate transformation between (β, ϵ) , i.e. the initial ejection angle β and energy ϵ of a proton, and the point of impact on the detector (x, y) . Thus, these formulas are not suited to transform the measured proton density distribution $\rho(x, y)$ into a distribution $\tilde{\rho}(\beta, \epsilon)$ that depends on the initial ejection angle β and energy ϵ of a proton.

For a quantitative analysis of the coordinate transformation between (β, ϵ) and (x, y) a commercial 3D-particle tracing software has been applied [102]. Using the particle tracer the ion trajectory within the electric and magnetic field configuration in the spectrometer can be simulated in three dimensions. Thus the point of impact on the MCP $(x(\beta, \epsilon), y(\beta, \epsilon))$ of a single proton can be calculated depending

on its initial ejection angle β and energy ϵ . Figure 5.5 illustrates the flight path and impact points of two protons with different initial energies (ϵ_1, ϵ_2) and ejection angles (β_1, β_2) in the x-z-plane. Their corresponding initial momenta are denoted by \vec{p}_1 and \vec{p}_2 , the impact points on the MCP by (x_1, y_1) and (x_2, y_2) .

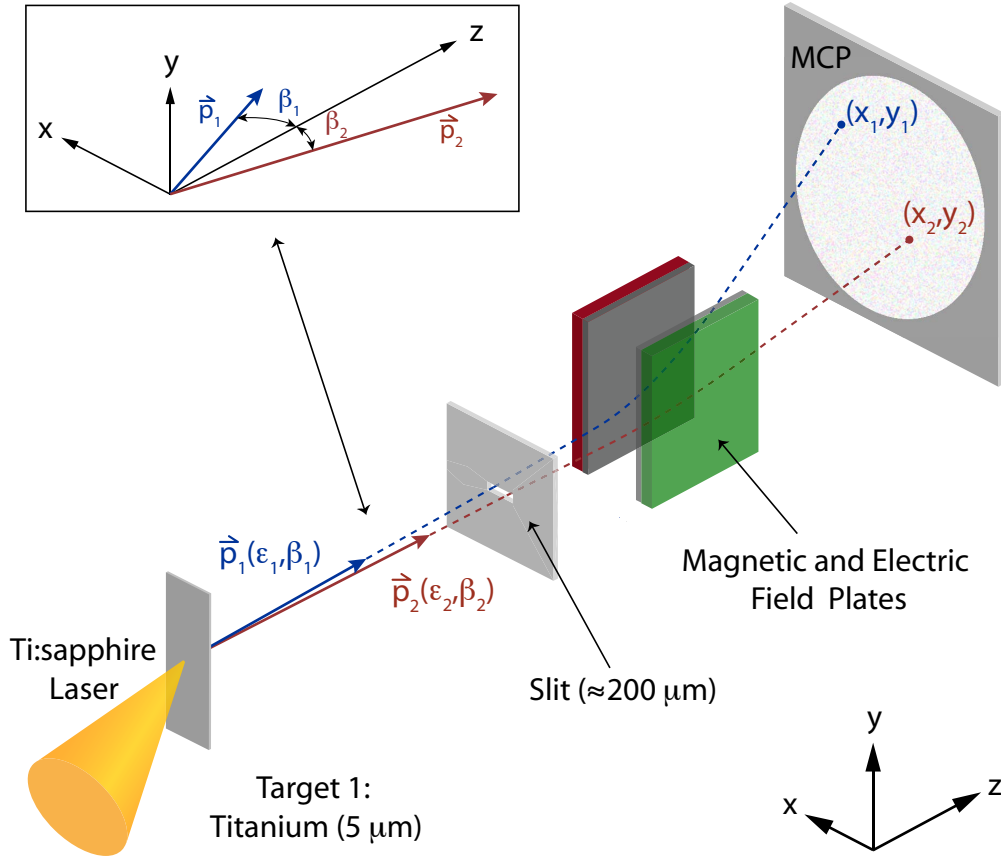


Figure 5.5: Flight path and impact points of two protons with different initial energies (ϵ_1, ϵ_2) and ejection angles (β_1, β_2) in the x-z-plane.

Mathematically this dependence can be described by means of a coordinate transformation

$$\Phi(\beta, \epsilon) = (\Phi_x(\beta, \epsilon), \Phi_y(\beta, \epsilon)) \quad (5.7)$$

$$x = \Phi_x(\beta, \epsilon), \quad y = \Phi_y(\beta, \epsilon), \quad (5.8)$$

whereby the function $\Phi(\beta, \epsilon)$ describes the simulated deflection in the x-y-plane of the detector. Its reverse function is denoted by $\Phi^{-1}(x, y)$ and formally given by

$$\Phi^{-1}(x, y) = (\Phi_\beta^{-1}(x, y), \Phi_\epsilon^{-1}(x, y)) \quad (5.9)$$

$$\beta = \Phi_\beta^{-1}(x, y), \quad \epsilon = \Phi_\epsilon^{-1}(x, y). \quad (5.10)$$

The existence of the reverse function is only justified if $\Phi(\beta, \epsilon)$ is a bijective function. This has been confirmed in the particle simulation by the fact that the family of curves $\Phi_{\epsilon_c}(\beta) = \Phi(\beta, \epsilon = \epsilon_c)$ does not intercross on the detector plane for different values of ϵ_c . The assumption that this behavior is realistic for a laser-accelerated proton beam is reasonable since the transversal emittance of such a beam is low and its source size is small compared to the distance between source and detector. The transformation theorem

$$\int_{\mathcal{F}} \rho(x, y) dx dy = \int_{\Phi^{-1}(\mathcal{F})} \rho(\Phi(\beta, \epsilon)) \cdot |\det(D\Phi(\beta, \epsilon))| d\beta d\epsilon \quad (5.11)$$

allows the proton density distribution $\tilde{\rho}(\beta, \epsilon)$ to be defined depending on the proton energy ϵ and the initial ejection angle β

$$\tilde{\rho}(\beta, \epsilon) = \rho(\Phi(\beta, \epsilon)) \cdot |\det(D\Phi(\beta, \epsilon))|. \quad (5.12)$$

Here the Jacobian determinant $|\det(D\Phi(\beta, \epsilon))|$ is defined by the equation

$$|\det(D\Phi(\beta, \epsilon))| = \left| \frac{\partial\Phi_x}{\partial\beta} \frac{\partial\Phi_y}{\partial\epsilon} - \frac{\partial\Phi_x}{\partial\epsilon} \frac{\partial\Phi_y}{\partial\beta} \right|. \quad (5.13)$$

Using the particle tracer the trajectories of $N = 5 \cdot 10^6$ particles with individual starting conditions were calculated. For this purpose the initial proton ejection angles β were distributed over an interval which is slightly bigger than $\beta \in [-\alpha/2, \alpha/2]$ and the proton energies were distributed over the interval $\epsilon \in [0.1, 5]$ MeV. This allowed for the determination of $x = \Phi_x(\beta, \epsilon)$ and $y = \Phi_y(\beta, \epsilon)$ for an area on the x-y-plane which corresponds to the region of the experimentally recorded proton density distribution $\rho(x, y)$ on the MCP.

An upper limit for the spatial resolution of the spectrometer is given by the photographed area of the phosphor screen (diameter ≈ 80 mm) and the resolution of the CCD camera with $N_\gamma \times N_\delta$ pixel, whereby $N_\gamma = 512$ and $N_\delta = 768$.

The projection of each pixel (γ, δ) on the MCP corresponds to a position $\mathbf{r}_{\gamma\delta}$ with the constant effective area $A_{\gamma\delta} = \Delta r_M^2$. Here Δr_M denotes the projected distance of two neighbored pixels on the MCP. In the presented experiments Δr_M has a value of approximately $100 \mu\text{m}$. Since the applied MCP (Section 5.2) has an open area ratio of 60% with a channel diameter of $25 \mu\text{m}$ the spatial resolution of the detection unit (MCP, phosphor screen, objective and CCD camera) is given by $\Delta r_D = \Delta r_M \approx 100 \mu\text{m}$.

The number of protons in the particle simulation that impinge on the area $A_{\gamma\delta}$ around the position $\mathbf{r}_{\gamma\delta}$ is denoted by $N_{\gamma\delta}$. In order to guarantee that the energy and angle resolution of the transformed density distribution $\tilde{\rho}(\beta, \epsilon)$ is not limited by the particle simulation, the shape of the simulated energy distribution function was chosen in a way that the number $N_{\gamma\delta} > 1$ for $\gamma = 1, 2, 3, \dots, N_\gamma$ and $\delta = 1, 2, 3, \dots, N_\delta$.

By means of a triangulation algorithm the N simulated data points $(x_s, y_s, \epsilon_s, \beta_s)$

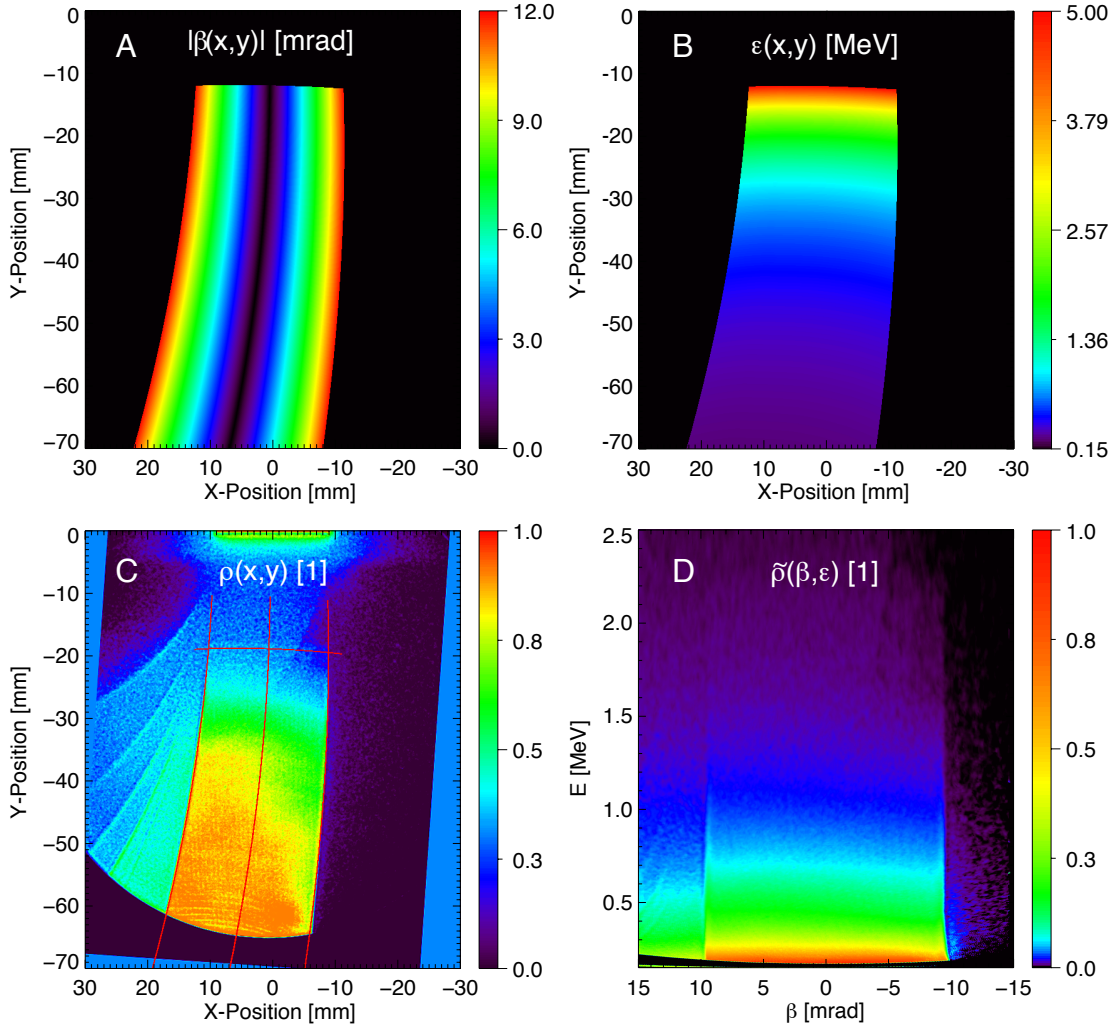


Figure 5.6: **A** - Simulated distribution of the proton ejection angle $\beta(x,y)$ (absolute values) on the MCP. **B** - Simulated distribution of the proton energy $\epsilon(x,y)$ on the MCP. **C** - Measured density distribution $\rho(x,y)$ on the MCP. **D** - Calculated proton density distribution $\tilde{\rho}(\beta, \epsilon)$ (Equation 5.12) depending on the initial ejection angle β and proton energy ϵ .

with $s = 1, 2, 3, \dots, N$ are interpolated on a two-dimensional equidistant grid of $N_i \times N_j$ data points ($N_i = 600$, $N_j = 700$) with an resolution of $100 \mu\text{m}$. This procedure results in the creation of the two-dimensional arrays β_{ij} and ϵ_{ij} with $i = 1, 2, 3, \dots, N_i$ and $j = 1, 2, 3, \dots, N_j$. These arrays are connected via (i,j) to (x,y) -coordinates and thus to the functions $\beta(x,y) = \Phi_\beta^{-1}(x,y)$ and $\epsilon(x,y) = \Phi_\epsilon^{-1}(x,y)$. Figure 5.6.A illustrates the distribution of $\beta(x,y)$ (absolute values) on the MCP and Figure 5.6.B the spatial dependence of $\epsilon(x,y)$. In the shown case the main field component B_x of the permanent magnet was orientated in negative x-direction,

which led to a deflection of the protons in negative y -direction. Therefore, the center of the MCP was placed below the slit height in experiment. At the same time the electric field component E_x was directed in positive x -direction.

The emission of neutral ions and gamma-radiation leads to the projection of the slit on the MCP. The position and rotation angle of the slit-projection is clearly visible in all pictures of the phosphor screen. In combination with the knowledge of the dimensions and distances of the spectrometer setup this can be used to identify the relation between the coordinate system of the recorded images and the coordinate system in the particle simulation. By means of rotation and interpolation of the recorded images the relevant region of the photographed phosphor screen can be transformed to a two-dimensional array ($N_i \times N_j$ pixel) with the same coordinate system as in the particle simulation. This array is denoted by ρ_{ij} ($i = 1, 2, 3, \dots, N_i$ and $j = 1, 2, 3, \dots, N_j$) and provides the ion density distribution $\rho(x, y)$ on the MCP.

Figure 5.6.C shows the measured 2D-distribution $\rho(x, y)$ in the same coordinate system as the calculated quantities $\beta(x, y)$ and $\epsilon(x, y)$. The red lines in y -direction correspond to the family of curves $\Phi_{\beta_c}(\epsilon) = \Phi(\beta_c, \epsilon)$ with $\beta_c \in \{-\alpha/2, 0, \alpha/2\}$ and illustrates that the calculated proton projections of the slit edges correspond well to the measured proton density distribution $\rho(x, y)$ on the detector screen. The line in x -direction corresponds to the curve $\Phi_{\epsilon_c}(\beta) = \Phi(\beta, \epsilon_c)$ with $\epsilon_c = 2.2$ MeV and its bending reflects the inhomogeneity of the permanent magnet.

In principle the knowledge of $x = \Phi_x(\beta, \epsilon)$ and $y = \Phi_y(\beta, \epsilon)$ and $\rho(x, y)$ can be used to determine proton density distribution $\tilde{\rho}(\beta, \epsilon)$ via Equations 5.12 and 5.13. However, for the visualization of $\tilde{\rho}(\beta, \epsilon)$ with equidistant grid points (β_l, ϵ_m) the values of $x_{lm} = \Phi_x(\beta_l, \epsilon_m)$ and $y_{lm} = \Phi_y(\beta_l, \epsilon_m)$ are needed for these exact grid points ($l = 1, 2, 3, \dots, N_l$ and $m = 1, 2, 3, \dots, N_m$). In this case the required values $\rho_{lm} = \rho(\Phi(\beta_l, \epsilon_m))$ have to be interpolated on the basis of the measured array ρ_{ij} . For practical reasons another way is chosen. As described the functions $\beta(x, y)$ and $\epsilon(x, y)$ are calculated in the same coordinate system and at the same grid points as $\rho(x, y)$. This way the alignment of the fields in the particle simulation can be examined with respect to the measured distribution $\rho(x, y)$. The reverse-transformation of Equation 5.11 yields

$$\rho(x, y) = \tilde{\rho}(\Phi^{-1}(x, y)) \cdot |\det(D\Phi^{-1}(x, y))|. \quad (5.14)$$

By means of the numerical derivatives of $\beta(x, y)$ and $\epsilon(x, y)$ with respect to x and y the Jacobian determinant $|\det(D\Phi^{-1}(x, y))|$ can be calculated

$$|\det(D\Phi^{-1}(x, y))| = \left| \frac{\partial\beta}{\partial x} \frac{\partial\epsilon}{\partial y} - \frac{\partial\epsilon}{\partial x} \frac{\partial\beta}{\partial y} \right|. \quad (5.15)$$

The division of the distribution ρ_{ij} with the corresponding 2D-array $|\det(D\Phi^{-1})|_{i,j}$ leads to the 2D-array $\tilde{\rho}'_{ij} = \rho_{ij} / |\det(D\Phi^{-1})|_{i,j}$ which is already density corrected, but still given in the x - y -coordinate system. Since the arrays β_{ij} , ϵ_{ij} and $\tilde{\rho}'_{ij}$ are

defined in the same coordinate system ($i = 1, 2, 3, \dots, N_i$ and $j = 1, 2, 3, \dots, N_j$), they provide a set of $N_p = N_i \times N_j$ data points $(\beta_p, \epsilon_p, \tilde{\rho}'_p)$. The triangulation and interpolation of these points to an equidistant grid of angle (β_l) and energy (ϵ_m) values ($l = 1, 2, 3, \dots, N_l$ and $m = 1, 2, 3, \dots, N_m$) leads to the 2D-array $\tilde{\rho}_{lm}$, which describes the proton density distribution $\tilde{\rho}(\beta, \epsilon)$ (Equation 5.12) depending on the initial ejection angle β and proton energy ϵ . Figure 5.6.D illustrates the distribution for a selected energy and ejection angle interval

As visible in Figure 5.6.D no other ion species than protons are detected within the interval $\beta \in [-9, -7]$ mrad. Therefore, the integration over this interval yields a pure one-dimensional proton energy spectrum, as illustrated in Figure 5.10.D.

5.5 Angle and Energy Resolution

As described in the previous section the spatial resolution Δr_D of the detection unit (MCP, phosphor screen, objective and CCD camera) is approximately $100 \mu\text{m}$. Neglecting the influence of the inhomogeneous electric and magnet fields within the Thomson slit spectrometer its angle resolution $\Delta\beta$ can be defined in first approximation by

$$\Delta\beta \approx \frac{\Delta r_D}{L}, \quad (5.16)$$

where L denotes the distance between the ion source and the detector. In the presented experiments the distance L was approximately 1 m. In combination with $\Delta r_D = 100 \mu\text{m}$ this leads to the value $\Delta\beta \approx 0.1$ mrad.

Before investigating the energy resolution of the Thomson slit spectrometer it is instructive to review the energy resolution of a conventional Thomson spectrometer. A general description of the energy resolution $\Delta\epsilon_T(\epsilon)$ which arises solely from the pinhole geometry and is independent of the location of the field region was proposed by Schneider et al. [103].

Figure 5.7.A illustrates the principal setup of a conventional Thomson spectrometer. In first approximation the ion traces on the detector can be described by Equations 5.1, 5.2 and 5.3 and the distribution of each ion species has a parabolic shape. However, these parabolas are not infinitely thin lines, but have a certain width d . Due to the finite diameter d_P of the used pinhole the ion beam is restricted to a divergent beam with the opening angle $\delta \approx d_P/L_1$. In first approximation, ions with the same energy are projected to a circular area on the detector with the diameter $d \approx L\delta$. For a continuous energy spectrum the spectrogram can be thought of as a superposition of these spots which are infinitely close together along the parabola as shown in Figure 5.7.B.

The blue circle marks the region where ions with the energy ϵ impinge on the detector, whereby the coordinates $(x, y) = (x(\epsilon), y(\epsilon))$ correspond to the position of its center. The intersection points of the edge of this circle with the central axis of the parabola have the coordinates $(x_{\min}, y_{\min}) = (x(\epsilon_{\min}), y(\epsilon_{\min}))$ and

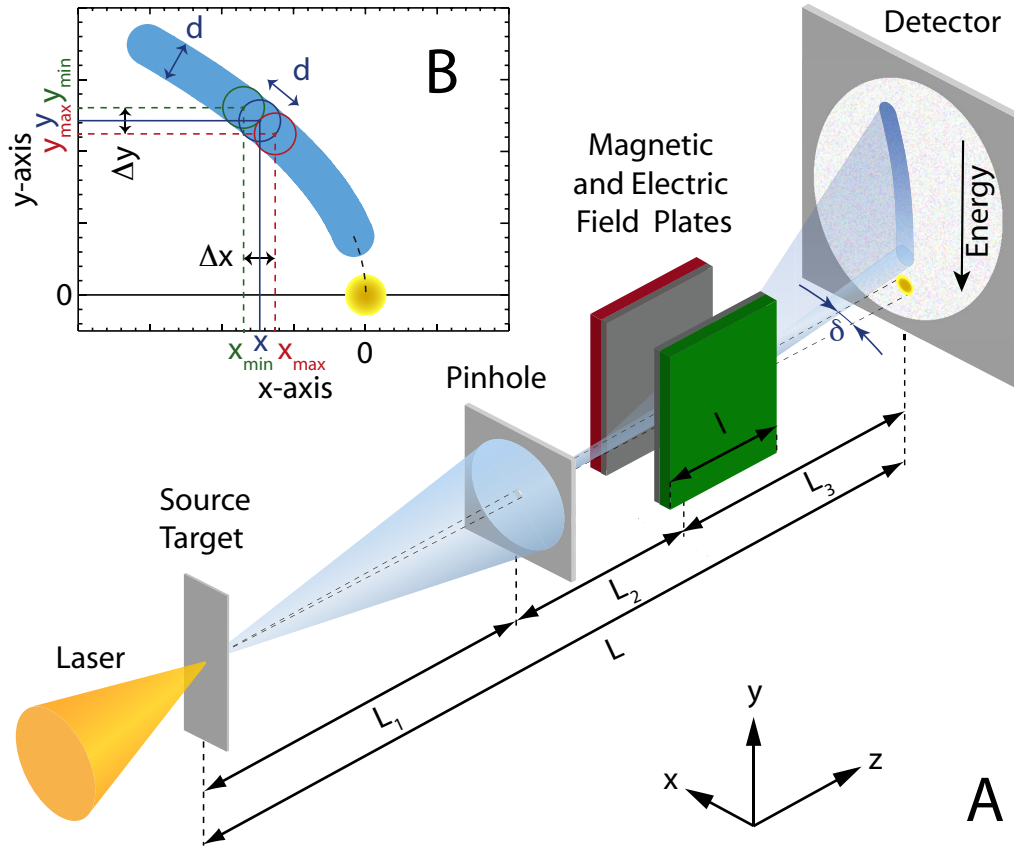


Figure 5.7: **A** - Principal setup of a conventional Thomson spectrometer. **B** - Parabolic spectrogram on the detector with the width $d \approx L\delta$.

$(x_{\max}, y_{\max}) = (x(\epsilon_{\max}), y(\epsilon_{\max}))$ and correspond to the energies ϵ_{\min} and ϵ_{\max} , respectively. These points can be regarded as the centers of two additional circles (green and red) which constitute regions on the detector that are reached by ions with the respective energies. The point of contact of these two circles is close to the position $(x, y) = (x(\epsilon), y(\epsilon))$. For this reason, this point is not only reached by ions with the energy ϵ but also by ions with the energies ϵ_{\min} and ϵ_{\max} , respectively. The full width of the interval $[\epsilon_{\min}, \epsilon_{\max}]$ allows for a definition of the energy resolution $\Delta\epsilon_T$ at this position

$$\Delta\epsilon_T = \epsilon_{\max} - \epsilon_{\min}. \quad (5.17)$$

The distances Δx and Δy in Figure 5.7.B. are defined by

$$\Delta x = x_{\max} - x_{\min}, \quad (5.18)$$

$$\Delta y = y_{\max} - y_{\min} \quad (5.19)$$

and are connected with the width of the parabola d by the equation

$$d^2 = \Delta x^2 + \Delta y^2. \quad (5.20)$$

The slope of the parabola $dy/dx = y/2x$ can be calculated by means of Equation 5.3 and is used to rewrite the last equation

$$d^2 = \left(1 + \left(\frac{y}{2x}\right)^2\right) \Delta x^2. \quad (5.21)$$

Using the approximation $\epsilon_{\max} \cdot \epsilon_{\min} \approx \epsilon^2$ as well as Equations 5.2, 5.17, 5.18 and 5.21 the energy resolution $\Delta\epsilon_T$ can be expressed as

$$\Delta\epsilon_T(\epsilon) \approx -\frac{\Delta x}{x} \epsilon = -\frac{2d \cdot \epsilon}{\sqrt{4x(\epsilon)^2 + y(\epsilon)^2}}. \quad (5.22)$$

This equation can be simplified further, if the relation $x \ll y$ is valid for the ion trace on the detector. Substitution of Equation 5.1 into Equation 5.22 and neglecting the term with x leads to the following dependence of the ion energy resolution

$$\Delta\tilde{\epsilon}_T(\epsilon) \approx \frac{d}{A} \cdot \epsilon^{\frac{3}{2}}, \quad A = \sqrt{\frac{C}{2D}} = \frac{QB_x l L_3}{\sqrt{2m}} \quad (5.23)$$

In order to calculate the energy resolution of the Thomson slit spectrometer and to compare it with the energy resolution $\Delta\tilde{\epsilon}_T(\epsilon)$ of a conventional Thomson spectrometer (Equation 5.23) a similar definition of the energy resolution is required. Figure 5.8 illustrates the trajectories of ions with different starting conditions in the Thomson slit spectrometer. For simplicity their propagation path and dependencies are restricted to the y-z-plane.

The divergence angle $\gamma = 2 \cdot \text{atan}(s_y/(2 \cdot L_1))$ confines the detectable initial ejection angle θ of an ion by $\theta \in [-\gamma/2, \gamma/2]$ and thus limits its possible velocity component in y-direction.

The blue line corresponds to an ion with the initial energy ϵ and initial ejection angle $\theta = 0$. Its point of impact on the detector has the coordinate $y(\epsilon)$.

The green color marks the trajectory of an ion with the energy ϵ_{\min} and the initial ejection angle $\theta_{\min} = -\gamma/2$. In comparison to the blue ion its ejection angle and energy are smaller, i.e. $\theta_{\min} < \theta$ and $\epsilon_{\min} < \epsilon$. For this reason, the green ion can reach the same position on the detector as the blue ion. In contrast, ions with either higher ejection angles or higher energies are deflected to higher positions on the detector $y > y(\epsilon)$. Therefore, the green ion has the minimal possible energy ϵ_{\min} which still reaches the position $y(\epsilon)$.

Similarly, the red color indicates an ion with the maximum possible energy $\epsilon_{\max} > \epsilon$

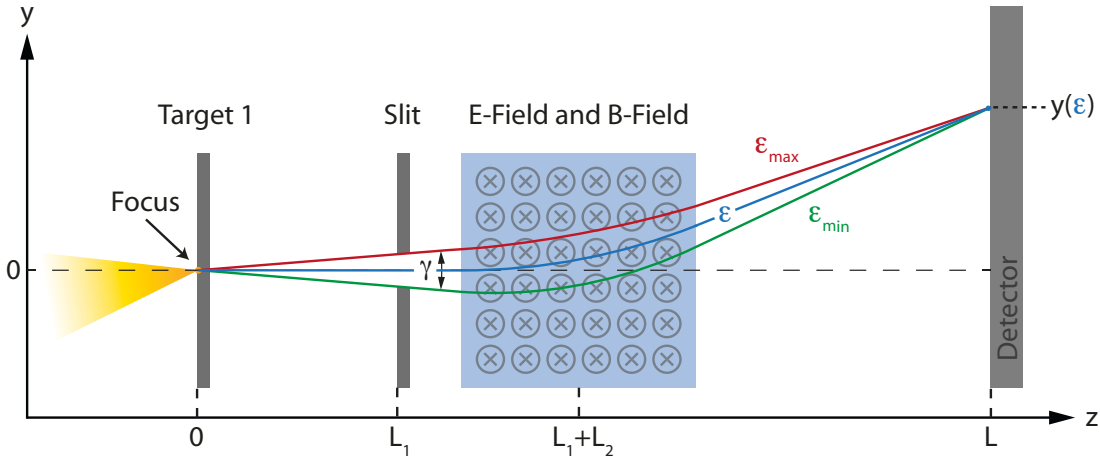


Figure 5.8: Limited energy resolution due to the geometrical design of the spectrometer.

that is not deflected to a position $y < y(\epsilon)$ on the detector. As in the case of the conventional Thomson spectrometer the full width of the interval $[\epsilon_{\min}, \epsilon_{\max}]$ allows for a definition of the energy resolution of the Thomson slit spectrometer

$$\Delta\epsilon_S(\epsilon) = \epsilon_{\max}(\epsilon) - \epsilon_{\min}(\epsilon), \quad (5.24)$$

which can easily be extended to two dimensions

$$\Delta\epsilon_S(\beta, \epsilon) = \epsilon_{\max}(\beta, \epsilon) - \epsilon_{\min}(\beta, \epsilon). \quad (5.25)$$

Due to the considerable inhomogeneity of the electric and magnetic field components within the spectrometer (Section 5.4) Equation 5.25 cannot be evaluated analytically. Instead a 3D-particle tracer [102] was employed to calculate the energy resolution $\Delta\epsilon_S(\beta, \epsilon)$ of the Thomson slit spectrometer depending on the initial ejection angle β and energy ϵ of a proton.

As Figure 5.9 shows, the dependence on the ejection angle β is negligible in the presented case. Integration over the shown interval of β yields the average energy resolution $\Delta\epsilon_S(\epsilon)$ which is illustrated by the blue curve in Figure 5.10.C.

Equations 5.22 and 5.23 describe the energy resolution $\Delta\epsilon_T(\epsilon)$ of a conventional Thomson spectrometer and are illustrated in Figure 5.10.A by the yellow and red dashed curve, respectively.

As shown in Figure 5.10.C these formulas can be applied to estimate the energy resolution of the Thomson slit spectrometer if the projected slit width c_y is used instead of the projected pinhole diameter d . The red dashed curve illustrates this estimation on the basis of Equation 5.23. The comparison with the blue curve shows, that Formula 5.23 is a good approximation to describe the energy resolution of the presented Thomson slit spectrometer.

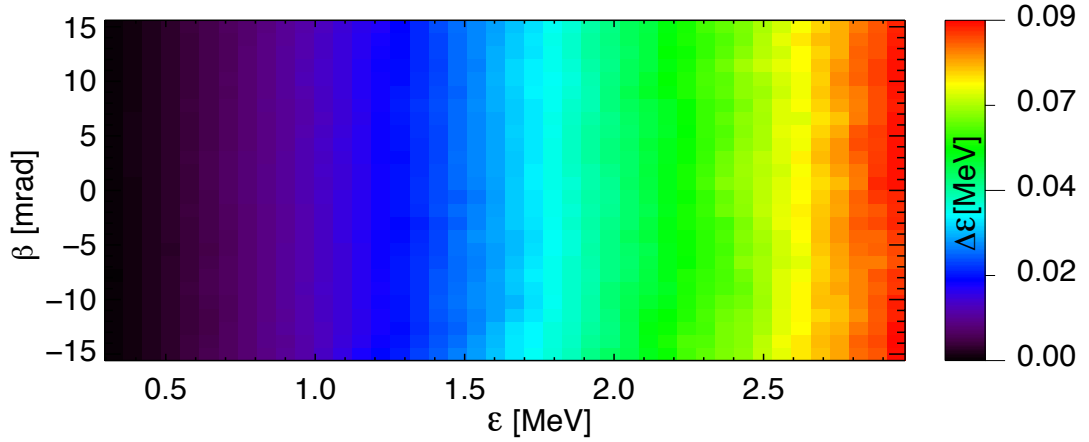


Figure 5.9: Calculated energy resolution $\Delta\epsilon_S(\beta, \epsilon)$ depending on the initial ejection angle β and energy ϵ of a proton. Here, the following parameters apply: $L_1 = 475$ mm, $L_2 = 205$ mm, $L_3 = 231$ mm, $s_y = 266$ μ m.

So far the derived equations of the energy resolution (Equations 5.22 to 5.25) do neither account for the spatial resolution of the detection unit Δr_D nor for the spatial extension of the ion source d_S .

First we consider the finite spatial resolution of the detection unit Δr_D . Figure 5.10.B illustrates the derivatives of the coordinates x and y with respect to energy. In the depicted energy interval $dy/d\epsilon$ is higher than $dx/d\epsilon$. Since the energy dispersion is higher in y -direction this direction is used to determine the energy resolution $\Delta\epsilon_P(\epsilon)$ of the spectrometer which is caused by the the spatial resolution of the detection unit Δr_D .

Substitution of Equation 5.2 into 5.3 yields a direct relation between the y -coordinate $y(\epsilon)$ on the detector plane and the ion energy ϵ which is given by

$$y(\epsilon) = \frac{A}{\sqrt{\epsilon}}, \quad (5.26)$$

where A is defined in Equation 5.23. Due to the spatial resolution of the detection unit Δr_D the energy ϵ can also be detected at the positions

$$\hat{y}_{\max}(\epsilon) = y(\epsilon) - \Delta r_D/2, \quad \hat{y}_{\min}(\epsilon) = y(\epsilon) + \Delta r_D/2, \quad (5.27)$$

where $\hat{y}_{\max}(\epsilon) < \hat{y}_{\min}(\epsilon)$. On the other hand the coordinates $\hat{y}_{\min}(\epsilon)$ and $\hat{y}_{\max}(\epsilon)$ refer to the energies

$$\hat{\epsilon}_{\min}(\epsilon) = (A/\hat{y}_{\min}(\epsilon))^2, \quad \hat{\epsilon}_{\max}(\epsilon) = (A/\hat{y}_{\max}(\epsilon))^2, \quad (5.28)$$

with $\hat{\epsilon}_{\min}(\epsilon) < \hat{\epsilon}_{\max}(\epsilon)$. The full width of the interval $[\hat{\epsilon}_{\min}, \hat{\epsilon}_{\max}]$ allows for a definition of the energy resolution of the Thomson slit spectrometer which is caused by

the spatial resolution Δr_D of the detection unit

$$\Delta\epsilon_P(\epsilon) = |\hat{\epsilon}_{\max}(\epsilon) - \hat{\epsilon}_{\min}(\epsilon)|, \quad (5.29)$$

which is illustrated by the blue curve in Figure 5.10.A. Derivation of Equation 5.26 with respect to ϵ yields the equation

$$dy/d\epsilon = (A/2) \cdot \epsilon^{-\frac{3}{2}} \quad (5.30)$$

and allows for a similar definition of the of the energy resolution in connection with the limited spatial resolution Δr_D of the detection unit

$$\Delta\tilde{\epsilon}_P(\epsilon) = |\Delta r_D (dy/d\epsilon)^{-1}|, \quad (5.31)$$

which is shown by the orange dashed line in Figure 5.10.A.

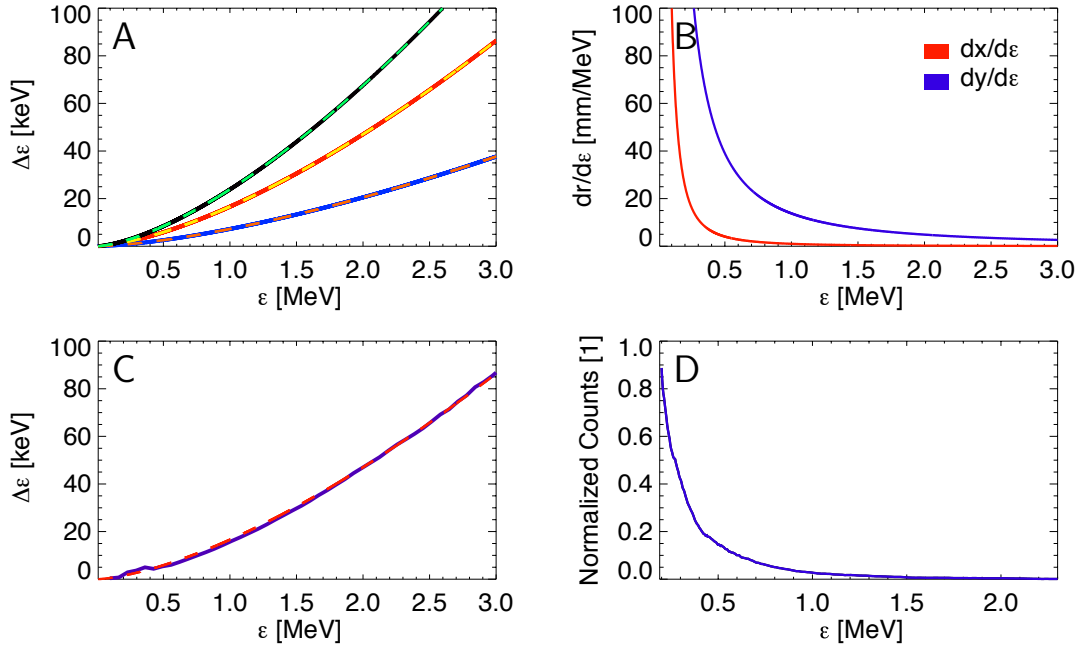


Figure 5.10: **A** - Energy resolution of a conventional Thomson spectrometer. Yellow curve - $\Delta\epsilon_T(\epsilon)$ (Equation 5.22). Red dashed curve - $\Delta\tilde{\epsilon}_T(\epsilon)$ (Equation 5.23). Blue curve - $\Delta\epsilon_P(\epsilon)$ (Equation 5.29). Orange dashed curve - $\Delta\tilde{\epsilon}_P(\epsilon)$ (Equation 5.31). Black curve - $\Delta\epsilon(\epsilon)$ (Equation 5.32). Green dashed curve - $\Delta\tilde{\epsilon}_T(\epsilon) + \Delta\tilde{\epsilon}_P(\epsilon)$. **B** - Derivatives of the coordinates x and y with respect to the proton energy ϵ . **C** - Spectrometer resolution as a function of the proton energy. Blue curve - Simulated energy resolution $\Delta\epsilon_S(\epsilon)$ using a 3D-particle tracer. Red dashed curve - Estimated energy resolution $\Delta\tilde{\epsilon}_T(\epsilon)$ using Formula 5.23. **D** - Proton energy spectrum for the angle interval $\beta \in [-9, -7]$ mrad (c.f. Section 5.4). - For all images the following parameters apply: $L_1 = 475$ mm, $L_2 = 205$ mm, $L_3 = 231$ mm, $s_x = 9$ mm, $s_y = 266 \mu\text{m}$, $d_P = 266 \mu\text{m}$, $c_x = 17.8$ mm, $c_y = 459 \mu\text{m}$, $d = 459 \mu\text{m}$, $\alpha = 18.8$ mrad, $l = 50$ mm, $B_x = 343$ mT, $E_x = 175$ kV/m.

In first approximation the energy resolution $\Delta\epsilon(\epsilon)$ which is caused by the combined effect of the finite pinhole diameter d_P and the finite spatial resolution of the detection unit Δr_D can be written as the sum of the two corresponding parts

$$\Delta\epsilon(\epsilon) = \Delta\epsilon_S(\epsilon) + \Delta\epsilon_P(\epsilon). \quad (5.32)$$

This dependency is illustrated by the black line in Figure 5.10.A.

In addition to the spatial resolution of the detection unit Δr_D the spatial extension of the ion source d_S can contribute to the total energy resolution of the Thomson spectrometer. In first approximation d_S can be regarded as the diameter of the ion source. Under the assumption that each point of the source emits protons isotropically in all directions, the projection of the source on the detector plane is given by

$$\tilde{d} = \frac{L - L_1}{L_1} (d_S + d_P) + d_P. \quad (5.33)$$

Therefore, the influence of a spatially extended ion source on the energy resolution can be considered by replacing d with \tilde{d} in Equations 5.22 and 5.23. However, in the case of the TNSA mechanism the ion source is characterized by an extremely low transversal emittance and an effective source size of ion emission with an extension of several micrometers (c.f. Section 7.1). Using the model of the virtual source [104] Equation 5.33 can be adapted

$$\tilde{d} = \frac{L - (L_1 + |z_v|)}{L_1 + |z_v|} (d_{VS} + d_P) + d_P. \quad (5.34)$$

where $|z_v|$ denotes the distance of the virtual source to the real source (c.f. Section B.1). In a previous experiment at the Max-Born-Institute [8] the extension of the virtual source d_{VS} and its distance z_v to the real source was investigated, whereby similar laser (laser arm B, c.f. Section 2) and target parameters were used. As a result, a virtual source diameter d_{VS} of approximately $8 \mu\text{m}$ was found. In addition a virtual source distance z_v with values between -7 mm and -23 mm was determined for the proton energy interval $[0.4, 2.5] \text{ MeV}$. In the case of laser arm A a virtual source distances z_v in the range between -0.8 mm and -1.7 mm could be determined as described in Section B.1. Considering these values, the relative change of the projected source diameter ($d \rightarrow \tilde{d}$) is less than 3%. Therefore, the effect of the ion source extension on the energy resolution can be neglected for the presented experiments in this theses.

6 The Beat in Ion Acceleration

This chapter describes a characteristic property of a laser-driven ion source, which has been observed for the first time [28]. In preparation for proton streak deflectometry measurements, a Thomson slit spectrometer was assembled and implemented into a setup for laser-induced ion acceleration. For the enhancement of the temporal contrast ($\sim 10^{10} - 10^{11}$) a new XPW front-end was designed [45] and implemented in the chain of the MBI High-Field laser system. In order to analyze the influence of the modified laser on the ion-acceleration process a thin foil was irradiated by high intensity femtosecond laser pulses.

The application of the Thomson slit spectrometer allowed for the detection of weak but regular modulations in the proton energy spectrum, which was not possible with a conventional Thomson spectrometer. The use of a thin and relatively long entrance slit of the spectrometer provided a reasonable energy resolution in combination with a spatial resolution that allowed the observed oscillations to be discriminated against noise.

In order to explain the experimental findings several particle in cell simulations were conducted and an analytical model was developed [28], which reflect the situation when intense femtosecond laser pulses with very high temporal contrast are used for target normal sheath acceleration of ions.

Based on the simulation results and the outcome of the analytical model, the modulations can be attributed to the pulsing of the acceleration field itself. From this standpoint the effect is a direct consequence of the periodical release of electron bunches and is therefore linked to the frequency of the laser pulse. These results are in good agreement with the experimental observations and strongly indicate, that the observed modulations are a fundamental property of the ion source and prove the extremely low longitudinal emittance of the accelerated ion beam.

The presented results are already published [28], however this chapter will provide further insight into this topic and present additional findings.

6.1 Experimental Setup

For the generation of the proton beam, a 5 micron thick titanium foil (with its adherent CH-contamination) was irradiated with a p-polarized laser pulse at a 10°

angle of incidence. The used Ti:sapphire laser (Chapter 2) provided a peak power of 70 TW at a pulse length of 35 fs and a nanosecond contrast ratio to the ASE background of $10^{10} - 10^{11}$ [45]. The resulting intensity of $I_L \approx 3 \cdot 10^{19} \text{ W/cm}^2$ was calculated as described in Section 2.1.

For the ion detection the Thomson slit spectrometer (Chapter 5) was used. Its entrance slit had a variable width s_y in the range of $50 \mu\text{m}$ to $100 \mu\text{m}$ and a length s_x of approximately 8 mm. The geometry of the setup is depicted in Figure 5.1. The distance between the proton source and the entrance slit L_1 was 475 mm and the length between the slit and the middle of the magnetic field plates L_2 was 230 mm. The center of the magnet had a separation distance L_3 of 230 mm to the detector.

Considering these distances, the magnetic field strength $B_x = 280 \text{ mT}$ within the spectrometer and a slit width s_y between $100 \mu\text{m}$ and $230 \mu\text{m}$ the proton energy resolution is about (2-4) % of the calculated kinetic energy values.

6.2 Experimental Results

Figure 6.1 shows a recorded picture of the light emitting phosphor screen. The density distribution reflects the dispersed ion energies on the MCP. Since the electric field for separating the ion species in the spectrometer was switched off, the density profile consists of protons and other accelerated ions overlaying in one trace. A faint but clearly visible modulation of short period is detectable along the trace. Here a slit width s_y of $100 \mu\text{m}$ was used.

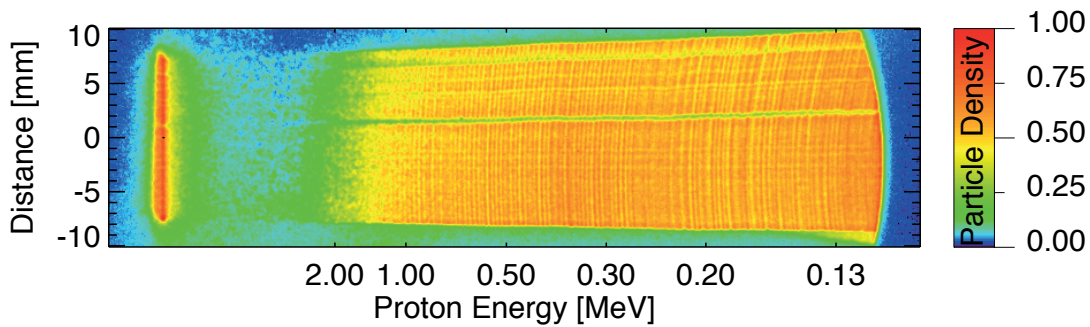


Figure 6.1: Photo of a recorded proton (ion) spectrum obtained with a MCP-detector

Additional experiments under similar conditions, but with the electric field switched on, clearly show that this density modulation can be attributed to the proton signal as shown in Figure 6.2.A. In this picture the proton trace was recorded with a energy resolution ($s_y \approx 230 \mu\text{m}$) approximately two times lower compared to Picture 6.1. Therefore, the modulation is blurred, but the features with stronger modulation depth are still visible in the low energy part of the proton spectrum.

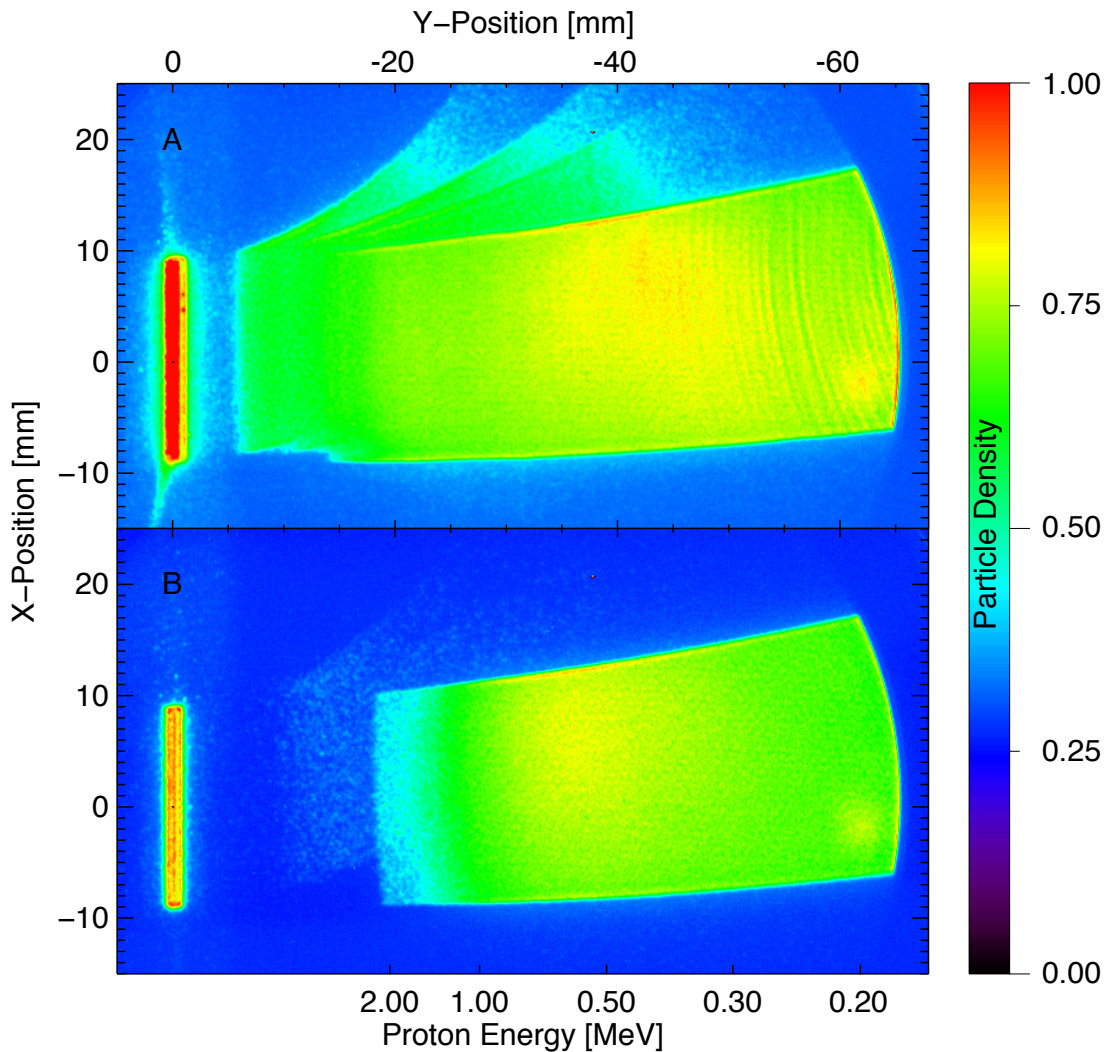


Figure 6.2: Ion traces of two selected measurements (camera view). **A** - Without beam filter and with modulations. **B** - With beam filter and without modulations.

In order to exclude that the observation is due to an artifact of the detection or the spectrometer, a 0.8 micrometer thick aluminum foil has been placed in the propagation path of the ion beam at a distance of 2 cm from the source. The second foil acted as a beam filter, because the small scale scattering within the foil was already sufficient to wash out the modulation, as depicted in Figure 6.2.B. Both spectrograms of Figure 6.2 were recorded with the same laser and setup parameters and correspond to the parameters proposed in Chapter 5.

The visible bending of the modulation lines in the spectrum is due to the variation of the magnetic field in the U-type magnet (Chapter 5.4). The appearance of such a characteristic curvature provides additional proof that the observed modulation is an inherent energy dependent beam property.

Former experiments [7] using a similar detection setup, but using a laser with a peak to ASE-intensity level of about 10^7 have not led to similar observations. A measurement of the temporal pulse shape [45] of laser arm 2, which was used in these experiments, shows intensity wings starting to decrease the 10^{10} peak to ASE contrast ratio at about 30 ps in front of the pulse peak.

The data set shown in Figure 6.1 has been chosen for further analysis because of its comparable higher energy resolution. In this case the density modulation is visible in the form of over one hundred banded lines. The numerical methods as described in Chapter 5.4 were applied to the two-dimensional ion density distribution of Image 6.1.

As a result, an averaged ($\beta \in [-8, 8]$ mrad) proton density spectrum as a function of energy is obtained, as illustrated by the blue curve in Figure 6.3. A contribution of other ion species to the density distribution cannot be excluded in this case. However, Measurement 6.2.A shows that the ion background has a slowly varying energy dependence in comparison to the observed energy modulation in the proton signal. The red curve in Figure 6.3 illustrates the average non-fluctuating signal which is composed of all accelerated ion species. A subtraction of this curve from the modulated spectrum (blue curve) allows for the determination of local maxima and minima in the proton energy spectrum. This so called *density difference spectrum* is illustrated in the insert of Figure 6.3 for the energy interval between 0.4 MeV and 1.3 MeV and shows that the modulation is not a strong effect. However, an increase of the modulation period with energy is clearly visible in the

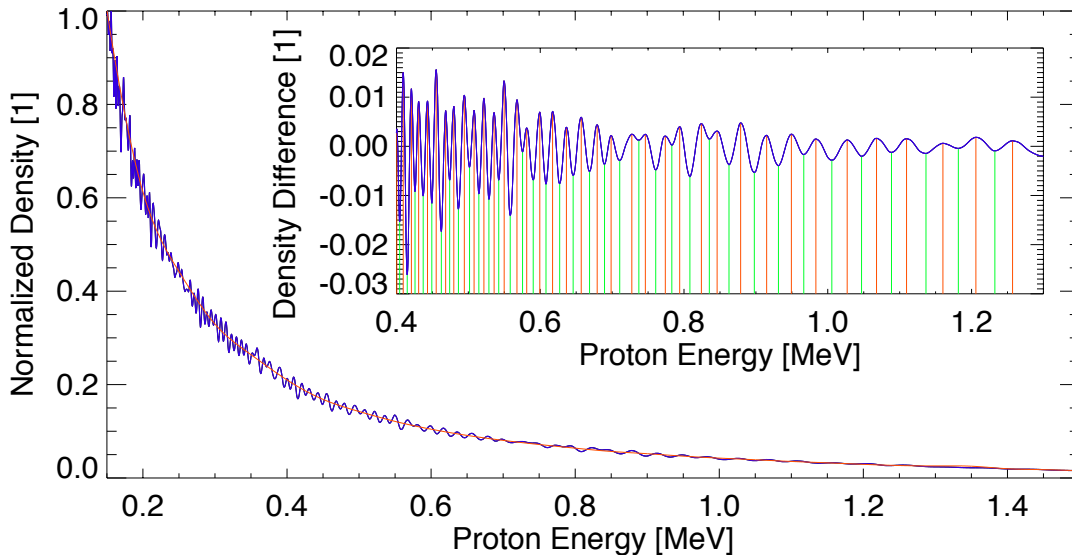


Figure 6.3: Blue line: Averaged ($\beta \in [-8, 8]$ mrad) proton density as a function of the energy, based on Image 6.1. Red line: Average non-fluctuating fit. Insert: Cutout and background subtraction (blue line - red line) to visualize the modulation feature.

spectrum.

A careful analysis of the two-dimensional density distribution in Figure 6.1 reveals that the signal noise along one of the modulation lines (at a certain energy) is comparable to the width and depth of the observed modulation itself or to the differential density spectrum. Therefore, it is relatively difficult to discriminate between noise and the weak modulation structure if only a single spectral trace without spatial information is recorded. This reflects the situation if an entrance pinhole of a few hundred micrometers is used, as in a conventional Thomson spectrometer. Only the use of a thin slit provided a reasonable energy resolution in combination with a spatial resolution that allowed the observed oscillations to be discriminated against noise. In this case, the resulting 2D-pictures immediately reveal the appearance of the modulation structure.

6.3 Simulation Results

In order to reach an understanding of the observation, a particle-in-cell (PIC) simulation has been conducted by A. Andreev [28]. For this numerical modeling of the experiment, a modified 2D-LSP-code [105] was applied, using 30 particles in a cell of 4×12 nm and a simulation box of 50×50 μm . The simulation step was of the order of 0.01 fs. The irradiation geometry of the model is identical to the experiment. A laser pulse with a slightly higher intensity of $I_L = 5 \cdot 10^{19}$ W/cm² is incident on a 1 μm thick titanium foil with a 50 nm hydrogen layer attached to the rear side of the foil. The temporal and spatial distribution of the laser field is modeled by the use of super-Gaussian (order of 8) functions with 10 oscillation periods τ_L (for $k_L \approx 0.8$ μm , $\tau_L \approx 2.7$ fs) and a spot size of 4 μm . The initial density profile has a rectangular shape and a value corresponding to the solid density of the target material. Thus the temporal pulse and target density distribution approximate the starting conditions for a laser-plasma interaction with a very high temporal intensity contrast.

The numerical simulation of the laser-plasma interaction clearly shows the generation of fast electrons, which move through the target as separated bunches. As illustrated in Figure 6.4.A, these bunches have a spatial separation length in the range of (0.3 – 0.4) μm . Considering that the electrons move with a velocity close to the speed of light, this corresponds to a temporal separation (1.00 fs – 1.34 fs) of approximately half the laser cycle ($\tau_L/2 = 1.35$ fs). Since the generation of electron bunches within the time interval of $\tau_L/2$ reflects the cyclic action of the ponderomotive force in this irradiation geometry, this situation is not unexpected.

Figure 6.4.B shows the simulated electric field, which accelerates the ions at the foil boundaries. The initial positions of these boundaries are indicated by blue vertical lines. The temporal evolution of this acceleration field at the position 1040 nm, i.e. at a distance of 40 nm from the initial rear foil surface is illustrated in Figure 6.5.A. Oscillations on a time scale of the second harmonic of the laser frequency $\tau_L/2$ are

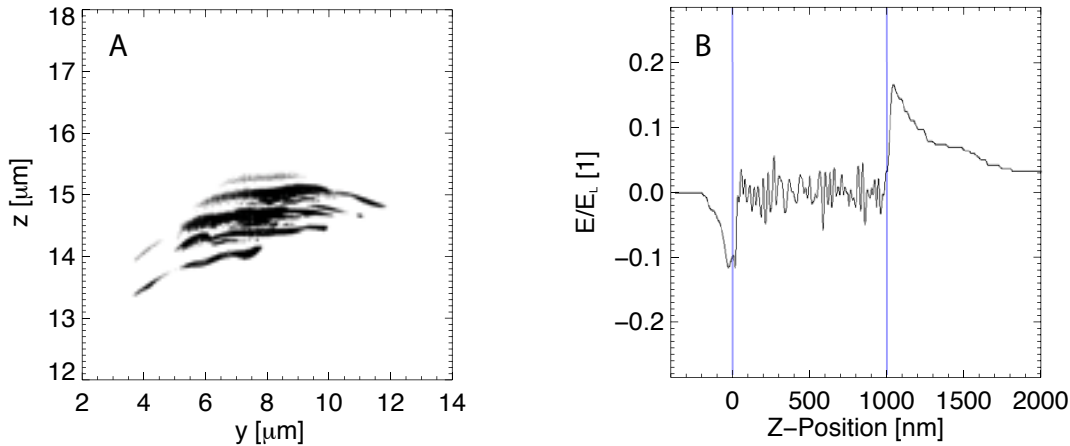


Figure 6.4: **A** - Calculated electron bunches in the coordinate space at the time moment 22.7 fs. **B** - Spatial electric field distribution at the time of laser pulse termination. Here, E_L denotes the electric field amplitude of the laser pulse and the blue lines show the initial positions of plasma boundaries. Simulation done by A. A. Andreev - MBI

clearly visible. This effect is only reproduced by PIC-simulations with high resolution and disappears if the resolution is decreased (Figure 6.5.B). The appearance of this modulation can be explained by the action of electron bunches at intervals of $\tau_L/2$. Each time an electron bunch passes through the boundary of the foil, the electric sheath field is modulated due to the charge of the particles.

Since the electric field is responsible for the ion acceleration in the case of TNSA, the temporal modulation of the acceleration field translates into a modulation of the proton energy distribution. This is illustrated by Figure 6.6.A which shows the simulated *density difference spectrum* of protons at a time moment of 200 fs after the laser-matter interaction has started. In order to exclude that the modulation is caused by numerical noise, several runs with different resolutions were conducted, which could validate the simulation result.

Comparing the number of maxima (or minima) in certain energy intervals shows that the modulation period (in terms of energy) is relatively independent on the proton energy. This becomes clear by applying a Fourier analysis to the *density difference spectrum*. Figure 6.7 shows the results of a numerical Fourier transformation for different energy intervals. The Fourier transform for the entire interval between 0.4 MeV and 1.3 MeV is illustrated in Figure 6.7.D. The frequency (in terms of MeV^{-1}) has a local maximum at $\sim 21 \text{ MeV}^{-1}$, which corresponds to a modulation period of $\sim 47 \text{ keV}$.

A comparison between the intervals [0.7, 1.0] MeV and [1.0, 1.3] MeV (Figures 6.7.B and 6.7.C) reveals that the position of the main frequency component (in terms of MeV^{-1}) is slightly smaller in the interval with higher energies. This tendency

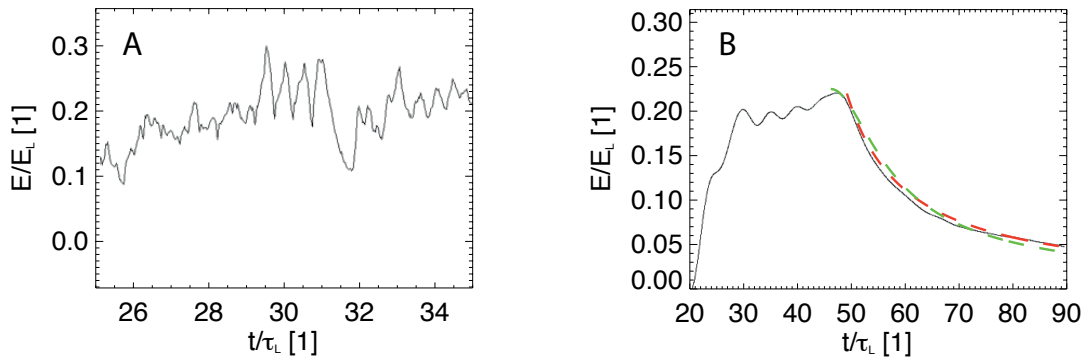


Figure 6.5: Temporal dependence of the electric field in laser periods τ_L at the point 1040 nm of Figure 6.4.B, e.g. 40 nm from the initial boundary of the foil rear side. **A** - With the proposed simulation parameters and high resolution. **B** - With a lower resolution but a longer time interval. The red curve is an approximation of the temporal decay when the laser pulse is gone using $\mathcal{E}_t = \mathcal{E}_N / (1 + (t - t_0)/\tau_s)$ with $\mathcal{E}_N = 0.22$, $t_0 = 132$ fs and $\tau_s = 30$ fs. For the green curve the function $\mathcal{E}_t = \mathcal{E}_N / \sqrt{1 + (t - t_0)/\tau_s)^2}$ with $\mathcal{E}_N = 0.225$, $t_0 = 124$ fs and $\tau_s = 22$ fs is used. Simulation done by A. A. Andreev - MBI

is not supported by Figure 6.7.A, which corresponds to the lowest energy interval [0.4, 1.3] MeV. However, it is likely that the resolution of the numerical simulation is not sufficient to resolve the modulation in this interval, which makes the comparison meaningless.

The increase of the modulation period with energy would be consistent with the experimental result which is illustrated in Figure 6.6.C and shows the final result of the acceleration process. In contrast, the simulation result of Figure 6.6.A corresponds to the energy distribution at the time instant 200 fs after the laser-matter interaction. Therefore, this spectrum will develop further in time until it reaches its final form.

The given simulation parameters can only guarantee a high accuracy of the calculated proton distribution function if the simulation time does not exceed a value of approximately 200 fs. This is due to the limited simulation box and the boundary conditions, which require that all particles are reflected at the edges of the box ($50 \mu\text{m} \times 50 \mu\text{m}$).

Since fast electrons move at a velocity close to the speed of light, their time of flight for a distance of $50 \mu\text{m}$ is around 170 fs. Therefore, reflected particles start to influence the ion acceleration process at higher simulation times and the proton distribution function is affected.

Nevertheless, a simulation was conducted which calculated until the protons reached their final velocities. In order to keep the computation time in reasonable limits, the time step of the simulation had to be increased by a factor of two. Thus the longer simulation time is a compromise with poorer time resolution. As a result,

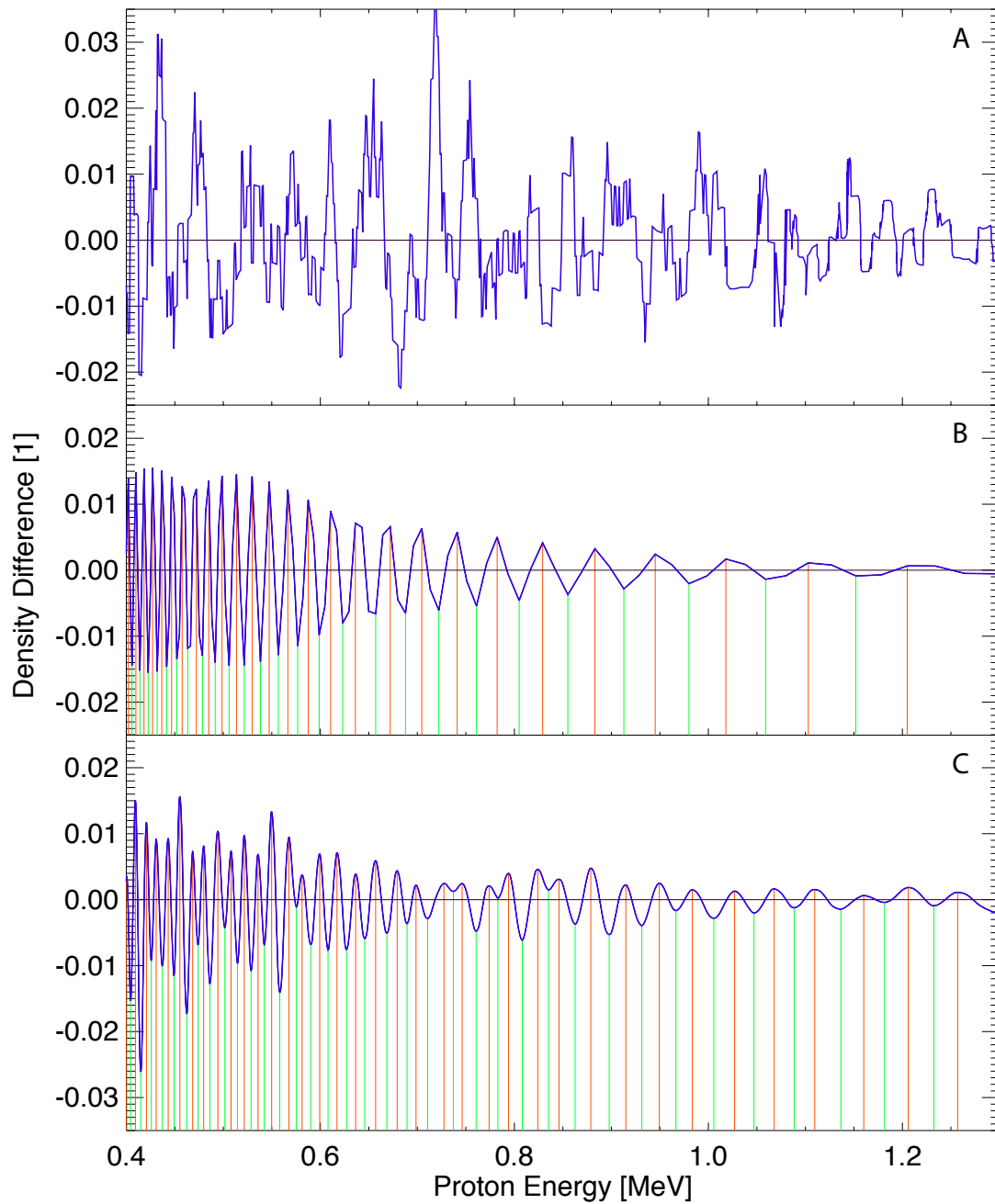


Figure 6.6: Modulations of the *density difference spectrum* as a function of the proton energy. In the case of Fig. A and Fig. C the averaged smooth signal was subtracted from the proton energy distribution. Simulation and model calculation done by A. A. Andreev - MBI. **A** - Calculated density modulations from 2D-PIC simulation at a time moment 200 fs after laser-target interaction has started. **B** - Analytical 1D-model calculation. **C** - Experimental result.

the distribution was shifted to higher energies and kept the same characteristics, but the fine modulation was blurred.

Considering that the calculated time duration of 200 fs is already close to the final acceleration instant, the number of local maxima (minima) visible in the numerical simulation (Figure 6.6.A) and the experiment (Figure 6.6.C) can be compared. In the energy intervals [0.7, 1.0] MeV and [1.0, 1.3] MeV these numbers are quite similar. This becomes obvious by comparing the Fourier transforms of the experimental and the simulated *density difference spectra*, which are shown in Figure 6.7.B and Figure 6.7.C for the respective intervals.

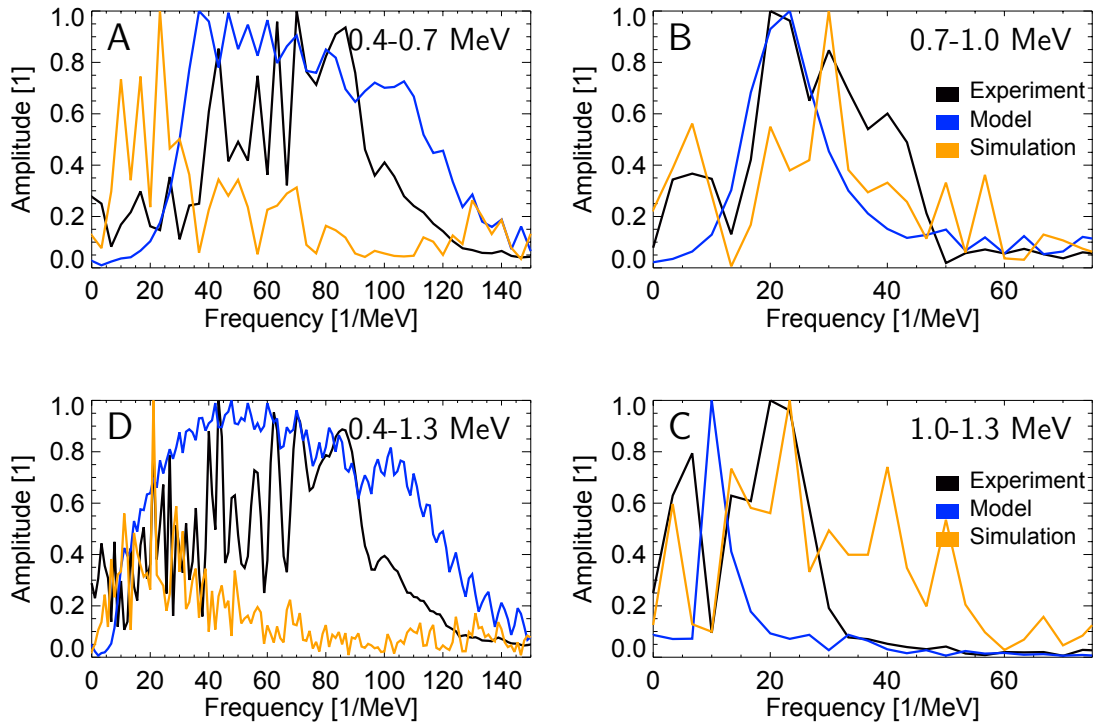


Figure 6.7: Fourier analysis of the *density difference spectra* of Figure 6.6 for different energy intervals. The black curves correspond to the experimental data, the blue curves to the model calculations and the yellow curves to the simulation results. **A** - Energy interval [0.4, 0.7] MeV. **B** - Energy interval [0.7, 1.0] MeV. **C** - Energy interval [1.0, 1.1] MeV. **D** - Energy interval [0.4, 1.3] MeV. All spectra are normalized separately.

6.4 Model Results

The modulation of the electron density in space and time and its direct relation to oscillations of the ponderomotive pressure is a substantial finding from the PIC simulation. Based on this result a one-dimensional analytical model [28] was developed by A. Andreev using a perturbation ansatz. The model is described in detail in Section B.4 of the appendix and discussed in relation to the simulation results of the last section.

In principle, the model accounts for the influence of the generated electron bunches by introducing a small perturbation of the electron density. The electron density is modulated in space and time by a perturbation structure which has a characteristic scale length of half the laser wavelength and propagates with a velocity close to the speed of light. The applied system of equations is linearized and solved in first order. As a result, the proton energy distribution function f (Equation B.23) is obtained, which can be written as the sum of two parts $f^{(0)}$ (Equation B.13) and $f^{(1)}$. The function $f^{(1)} = f - f^{(0)}$ can be interpreted in analogy to the experimentally determined *density difference spectrum* and is illustrated in Figure 6.6.B for $\xi \gg 1$. The trend of an increasing modulation period with higher proton energies is clearly reproduced by the model. Furthermore, the number of maxima and minima in a certain energy interval is similar to the experimental result. In the shown case this number corresponds well for lower energies, i.e. the interval [0.4, 0.6] MeV. The reason that the model only reproduces the number of peaks in a limited but adjustable energy range is due to the applied low order approximation.

6.5 Discussion

The change of the modulation period with energy can be explained by the deceleration of the electron bunch in the ambipolar field, as demonstrated in Equations B.19 and B.23. The experimental result confirms a property of ion beams accelerated by means of the TNSA mechanism. The beam has an extremely low longitudinal emittance and the ions are well ordered in energy and time, similar to a chirped optical pulse. The proposed theoretical analysis gives strong indication that the observed modulation in the distribution function of proton energies is related to the half-period of the laser cycle $\tau_L/2$. Therefore, the modulations can be used as relative time stamps to draw conclusions concerning the acceleration process.

Assuming that the accelerating field only changes insignificantly within 1 fs, the acceleration a_p of protons with mass m_p can be easily estimated for the time interval $\tau_L/2$ in which adjacent energy maxima with $\epsilon_{p,i} > \epsilon_{p,i+1}$ are created

$$a_{p,i} \cdot \frac{\tau_L}{2} \approx \left(\frac{2\epsilon_{p,i}}{m_p} \right)^{\frac{1}{2}} - \left(\frac{2\epsilon_{p,i+1}}{m_p} \right)^{\frac{1}{2}} = v_{p,i} - v_{p,i+1} = \Delta v_{p,i}. \quad (6.1)$$

This acceleration is of the order of 10^{20} m/s² and corresponds to an accelerating electrical field of about 1 MV/ μ m. These numbers had already been deduced from several previous model calculations and simulations. Here they are derived directly from a distinct experimental observation and one basic assumption. Both the experimental result and the model calculation show that the modulation period decreases with decreasing energy. Based on Formula 6.1 this signifies that a lower acceleration and corresponding lower field strength is obtained for lower proton energies. Using the modulations as definite time stamps, the temporal dependence of the electric acceleration field can be derived using the equations

$$E_{p,i} = \frac{m_p}{q_p} \cdot a_{p,i} = \frac{m_p}{q_p} \cdot \frac{\Delta v_{p,i}}{\tau_L/2}, \quad (6.2)$$

$$t_{p,i} = (\tau_L/2) \cdot i, \quad (6.3)$$

whereby N denotes the maximum number of used modulation points. In this case the electric field $E_{p,0}$ corresponds to the density modulation with the highest (used) energy and $t_{p,0}$ defines time zero.

Figure 6.8 illustrates this dependency (black curve), whereby the modulations between 0.15 MeV and 1.3 MeV were used for the calculation. Several functions were tested to fit the decrease in time:

$$\mathcal{E}_1(t) = \frac{\mathcal{E}_0}{\sqrt{1 + ((t - t_0)/\tau_s)^2}}, \quad \mathcal{E}_3(t) = \frac{\mathcal{E}_0}{(1 + ((t - t_0)/\tau_s))^2}, \quad (6.4)$$

$$\mathcal{E}_2(t) = \frac{\mathcal{E}_0}{1 + ((t - t_0)/\tau_s)}, \quad \mathcal{E}_4(t) = \frac{\mathcal{E}_0}{1 + ((t - t_0)/\tau_s)^2}. \quad (6.5)$$

The green and red curves in Figure 6.8.A are based on formula $\mathcal{E}_1(t)$ and $\mathcal{E}_2(t)$, respectively. These equations were used in Section 6.3 to approximate the tem-

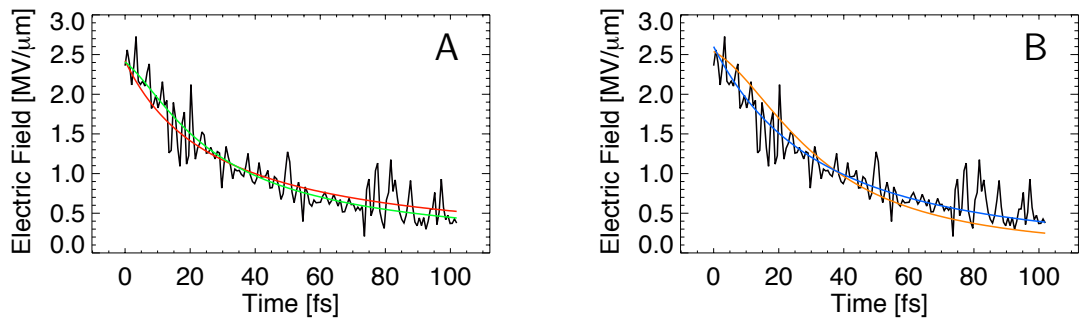


Figure 6.8: Temporal dependence of the electric field amplitude. **A** - The green curve is based on formula $\mathcal{E}_1(t)$ (Equation 6.4) with $\mathcal{E}_0 = 2.5$ MV/ μ m and $\tau_s = 19$ fs. The red fit is uses formula $\mathcal{E}_2(t)$ (Equation 6.5) with $\mathcal{E}_0 = 3.0$ MV/ μ m and $\tau_s = 23$ fs. **B** - The blue curve is based on formula $\mathcal{E}_3(t)$ (Equation 6.4) with $\mathcal{E}_0 = 3.1$ MV/ μ m and $\tau_s = 59$ fs. The yellow fit is uses formula $\mathcal{E}_4(t)$ (Equation 6.5) with $\mathcal{E}_0 = 2.6$ MV/ μ m and $\tau_s = 35$ fs. In all cases $t_0 = -5.4$ fs.

poral field decay found by the PIC-simulation (cf. Figure 6.5.B). Formulas $\mathcal{E}_1(t)$, $\mathcal{E}_2(t)$ and $\mathcal{E}_3(t)$ corresponds well to accepted model considerations [73, 106] and are used to describe the temporal field decay of an expanding ion front. Here, \mathcal{E}_0 is the initial electric amplitude and τ_s the characteristic temporal decay constant. The constant shift in time t_0 is introduced, since the zero point in Figure 6.8 is not clearly determined and is set in accordance to the proton energy of 1.3 MeV. A temporal shift of $t_0 = -3 \cdot \tau/2 = -5.4$ fs is used, since at least three additional modulations are visible at energies > 1.3 MeV.

As shown in Figure 6.1, more than one hundred modulations appear in the proton spectrum within the energy interval between 0.12 MeV and 1.3 MeV. Let's assume that each of these modulations is caused by the action of a separate electron bunch and that the bunches are accelerated within a temporal distance of half the laser cycle ($\tau_L/2 = 1.35$ fs) due to the laser-plasma interaction. In this case, the process that generates the acting electron bunches lasts at minimum 135 fs, which is approximately four times the laser pulse duration $\tau_p = 35$ fs (FWHM of intensity). One possible explanation for this behavior could be that the real duration of ion (and electron) acceleration process is much longer than 35 fs. Possibly, the electrons causing the observed effect are accelerated at intensities, which are much smaller than the peak intensity $I_L \approx 3 \cdot 10^{19}$. This assumption is reasonable, since energetic protons (with energies at the low energy side of the presented spectrum)

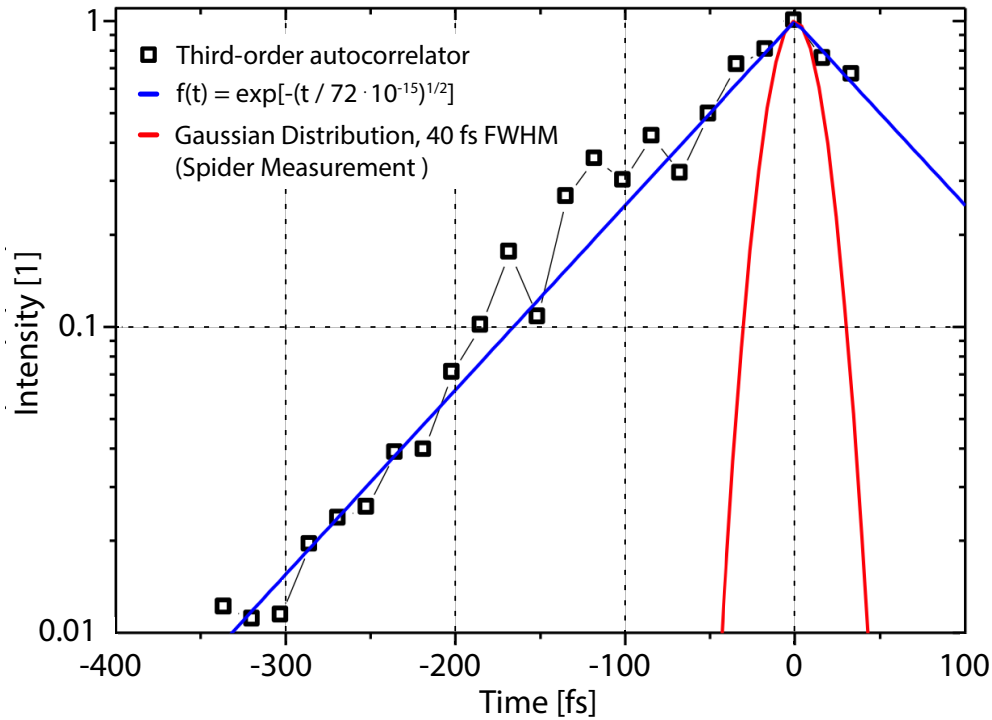


Figure 6.9: Temporal distribution of the laser intensity $I_L(t)$.

were also produced with a laser energy ten times reduced. This interpretation is supported by the results of a third-order autocorrelation measurement of the laser intensity $I_L(t)$ which is illustrated in Figure 6.9.

In Section 4.1 several mechanisms of laser light absorption in plasmas were presented which can lead to the collective acceleration of plasma electrons. For the explanation of the observed modulations two mechanisms are of particular interest. These are the Brunel absorption and the $\mathbf{J} \times \mathbf{B}$ heating. Both mechanisms are relatively effective for the presented laser and target parameters of this section. In addition, both mechanisms result in the generation of electron bunches with a periodicity in the range of the laser cycle τ_L . In the case of $\mathbf{J} \times \mathbf{B}$ heating the driving term of the acceleration is connected with the (not time averaged) ponderomotive force which oscillates at twice the laser frequency. The cyclic action at this frequency is in good agreement with the results of the PIC-simulation and is consistent with the perturbation ansatz for the electron density n_e of the analytical model (c.f. Equation B.9).

For the occurrence of Brunel absorption a component of the incident electric field parallel to the (sharp) plasma density gradient is needed. $\mathbf{J} \times \mathbf{B}$ heating works for any polarization apart from circular and is most efficient for normal incidence. Since a p-polarized laser pulse with an angle of incidence of 10° was used in the presented experiments, both mechanisms can be relevant for the appearance of the modulations in the proton energy spectrum.

In order to investigate the impact of the laser polarization on the observed effect, subsequent experiments with circular polarization at oblique incidence (10°) were conducted. Interestingly, the modulations in the energy spectrum were still detectable. Under these conditions it is problematic to explain the observed effect on the basis of $\mathbf{J} \times \mathbf{B}$ heating (ponderomotive acceleration) or Brunel absorption since the standard descriptions of both mechanisms rely on the assumption of linear polarization. However, even for circularly polarized laser pulses the generation of electron bunches is possible and can even be more effective than for linear polarization under certain conditions [107, 108]. So far the influence of the polarization state has not yet been completely clarified and further research is required.

Another interesting question is whether the observed phenomenon is restricted to a specific contrast of high order or can also appear at even higher contrast values. To clarify this issue experiments with a plasma mirror were conducted by M. Schnürer and J. Bränzel. The results clearly show that the modulations disappear at this further increased contrast level. Here the combination of the XPW-process [45] and the applied double plasma mirror [40, 41] leads to a pre-pulse free peak-to-ASE contrast between 10^{13} and 10^{14} in the minor ps range.

Further experiments have also shown that the appearance of the modulations is not restricted to the proton signal. In several cases modulations in the energy spectra of carbons in different ionization states could be detected simultaneously. The connection of this effect with the laser and target parameters is has not been studied yet.

Part III
Proton Imaging

7 Principle of Proton Imaging

This chapter will explain why laser-driven proton beams are well suited for imaging purposes and how they can be used to investigate electromagnetic fields of laser-induced plasmas. After the introduction of the principle experimental setup, two specific imaging geometries are presented which allow the different components of the spatially extended fields that are initiated on thin foils to be probed. In addition, several definitions of new terms are introduced in order to facilitate the explanations of the next chapters. Finally, different energy sensitive proton detection methods are discussed, which provide the time resolution in imaging experiments.

7.1 Imaging with Laser-driven Proton Beams

The acceleration of protons on the basis of the TNSA process exhibits attributes which are well suited for imaging purposes. The generated proton beam is divergent and provides a broad and continuous energy spectrum. The acceleration time of this laser-driven ion beam is ultra-short, typically between hundreds of femtoseconds and several picoseconds [4, 109, 110]. The effective source size of ion emission has an extension of several micrometers, which is extremely small compared to conventional accelerators [104, 111, 112]. In addition, it provides a very low transverse (< 0.004 mm mrad) and longitudinal ($< 10^4$ eV s) emittance, which is at least 100-fold better than conventionally accelerated ion beams [4].

These properties allow for the observation of fast dynamic phenomena with high resolution and the use of the generated proton beam for different objectives. Naturally, protons can be scattered and stopped by the interaction with matter and are, due to their charge, sensitive to electromagnetic fields. For these reasons, the so called *proton imaging* and *proton radiography* techniques can provide space- and time-resolved information about field and density distributions. Among the applications of laser-induced proton beams, these techniques have not only been successfully applied [5], but have also been used for the investigation of laser-driven plasmas in several experiments [106, 113, 114]. In particular, the ion acceleration process was investigated by probing the electric and magnetic fields inside a second laser-induced plasma [6, 84, 106, 113, 115–121].

7.2 Principal Experimental Setup

Figure 7.1.A illustrates the basic concept of proton imaging which relies on the source point projection technique. If a source emits rays with a certain divergence it can be used to illuminate an object and to project its magnified image on a detector. If the beam emittance is low, the trajectories of the rays do not intercross and the projected image appears sharp. As described, the TNSA mechanism generates a (proton) beam with the required properties. For this reason, a thin foil (*source target*) is irradiated with an intensity $\sim 10^{19}$ W/cm². The resulting proton beam is referred to as a *probing proton beam* in the following. The energy distribution of the created probing proton beam is broad and continues and has a maximum energy of several MeV. If a mesh is placed at the distance m behind the

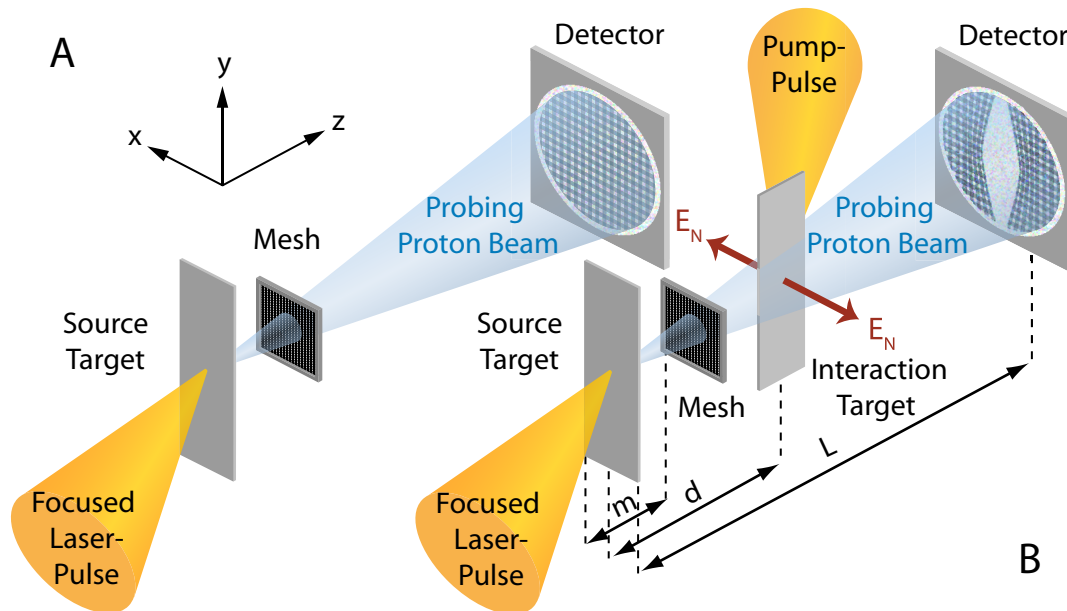


Figure 7.1: Setup of a *pump-probe experiment* using proton imaging

foil, the probing proton beam is intersected in single beamlets. These beamlets are projected on the detector with the magnification $M_{\text{Mesh}} = L/m$, where L denotes the distance between the source target and the detector. In a more accurate description the extension of the laser induced ion source and its dynamics have to be considered [8] (c.f. Section B.1).

Figure 7.1.B shows the basic setup of a *pump-probe experiment*, using proton imaging. In the shown case a second thin foil (*interaction target*) is inserted in the proton beam between the mesh and the detector. The surface of the second foil is orientated perpendicular to the surface of the source target. By focussing the laser pump-pulse on the interaction target a plasma is generated and the *probing*

proton beam, is used as a probe to investigate the laser-plasma interaction and the associated electromagnetic fields. The energy of a probing proton determines its time of flight from the source to the interaction target. For protons with energies in the range of 1 – 3 MeV and a target distance of several millimeter this time of flight is relatively high in comparison to its acceleration time. Therefore, fast protons reach the object to probe earlier than slower protons and the probing time can be attributed to the proton energy. On their way to the detector the protons are deflected due to the Lorentz force

$$\mathbf{F} = q(\mathbf{E} + \mathbf{v} \times \mathbf{B}) \quad (7.1)$$

and the extended electromagnetic fields which are initiated in the surrounding of the interaction target. In this situation both the amplitude and direction of the deflection depends on: (1) the initial conditions of the proton, such as its energy, ejection angle and starting position; (2) the spatial distribution and temporal evolution of the electromagnetic fields in the surrounding of the interaction target. The relation between electric and magnetic field structures and their proton-beam images is discussed in detail by Kugland et al. [122].

If all protons were accelerated at the same time and had the same energy, the field distribution would be probed at a certain moment in time and the deflection of all protons within a single beamlet would be similar. In this case the deflection of the beamlets would provide information about the strength, the spatial distribution and the direction of the fields for the corresponding moment in time.

In reality the energy distribution of the probing proton beam is continuous. For this reason, the protons of a single beamlet probe the field at different times and the deflection of each beamlet becomes time dependent. For the experiments which were conducted in the framework of this thesis a high temporal resolution was crucial. Therefore, the energy sensitive detection of the proton signal was most important. Conventionally stacks of CR-39 plates or radiochromic films are used for the proton detection [123] in imaging experiments. Furthermore a MCP coupled with a phosphor screen (Section 5.2) with an attached CCD camera can be applied. These methods can be used to detect both the spatial and the energy distribution of the proton signal and are presented in Section A.8 of the appendix.

7.3 Probing Configurations

In order to facilitate the explanations of the next chapters, two different probing geometries for thin foils are presented, which were used for several experiments in this thesis. The so called *transversal* and *longitudinal configuration* (or *longitudinal probing geometry*) differ with regard to the orientation of the interaction target (interaction foil). In *transversal configuration* the propagation direction of the probing proton beam is perpendicular to the surface normal of the interaction target (Figure 7.2.A), whereas in *longitudinal configuration* the probing proton beam

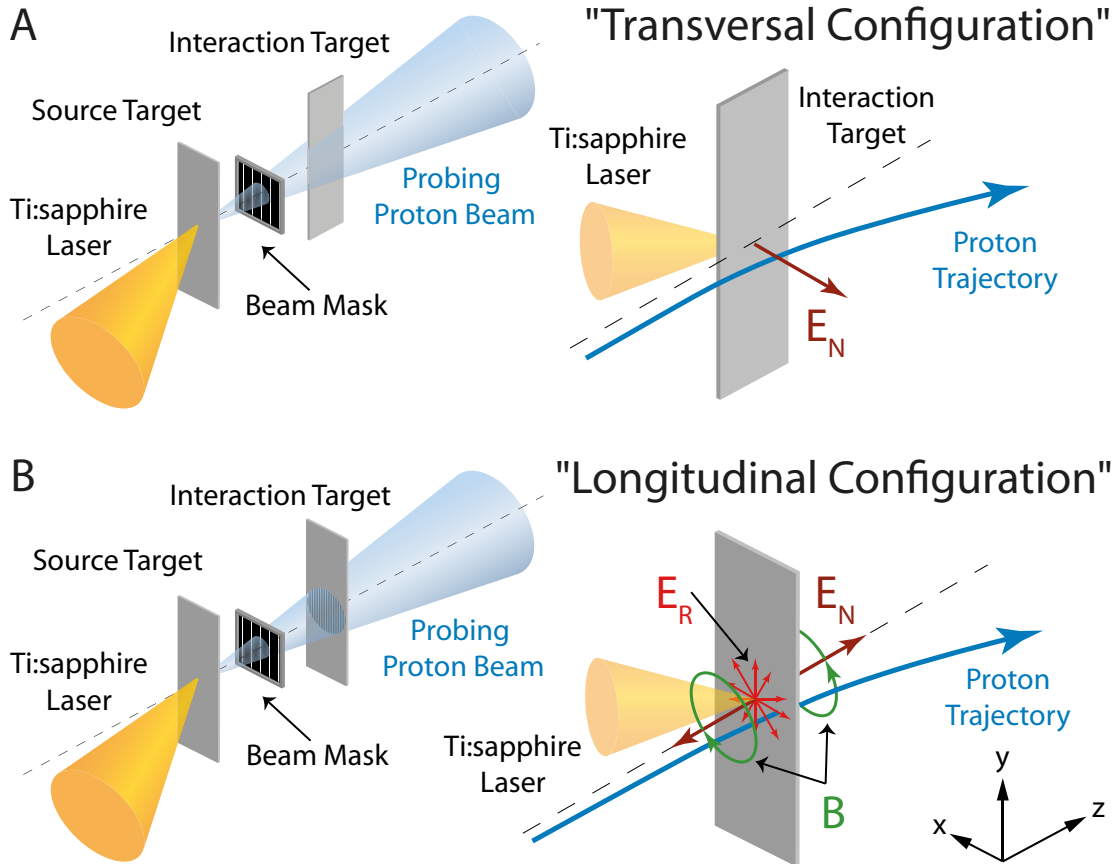


Figure 7.2: Probing geometries for imaging laser-induced electromagnetic fields on thin foils.

is directed parallel to the surface normal of the interaction foil (Figure 7.2.B). Depending on the dominant acceleration mechanism, the angle of incidence of the laser pulse on the target surface can have a strong impact on the induced electromagnetic field distribution. However, in the case of TNSA (Section 4.2) the acceleration fields are mainly directed in target normal direction. Naturally if both the foil and the irradiating laser pulse are rotated by 90° around the y-axis, this happens also to the orientation of the laser-induced fields.

For this reason, the action of different field components can be investigated depending on the applied probing configuration.

Using the *transversal probing geometry* a variety of imaging experiments were conducted to investigate the electrostatic acceleration field and the field of the expanding ion front [7, 106]. If TNSA (Section 4.2) is the dominant mechanism of ion acceleration, the main electric field component E_N is directed normal to the target surface and is dominant over other ones. Therefore, the assumption is reasonable that the deflection of the probing proton beam in *transversal configuration*

is mainly caused by this component, as illustrated in Figure 7.2.A.

Current research particularly focuses on the quantitative spatial and temporal reconstruction of the magnetic field distribution [84, 94, 120, 122, 124–130]. Since intense laser pulses drive strong electron currents in plasma, magnetic fields with amplitudes of above 10^4 T at femtosecond time-scale can be generated [130]. In this situation the direction of the electron currents determines the geometry and orientation of the induced magnetic fields. In the case of thin foils the magnetic field \mathbf{B} has usually a toroidal form [94, 127, 130, 131] and points predominantly in $(\mathbf{e}_z \times \mathbf{e}_\rho)$ -direction, with $\mathbf{e}_\rho = (x \cdot \mathbf{e}_x + y \cdot \mathbf{e}_y) / \sqrt{x^2 + y^2}$ (Figure 7.2.B). In this connection, the sign of the field depends on the dominant mechanism that generates the magnetic field (c.f. Section 4.3).

Due to the $(\mathbf{v} \times \mathbf{B})$ -term of the Lorentz force (Equation 7.1) the proton deflection is highly sensitive to this specific magnetic field distribution if the *longitudinal probing geometry* is applied in proton imaging experiments [84, 94, 120, 124, 127, 129]. Naturally, the electric fields can also influence the proton deflection in *longitudinal configuration*, especially if they point in transversal direction i.e. parallel to the target surface. For instance, the radial electric field component E_R (Figure 7.2.B) of laser-induced plasmas on thin foils can exhibit a pronounced effect on the proton deflection [126].

In addition to the deflecting action of the fields, other effects have to be considered in *longitudinal configuration*. Since the propagation direction of the probing proton beam is parallel to the surface normal of the interaction target, it is also parallel to the dominant electric field component E_N . When the protons propagate through the laser-irradiated interaction target their velocity is changed depending on the accelerating and decelerating effect of the transient fields at the front and rear sides of the foil. This effect was already used to investigate its potential for ion-post acceleration [132].

In addition, protons are scattered if they propagate through matter. Depending on the proton energy and the thickness of the foil, this effect can be significant and deteriorate the image of the beam mask, which is imprinted on the probing proton beam.

8 Streak Deflectometry

In this chapter the so called *proton streak deflectometry* method [8] is introduced, which allows for a continuous record of transient fields on a picosecond time scale. The basic principle is explained first, then a further development of the method is presented, through which different parts of an extended field distribution can be investigated. The different parts are probed in consecutive shots, where both the magnification and the time resolution remain constant. This is possible by displacing the initiated fields laterally with respect to the propagation path of the probing proton beam, which is not altered in different shots. In order to test the usability of the generated proton beam for streak deflectometry experiments, particular source properties of the beam were investigated. In particular, these are the composition of the accelerated ion species, the energy distribution, pointing and reproducibility of the proton beam, as well as the distance of the virtual source point and its energy dependence [8].

The applicability of the *lateral displacement technique* and the data analysis is exemplified based on a series of proton streak deflectometry measurements in *transversal configuration*. In these experiments thin aluminum foils were irradiated with high-contrast laser pulses and the initiated electric field distribution was probed on the rear and front side of the foil. For the first time, the electric field evolutions at both sides of a thin foil were recorded simultaneously (in one shot). Finally, the time resolution of the method is discussed. As a result, it will be shown that the time resolution of streak deflectometry measurements in *transversal configuration* is insufficient to investigate the laser-induced acceleration process that takes place on timescales from hundreds of femtoseconds to a few picoseconds.

8.1 Principle of Streak Deflectometry

As explicated in Section 7.2 the kinetic energy of the protons which constitute the probing proton beam can be attributed to their arrival time (probing time) at the interaction object and thus to the temporal evolution of the investigated process. If the proton signal is measured with an energy sensitive detection method, the influence of the scanned process on the proton beam can be tracked back in time. For this reason, an energy sensitive proton detector (Section A.8) is needed.

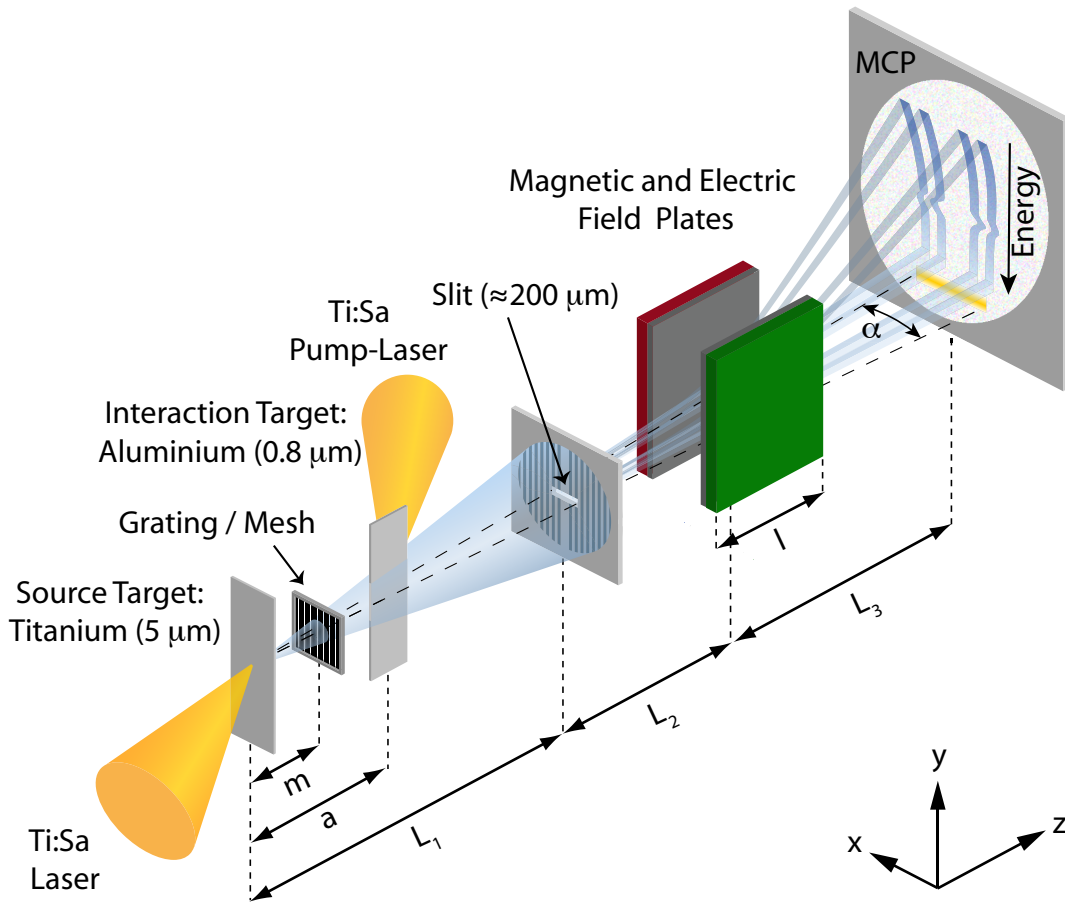


Figure 8.1: Principle setup of an proton streak deflectometry experiment in transversal configuration.

Figure 8.1 illustrates the principle setup of a proton streak deflectometry experiment. The lower left part of the schematic diagram is identical to Figure 7.1 in Section 7.2. The creation of the proton beam at the source target, as well as the plasma generation at the interaction target, also corresponds to the explanation given in that section. However, instead of a proton detector with a two-dimensional spatial resolution (Section A.8) a Thomson slit spectrometer (Chapter 5) was implemented in the shown setup. The proton beam is intersected by a beam mask (e.g. grating or mesh) and consists of single beamlets which pass the interaction target at a defined distance and with a defined angle. The fields in the surrounding of the interaction target deflect the protons depending on their energy. Because of the slit ($\approx 200 \mu\text{m}$) only protons close to the x - z -plane can propagate further in the direction of the detector. The probing proton beam is restricted to the x - z -plane. For this reason, the beamlets take the form of thin stripes and their deflection is

only measurable in x-direction. When the protons that constitute these beamlets (stripes) enter the field of the permanent magnet they are dispersed in y-direction according to their energy. This allows for energy sensitive proton detection, which is explicated in greater detail in Section 5. Because each proton energy corresponds to a different probing time, the continuous temporal evolution of the field can be recorded.

8.2 Lateral Displacement Setup

In order to test the usability of the probing proton beam for streak deflectometry experiments, particular source properties of the beam were investigated. These are the composition of the accelerated ion species as well as the energy distribution, pointing and reproducibility of the proton beam. The determination of the virtual source distance and its energy dependence was of particular interest, since this parameter affects the magnification in proton imaging experiments [8]. For this purpose separate experiments were conducted, which are explicated in detail in Section B.1 in the appendix. As a result, it was found that the model of the virtual source [104] can be used to describe the laser-induced proton emission from the source target. In this case the proton trajectories are represented by straight lines and can be traced back to a virtual source point in front of the target, as illustrated in Figure 8.2. In addition, it can be shown that the position of the virtual source distance in z-direction is relatively constant for the proton energy interval between 1 MeV and 3 MeV.

The slit length s_x (in x-direction) determines the maximum opening angle α and thus the detectable angle interval. Only protons with an initial ejection angle β within the range $-\alpha/2 < \beta < \alpha/2$ can reach the detector. Therefore, only the field region which is probed by these protons is recorded. The extension S_R of the probed field region in lateral direction (x-direction) is given by $S_R = 2a_v \cdot \tan(\alpha/2)$, with $a_v = a - z_v$, where z_v denotes the position of the virtual source point (Section B.1) in z-direction and a_v is the distance between the this point and the interaction target in z-direction. The recorded field region can be maximized if either the slit length s_x or the target distance a is increased. However, the elongation of the slit is only possible to a certain extent. At some point either the gap width of the permanent magnet or the diameter of the MCP itself will set the limit for the maximum opening angle α . An increment of the target distance a will both reduce the magnification M and deteriorate the temporal resolution as explicated in Section 8.3.

In the presented work a new imaging setup is applied which allows for the lateral displacement of the interaction target and the irradiating pump focus in between two consecutive laser shots. By varying the lateral displacement d (Figure 8.2), the initiated fields can be probed both in the close vicinity of the interaction target and at a distance which would normally exceed the recordable field extension S_R .

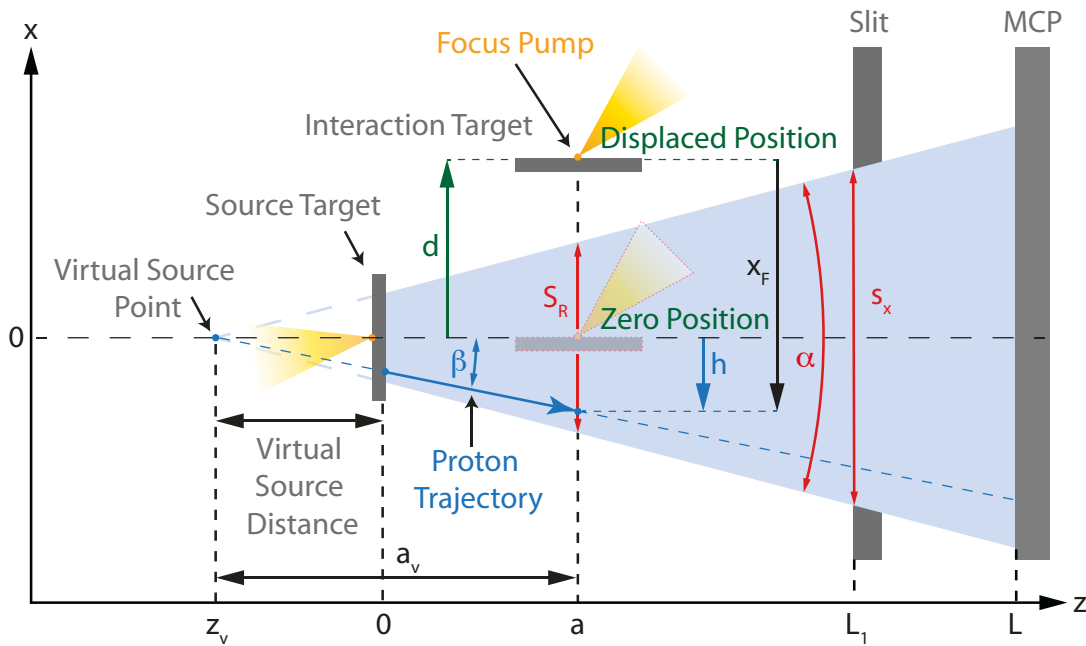


Figure 8.2: Lateral displacement of the Interaction target and the irradiating pump laser

At the same time both the magnification and time resolution remain constant. Figure 8.2 illustrates the trajectory of a single proton in the x - z -plane which has the initial ejection angle β . In addition the position of the proton is indicated at the time ($t = t_p$) when it would arrive at the interaction plane ($z = a$) if no deflecting fields were present. Its x -position is given by $h = a_v \cdot \tan(\beta)$. In the shown case β and h have negative values. Depending on β and the lateral displacement d the proton has a certain distance to the pump focus (interaction target) in x -direction. This distance is defined by

$$x_F := h - d = a_v \cdot \tan(\beta) - d \quad (8.1)$$

and is referred to as "focal distance". For $d > h$ its sign is negative, as in the case shown. If the interaction target is at zero position ($d = 0$) the values of h and x_F are identical.

8.3 Measurements and Data Analysis

The usability of the *lateral displacement technique* and the data analysis is exemplified based on a series of proton streak deflectometry measurements in *transversal configuration*.

Figures 8.3.A and 8.3.B are pictures of the light emitting phosphor screen and

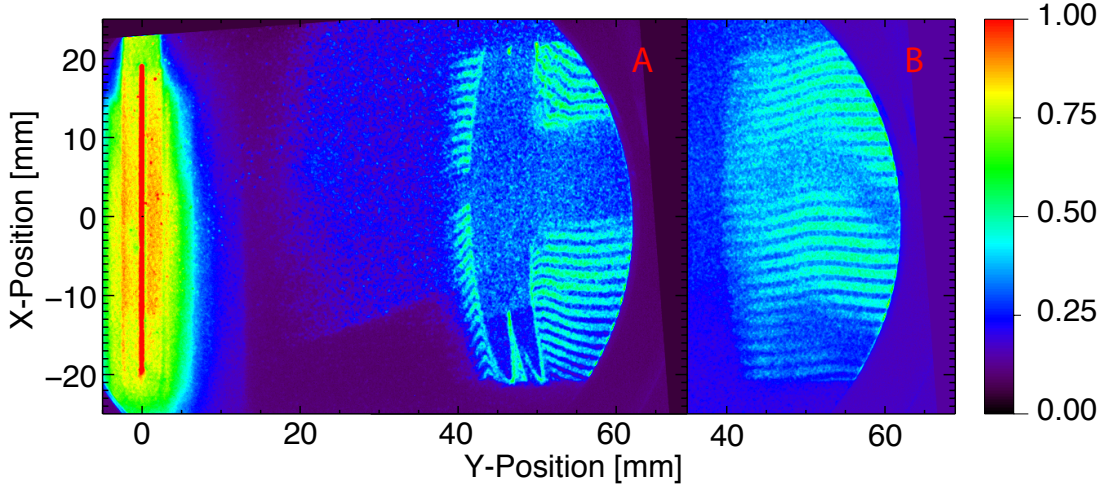


Figure 8.3: Recorded images in the proton streak deflectometry setup. **A** - With irradiated interaction target. **B** - Without interaction target. For both images the following experimental parameters apply: $L_1 = 475$ mm, $L_2 = 229$ mm, $L_3 = 522$ mm, $a = 35$ mm, $z_v = -1.75 \pm 0.5$ mm, $m = 20 \pm 0.5$ mm, $d = 80$ μ m, $s_x = 14.2$ mm, $s_y = 233$ μ m, $c_x = 36.7$ mm, $c_y = 600$ μ m, $\alpha = 31.9$ mrad, $l = 50$ mm, $B_x = 343$ mT, $E_x = 275$ kV/m, $N_{\text{mesh}} = 1000$ LPI.

show the recorded density distribution $\rho(x, y)$ depending on the x- and y-position in the detector plane, corresponding to the setup (cf. Figure 8.1). Both pictures are recorded with the proton streak deflectometry method. The y-position refers to the proton energy, whereas the x-position visualizes the deflection of the probing protons. The chosen experimental parameters are summarized in the figure caption. The used denotations correspond to the denominations of Section 5.3 and to the denotations which are used in Figures 8.1 and 8.2.

Picture 8.3.A shows the proton deflections when the pump beam irradiates a 0.8 μ m thick aluminum foil (interaction target) at an intensity between $1 \cdot 10^{18}$ W/cm² and $5 \cdot 10^{18}$ W/cm² (FWHM) and with a pulse duration $\tau_p = 72$ fs. In contrast, Picture 8.3.B illustrates the undisturbed traces of the dispersed proton stripes when the interaction target is removed from the probing proton beam. The signal of other detected ion species is also visible in the background of both images. Nevertheless, the proton stripes are clearly distinguishable.

The minimum energy in the measurements is set by the boundary of the MCP, whereas the energy cut-off of the probing proton beam sets the maximum observable energy.

Without the interaction at the second foil small trace-fluctuations are visible. These appear as "wiggly" traces on the detector and can be explained by small movements of the proton source which causes beam pointing variations [8, 109, 133].

However, this effect is not the reason for some small systematic bending of the

traces. The inhomogeneous electric and magnetic field distribution within the permanent magnet influences the specific form of the proton traces on the detector. The curvature of the energy cut-off is also due to this influence.

In Section 5.4 this relationship is explained in greater detail. Moreover a numerical algorithm is proposed which allows the image to be *rectified* by means of a coordinate transformation. The recorded image describes in principle the proton density $\rho(x, y)$ as a function of the detector position. In the absence of the interaction field the point of impact (x, y) of a single proton on the detector and the pair (β, ϵ) are related through a bijective function (Figure 5.5). The initial ejection angle of the proton is denoted by β and its energy by ϵ . The proposed algorithm numerically transforms $\rho(x, y)$ and allows the proton density $\tilde{\rho}(\beta, \epsilon)$ to be visualized in an orthogonal coordinate system as a function of β and ϵ .

The probing time t_p is defined as the time of arrival of a single proton in the x-y-plane of the interaction region at the position $z = a$. In this case a is the target distance or the position of the pump focus (Figure 8.2). Due to the narrow slit only particles are recorded which are ejected in the x-z-plane and are thus relevant for the coordinate transformation. Therefore, the probing time $t_p(\beta, \epsilon)$ can be defined as a function of β and ϵ . Obviously the pairs (β, ϵ) and (β, t_p) are bijective and consequently the same applies for the pairs (x, y) and (β, t_p) . For this reason, the complete derivation of the numerical transformation between $\rho(x, y)$ and $\tilde{\rho}(\beta, \epsilon)$ which is explicated in Section 5.4 can be applied on the pairs (x, y) and (β, t_p) . As a result the proton density distribution $\tilde{\rho}(\beta, t_p)$ can be described as a function of β and t_p .

Figure 8.4 shows the density distribution $\tilde{\rho}(\beta, t_p)$ as a result of the numerical transformation of Image 8.3.A. The upper abscissa represents the probing time t_p and the lower abscissa indicates the corresponding proton energy for $\beta = 0$. The left ordinate shows the values of β . The distance from the proton to the pump focus in the interaction plane $x_F(\beta, d)$ (focal distance) is a function of β and d and is shown on the right ordinate. In the proposed case $d = 80 \mu\text{m}$.

For the interpretation of the presented images it is highly important to consider the exact meaning of β , x_F , t_p and ϵ . As explicated in Section 8.3 each point of impact (x, y) on the detector corresponds to a certain pair (β, ϵ) . This is only valid if the protons are not deflected (by the interaction fields) on their way to the detector. Conversely, a high proton signal at a certain point $(\beta_0, t_{p,0})$ in Figure 8.4 does not necessarily signify that each proton which contributes to the signal of this point is emitted with β_0 . It only means that (due to the deflection at the interaction target) an increased amount of particles has been deflected to the point (x_0, y_0) on the detector which corresponds to a certain $(\beta_0, t_{p,0})$. In principle, this also applies for the interpretation of t_p and ϵ if the interaction fields have a pronounced accelerating or decelerating influence on the probing proton beam.

The focal distance $x_F(\beta, d)$ is a projection of the proton position from the detector plane ($z=L$) to the interaction plane ($z=a$) and corresponds only to the real proton position at the time t_p if no deflecting fields are present.

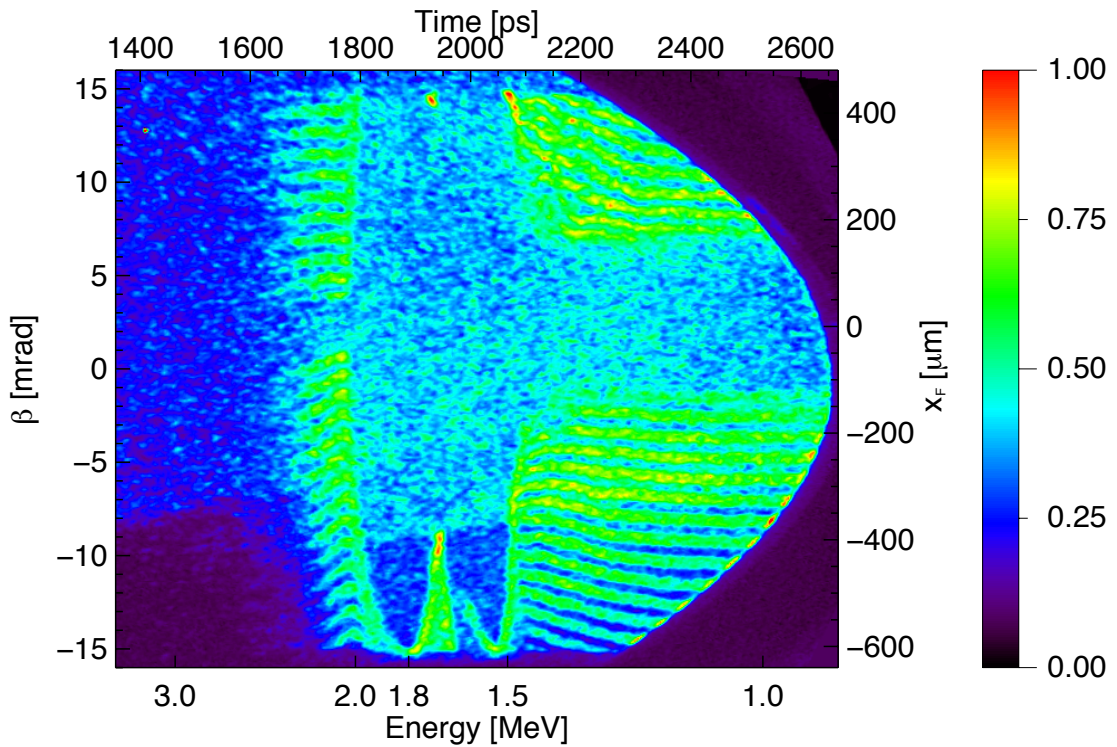


Figure 8.4: Numerically transformed density distribution $\tilde{\rho}(\beta, t_p)$.

The arrival of the laser pulse at the source target initiates the creation of the probing proton beam and defines the absolute time zero. By means of an optical delay stage within the experimental chamber the arrival time t_{pump} of the pump pulse at the interaction target was adjustable with respect to time zero (Section 2.2). Thus the time t_{pump} is defined as the arrival time of the pump laser pulse at the interaction target with regard to the creation of the probing proton beam at the source target. In addition the time t_{pump} can be regarded as the arrival time of protons at the interaction target which are accelerated at the source target at time zero and propagate with a certain energy $\epsilon = \epsilon_{\text{pump}}$. In fact this relation is the definition of the so called t-pump energy ϵ_{pump} . In other words a proton with the kinetic energy $\epsilon = \epsilon_{\text{pump}}$ needs the time $t_p = t_{\text{pump}}$ to propagate from the source to the interaction target.

8.4 Results and Discussion

In the presented experiment the t-pump energy ϵ_{pump} was chosen to be 1.8 MeV which corresponds to a pump time t_{pump} of 1887 ps. At first protons with energies $> \epsilon_{\text{pump}}$ reach the interaction target. Because of the absence of the laser pump pulse no fields were created at this time. When the laser pump pulse hits the interaction target electric fields are created and thus the protons of the probing proton beam are deflected away from the target surface. At first, the deflection increases and reaches its maximum at the probing time $t_p = 1883$ ps, as illustrated by the blue dashed line in Figure 10.4.A. This time corresponds well with the chosen pump time t_{pump} of 1887 ps with regard to the accuracy and the time resolution that is discussed in the next section. Then the deflection decreases relatively fast, increases again and shows a second peak at the probing time $t_p = 2044$ ps. Subsequently the deflection diminishes within several picoseconds. The temporal distance between the peaks is 205 ps. The recorded traces show a pronounced deflection symmetry at both target surfaces. On both sides of the foil the deflections depend strongly on the distance to the target surface. Protons passing closer to the foil surface are deflected stronger than protons which pass at a further distance. At later times the deflection seems to stagnate, but does not completely disappear within the observed time window. The later effect is probably related to a charge compensation of the target which occurs on a nanosecond timescale. This behavior was found in similar experiments in which a picosecond laser pulse was used for the field generation [8].

It is important to note that the traces contain a convolution with the field extension. The deflection of all traces is the result of the force which acts on the protons while they propagate through a spatially extended field $\mathbf{E}(\mathbf{r}, t)$. For this reason, the field extension in propagation direction (along the target surface in z -direction) is not only important for the degree of the proton deflection, but it also affects the energy range of the influenced particles. The fastest protons which show a deflection in x -direction have the kinetic energy $\epsilon_f = 2.02$ MeV. As illustrated by the green dashed line in Figure 8.5.A this energy corresponds to the probing time $t_f \approx 1780$ ps. The corresponding velocity value can be used to estimate the extension of the electric field in z -direction under the assumption that the electric field component in z -direction is negligible.

In a simple model (Figure 8.5.B) the dependence of the electric field $E_x(z)$ in z -direction can be described by a rectangular function with the extension length $l_f = 2 \cdot r_f$. At the moment $t = t_{\text{pump}}$ a proton (blue color) with the kinetic energy $\epsilon_p = \epsilon_{\text{pump}}$ is situated exactly at the target distance $z = a$, in the vicinity of the interaction center. At the same time a faster proton (green color) with the energy $\epsilon_p = \epsilon_f$ is located at the edge of the field $z = a + r_f$. Since no deflection is visible for protons with higher energies $\epsilon_p > \epsilon_f$, the effective extension radius r_f of the field can be assigned to the proton energy ϵ_f .

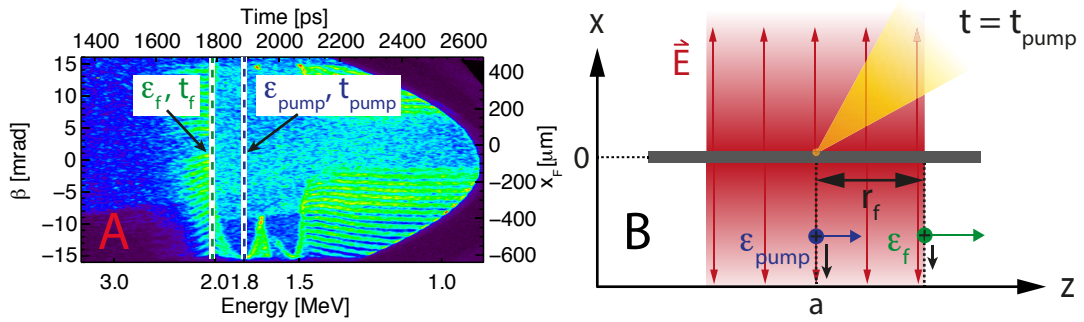


Figure 8.5: **A** - Density distribution $\tilde{\rho}(\beta, t_p)$. The dashed green line shows the start of the deflection and the dashed blue line indicates the first deflection maximum. **B** - Simple description of the electric field distribution in z -direction and its influence on probing protons.

In the case of Figure 8.4 ($\epsilon_f = 2.02$ MeV) an effective extension radius r_f of 2.11 mm is obtained. In reality the electric field is not created instantaneously with a fixed field extension, but a complex field distribution is initiated which expands in time. The speed of light c can be used as an upper limit for the radial expansion velocity v_e of the field. By taking into account the initial extension of the field which is of the order of the laser spot size $\approx 5 \mu\text{m}$ and the expansion velocity $v_e = c$ a slightly higher extension radius r_f of 2.26 mm is obtained. Since lower values of v_e result in even higher values of r_f , the given definition of r_f can be regarded as a lower limit of the field extension.

The appearance of the double peak structure has not been clearly resolved yet. However, the temporal distance between the two peaks (205 ps) gives rise to the assumption that the phenomenon is connected with a second irradiation of the interaction target. At first implications of a beamsplitter are discussed. This beamsplitter was implemented in the experimental chamber and was used for the creation of two laser pulses. One to irradiate the source target (source pulse) and one to irradiate the interaction target (pump pulse). The reflectivity of the beamsplitter is 81.35% at the central wavelength of 800 nm and an angle of incidence of 45° . This leads to an energy reduction of the transmitted pump pulse by the factor of 0.1865. The width of the substrate is 18 mm and elongates the pump pulse from $\tau_p = 30$ fs to $\tau_p = 72$ fs under consideration of refraction.

Due to internal reflection within the beamsplitter, a second pump pulse is created. Considering the dispersion and refraction within the medium (quartz), this post pulse is delayed by 201.73 ps and elongated from $\tau_p = 30$ fs to $\tau_p = 217$ fs. The back surface of the beamsplitter is not coated. Therefore, the transmitted pump beam is reflected at this surface with an angle of incidence of 29.1° and a reflectivity of 0.656. After a second reflection at the coated front side and the subsequent transmission through the back side of the beamsplitter the transmitted energy is

reduced by a factor of more than 0.0053. In combination with the elongation of the pulse this leads to an intensity reduction of the second pump pulse by a factor of $1.75 \cdot 10^{-3}$ with respect to the first pump pulse.

Even if the pulse delay can explain the temporal occurrence of the second peak, it is not clear how the strongly attenuated second pulse can lead to a field deflection which is of the order of the first peak. On the other hand, only one strong deflection peak was observed when no beamsplitter was used and laser arm B (Chapter 2) served as a pump to irradiate an ultra-thin CH-foil (Chapter 10).

Since several laser and target parameters (target thickness, target material, laser system, beamsplitter) were changed at once in this experiment, it cannot be clearly retraced which of these changes is responsible for the occurrence of the double-peak structure. The cause for the structural change of the deflection pattern could have been determined by a more systematic approach. However, this was not the main objective of the experiment which is presented and discussed in detail in Chapter 10.

Figure 8.6 shows a series of processed proton streak deflectometry measurements. The experimental conditions correspond to the descriptions given in this section and are identical for all images. The data have been recorded in consecutive shots and with different values of the lateral displacement d .

The shown images demonstrate the capability of proton deflectometry in combination with the lateral displacement of the probed interaction fields. This setup allowed for an investigation of the field distribution at both sides of the irradiated foil and allowed for the probing of its lateral extension in between the total range of $-2800 \mu\text{m}$ to $1800 \mu\text{m}$. Different parts of the extended field distribution were probed in consecutive shots, where both the magnification and the time resolution remained constant.

For the first time, the electric field evolutions at both sides of a thin foil were recorded simultaneously (in one shot). The acting fields can be traced up to $\sim 1500 \mu\text{m}$ far from the target surface, which shows the complexity of the field configuration.

The deflection measurements indicate a pronounced symmetry of the field distribution. Protons passing the interaction target on different sides but with similar energies ϵ_p and similar initial focal distances $|x_F|$ show similar deflection amplitudes.

The use of different field deflection setups to build field models which cause no contradicting effects will be followed in Chapters 9 and 10.

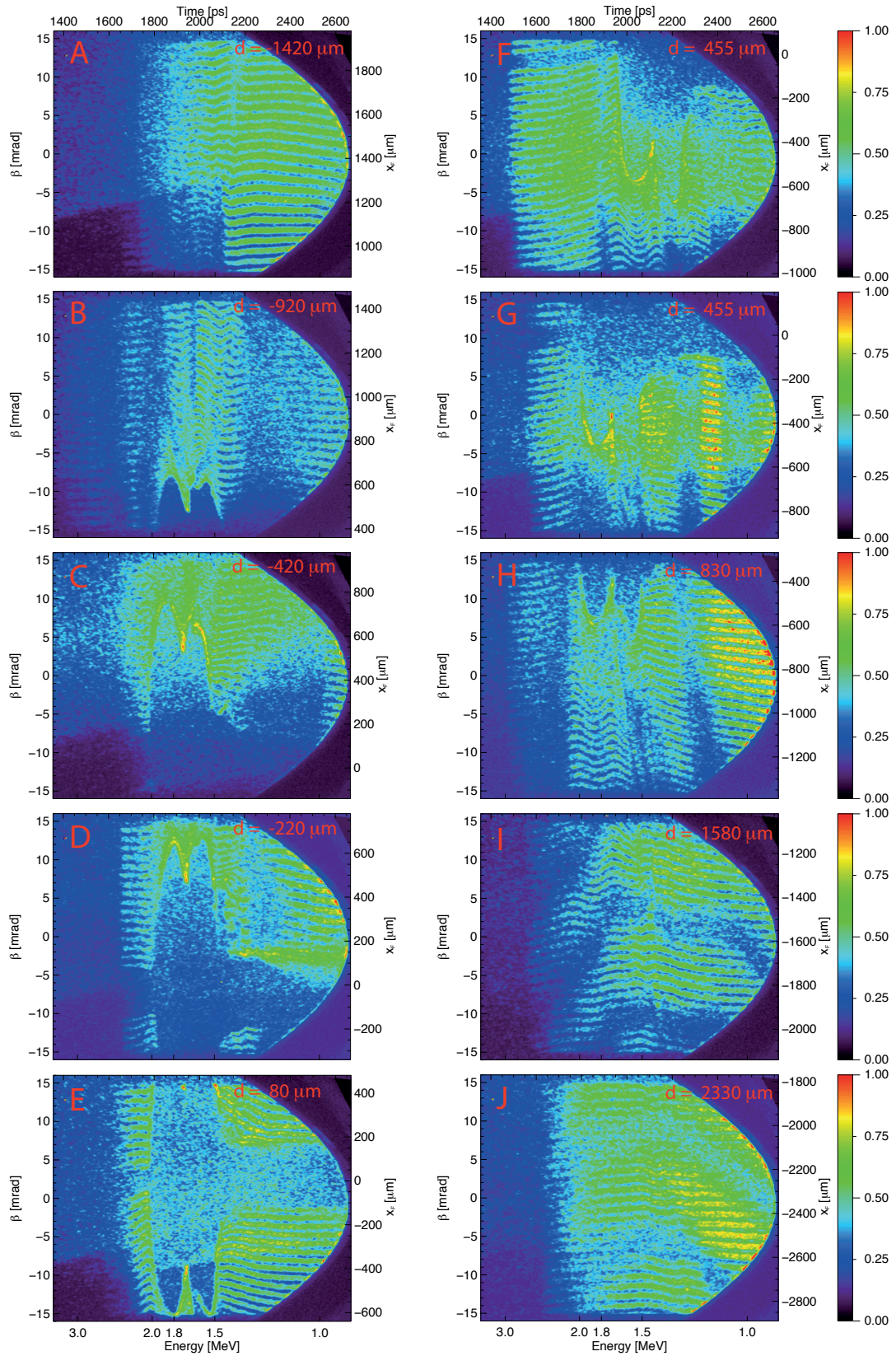


Figure 8.6: Numerically transformed density distribution $\tilde{\rho}(\beta, t_p)$ for different values of the lateral displacement d .

8.5 Time Resolution

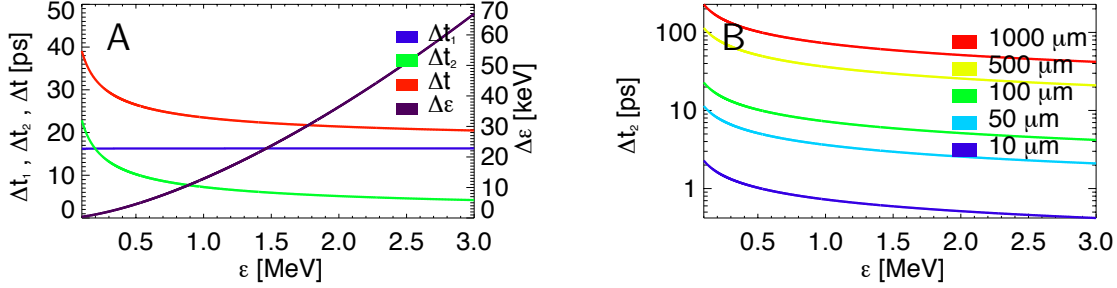


Figure 8.7: **A** - Functional dependence of the energy resolution $\Delta\epsilon$ and the time resolutions Δt , Δt_1 and Δt_2 . **B** - Time resolution Δt_2 for different values of the field extension l_I .

Using proton streak deflectometry, the temporal evolution of the investigated process (e.g. the evolution of electric and magnetic fields) is determined on the basis of the detected proton energy. For this reason, the time resolution depends on the energy resolution $\Delta\epsilon(\epsilon)$ (Equation 5.32) of the spectrometer (c.f. Section 5.5). Assuming a proton with the kinetic energy ϵ propagates along the z -axis, its time of arrival at the interaction plane ($z = a$) is given by

$$t_p = a \sqrt{\frac{m_p}{2\epsilon}} \quad (8.2)$$

Because its energy is only measurable with the resolution $\Delta\epsilon(\epsilon)$ the time resolution Δt_1 is determined by

$$\Delta t_1 = a \left(\sqrt{\frac{m_p}{2\left(\epsilon - \frac{\Delta\epsilon(\epsilon)}{2}\right)}} - \sqrt{\frac{m_p}{2\left(\epsilon + \frac{\Delta\epsilon(\epsilon)}{2}\right)}} \right). \quad (8.3)$$

Therefore, the time resolution $\Delta t_1(a, \epsilon, \Delta\epsilon(\epsilon))$ depends in first approximation on the distance a to the interaction plane, the proton energy ϵ and the energy resolution of the spectrometer $\Delta\epsilon(\epsilon)$.

In addition, the time of flight through the interaction region (i.e. the extended electromagnetic fields) in z -direction has to be taken into account. The time resolution $\Delta t_2(l_I, \epsilon, \Delta\epsilon(\epsilon))$ is defined by

$$\Delta t_2 = l_I \sqrt{\frac{m_p}{2\left(\epsilon - \frac{\Delta\epsilon(\epsilon)}{2}\right)}}, \quad (8.4)$$

where l_I is the extension of the interaction region in z -direction. The final time resolution consists in the convolution of both terms.

The upper boundary (maximum time window) is given by the inequality

$$\Delta t \leq \Delta t_1 + \Delta t_2. \quad (8.5)$$

Figure 8.7.A shows the energy resolution $\Delta\epsilon$ of the spectrometer, the time resolution Δt and its components Δt_1 and Δt_2 . The experimental parameters which correspond to the calculated resolution are given in the caption of Figure 8.3. Their denotations refer to the denominations provided in Section 5.3 and in Figures 8.1 and 8.2. In Figure 8.7.A a field extension of $l_I = 100 \mu\text{m}$ is assumed, whereas Figure 8.7.B illustrates the dependence of Δt_2 for different values of l_I between $10 \mu\text{m}$ and $5000 \mu\text{m}$.

The TNSA process is ultra-short and takes place on timescales from hundreds of femtoseconds to a few picoseconds [4, 109, 110]. At the same time the radial extension of the accelerating fields can have a length from one hundred micrometers up to values greater than a millimeter [104, 106]. In this case the time resolution of streak deflectometry measurements in transversal configuration is insufficient to resolve this process.

For this reason, the longitudinal probing geometry will be used in the next chapter to investigate the electric field evolution. In this case the propagation direction of the probing proton beam is parallel to the surface normal of the interaction target and therefore parallel to the dominant electric field component. When the protons propagate through the laser-irradiated interaction target their velocity is changed depending on the accelerating and decelerating effect of the transient fields at the front and rear sides of the foil. This effect will be used to infer a field evolution which changes on a time scale of approximately 100 fs.

9 Energy Redistribution Effects in Proton Beams by Probing Strong Fields at Plasma Vacuum Interfaces

This chapter deals with energy redistribution effects in proton beams while transversing the strong electric fields that are created at plasma vacuum interfaces of laser irradiated thin foils [134]. This effect is used to infer a field evolution with a characteristic time scale of 100 fs. In the cases considered, the laser and target parameters were chosen in a way that TNSA (Section 4.2) is the dominant mechanism of ion acceleration. In this case the main electric field components are directed normally to the target surface and are dominant over others. In further development of previous experiments [7] very thin foils with a thickness below one micrometer were used. This allowed for an enhancement of the TNSA-process [135, 136] by applying a driving laser pulse having a temporal envelope with high contrast.

9.1 Conception

Using proton imaging, electrical fields have been mainly investigated with transversal deflection geometry [7, 106, 116] as discussed in Chapters 7 and 8. In this chapter the accelerating electric field distribution is investigated in longitudinal probing geometry. In this case, the propagation direction of the probing proton beam is parallel to the surface normal of the interaction target and is therefore parallel to the dominant electric field components as illustrated in Figure 9.1.

When the protons propagate through the laser-irradiated interaction target their velocity is changed depending on the accelerating and decelerating effect of the transient fields at the front and rear sides of the foil. The use of thin foils reduces the scattering of the penetrating probe particles.

The characteristic properties of the laser-accelerated protons and their energy sensitive detection allow these effects of first order to be investigated. Indeed, the induced change of the velocity (kinetic energy) distribution of the probing proton

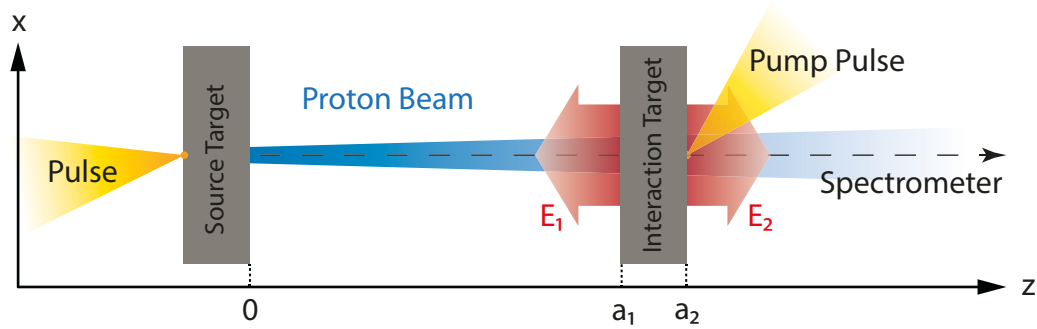


Figure 9.1: Proton propagation in longitudinal probing geometry

beam is the main difference to the transversal probing geometry.

In transversal probing geometry, the temporal information of the investigated process is restricted by the time resolution of the experimental setup. In contrast, the longitudinal probing geometry can be applied to monitor energy redistribution effects which result from field dynamics on a much faster time scale. If specific prerequisites are fulfilled this situation provides insight to ultrafast changes of the temporal and spatial field distribution itself.

For example, the following calculation is possible: the energy of a proton which probes an electric field of about $1 \text{ MV}/\mu\text{m}$ strength is changed by 50% of its original 2 MeV kinetic energy within 50 fs and an acceleration distance of $1 \mu\text{m}$ in the field. If a sufficiently high number of protons is influenced, such a change is detectable. However, ambiguous situations can arise since different field configurations can result in similar changes of the proton distribution function. For this reason, comparative measurement at different field locations and restrictions in the model discussion are required.

9.2 Experimental Setup

The experimental setup and probing geometry is illustrated in Figure 9.2. As a source for the generation of the probing proton beam a $5 \mu\text{m}$ thick titanium foil and its adherent CH-contamination layer is irradiated by a laser pulse. On their way to the detector the protons propagate along the surface normal through an aluminum foil with a thickness Δa of 800 nm. In this connection, the beam is used to probe the electric fields which are created as a result of an interaction between the laser pump pulse and the aluminum foil (interaction target).

The focal intensities of the laser pulses were calculated with respect to the measured focal spot-sizes, pulse energies and pulse durations (Section 2.1). The calculated intensity value I_{source} of the laser pulse that irradiates the source target is $\geq 1 \cdot 10^{19} \text{ W}/\text{cm}^2$. The intensity of the pump pulse I_{pump} had values between

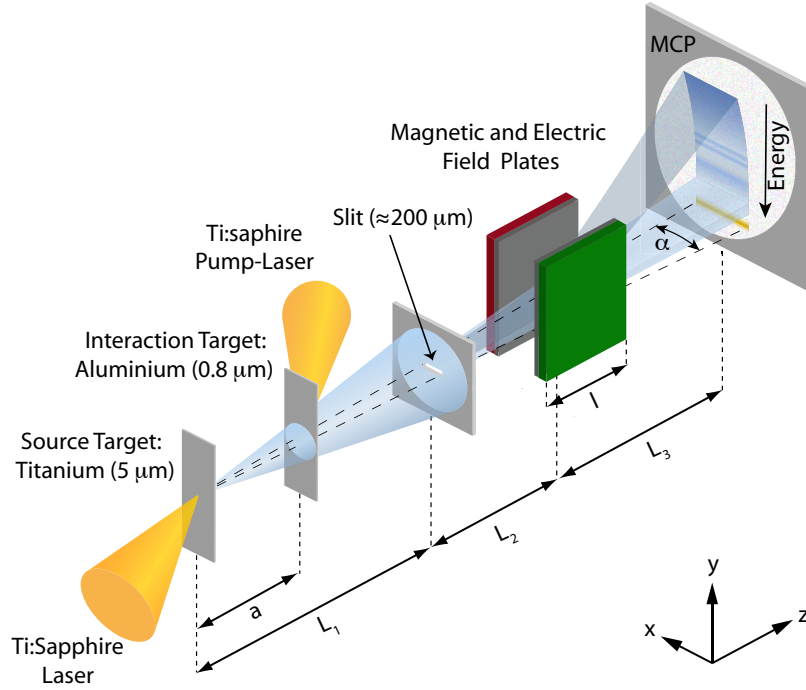


Figure 9.2: Experimental setup for longitudinal probing of thin foils

$1 \cdot 10^{18} \text{ W/cm}^2$ and $5 \cdot 10^{18} \text{ W/cm}^2$. Due to the specific architecture of the amplifier chains, laser pulses with different temporal contrast and pulse duration can be used, for both the probe and for the pump. For the presented experiments laser arm A (Section 2) was used, which provides an pulse length τ_p (FWHM of intensity) of 25 fs and an ASE background level of $10^{-10} - 10^{-9}$. The laser pulse was divided within the experimental chamber using a semi-transparent mirror. The reflected pulse was used as the probe (80% pulse power) and the transmitted pulses as the pump (20% pulse power). Due to the dispersion of the glass substrate the duration of the pump pulse changed from 25 fs to 87 fs (Section A.4).

The energy distribution of the probing proton beam is registered with a Thomson slit spectrometer (Chapter 5). The denotations shown in Figure 9.2 are the same as in Section 5.1 but their values differ for the presented measurements of this chapter. The depicted distances L_1 to L_3 have the values: $L_1 = 475 \text{ mm}$, $L_2 = 229 \text{ mm}$, $L_3 = 523 \text{ mm}$. The applied magnet ($B_x = 0.34 \text{ T}$, $l = 50 \text{ mm}$) is identical to that of Section 5.1. The virtual source distance $|z_v|$ was determined in a separate experiment (Section B.1) and has a constant value of $1.75 \pm 0.5 \text{ mm}$ for the relevant energy interval. The entrance slit has a width s_y of about $230 \mu\text{m}$. This leads to an energy resolution $\Delta\epsilon$ of approximately 60 keV for proton energies of around 2.0 MeV (Section 5.5). In general, the relative energy resolution is better than 4% of the relevant kinetic energy values. Due to the limited slit length $s_x \approx 1 \text{ cm}$, the

projected observation line from the interaction target is $120\ \mu\text{m}$ long.

The implementation of several translation stages within the experimental chamber allowed the position of the pump-focus to be shifted in x- and z-direction, without deteriorating the focus quality. In addition, a mobile target holder was equipped with several titanium (source targets) and aluminum (interaction targets) foils at fixed but different distances from each other. The selection of a certain target distance was possible by moving the holder in y-direction. By changing the z-position of the holder the source laser pulse could be focused on the titanium foil.

The setup allowed for the translating of laser-induced interaction fields in x- and z-direction with regard to the fixed probing proton beam and was applied to probe specific parts of the field distribution in consecutive shots. After careful stage calibration different geometries could be calculated and aligned while keeping the reflection angles of the off-axis parabolic focussing mirrors at high precision.

9.3 Experimental Results

For a systematic investigation of laser-induced strong fields on plasma vacuum interfaces, several experiments in longitudinal configuration were conducted. The changing of specific parameters of the pump-laser or the setup allowed the observed redistribution effects in the proton energy spectrum to be modified. The presented experiments differ with regard to the target distance a , the lateral displacement d , the setting of the pump time t_{pump} and the illumination direction of the pump-laser pulse

Due to instability problems of laser arm A (Section 2) the contrast and pre-pulse conditions as well as the beam divergence could vary between different experiments. For reasons of time all of these parameters could not be measured on a daily basis. Thus the constancy of these parameters was only guaranteed for the time duration of one series of measurements.

Each of the following sections shows only measurements that belong to the same series. In addition selected parameters (target distance, lateral focus position) are systematically changed within each section. Since only measurements of the same series are compared with each other the exclusive influence of the varied parameter on the measurements can be investigated.

9.3.1 Variation of the Target Distance

Using an optical delay stage the arrival time t_{pump} of the pump pulse at the interaction target was adjustable with respect to time zero (Section 2.2). In the presented experiments the pump time $t_{\text{pump}}(\epsilon_{\text{pump}}, a)$ was set to the time of flight of protons which had the specific kinetic energy ϵ_{pump} and propagated along the z-axis from the source target to the interaction plane ($z = a$).

Two cases are presented: in the case of Figure 9.3.A the proton t-pump energy

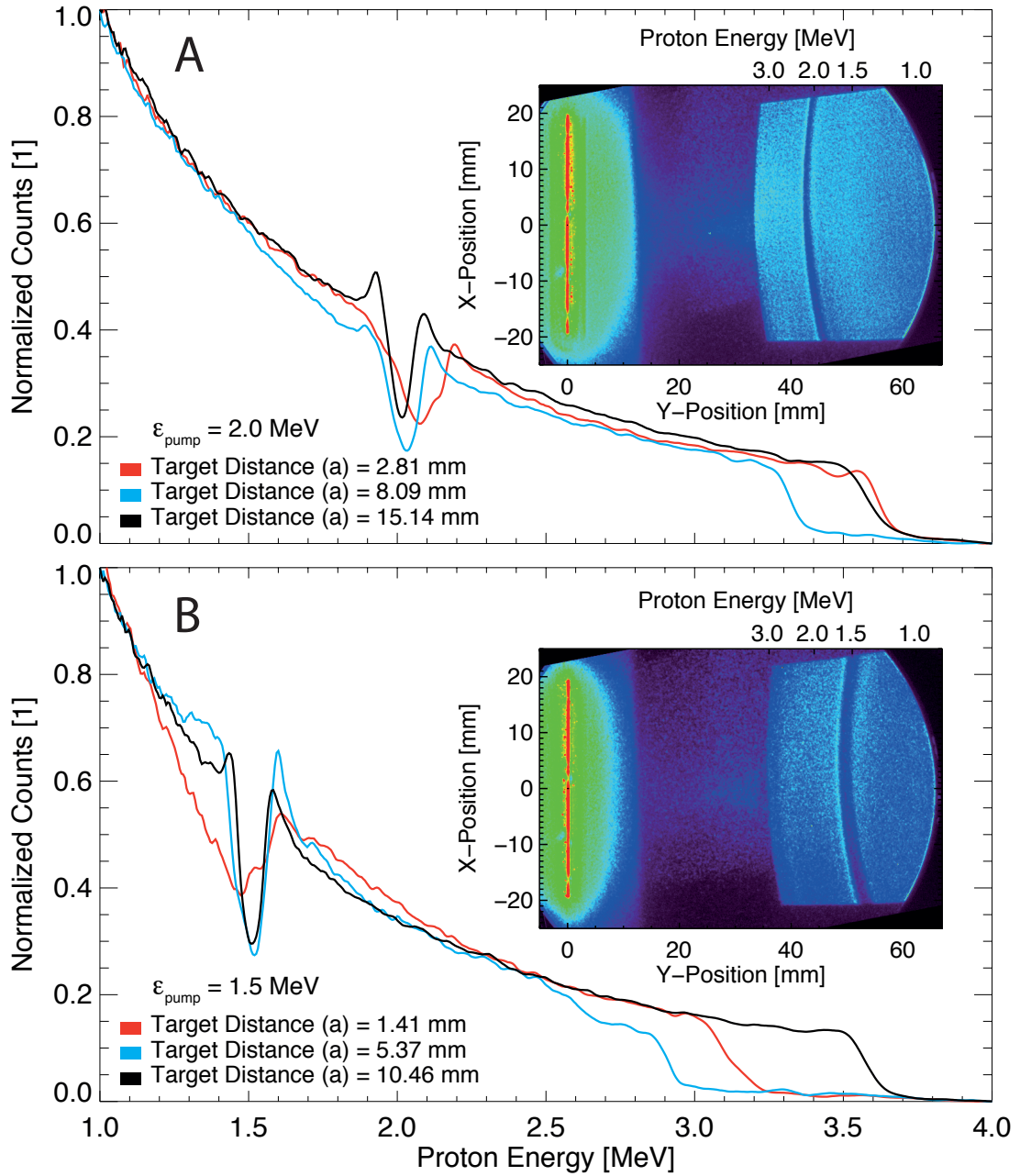


Figure 9.3: Redistribution effects in the proton energy spectrum depending on the target distance a . **A** - $\epsilon_{\text{pump}} = 2.0$ MeV. **B** - $\epsilon_{\text{pump}} = 1.5$ MeV.

ϵ_{pump} is set to 2.0 MeV and in the case of Figure 9.3.B ϵ_{pump} is 1.5 MeV. The inserts of Figures 9.3.A and 9.3.B are photographs of the light emitting phosphor screen and show the particle density distribution $\rho(x, y)$ on the detector. The electrical field plates in the spectrometer are switched on, nevertheless the proton signal is partly covered with a carbon ion background signal.

In additional measurements the voltage of the phosphorous screen (Section 5.2) was gated in order to suppress the signal of heavier ion species. This confirmed that its contribution to the total signal is only marginal and can be neglected. The dispersion of the proton signal on the detector is relatively homogeneous with the exception of a vertically extended region in the form of a pronounced and sharp gap, which occurs in a certain energy range.

Setting the pump conditions with respect to the source excitation ($I_{\text{pump}} \ll I_{\text{source}}$) assured that the proton signal of the interaction target did not contribute to this specific part of the energy spectrum of the probing proton beam. A comparison with measurements with deactivated pump laser confirms that this effect on the probing proton beam can be attributed to the influence of the second laser-plasma interaction.

For quantitative analysis of the observation, the two-dimensional proton density distributions on the detector $\rho(x, y)$ are processed with the numerical methods of Chapter 5.4. As a result averaged ($\beta \in [-10, 10]$ mrad) one-dimensional proton energy spectra (not background corrected) are obtained, as illustrated by the blue curves in Figures 9.3.A and 9.3.B.

Prominent dips enclosed by two local maxima on the low and high energy side of the minimum were found in both cases. The position of the minimum (ϵ_{min}) is in good agreement with the setting of the respective proton t-pump energy ϵ_{pump} . This (indirectly) confirms the right timing of the experiment. The specific shape of the proton redistribution was reproduced in consecutive shots and a characteristic dependence on the target distance a was found.

In comparison with the blue curves, a larger target distance a was used for the black curves and a smaller one for the red curves. Apart from that all other experimental conditions were identical.

If the target distance a is larger, the time of flight of the probing protons to the interaction target is increased. Due to the broad energy spectrum of the probing proton beam, this leads to a higher spatial dispersion of the beam. As a consequence, a smaller part of the proton energy spectrum is affected by the spatially extended fields of the second laser-plasma interaction. This explains the decreased width of the density gap in the black curves and the increased gap width in the red curves.

In addition, the appearance of the local maxima on the low energy side of the density gap shows a systematic dependence on the target distance a . The low energy maximum gets more pronounced with higher distances and seems to disappear at lower distances.

The positions of the local minimum and local maximum can be used to infer an effective extension l_{eff} of the field. One can assume that the energy change of a probing proton is maximum if its propagation length z_p coincides with the position of the interaction target ($z_p = a$) at the time $t = t_{\text{pump}}$ when the field is initiated. By definition, such a proton has the initial energy $\epsilon_0 = \epsilon_{\text{pump}}$ which corresponds to the energy of the density minimum. The energies of the local max-

ima on the low and high energy side of the minimum are denoted by ϵ_{low} and ϵ_{high} , respectively. A proton with the initial energy $\epsilon_0 = \epsilon_{\text{low}}$ reaches the position $z_p = z_{\text{low}} = \sqrt{2\epsilon_{\text{low}}/m} \cdot t_{\text{pump}}$ when the interaction fields are generated. At this time, its relative distance to the interaction target Δz_{low} is $a - z_{\text{low}}$. Similarly, the relative position of a proton with the energy $\epsilon_0 = \epsilon_{\text{high}}$ can be defined by $\Delta z_{\text{high}} = z_{\text{high}} - a$. Since the particle density is increased at ϵ_{low} and ϵ_{high} , the assumption is reasonable that the corresponding initial proton energy is not significantly changed and that the increment is caused by protons which were accelerated or decelerated by the field. Therefore, the field amplitude at the relative distances Δz_{low} and Δz_{high} seems to be reduced to an extent that prohibits a strong decrease of the initial energy density. For this reason, these distances can be used as a measure of the effective extension l_{eff} .

In case of the black curve of Figure 9.3.A the energy ϵ_{low} is 1.93 MeV, ϵ_{high} is 2.09 MeV and the density minimum is located at the energy $\epsilon_{\text{min}} = 2.01$ MeV. Using $\epsilon_{\text{pump}} = 2.0$ MeV leads to $\Delta z_{\text{low}} = 266 \mu\text{m}$ and $\Delta z_{\text{high}} = 335 \mu\text{m}$. This allows for an estimation of the effective extension of the field $l_{\text{eff}} \approx 300 \mu\text{m}$.

9.3.2 Variation of the Lateral Focus Position

In order to study the lateral extension (x-direction) of the laser-induced electric fields, an additional series of experiments was conducted to measure the redistribution effects within the probing proton beam. In principle, the same laser parameters (cf. previous remarks) as in the last section were used. The proton t-pump energy ϵ_{pump} was set to 1.5 MeV and a target distance a of 7.4 mm was used. The lateral displacement parameter d (Section 8.2) was varied in consecutive shots.

Figure 9.4 illustrates the basic setup and the experimental results for two different settings of d . Whereas Figure 9.4.A shows the redistribution effects when the interaction center ($d = 0 \mu\text{m}$) of the aluminum foil is probed, Figure 9.4.B shows the resulting effects that occur at $250 \mu\text{m}$ aside of the center.

The inserts of Figure 9.4 illustrate the target geometry and show the respective focus positions of the pump beam in accordance with the parameter d . In addition the processed density distributions $\tilde{\rho}(\beta, \epsilon)$ (Section 5.4, Equation 5.12) are shown as a function of the initial ejection angle β and the proton energy ϵ . An integration of the proton traces over the interval $\beta \in [-10, -10] \text{ mrad}$ yields one-dimensional proton energy spectra (not background corrected) which are illustrated by the red curves.

The blue curves show the outcome of two independent laser shots with respectively identical values of d and illustrate the ability of the phenomenon to be reproduced. In both cases a pronounced gap in the distribution in the energy range between 1.2 MeV and 1.5 MeV is found. While in the case of $d = 0 \mu\text{m}$ (Figure 9.4.A) the gap is followed by two local maxima on the high energy side of the gap, in the case of $d = 250 \mu\text{m}$ (Figure 9.4.B) only one maxima is visible.

Other experiments in this series show that the generation of the two high energy

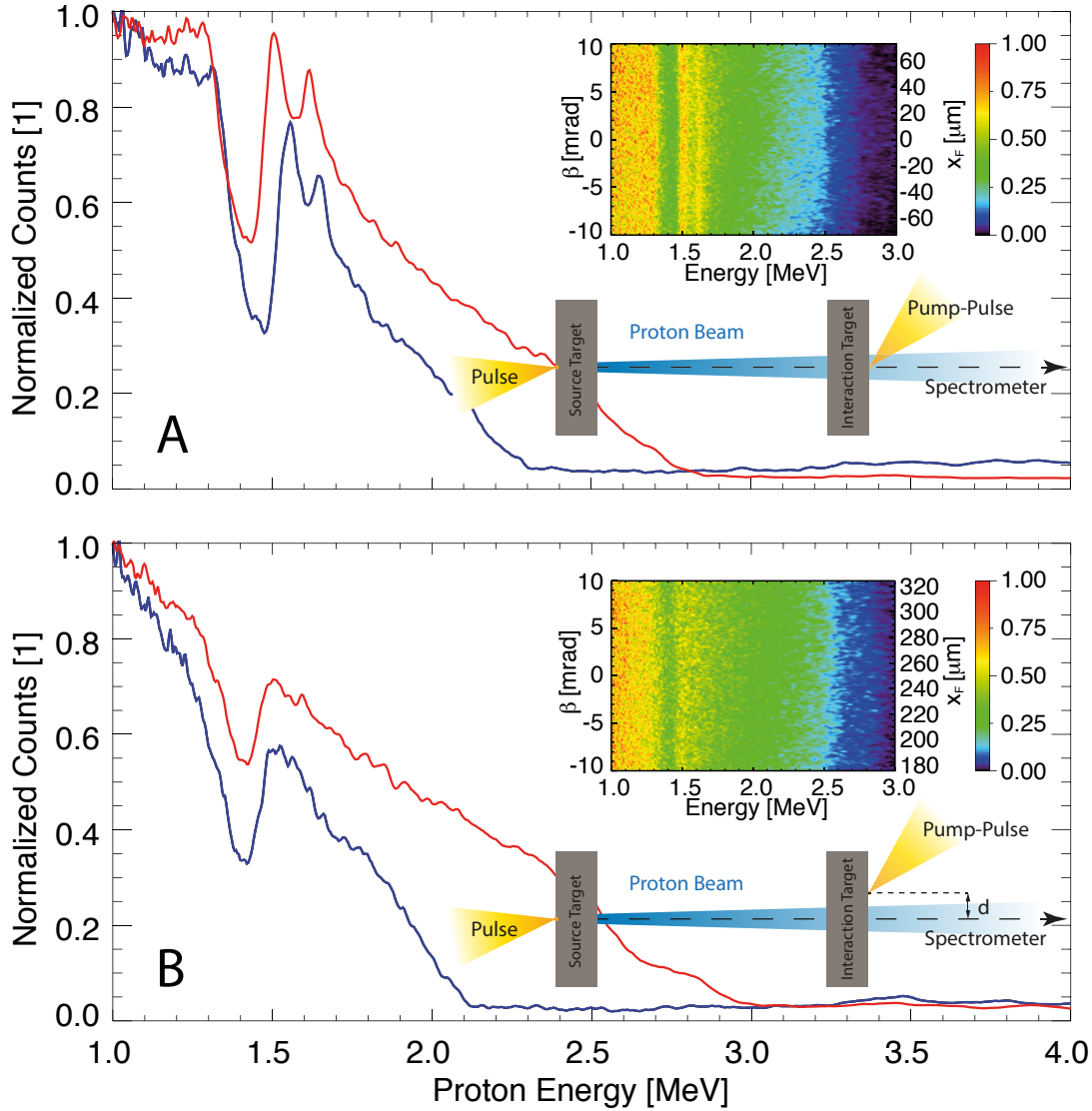


Figure 9.4: Redistribution effects depending on the lateral displacement d of the pump-focus. **A** - Probing of the interaction center ($d = 0 \mu\text{m}$). **B** - Probing aside from the interaction center ($d = 250 \mu\text{m}$).

peaks in the spectrum is possible for different settings of ϵ_{pump} . In these experiments, d is set to $0 \mu\text{m}$ and ϵ_{pump} is varied between 1.3 MeV and 2.0 MeV . As a result, the whole redistribution structure (including the second high energy maximum) changes its relative position in the energy spectrum, according to the setting of ϵ_{pump} or t_{pump} , respectively.

Both the variation of the lateral displacement d and the variation of the proton t-pump energy ϵ_{pump} affirm that the second high energy peak observed is not caused by a possible proton (background) distribution that originates from the acceleration

at the interaction target itself. Instead, it proves that the observed phenomenon is an effect that is created by the interaction of the probing proton beam and the induced field structure around the interaction target.

The appearance of two distinct peaks on the high energy side of the gap was also observed in other series of measurements. However, it was not possible to identify the experimental conditions that triggered the specific field configuration, which led to this particular effect. The occurrence of the two peaks might be connected with a change in the contrast or pre-pulse conditions of laser arm A (Section 2), which are not known precisely in the presented case.

In another series of measurements under similar experimental conditions, the lateral field extension was probed up to much higher displacement values d . At $d = 2000 \mu\text{m}$ a weak but systematic redistribution of the proton energy spectrum was still visible. However, the redistribution effect was not distinguishable from the background noise at the value $d = 2500 \mu\text{m}$.

These values are in excellent agreement with the findings of Section 8.4. In this connection, a field extension radius r_f of $2260 \mu\text{m}$ was estimated under the assumption that radial field components are negligible.

9.3.3 Variation of the Irradiation Geometry

In the presented series of measurements the foil surface was irradiated from the other side but under the same angle of incidence (45°). In addition the same laser parameters as in the previous experiments were used, even if a possible change of the contrast or pre-pulse conditions of laser arm A (Section 2) must be considered. The aim of this experiment was to study the influence of the illumination direction on the induced field distribution, which could possibly influence the redistribution effects within the probing proton beam. In principle an asymmetric field distribution at the front and rear side of the foil could change the accelerating and decelerating action of the fields on the probing proton beam. Therefore, a significant change of the observed redistribution effects in comparison to the previous sections would be an indication for the asymmetry of the fields.

Figure 9.5 illustrates the basic setup and the experimental results for two different target distances a . The insert of Figure 9.5 is a photograph of the light emitting phosphor screen and shows the particle density distribution $\rho(x, y)$ on the detector. The electrical field plates in the spectrometer are switched on, nevertheless the proton signal is significantly covered with a background signal which consists of heavier ion species. Nevertheless, the redistribution effect in the probing proton beam is clearly visible. Using the numerical methods of Chapter 5.4, an averaged one-dimensional proton energy spectrum (not background corrected) is obtained, as illustrated by the red curve in Figure 9.5. In contrast a smaller target distance a was used in case of the blue curve.

A comparison of these curves with the measurements of Section 9.3.1 (Figure 9.3) shows that the observed effects are qualitatively similar. Also the dependency of

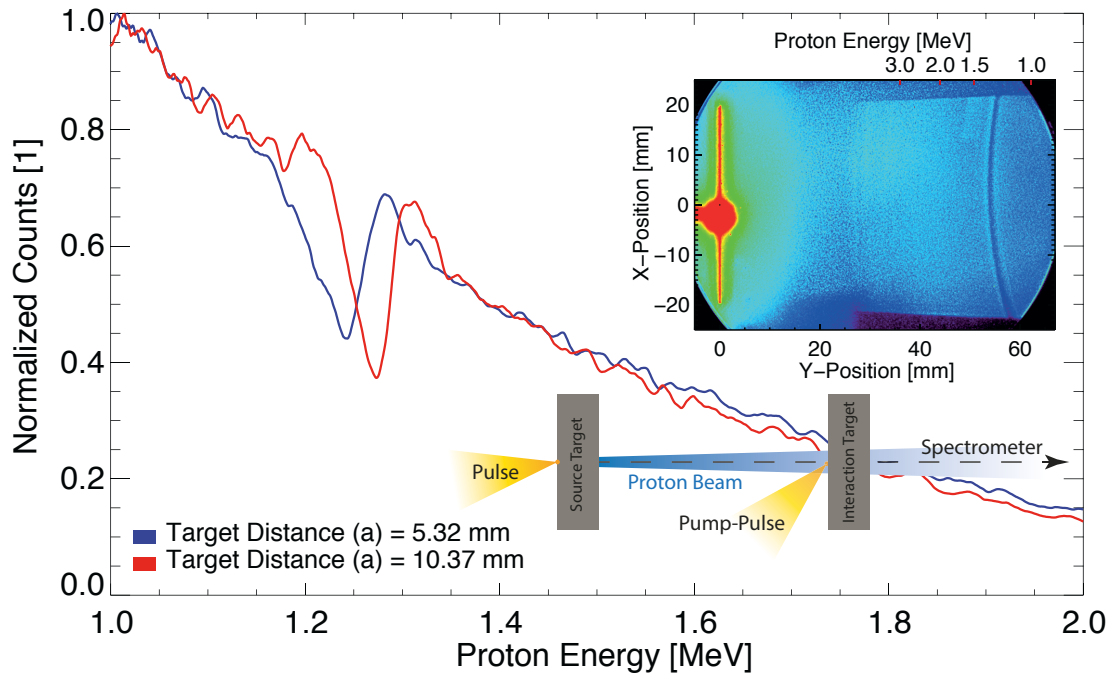


Figure 9.5: Redistributive effects in the proton energy spectrum depending on the target distance a with changed irradiation side of the interaction target.

the redistribution effect on the target distance a is consistent with the results of Section 9.3.1. Irrespective of which side of the thin interaction foil is irradiated, the appearance of the local maxima on the low energy side of the density gap is more pronounced at a higher target distance a and disappears at lower distances. The similarities of the observed redistribution effects indicate a significant symmetry of the field distribution between the target front and rear side. This conclusion is consistent with the results of the streak deflectometry measurements in transversal configuration (Chapter 8.4), which show a pronounced deflection symmetry at both target surfaces.

The post-acceleration of the probing protons in the field of the second laser-plasma interaction can be quantified by the energy difference between the gap minimum and the peak on its high energy side. In the presented case this energy gain $\Delta\epsilon$ is approximately 0.05 MeV, which is in good agreement with the results of a cascaded laser acceleration experiment [132] which was conducted under similar experimental conditions.

9.4 Theoretical Description

In this section several analytical models are proposed which describe the laser-induced electric fields at the front and rear side of a thin foil. Furthermore numerical and mathematical methods are proposed which enable the proton energy redistribution effects under the influence of transient electric fields to be calculated. These methods and analytical field descriptions are applied in Section 9.5 to simulate the accelerating and decelerating effect on a proton beam that propagates through the laser-driven fields around the interaction target. If the reader is mainly interested in the modeling of the experimental results and the applicability of the individual models for the explanation of the observed redistribution effects, he should skip this section. Relevant equations and results of this section will be referenced.

9.4.1 Analytical Field Description of Moving Ion Fronts

As described in reference [106] the field of an moving ion front can be modeled using PIC and fluid simulations. The spatial dependence of the field structure is described by a plateau region followed by an exponential rise up to the front field peak and a decay of the expanding Gaussian-shaped front. As an approximation for the spatial decay of the front region a function with the proportionality

$$\mathcal{Z}_{\text{front}}(z) \simeq (1 + z/l_s)^{-1} \quad (9.1)$$

is proposed. Similarly, the temporal decay of the front peak ($\mathcal{T}_{\text{front,(R)}}(t)$) and of the of the plateau region ($\mathcal{T}_{\text{plateau,(R)}}(t)$) is approximated by functions proportional to

$$\mathcal{T}_{\text{front,(R)}}(t) \simeq (1 + t/\tau_s)^{-1}, \quad \mathcal{T}_{\text{plateau,(R)}}(t) \simeq (1 + t/\tau_s)^{-2}. \quad (9.2)$$

Following this description the temporal and spatial field structure of two ion fronts that propagate in opposite directions can be described by the equation

$$E(z, t) = E_1(z, t) + E_2(z, t), \quad (9.3)$$

which is illustrated in Figure 9.6 for a specific set of parameters. Here, $E_1(z, t)$ defines the field of the ion front that starts at surface 1 and propagates in negative z -direction. The field $E_2(z, t)$ is caused by the ion front which propagates in positive z -direction and starts at surface 2. Both fields are initiated at the time t_{pump} and can be written as

$$E_1(z, t) = E_{\text{F}}(\mathcal{E}_{0,1}, a_1 - z, t - t_{\text{pump}}), \quad (9.4)$$

$$E_2(z, t) = E_{\text{F}}(\mathcal{E}_{0,2}, z - a_2, t - t_{\text{pump}}). \quad (9.5)$$

The initial field amplitudes $\mathcal{E}_{0,1}$ and $\mathcal{E}_{0,2}$ of the expanding ion fronts are connected with the constant field amplitude factor \mathcal{E}_c (Equation 4.6) by the relation

$$-\mathcal{E}_{0,1} = \mathcal{E}_{0,2} = \mathcal{E}_c. \quad (9.6)$$

The distances a_1 and a_2 are the surface positions of the interaction target in relation to the source target, as illustrated in Figure 9.1. The function E_F describes the unshifted temporal and spatial field dependence of one separate front and is defined by

$$E_F(\mathcal{E}_0, z, t) = \begin{cases} \mathcal{E}_0 \cdot \mathcal{F}_p(z, t), & \text{if } \tilde{z}(z, t) < 0, \\ \mathcal{E}_0 \cdot \mathcal{F}_f(z, t), & \text{if } \tilde{z}(z, t) \geq 0, \end{cases} \quad (9.7)$$

where $\tilde{z}(z, t)$ defines the position in relation to the position of the moving ion front $z_f(t)$

$$\tilde{z}(z, t) = z - z_f(t). \quad (9.8)$$

Depending on $\tilde{z}(z, t)$ the function $E_F(\mathcal{E}_0, z, t)$ is divided in two parts, the front region $\mathcal{F}_f(z, t)$ and the plateau region $\mathcal{F}_p(z, t)$. The front region is defined by the equation

$$\mathcal{F}_f(z, t) = \mathcal{T}_{\text{front}}(t) \cdot \mathcal{Z}_{\text{front}}(z). \quad (9.9)$$

The plateau region is split in two, a constant only temporally changing part $\mathcal{F}_{p,c}$ and the exponential rise up to the front $\mathcal{F}_{p,e}$:

$$\mathcal{F}_p(z, t) = \begin{cases} \mathcal{F}_{p,c}, & \text{if } \mathcal{F}_{p,c} > \mathcal{F}_{p,e}, & \mathcal{F}_{p,c} = \mathcal{T}_{\text{plateau}}(t), \\ \mathcal{F}_{p,e}, & \text{if } \mathcal{F}_{p,c} < \mathcal{F}_{p,e}, & \mathcal{F}_{p,e} = \mathcal{T}_{\text{front}}(t) \cdot \exp(-2|z|/(3l_s)). \end{cases} \quad (9.10)$$

Besides Equations 9.1 and 9.2, other functional dependencies are also applied to approximate the field of an expanding ion front. In the following several descriptions for $\mathcal{T}_{\text{front}}(t)$ and $\mathcal{T}_{\text{plateau}}(t)$ are proposed.

Isothermal Approximation

The following description is based on the isothermal expansion model [73] which assumes a constant electron temperature and is introduced in Section 4.2. In this case the temporal dependence of the front region can be approximated by Equation 4.6, which has a time dependence similar to Equation 9.2. As explained in reference [73], the plateau region is almost constant in space and has a field strength of approximately half the value of the front peak. However, the application of $\mathcal{T}_{\text{plateau,(IT)}}(t) = (1/2) \cdot \mathcal{T}_{\text{front,(IT)}}(t)$ did not lead to reasonable simulation results. For this reason, a function with a similar time dependence to Equation 9.2 is used

to model the temporal decay of the plateau. The explicit form of the applied functions is given by

$$\mathcal{T}_{\text{front,(IT)}}(t) = \frac{2}{\sqrt{2e_m + (t/\tau_s)^2}}, \quad \mathcal{T}_{\text{plateau,(IT)}}(t) = \frac{2}{\sqrt{2e_m + (t/\tau_s)^2}}, \quad (9.11)$$

whereby e_m is the base of the natural logarithm. The characteristic temporal decay constant τ_s is connected with ion plasma frequency ω_{pi} (Equation 4.7) via $\tau_s = 1/\omega_{pi}$.

So far the proposed system of equations (cf. Equation 9.8) is not fully defined, since the time dependent position of the ion front $z_f(t)$ is unknown. In principle, the field of the ion front (Equation 4.6) itself is responsible for the ion acceleration and could be used to calculate the movement of the front. The equation of motion can be solved analytically and the resulting velocity and position of the front are given by Equations 4.8 and 4.9, respectively. However, in this approximation the integral $\int \mathcal{T}_{\text{front}} dt$ is not convergent and the velocity of the ion front is divergent for $t \rightarrow \infty$. For this reason, the limiting maximum ion velocity $v_{f,\text{max}}$ and the maximum ion energy $\epsilon_{f,\text{max}} = 1/2 m_i v_{f,\text{max}}$ is introduced accordingly. This energy can either be measured in experiment or estimated.

Using Formula 4.8 the time $t_{f,\text{max}}$ at which the velocity $v_{f,\text{max}}$ is reached can be calculated numerically. This allows for a more realistic approximation of the front position

$$z_f(t) = \begin{cases} z_{\text{front}}(t), & \text{if } t \leq t_{f,\text{max}}, \\ z_{f,\text{max}} + v_{f,\text{max}}(t - t_{f,\text{max}}), & \text{if } t > t_{f,\text{max}}, \end{cases} \quad (9.12)$$

whereby $z_{f,\text{max}}$ is determined by substituting $t_{f,\text{max}}$ into Formula 4.9. The corresponding corrected front velocity $v_f(t)$ is defined in the same way.

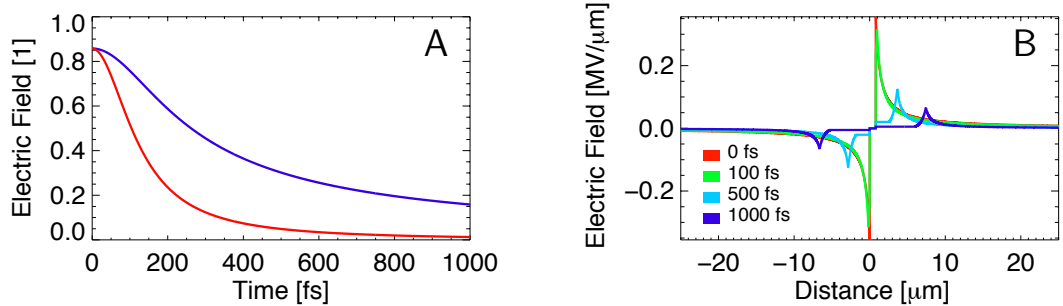


Figure 9.6: **A** - Temporal decay of the electric field using the isothermal approximation (Equation 9.11). Blue curve - Field front. Red curve - Plateau region. **B** - Spatial electric field distribution of two ion fronts which propagate in opposite directions (Equation 9.3). For both figures the parameters of Table 9.1 were used.

Adiabatic Approximation

In the following, analytic expressions are proposed that approximate the spatial and temporal field decay of an adiabatic plasma expansion. The description is based on reference [74] which deals with the collisionless expansion into a vacuum of a thin foil that is heated by an ultrashort laser pulse. The model takes into account the charge separation effects and the cooling of the electrons due to the energy transfer to the ions. According to this model the expansion can be divided into three regions: a linear increase, a plateau region and an ion front characterized by a field peak. Depending on the parameter $\theta = (k_B T_e)/(m_e c^2)$ which is zero in the classical limit and converges to infinity in the ultrarelativistic regime, different scalings of the plateau and front region are proposed. In the classical limit ($\theta = 0$) the scaling $E_{\text{front}} \propto t^{-2}$ and $E_{\text{plateau}} \propto t^{-3}$ applies, whereas in the ultrarelativistic regime ($\theta = \infty$) the scaling $E_{\text{front}} \propto t^{-3/2}$ and $E_{\text{plateau}} \propto t^{-2}$ is found. In order to approximate the field decay of the plateau and front region in the respective regimes the expressions

$$\mathcal{T}_{\text{front,(CL)}}(t) = \mathcal{T}_{\text{front,(IT)}}(t) \cdot \frac{a_{\text{f,cl}}}{\sqrt{a_{\text{f,cl}}^2 + (t/\tau_s)^2}}, \quad (9.13)$$

$$\mathcal{T}_{\text{plateau,(CL)}}(t) = \mathcal{T}_{\text{front,(IT)}}(t) \cdot \frac{a_{\text{p,cl}}}{a_{\text{p,cl}} + (t/\tau_s)^2}, \quad (9.14)$$

$$\mathcal{T}_{\text{front,(UR)}}(t) = \mathcal{T}_{\text{front,(IT)}}(t) \cdot \frac{a_{\text{f,ur}}}{\sqrt{a_{\text{f,ur}}^2 + t/\tau_s}}, \quad (9.15)$$

$$\mathcal{T}_{\text{plateau,(UR)}}(t) = \mathcal{T}_{\text{front,(IT)}}(t) \cdot \frac{a_{\text{p,ur}}}{a_{\text{p,ur}} + t/\tau_s} \quad (9.16)$$

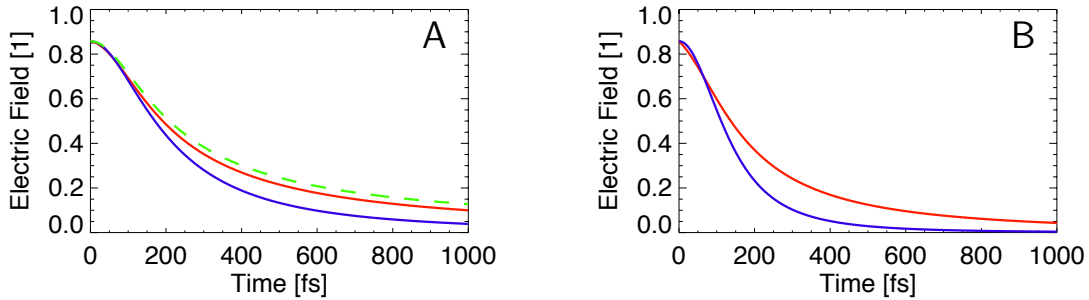


Figure 9.7: **A** - Approximation of the adiabatic time decay of the front region. Blue curve - $\mathcal{T}_{\text{front,(CL)}}$ (Equation 9.13). Red curve - $\mathcal{T}_{\text{front,(UR)}}$ (Equation 9.15). Green curve - $\mathcal{T}_{\text{front,(IT)}}$ (Equation 9.11). **B** - Temporal decay of the plateau region. Blue curve - $\mathcal{T}_{\text{plateau,(CL)}}$ (Equation 9.14). Red curve - $\mathcal{T}_{\text{plateau,(UR)}}$ (Equation 9.16). For all curves the parameter $\tau_s = 64.3$ fs as well as the coefficients $a_{\text{f,cl}} = 5$, $a_{\text{f,ur}} = 5$, $a_{\text{p,cl}} = 8$ and $a_{\text{p,ur}} = 8$ were used.

are proposed, where (CL) stands for classical limit and (UR) for ultrarelativistic regime. Figure 9.7 illustrates the proposed functions in comparison to the isothermal case (Equation 9.11) for a specific set of coefficients. By definition all functions are limited by $\mathcal{T}_{\text{front,(IT)}}(t)$ (Equation 9.11). For small times the adiabatic decay of the field is similar to the isothermal description, which was also found in simulation [74]. At later times ($t \gg \tau_s$) the proposed scalings are valid. In addition the proposed functional dependencies satisfy the conditions $\mathcal{T}_{\text{plateau,(CL)}} \lesssim \mathcal{T}_{\text{front,(CL)}}$ and $\mathcal{T}_{\text{plateau,(UR)}} \lesssim \mathcal{T}_{\text{front,(UR)}}$ for $a_{\text{p,cl}} \simeq a_{\text{f,cl}}$ and $a_{\text{p,ur}} \simeq a_{\text{f,ur}}$, respectively. Depending on θ the adiabatic decay (AD) of the field is approximated by a normalized superposition of both regimes

$$\mathcal{T}_{\text{front,(AD)}}(t) = F_{\text{CL}}(\theta) \cdot \mathcal{T}_{\text{front,(CL)}}(t) + F_{\text{AD}}(\theta) \cdot \mathcal{T}_{\text{front,(AD)}}(t), \quad (9.17)$$

$$\mathcal{T}_{\text{plateau,(AD)}}(t) = F_{\text{CL}}(\theta) \cdot \mathcal{T}_{\text{plateau,(CL)}}(t) + F_{\text{AD}}(\theta) \cdot \mathcal{T}_{\text{plateau,(AD)}}(t), \quad (9.18)$$

whereby $F_{\text{CL}}(\theta) := 1/(1 + \theta)$ and $F_{\text{UR}}(\theta) := 1 - F_{\text{CL}}(\theta)$.

In order to determine the coefficients $a_{\text{f,cl}}$, $a_{\text{f,ur}}$, $a_{\text{p,cl}}$ and $a_{\text{p,ur}}$ and to test the proposed approximation of the adiabatic field evolution (Equations 9.17 and 9.18) the model is compared to published simulation results [106] as illustrated by Figure 9.8.

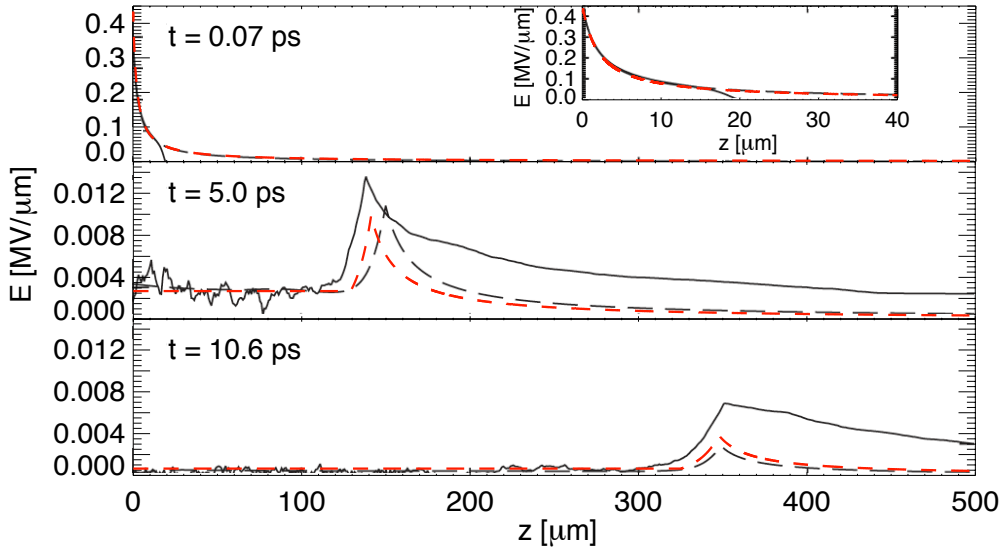


Figure 9.8: Comparison between the adiabatic field approximation and published simulation results. The black lines are copied from the original publication [106] with permission of J. Fuchs. The solid line represents the outcome of a PIC-simulation and the black dashed line is the result of the fluid simulation [74] for $T_e = 500 \text{ keV}$ and $n_{e,0} = 3.0 \cdot 10^{19} \text{ 1/cm}^3$. For comparison the red dashed line shows the adiabatic approximation (Equations 9.17 and 9.18) using the same parameters. Here, the coefficients $a_{\text{f,cl}} = 5$, $a_{\text{f,ur}} = 5$, $a_{\text{p,cl}} = 8$ and $a_{\text{p,ur}} = 8$ as well as $\beta_v = 2$, $\delta_v = 1/2$ and $\gamma_v = 20$ (Equation 9.40) were used to match the results of the fluid simulation.

The parameters β_v , δ_v and γ_v determine the time dependence of the scale length $l_s(t)$ (Equation 9.40) and thus the temporal increment of the spatial field decay of the ion front. The use of $\beta_v = 2$, $\delta_v = 1/2$ and $\gamma_v = 20$ allows a good match between the adiabatic approximation (red dashed curve) and the fluid simulation (black dashed curve).

In contrast to these parameters, the coefficients of Equations 9.13 to 9.16 cannot be identified without ambiguity on the basis of Figure 9.8. In particular the ratios $a_{f,cl}/a_{f,ur}$ and $a_{p,cl}/a_{p,ur}$ are not clearly determined. In addition, a possible dependence of these coefficients on the hot electron temperature T_e , the initial electron density $n_{e,0}$ or the target thickness Δa cannot be excluded and is not investigated in the framework of this thesis.

However, the initial simulation conditions ($T_e = 500$ keV and $n_{e,0} = 3.0 \cdot 10^{19}$ 1/cm³) in reference [106] are similar to the model parameters which are used in Section 9.5.1 to reproduce the experimental results. For this reason, the coefficients $a_{f,cl} = a_{f,ur} = 5$ and $a_{p,cl} = a_{p,ur} = 8$ which are used in Figure 9.8 are also applied to model the experimental results.

Figure 9.9.A shows the time decay of the field front (Equation 9.19) together with the numerically calculated front velocity. In this connection, the time decay corresponding to the adiabatic approximation (Equation 9.17) is used. The position of the front is illustrated by Figure 9.9.B.

The advantage of the adiabatic approximation is that the integral $\int \mathcal{T}_{\text{front}} dt$ converges for $t \rightarrow \infty$. Therefore, the maximum front velocity $v_{f,\text{max}}$ and accordingly the maximum proton energy $\epsilon_{f,\text{max}} = 1/2 m_i v_{f,\text{max}}$ can be calculated numerically. The position of the proton front $z_f(t)$ does not depend on an estimation of $v_{f,\text{max}}$ and is obtained by solving the equation of motion of a proton in the field

$$E_{\text{front}}(t) = \mathcal{E}_c \cdot \mathcal{T}_{\text{front}}(t) = \sqrt{\frac{n_{e,0} k_B T_e}{\epsilon_0}} \cdot \mathcal{T}_{\text{front}}(t). \quad (9.19)$$

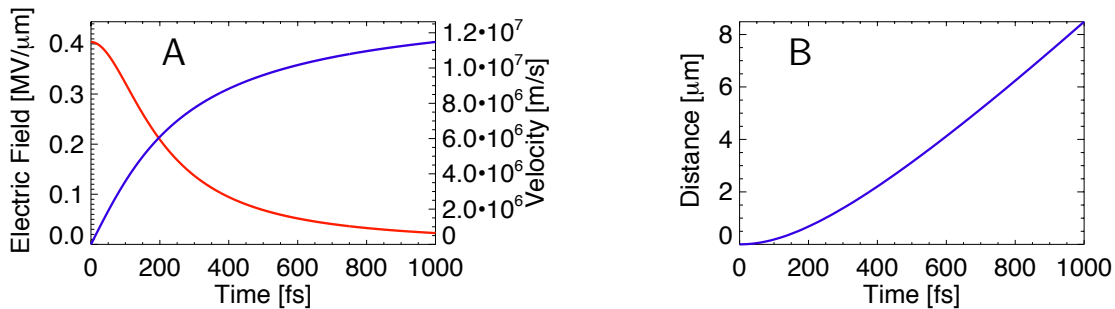


Figure 9.9: **A** - Time decay of the field front (red curve) in comparison to the numerically calculated front velocity (blue curve). **B** - Position of the proton front. For the calculation of both figures Equations 9.19, 9.18) and 9.17) were used in combination with the parameters of Table 9.2.

9.4.2 Numerical Method

The velocity change of a proton in a temporally and spatially changing one-dimensional electric field $E(x, t)$ can be calculated by means of the following simple algorithm:

```

for  $i \in 1, 2, \dots$ 
 $t_i \leftarrow t_{i-1} + dt_i$ 
 $a_i \leftarrow \frac{q_p}{m_p} \cdot E(x_{i-1}, t_{i-1})$ 
 $v_i \leftarrow v_{i-1} + dt_i \cdot a_i$ 
 $x_i \leftarrow x_{i-1} + \left[ dt_i \cdot \left( \frac{v_{i-1} + v_i}{2} \right) \right]$ 
endfor

```

The width dt_i defines the length of each applied time step. In order to account for fast changes of the field, a minimal step size $dt_{\min} = 1 \cdot 10^{-18}$ s is used. Simultaneously the computation time has to be limited. For this purpose a procedure which adaptively controls the temporal step width dt_i depending on the ratio $|(a_i - a_{i-1})/a_{i-1}|$ and a certain accuracy value are introduced. Simulation steps are repeated if necessary. The initial conditions of the particle (t_0, x_0, v_0) are set depending on the initial energy ϵ_0 and the time of the pump pulse t_{pump}

$$t_0 = t_{\text{pump}}, \quad v_0 = \sqrt{\frac{2\epsilon_0}{m_p}}, \quad x_0 = v_0 \cdot t_0.$$

After the simulation time t_{Sim} the algorithm stops. At this time ($t_N = t_{\text{Sim}}$) the particle is located at the position x_N and has the velocity v_N . If the decay of the electric field strength $E(x_N, t_N)$ at the particle position is big enough, further contributions of the field to the energy change of the particle are negligible. Otherwise a longer simulation time has to be chosen. This way the final proton energy $\epsilon_f(\epsilon_0)$

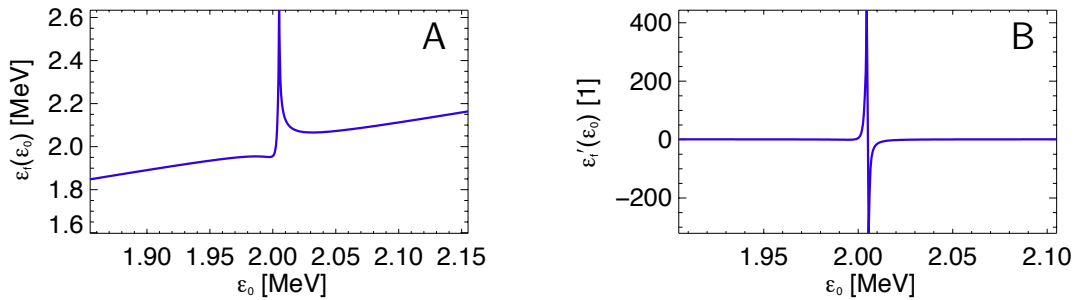


Figure 9.10: **A** - Energy change $\epsilon_f(\epsilon_0)$. **B** - Derivative of the energy change $d\epsilon_f/d\epsilon_0$.

can be calculated for each initial energy value ϵ_0 and is expressed by

$$\epsilon_f(\epsilon_0) = \frac{1}{2}m_p v_N^2(\epsilon_0). \quad (9.20)$$

Using this code the energy change $\epsilon_f(\epsilon_0)$ of protons which propagate through the field of two ion fronts (Section 9.4.1, Figure 9.6) has been calculated (Target distance $a = 8.0$ mm). Figure 9.10 illustrates this energy change $\epsilon_f(\epsilon_0)$ and its derivative $d\epsilon_f/d\epsilon(\epsilon_0)$, which serve as input parameters for calculating the proton redistribution as explicated in Section 9.4.4.

9.4.3 Surface Potential Model

As PIC-simulations show (cf. Figure 6.4), the electric field distribution which is initiated on both sides of a laser irradiated thin foil can exhibit a certain asymmetry of the field amplitude. A proton that propagates along the target normal through the foil is generally subjected to the action of both fields. Under certain circumstances, the field asymmetry allows the action of both fields to be described by a net force that acts in one direction.

A simple approach for describing the action of a ambipolar field on a probing proton is given by the so called surface potential model (SPM) [134]. In this connection, the spatially and temporally dependent electric fields of a laser irradiated thin foil are modeled as the product of a time dependent function and a delta function in space

$$E_1(z, t) = -\mathcal{U}_1 \cdot \mathcal{F}_t(t - t_{\text{pump}}) \cdot \delta(z - a_1), \quad (9.21)$$

$$E_2(z, t) = \mathcal{U}_2 \cdot \mathcal{F}_t(t - t_{\text{pump}}) \cdot \delta(z - a_2). \quad (9.22)$$

Here \mathcal{U}_1 and \mathcal{U}_2 denote positive and constant amplitude factors and a_1 and a_2 are the distances of the rear and front surface of the interaction target in relation to the position of the source target, as illustrated in Figure 9.1. The function \mathcal{F}_t describes the temporal dependence of the field and can be modeled by the expression

$$\mathcal{F}_t(t) = \frac{1}{\sqrt{1 + (\omega_{pi}t)^2}} \Theta(t), \quad (9.23)$$

where $\Theta(t)$ is the Heaviside step function

$$\Theta(t) = \begin{cases} 1, & \text{if } t \geq 0, \\ 0, & \text{if } t < 0 \end{cases} \quad (9.24)$$

and ω_{pi} the ion plasma frequency. Thus the force which acts on a proton when it propagates through the first surface amounts to $F_1(z, t) = q_p \cdot E_1(z, t)$ and is given by $F_2(z, t) = q_p \cdot E_2(z, t)$ for the second surface.

If a proton with the initial energy ϵ_0 starts at the source target ($z = 0, t = 0$) in

z-direction, it will arrive at the first surface of the interaction target ($z = a_1$) at the time $t = t_{a1}(\epsilon_0)$. According to Equation 9.22 the time dependent force $F_1(z, t)$ acts on the particle and its energy is changed to $\epsilon_1(\epsilon_0)$. At the time moment $t = t_{a2}(\epsilon_0)$ it arrives at the second surface of the interaction target ($z = a_2$) and its energy is changed again depending on $F_2(z, t)$. Now the proton has reached its final energy $\epsilon_2(\epsilon_0)$. The energy change at surface 1 can be described by the simple equations

$$\epsilon_1(\epsilon_0) = \epsilon_0 - \mathcal{U}_1 \mathcal{F}_t(t_{a1}(\epsilon_0)), \quad (9.25)$$

$$t_{a1}(\epsilon_0) = \frac{a_1}{\sqrt{2\epsilon_0/m_p}}. \quad (9.26)$$

Correspondingly the final energy change at the second surface is obtained by

$$\epsilon_f(\epsilon_0) = \epsilon_2(\epsilon_0) = \epsilon_1(\epsilon_0) + \mathcal{U}_2 \mathcal{F}_t(t_{a2}(\epsilon_0)). \quad (9.27)$$

The energy change of the proton at the first surface has to be considered in order to calculate the time of arrival $t_{a2}(\epsilon_0)$ at the second surface.

As the PIC-simulation shows, a laser intensity of $\sim 1 \cdot 10^{-19} \text{ W/cm}^2$ leads to an initial Debye length λ_D of approximately $1 \mu\text{m}$ at the target surface. If the spatial extension of the electric field normal to the surface is assumed to be of the order of the Debye length λ_D , the time of flight of a proton for this scale length is given by

$$\tau_D = \frac{\lambda_D}{\sqrt{2\epsilon/m_p}}. \quad (9.28)$$

If the time scale τ_f of the field evolution is much smaller than τ_D the proton is subjected to a temporally changing force inside the field, thus the use of delta function like field distribution, is only valid in the opposite case, when the condition

$$\tau_f \gg \tau_D \quad (9.29)$$

is fulfilled. The time of flight τ_D of a 2 MeV proton for $\lambda_D = 1 \mu\text{m}$ is around 100 fs. If the time of flight of a proton τ_D through a spatially extended field is much larger than the characteristic time scale of the field evolution τ_f Condition 9.29 is not valid any more. In this case, the final energy change of the proton $\epsilon_f(\epsilon_0)$ cannot be derived through the use of Equation 9.27.

9.4.4 Proton Energy Redistribution

If the initial proton density distribution function $f(\epsilon_0)$ and the energy change of a proton in the field $\epsilon_f(\epsilon_0)$ (Equation 9.20) are known, the proton redistribution $\bar{f}(\epsilon_0)$ can be calculated by means of the equation

$$\bar{f}(\epsilon_0) = \int_0^\infty f(\epsilon) \delta(\epsilon_f(\epsilon) - \epsilon_0) d\epsilon. \quad (9.30)$$

Using the relations

$$g(\epsilon, \epsilon_0) := \epsilon_f(\epsilon) - \epsilon_0, \quad (9.31)$$

$$g'(\epsilon) := \frac{dg(\epsilon, \epsilon_0)}{d\epsilon} = \frac{d\epsilon_f(\epsilon)}{d\epsilon} = \epsilon'_f(\epsilon) \quad (9.32)$$

and the generalized scaling property of the Dirac delta function Equation 9.30 can be transformed

$$\bar{f}(\epsilon_0) = \int_0^\infty f(\epsilon) \delta(g(\epsilon, \epsilon_0)) d\epsilon = \sum_{i=0}^{N(\epsilon_0)} \frac{f(\epsilon_{(i)})}{|g'(\epsilon_{(i)})|} = \sum_{i=0}^{N(\epsilon_0)} \frac{f(\tilde{\epsilon}_{f,(i)}(\epsilon_0))}{|g'(\tilde{\epsilon}_{f,(i)}(\epsilon_0))|} \quad (9.33)$$

$$= \sum_{i=0}^{N(\epsilon_0)} f(\tilde{\epsilon}_{f,(i)}(\epsilon_0)) \cdot \left| \frac{d\epsilon_f(\tilde{\epsilon}_{f,(i)}(\epsilon_0))}{d\epsilon} \right|^{-1} = \sum_{i=0}^{N(\epsilon_0)} \bar{f}_{(i)}(\epsilon_0). \quad (9.34)$$

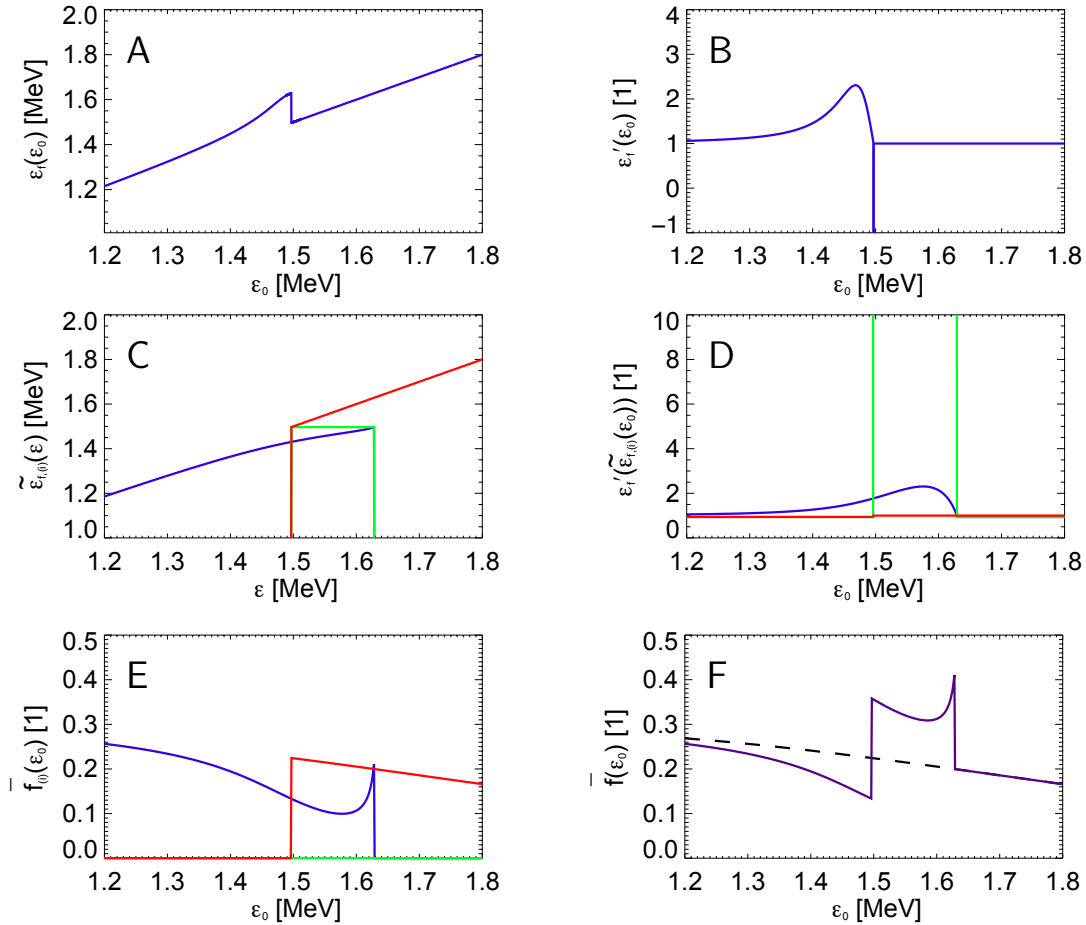


Figure 9.11: Contributing parts of Equation 9.34.

Here the sum extends over all roots $\epsilon_{(i)}$ of $g(\epsilon, \epsilon_0)$ with respect to ϵ , which are assumed to be simple. Since $g(\epsilon, \epsilon_0)$ is also a function of ϵ_0 , the number of existing roots $N(\epsilon_0)$ depends on ϵ_0 . The values of the roots are determined by the inverse functions $\tilde{\epsilon}_{f,(i)}(\epsilon)$ of $\epsilon_f(\epsilon)$ which can be defined for a given ϵ_0 .

Figure 9.11 exemplifies a possible proton redistribution and illustrates several contributing parts of Formula 9.34. The shown energy change $\epsilon_f(\epsilon_0)$ (Figure 9.11.A) and its derivative $d\epsilon_f(\epsilon_0)/d\epsilon_0$ (Figure 9.11.B) are calculated using the SPM (Section 9.4.3) and with a specific set of parameters which are proposed in Table 9.3. The inverse function parts $\tilde{\epsilon}_{f,(i)}(\epsilon)$ are illustrated in Figure 9.11.C using different colors. Figure 9.11.D shows the functions $\epsilon'_f(\tilde{\epsilon}_{f,(i)}(\epsilon_0))$ which are used in Equation 9.34 to calculate the redistribution parts $\bar{f}_{(i)}(\epsilon_0)$ (Figure 9.11.E) which contribute to the final redistribution $\bar{f}(\epsilon_0)$ (Figure 9.11.F). Here, the initial distribution is indicated by the dashed black line.

9.5 Modeling of the Experiments and Discussion

In order to explain the experimental observations several analytical field descriptions and theoretical models are presented and used to reproduce the particular features of the observed proton redistribution effects. In Section 9.4.4 the mathematical procedure is introduced which enables the numerical calculation of the proton energy redistribution $\bar{f}(\epsilon_0)$ depending on: (1) the initial (undisturbed) proton distribution function $f(\epsilon_0)$; (2) the functional dependency that describes the energy change $\epsilon_f(\epsilon_0)$ of a proton in the electric field.

According to the applied physical model that describes the laser-induced field distribution, this energy change $\epsilon_f(\epsilon_0)$ is either calculated analytically or by means of a numerical method, which is presented in Section 9.4.2.

In this connection several simplifying assumptions were made. Firstly, it is assumed that a one-dimensional model is sufficient to describe the redistribution effects and that only the electric field component normal to the target surface has to be considered. Secondly, it is assumed that the protons of the probing beam can be treated as test particles and do not affect the laser-induced fields at the interaction target. This assumption is reasonable since the transverse spatial spreading and the velocity dispersion cause a significant rarefaction of the probing protons by the time they reach the interaction fields.

9.5.1 Redistribution Effects due to Expanding Ion Fronts

In order to approach an understanding of the laser-induced field configuration in the surrounding of a thin foil, a PIC-simulation was conducted by A. Andreev [134]. The results show that during the initial stage of the field evolution the electric field distribution in the proximity of the surface can be approximated by an exponential

decay in space. On this basis a simple analytical model is developed and applied to simulate the redistribution effects in proton beams. The proposed model and the simulation results are presented in detail in Section B.2 of the appendix. The proposed model can reproduce the results of selected measurements, but fails to describe the systematic dependency of the redistribution effect on the target distance a , which was found in Section 9.3.1. For this reason, more accurate descriptions of the field evolution are discussed in the following.

In Section 4.2 model and simulation results are introduced that describe the isothermal and adiabatic expansion of an ion front into vacuum [73, 74]. Based on these results and experimental findings [106] analytical descriptions are developed that approximate the electric field which is created by two proton fronts starting at the interaction target and propagating in opposite directions. Both the isothermal and the adiabatic case are considered. The analytical expressions are presented in detail in Section 9.4.1. The proposed electric field structures do not only explain selected measurements but also describe the systematic dependency of the redistribution effects on the target distance a , which was found in Section 9.3.1.

In order to define the electric field structure of Equation 9.3 precisely, several parameters have to be determined. These are the constant field amplitude \mathcal{E}_c , the characteristic temporal decay constant τ_s and the spatial scale length l_s of the field (Equations 9.10 and 9.9). For the isothermal approximation the determination of the maximum velocity of the proton front $v_{f,\max}$ (Equation 9.12) is also necessary. By introducing the model variable α_v the initial electron density of the interaction target is connected with the critical density n_c (Equation 3.78)

$$n_{e,0} = \alpha_v n_c. \quad (9.35)$$

The ponderomotive potential (Equation 3.51) can be used to estimate the temperature T_e of (hot) electrons [47, 137]

$$T_e \simeq \Phi_p = mc^2 \cdot \left(\sqrt{1 + \frac{I_L \lambda^2}{1.37 \cdot 10^{18}}} - 1 \right) [\text{J}], \quad (9.36)$$

whereby the laser wavelength λ is given in μm and the laser intensity I_L in W/cm^2 . For the relevant intensity range ($I_{\text{pump}} \approx (1 - 5) \cdot 10^{18} \text{ W}/\text{cm}^2$) this description corresponds well to experimental findings, where the electron temperature T_e was measured using similar laser parameters [47, 138, 139].

The knowledge of the initial electron density $n_{e,0}$ and the (hot) electron temperature T_e enables to calculate the initial electric amplitude

$$\mathcal{E}_c = \sqrt{\frac{n_{e,0} k_B T_e}{\epsilon_0}} \quad (9.37)$$

as proposed in Section 4.2.

The characteristic temporal decay of the field τ_s can be defined by the reciprocal

value of the ion (hydrogen) plasma frequency (Equations 4.6 and 4.7)

$$\tau_s := \frac{1}{\omega_{pi}} = \sqrt{\frac{\epsilon_0 m_p}{n_{e,0} e^2}}, \quad (9.38)$$

whereby e denotes the elementary charge.

In order to define the spatial decay of the field front the model variable β_v is introduced. It connects the scale length of the field l_s with the Debye length of the plasma expansion. Either a constant mean scale length

$$l_s = \beta_v \lambda_{D,0} \quad (9.39)$$

is used, whereby the initial Debye length $\lambda_{D,0}$ is defined by Equation 4.12, or the scale length is connected with the time dependent local Debye length of the ion front $\lambda_{D,\text{front}}(t)$ (Equation 4.15) and is given by

$$l_s(t) = \begin{cases} \beta_v \cdot \lambda_{D,0} + \delta_v \cdot \lambda_{D,\text{front}}(t), & \text{if } \beta_v \cdot \lambda_{D,0} + \delta_v \cdot \lambda_{D,\text{front}}(t) < \gamma_v \cdot \lambda_{D,0} \\ \gamma_v \cdot \lambda_{D,0}, & \text{if } \beta_v \cdot \lambda_{D,0} + \delta_v \cdot \lambda_{D,\text{front}}(t) \geq \gamma_v \cdot \lambda_{D,0} \end{cases} \quad (9.40)$$

In this case the scale length $l_s(t)$ increases linearly in time, but is limited by a minimum ($\beta_v \cdot \lambda_{D,0}$) and a maximum value ($\gamma_v \cdot \lambda_{D,0}$).

Isothermal Approximation

The following modeling of the experimental results is based on the isothermal approximation model which is proposed in Section 9.4.1. In the presented case the model variables $\alpha_v = 0.051$ and $\beta_v = 2.2$ are assumed. The laser intensity I_L is set to $1 \cdot 10^{18} \text{ W/cm}^2$ which is in agreement with the experimental value of $I_{\text{pump}} \approx (1 - 5) \cdot 10^{18} \text{ W/cm}^2$. The resulting model parameters are summarized in Table 9.1.

The spatial decay of the field front is approximated by Formula 9.1 in combination with the constant mean scale length l_s of Equation 9.39. The temporal decay of the front and plateau region are described by Equation 9.11 and are illustrated by Figure 9.12.A. The motion of the ion front $z_f(t)$ is determined using Equations 9.12, 4.8 and 4.9, whereby a limiting maximum front velocity $v_{f,\text{max}}$ is applied. The corresponding maximum proton (front) energy $\epsilon_{f,\text{max}} = 1/2 m_i v_{f,\text{max}}$ is set to 0.3 MeV. This value is a rough estimation but is consistent with the results of another series of experiments, where only the interaction target was irradiated using the same laser parameters as in Section 9.3.1. In this case the cut-off proton energy was below the detection limit of the spectrometer ($< 1.0 \text{ MeV}$). The time dependent velocity of the proton front is shown in Figure 9.12.B.

The proposed parameters and functional dependencies allow for the exact determination of Equation 9.3 which represents the electric field $E(z, t)$ of two ion fronts

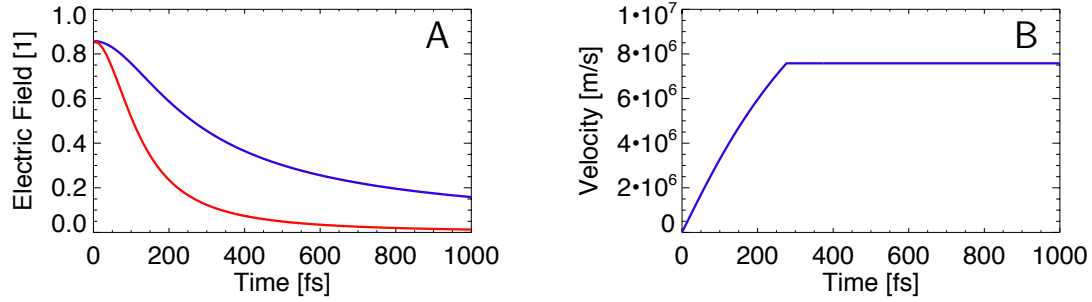


Figure 9.12: **A** - Temporal decay of the electric field (Equation 9.11). Blue curve - Field front. Red curve - Plateau region. **B** - Velocity of the proton front (Equation 4.8) in combination with a limiting maximum front velocity $v_{f,\max}$. For both figures the parameters of Table 9.1 were used.

that propagate in opposite directions. The resulting spatial field distribution is shown in Figure 9.13.B at different moments in time.

Using the numerical algorithm of Section 9.4.2 the energy change $\epsilon_f(\epsilon_0)$ of protons which propagate through this temporally and spatially changing field was calculated (Figure 9.10). The knowledge of these functions and the explicit form of the initial (undisturbed) proton density distribution can be used to calculate the redistribution of the initial proton spectrum by means of Formula 9.34.

Figure 9.13 shows the calculated model curve (yellow curve) in comparison to the experimental result (blue curve) of Section 9.3.1. The dashed black curve is a fit of the unaffected and thus not redistributed parts of the experimental spectrum. A background correction of this curve can be used to estimate the contribution of the pure and unaffected proton signal to the total ion distribution. This estimation serves as the initial energy distribution $f(\epsilon_0)$ for the model calculation.

The model (yellow curve) shows qualitatively the observed effects - a dip with adjacent maxima. However, the real shape is far from being reproduced indicating additional effects. In order to account for the energy resolution of the spectrometer and the energy dispersion of protons due to scattering within the interaction target, the model curve was smoothed (red curve) using a Gaussian filter ($\Delta\epsilon_{2\sigma} = 42.5$ keV). A comparison with the measurement (blue curve) shows that the presented model calculations can qualitatively and quantitatively explain the observed redistribution effect.

In the proposed case the model variables α_v and β_v were varied to determine a good match between the model and the experiment. In this connection not only the experimental result of Figure 9.13 was taken into account, but the other experiments of Section 9.3.1 as well.

Figure 9.14 shows a selection of four measurements which were obtained with different settings of the target distances a and t-pump energies ϵ_{pump} . In all cases the same model parameters (Table 9.1) were used.

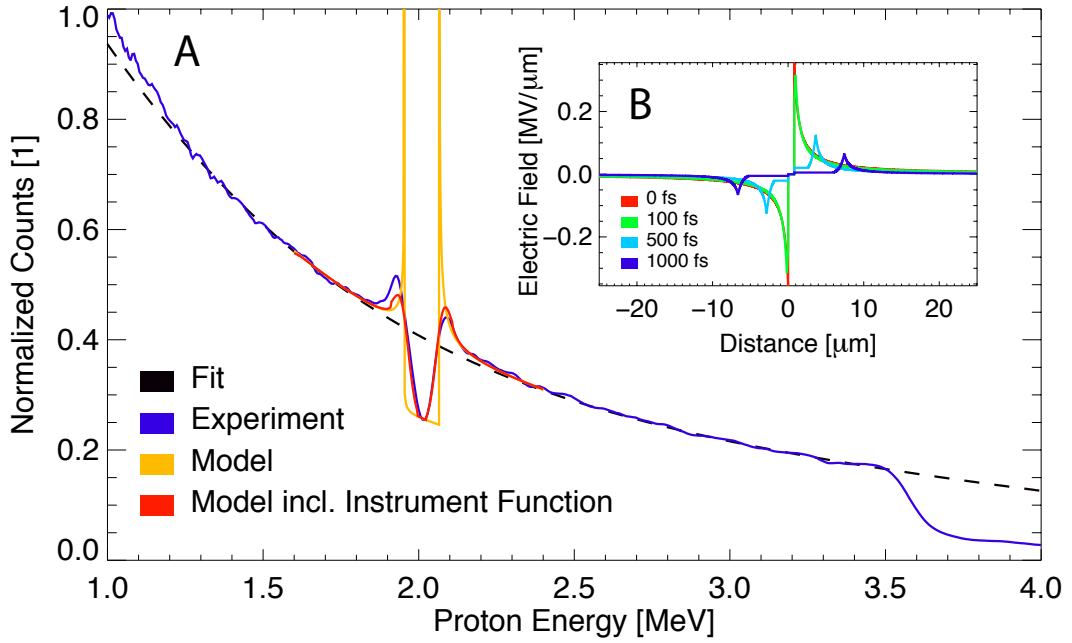


Figure 9.13: **A** - Simulated and experimentally obtained proton redistribution effects. **B** - Spatial electric field distribution of two ion fronts which propagate in opposite directions (Equation 9.3). For both figures the parameters of Table 9.1 were used.

The proposed simulation parameters and the resulting electric field structure (Equation 9.3) can not only reproduce the selected measurements, but also describe the systematic dependency of the redistribution effect on the target distance a , which is presented in Section 9.3.1. Both in experiment and simulation, the ratio between the low and high energy peak changes with the setting of the target distance a . It should be stressed that the selected set of parameters and the resulting field distribution are not the only way to reproduce the experimental results. In principle ambiguous field distributions can lead to similar redistribution effects. A good match between the experimental results and the simulations is possible especially when the parameters \mathcal{E}_c , τ_s , l_s and $\epsilon_{f,\max}$ are treated as free variables and chosen independently.

In any case, the position of the moving ion front is determined by Equation 9.12. It depends on $\epsilon_{f,\max}$, but is also connected to the setting of I_L and α_v via several equations (cf. Sections 4.2 and 9.4.1).

However, due to the spatial dependency of Equation 9.1 which is characterized by a slow decay, the electric field has a relatively long range. Therefore, the influence of the front expansion on the simulated proton redistribution is small for low expansion velocities $\epsilon_{f,\max} \lesssim 1.5$ MeV.

The change of a parameter that determines the position of the proton front (I_L , α_v , $\epsilon_{f,\max}$) can be compensated by changing \mathcal{E}_c , τ_s and l_s . The experimental results

of Figure 9.14 can be reproduced even if $v_{f,\max} = 0$ m/s is used in simulation. This indicates that the longitudinal probing geometry is not ideal to obtain information concerning the front expansion. On the other hand it affirms that the relatively long extension is a characteristic property of the field, which is necessary for explaining the observed proton redistribution effect.

The drawback of the isothermal approximation model is that the velocity of the ion front diverges for $t \rightarrow \infty$ and has to be limited by the additional variable $v_{f,\max}$. Firstly, this variable is not directly connected with the laser intensity I_L and the choice of the model variable α_v , but has to be estimated. Thus, an additional degree of freedom is added to the modeling. Secondly, the form of the electric field evolution itself is artificial, which is reflected by Figure 9.12.B showing the evolution of the proton front velocity. For this reason, an adiabatic model is proposed to approximate the fields of the expanding proton front.

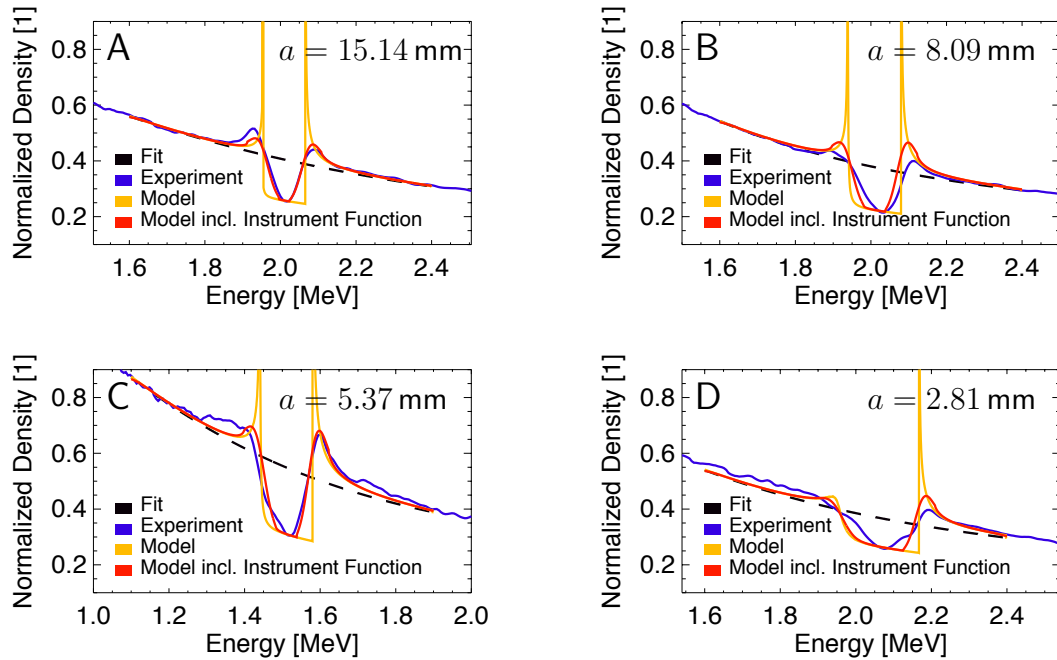


Figure 9.14: Simulated and experimentally obtained proton redistribution effects for different settings of the target distance a and the proton t-pump energy ϵ_{pump} . **A** - $a = 15.1$ mm, $\epsilon_{\text{pump}} = 2.0$ MeV. **B** - $a = 8.09$ mm, $\epsilon_{\text{pump}} = 2.0$ MeV. **C** - $a = 5.37$ mm, $\epsilon_{\text{pump}} = 1.5$ MeV. **D** - $a = 2.81$ mm, $\epsilon_{\text{pump}} = 2.0$ MeV. In all cases the same parameters were used as shown by Table 9.1 were used.

Adiabatic Approximation

In this section the adiabatic approximation model of Section 9.4.1 is applied to model the experimental results. In this connection the model variable α_v is set to 0.08 and the laser intensity I_L to $8 \cdot 10^{17} \text{ W/cm}^2$ which is slightly smaller than the experimental value $I_{\text{pump}} \approx (1 - 5) \cdot 10^{18} \text{ W/cm}^2$. The parameters β_v , δ_v and γ_v as well as the coefficients $a_{f,\text{cl}}$, $a_{f,\text{ur}}$, $a_{p,\text{cl}}$ and $a_{p,\text{ur}}$ are not varied, but set to the exact values which were determined in Section 9.4.1. The resulting model parameters are summarized in Table 9.2.

The temporal decay of the front ($\mathcal{T}_{\text{front}}$) and plateau ($\mathcal{T}_{\text{plateau}}$) region are described by Equations 9.17 and 9.18 and are illustrated by Figure 9.7. The advantage of the adiabatic approximation is that the integral $\int \mathcal{T}_{\text{front}} dt$ converges for $t \rightarrow \infty$. Therefore, the maximum front velocity $v_{f,\text{max}}$ and accordingly the maximum proton energy $\epsilon_{f,\text{max}} = 1/2 m_i v_{f,\text{max}}$ can be calculated numerically. Also the position of the

Model Variables		
I_L	$1 \cdot 10^{18}$	W/cm^2
α_v	0.051	1
β_v	2.2	1
Simulation Parameters		
δ_v	—	1
γ_v	—	1
\mathcal{E}_c	$4.17 \cdot 10^{11}$	V/m
τ_s	80.1	fs
l_s	0.57	μm
$\epsilon_{f,\text{max}}$	0.3	MeV
T_e	108	keV
$\lambda_{D,0}$	0.26	μm
c_s	$3.22 \cdot 10^6$	m/s
Φ_p	108	keV
$n_{e,0}$	$8.88 \cdot 10^{19}$	$1/\text{cm}^3$
n_c	$1.74 \cdot 10^{21}$	$1/\text{cm}^3$
ω_{pi}	$1.24 \cdot 10^{13}$	1/s
Δa	800	nm
$a_{f,\text{cl}}, a_{f,\text{ur}}$	—	1
$a_{p,\text{cl}}, a_{p,\text{ur}}$	—	1
Parameter	Value	Unit

Table 9.1: Model variables and simulation parameters for the isothermal approximation model.

Model Variables		
I_L	$8 \cdot 10^{17}$	W/cm^2
α_v	0.08	1
Simulation Parameters		
β_v	1.9	1
δ_v	0.5	1
γ_v	20	1
\mathcal{E}_c	$3.20 \cdot 10^{11}$	V/m
τ_s	64.34	fs
$l_s(t)$	0.35-3.73	μm
$\epsilon_{f,\text{max}}$	1.13	MeV
T_e	88	keV
$\lambda_{D,0}$	0.338	μm
c_s	$2.9 \cdot 10^6$	m/s
Φ_p	88	keV
$n_{e,0}$	$1.39 \cdot 10^{20}$	$1/\text{cm}^3$
n_c	$1.74 \cdot 10^{21}$	$1/\text{cm}^3$
ω_{pi}	$1.55 \cdot 10^{13}$	1/s
Δa	800	nm
$a_{f,\text{cl}}, a_{f,\text{ur}}$	5	1
$a_{p,\text{cl}}, a_{p,\text{ur}}$	8	1
Parameter	Value	Unit

Table 9.2: Model variables and simulation parameters for the adiabatic approximation model.

proton front $z_f(t)$ does not depend on an estimation of $v_{f,\max}$, as in the isothermal case. It is only connected with the laser intensity I_L and the choice of the model variable α_v and can be calculated by means of Equation 9.19. Figure 9.9.A shows the time decay of the field front (Equation 9.19) in comparison to the numerically calculated front velocity. In the presented case a maximum proton (front) energy $\epsilon_{f,\max}$ of 1.13 MeV is reached.

The spatial decay of the field front is approximated by Formula 9.1 in combination with the time dependent scale length $l_s(t)$ (Equation 9.40). The scale length $l_s(t)$ increases linearly in time, but is limited by a minimal ($\beta_v \cdot \lambda_{D,0}$) and a maximum value ($\gamma_v \cdot \lambda_{D,0}$), as illustrated in Figure 9.15.A. The introduction of the limiting maximum value is in agreement with the adiabatic expansion model [74], where the Debye length at the ion front is not increasing indefinitely with time, but saturates to a certain value.

The proposed parameters and functional dependencies allow for the determination of Equation 9.3 which represents the electric field $E(z, t)$ of two ion fronts that propagate in opposite directions. The resulting spatial field distribution is shown in Figure 9.15.B at different moments in time.

Figure 9.16 shows a selection of four measurements which were obtained with different settings of the target distances a and t-pump energies ϵ_{pump} . The shown simulated proton redistributions are evaluated in the same manner as in the isothermal case. For all simulations the same model parameters (Table 9.2) were used.

The adiabatic approximation model can explain the systematic dependency of the redistribution effect on the target distance a , which was found in Section 9.3.1. The agreement between the simulated redistribution effects and the experimental results is even better when compared to the isothermal approximation model.

The applied simulation parameters do not differ significantly from the isothermal case and are all in the same order of magnitude. However, it is necessary to be cautious concerning the accuracy of the indirectly determined plasma parameters. The proposed adiabatic approximation is not a self consistent model, but relies on

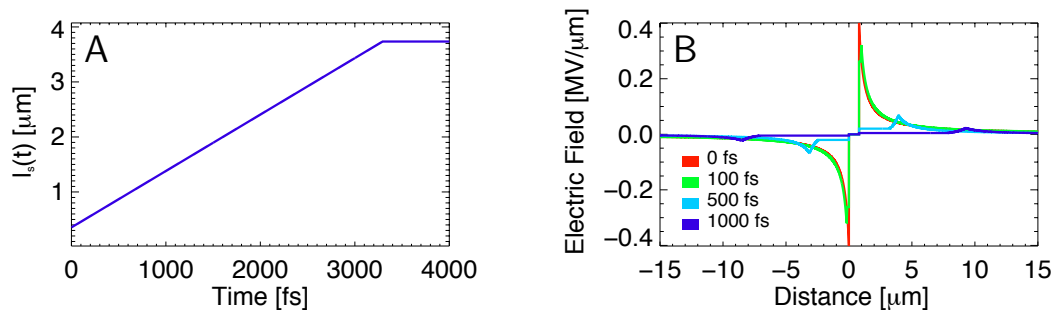


Figure 9.15: **A** - Temporal evolution of the scale length $l_s(t)$ (Equation 9.40). **B** - Spatial electric field distribution of two ion fronts which propagate in opposite directions (Equation 9.3). For both figures the parameters of Table 9.2 were used.

the determination of the coefficients $a_{f,cl}$, $a_{f,ur}$, $a_{p,cl}$ and $a_{p,ur}$ as well as β_v , δ_v and γ_v , as described in Section 9.4.1. In principle these parameters can depend on the hot electron temperature T_e , the initial electron density $n_{e,0}$ or the target thickness Δa which is not considered here. A comparison to other analytical models [140] and simulations [74] could possibly provide a more accurate determination of the characteristic plasma parameters.

Nevertheless, the proposed approximation reflects the principle functional dependence of the temporal and spatial field evolution of an expanding proton front, as shown in Section 9.4.1 (Figure 9.8). Therefore, the model allows for an interpretation of the characteristic properties of the redistribution effects and can be applied to explain the systematic decrease of the low energy peak with lower target distances a .

When protons propagate through the ambipolar field of the expanding proton fronts their energy is changed depending on the time when the field is initiated (t_{pump}) and their relative position in the field. This position depends on their initial energy ϵ_0 and the target distance a . The field is initiated at the time t_{pump} which corresponds to the moment in time when a probing proton with the initial energy $\epsilon_0 = \epsilon_{pump} = 2.0$ MeV reaches the interaction plane at the distance a . The char-

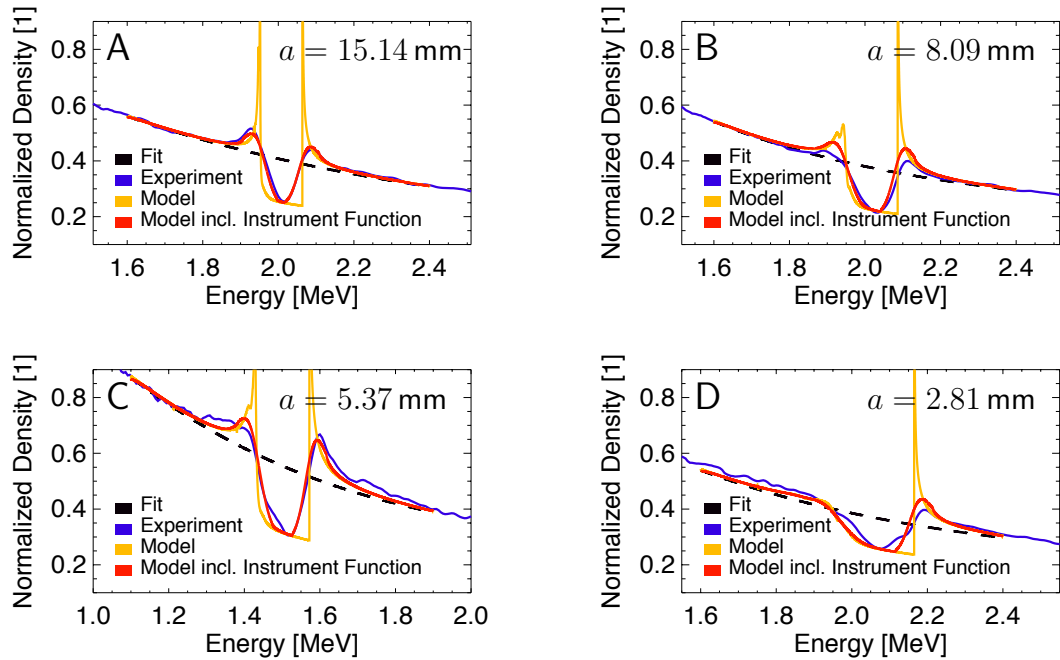


Figure 9.16: Simulated and experimentally obtained proton redistribution effects for different settings of the target distance a and the proton t_{pump} energy ϵ_{pump} . **A** - $a = 15.1$ mm, $\epsilon_{pump} = 2.0$ MeV. **B** - $a = 8.09$ mm, $\epsilon_{pump} = 2.0$ MeV. **C** - $a = 5.37$ mm, $\epsilon_{pump} = 1.5$ MeV. **D** - $a = 2.81$ mm, $\epsilon_{pump} = 2.0$ MeV. In all cases the same parameters as shown in Table 9.2 were used.

acteristic time of the field evolution is given by the reciprocal value of the plasma frequency ($\tau_s = 1/\omega_{pi}$) and is of the order of 100 fs. Within this time a 2 MeV proton propagates along a distance of approximately 2 micrometers, which is small compared to the effective extension of the field $l_{\text{eff}} \approx 300 \mu\text{m}$ (Section 9.3.1).

The spatial decay of the field is described in Equation 9.1. The slope of this function is maximum at $z = 0$ and decreases with distance. A significant spatial change of the field appears only at close distances to the foil surface. Using the parameters of Table 9.2, the relative change of the field between $z = 0$ and $z = 2 \mu\text{m}$ is approximately 85% at $t = t_{\text{pump}}$.

In comparison, the change between $z = l_{\text{eff}}$ and $z = l_{\text{eff}} + 2 \mu\text{m}$ drops down to 0.6%. Therefore, the change of the proton position during the fast evolving acceleration process can be neglected for most of the protons. The energy change of a proton is dominated by the temporal evolution of the field at a fixed position.

For this reason, the following simplified view on the redistribution process is reasonable: all particles with initial energies $\epsilon_0 > \epsilon_{\text{pump}}$ have already passed through the interaction target ($z_p > a$) and are accelerated further when the field is initiated. In contrast, particles with energies $\epsilon_0 < \epsilon_{\text{pump}}$ have an initial position $z_p < a$ and are decelerated. A possible re-acceleration of these particles after passing through the foil ($z_p > a$) can be neglected for the most part of protons.

The black curves in Figures 9.17.A and 9.17.B show the energy change of protons due to the field action for the target distances $a = 15.14 \text{ mm}$ and $a = 2.81 \text{ mm}$, respectively. The blue dashed lines are identity functions and represent the case in which the probing proton energies are not changed. The red dashed lines mark the position of the proton t-pump energy ϵ_{pump} for comparison. The applied simulation parameters correspond exactly to the cases of Figure 9.16.A and 9.16.D (Table 9.2). As shown the fraction of proton energies which are initially below the proton t-pump energy ($\epsilon_0 < \epsilon_{\text{pump}}$) but experience a net acceleration by the field is very small in comparison to the overall affected energy range. This is also valid in the case of lower dispersion (9.17.B), even though the absolute number of decelerated and then re-accelerated particles increases.

The resulting proton redistribution effects are illustrated by Figures 9.17.C and 9.17.D, where the same constant initial energy distribution (black line) is used.

In both cases a local maximum appears at the low and high energy sides of the gap. However, in Figure 9.17.C (longer target distance) the peak on the low energy side is much more pronounced.

This can be explained by the shape of the corresponding function $\epsilon(\epsilon_0)$ in Figure 9.17.A. Around the initial energy $\epsilon_0 \simeq 1.98 \text{ MeV}$ the slope of this function is almost zero. Therefore, protons of a certain initial energy range ($\epsilon_0 \in M_\epsilon$) are mapped to the same final energy $\epsilon \simeq 1.94 \text{ MeV}$, which is the position of the low energy peak.

In comparison, the slope in Figure 9.17.B is higher for initial energies $\epsilon_0 < 2.0 \text{ MeV}$ and the peak on the low energy side is less pronounced. Due to the higher dispersion in case A (C) the protons of the interval M_ϵ are distributed over a relative

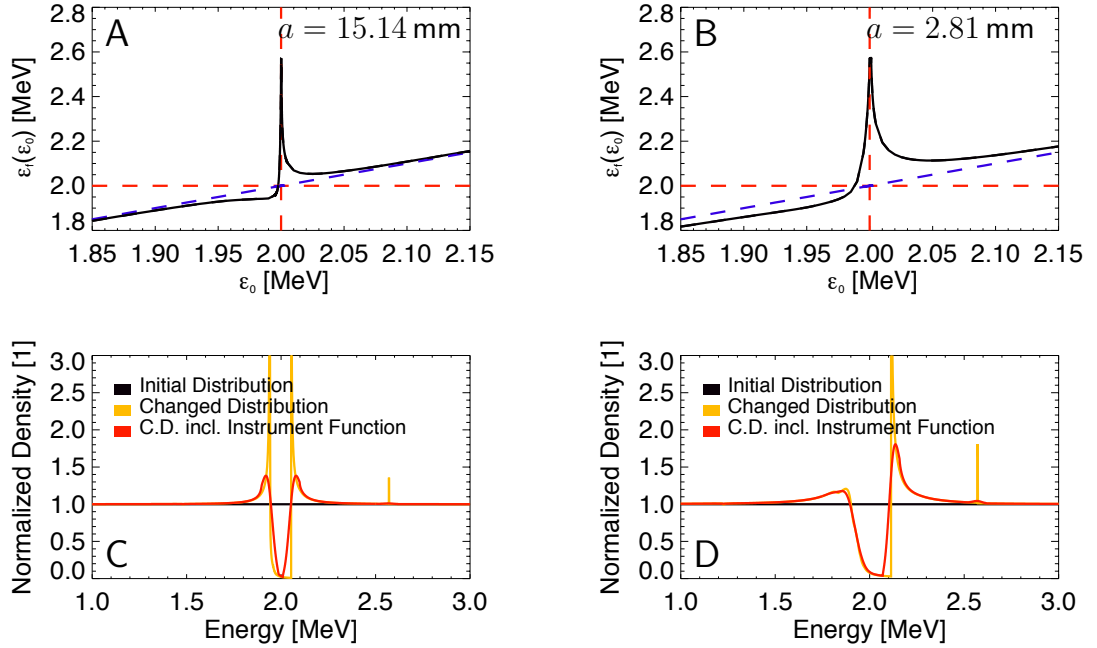


Figure 9.17: Energy change $\epsilon(\epsilon_0)$ of protons (upper figures) due to the action of the ambipolar field of expanding proton fronts (Equations 9.3, 9.17 and 9.18) and resulting redistribution effects for a constant initial particle distribution (lower figures). **A, C** - Target distance $a = 15.14$ mm. **B, D** - Target distance $a = 2.81$ mm. The applied simulation parameters correspond to the cases of Figure 9.16.A and 9.16.D (Table 9.2).

long extension along the z -axis at the time t_{pump} . Therefore, these particles are affected by very different parts of the spatially dependent field. Faster particles are decelerated more strongly than the slower ones and can reach the same final energy.

In case B (D) this is not possible. Due to the lower dispersion the particles of the same energy range ($\epsilon_0 \in M_\epsilon$) are much closer to each other. Therefore, a relatively similar field amplitude acts on each of these particles. This leads to a quasi-constant shift of the initially different particle energies, but not to a mapping to the same final energy.

Naturally, this effect is favored in the case of lower field gradients, i.e. for higher values of the spatial scale length l_s . The limit $l_s \rightarrow \infty$ leads to a quasi-constant field in space and suppresses the creation of local peaks in the energy spectrum. In principle, the local maxima on the high energy side of the gap, which appears in both cases can be explained in a similar way.

In conclusion, all results discussed in this section show that specific energy redistribution effects can be explained with adapted field descriptions of accepted models. The longitudinal probing configuration in combination with model calculations can be used to infer characteristic properties of laser-induced acceleration fields. This

is possible even if the temporal resolution of the spectrometer is poorer than the characteristic time scale of the investigated process.

9.5.2 Special Redistribution Effects

The most prominent difference between the redistributed proton spectra of Section 9.3.1 and the spectra of Section 9.3.2 is the appearance of two peaks at the high energy side of the gap. The adiabatic approximation model (Section 9.4.1) which was successfully applied in the previous section fails to describe this specific feature in a consistent way. In order to approach an understanding of the phenomenon two models are investigated: the so called surface potential model (SPM) and the isothermal approximation model.

Surface Potential Model

The surface potential model is presented in detail in Section 9.4.3 and offers a qualitative explanation for the generation of the phenomenon. As PIC-simulations show (cf. Figure 6.4), the electric field distribution which is initiated on both sides of a laser irradiated thin foil can exhibit a certain asymmetry of the field amplitude. This motivated the development of the surface potential model (SPM) [134], which describes the action of both fields by a net force that acts in one direction.

As described in Section 9.4.3 a specific set of parameters has to be defined to calculate the energy change of a proton which propagates through the surface potentials of the interaction target (Equation 9.27). These are the amplitude values of the surface potentials $\mathcal{U}_{0,1}$ and $\mathcal{U}_{0,2}$ and the value of the ion plasma frequency ω_{pi} which determines the characteristic decay time of the potential field (Equation 9.23). In the most simple case the amplitude $\mathcal{U}_{0,1}$ is set to zero and only the accelerating effect of $\mathcal{U}_{0,2}$ is taken into account.

In the presented case $\mathcal{U}_{0,1} = 0$ MeV and $\mathcal{U}_{0,2}$ is approximated by the ponderomotive potential Φ_p which is connected with the laser intensity via Equation 3.51.

To allow for a direct comparison with the previous model parameters the model variable α_v is used again. The variable is connected with the hot electron density $n_{e,0}$ via Equation 9.35 and thus determines the ion plasma frequency ω_{pi} as well as the characteristic time decay τ_s by means of Equation 9.38.

In order to reproduce the measurement of Section 9.3.2 (red curve, Figure 9.5) a laser intensity I_L of $1.4 \cdot 10^{18}$ W/cm² was assumed for the model calculation, which corresponds to the ponderomotive potential $\Phi_p = 126$ keV.

The model variable α was set to 10^{-5} . The resulting electron density $n_{e,0} = 1.74 \cdot 10^{16}$ cm⁻³ is connected with the plasma frequency (hydrogen) $\omega_{pi} = 1.74 \cdot 10^{11}$ 1/s and the characteristic decay time $\tau_s = 5.75$ ps.

All other resulting simulation parameters which are relevant for the presented model calculations are summarized in Table 9.3.

An almost identical model result is obtained if the laser intensity I_L is set to

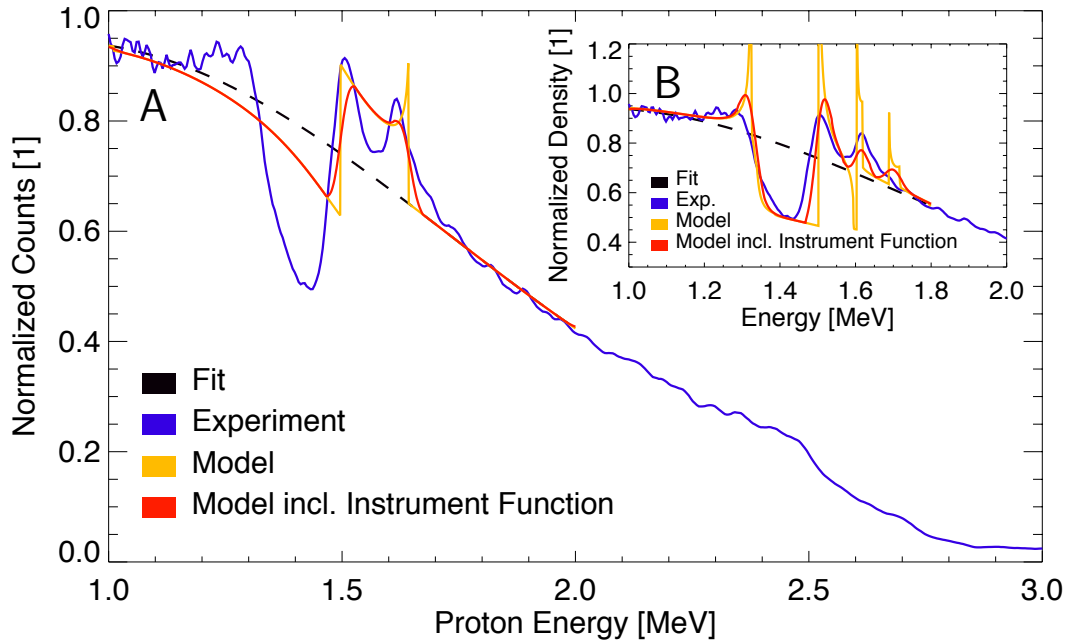


Figure 9.18: Simulated and experimentally obtained proton redistribution effects. The calculated model curves are shown in comparison to the experimental result of Section 9.3.2, Figure 9.5.A. **A** - Surface potential model (Section 9.4.3), Parameter Table 9.3. **B** - Isothermal approximation (Section 9.4.1), Parameter Table 9.4.

$5 \cdot 10^{18} \text{W/cm}^2$ and the amplitude values $\mathcal{U}_{0,2} = \Phi_p$ and $\mathcal{U}_{0,1} = 0.7 \cdot \Phi_p$ are used, with $\Phi_p = 422 \text{keV}$.

The explicit form of the initial (undisturbed) proton energy distribution and the proposed parameters can be used to calculate the redistribution of the proton spectrum by means of Formula 9.34.

Figure 9.18.A shows the calculated model curve (yellow curve) in comparison to the experimental result (blue curve) of Section 9.3.2. The dashed black curve is a fit of the unaffected and thus not redistributed parts of the experimental spectrum. A background correction of this curve is used to estimate the contribution of the pure and unaffected proton signal. This estimation serves as the initial energy distribution $f(\epsilon_0)$ for the model calculation. As previously discussed, the measurement resolution has to be taken into account. For this reason, the model curve was smoothed using a Gaussian filter ($\Delta\epsilon_{2\sigma} = 30 \text{keV}$). The result is illustrated by the red curve.

According to the applied theoretical model, the creation of this double peak structure can be understood as follows: In accordance with the definition of the surface potential model and the given set of parameters the electric field is strongly localized and exerts a net force on the proton beam which acts in propagation direction. The temporal evolution of the field (Equation 9.23) is characterized by a sharp in-

crease and a slow decay as shown in Figure 9.19. The time decay at which this function drops to $1/e$ of its initial value is denoted by τ_f . In the presented case the choice of $\alpha = 10^{-5}$ leads to $\tau_f \approx 15$ ps.

Due to the sharp increase of the electric field in space and time all particles which arrive at a time before t_{pump} at the interaction target ($\epsilon_0 > \epsilon_{\text{pump}}$) are not affected. Therefore, the corresponding part of the initial energy distribution is not changed (Figure 9.11.E, red curve).

All protons which arrive at a time after the interaction ($\epsilon_0 < \epsilon_{\text{pump}}$) are accelerated (Figure 9.11.E, blue curve) depending on the temporal evolution of the field. The protons which arrive shortly after the interaction ($\epsilon_0 \lesssim \epsilon_{\text{pump}}$) are accelerated most effectively to energies $\epsilon > \epsilon_{\text{pump}}$ and therefore contribute to the unchanged high energy part of the initial spectrum.

For the creation of the high energy peak the time dependence of the field evolution and its temporal derivative play the key role. As shown in Figure 9.19 the derivative of the electric field is zero when the interaction starts ($t = 0$). Initially the absolute values of the derivative are small. They increase in time until a local maximum is reached and decrease afterwards. This functional dependence is translated to the functional behavior of $d\epsilon_f(\epsilon_0)/d\epsilon_0$ as shown in Figure 9.11.B. Since Formula 9.34 is dependent on $\epsilon'_f(\tilde{\epsilon}_{f,(i)}(\epsilon_0))$ this signature is found in one of the redistribution parts $\tilde{f}_{(i)}(\epsilon_0)$ and manifests itself in the form of the second high energy peak (Figure 9.11.D and 9.11.E).

Obviously the model calculation and the measurement do not match very well. Nevertheless, the model reproduces the appearance of two peaks at the high energy side of the gap.

In order to obtain a better agreement between model and experimental various functions were used to describe the temporal field evolution (Equation 9.23), however a substantial improvement was not achieved. For instance, similar results are obtained with a Gaussian shaped function. In contrast, a strictly exponential decay does not create a second peak. In any case, the double peak structure can only be reproduced for decay times $\tau_f \gtrsim 1$ ps. For smaller times, the amount of

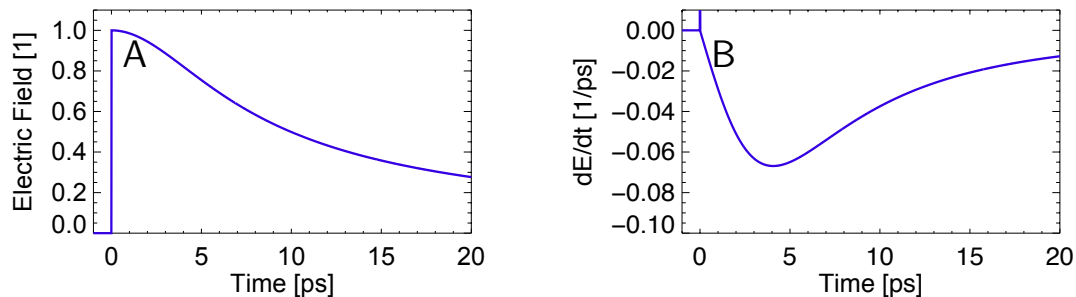


Figure 9.19: **A** - Time dependence of the electric field. **B** - Temporal derivative of of the electric field.

re-accelerated particles is simply too small to approximate the observed structure quantitatively.

The applied high temporal decay time of the field ($\tau_s = 5.75$ ps) and the re-acceleration process is in fundamental contradiction to the results of the last section. In this case a characteristic decay time of the order of 100 fs was found, using the description of expanding ion fronts (Section 9.4.1).

The double peak structure is only generated by the model if $\mathcal{U}_{0,2} > \mathcal{U}_{0,1}$ is assumed, which leads to a resulting force pointing in propagation direction. This is a major drawback of the proposed model, because it is not clear how the electric field can be directed in propagation direction over a time scale of several picoseconds. It can be expected that a charge up of the whole foil would result in symmetrical field distribution near the front and rear surfaces of the target. This situation would not lead to a net force in one direction.

Also the sharp spatial increase of the field (δ -function) contradicts the experimental results of Section 9.3.1, where the characteristic extension $l_{\text{eff}} \approx 300 \mu\text{m}$ was estimated. However, if an exponential decay of the field with a decay length l_s of several micrometers and a time decay $\tau_s \approx 5$ ps is used in simulation, the double peak structure can still be generated. In any case a better agreement between simulation and experiment could not be achieved.

Isothermal Approximation

In order to find an explanation for the two high energy peaks which is in agreement with the results of the previous sections, the isothermal approximation model (Section 9.4.1) was investigated. As a result it was found that the model is capable of creating a second high energy peak if the maximum energy of the proton front $\epsilon_{f,\text{max}}$ exceeds the proton t-pump energy ϵ_{pump} , i.e. $\epsilon_{f,\text{max}} > \epsilon_{\text{pump}}$.

In this case a certain part of the probing proton beam propagates with the same velocity as the field front of the interaction target. This elongates the effective interaction time between these protons and the expanding field front and leads to additional modulations in the redistributed proton energy spectrum close to $\epsilon_{f,\text{max}}$. The spatial decay of the field front is approximated by Formula 9.1 in combination with the time dependent scale length $l_s(t)$ (Equation 9.40). The time decay of the front and plateau region are described by Equation 9.11 and the position of the ion front $z_f(t)$ is determined using Equations 9.12, 4.8 and 4.9, whereby the limiting maximum front velocity $v_{f,\text{max}}$ corresponds to the kinetic energy $\epsilon_{f,\text{max}}$ of a proton. For the reproduction of the experimental result of Section 9.3.2 (red curve, Figure 9.5) several model parameters were adjusted and are listed in Table 9.4 in the category *model variables*. In order to adapt the position of the gap the proton t-pump energy $\epsilon_{\text{pump}} = 1.5$ MeV was decreased by 100 keV for the model calculation. This discrepancy is probably connected with the aforementioned problem with the stepper motor control, which is responsible for the optical delay between pump and probe pulse.

Experimental Parameters		
I_{pump}	$(1 - 5) \cdot 10^{18}$	W/cm ²
d	0.0	μm
a	7.3	mm
Δa	800	nm
ϵ_{pump}	1.50	MeV
t_{pump}	430	ps
Model Variables		
I_L	$1.4 \cdot 10^{18}$	W/cm ²
α	0.00001	1
$\mathcal{U}_{0,1}$	0	J
$\mathcal{U}_{0,2}$	Φ_p	J
Model Parameters		
τ_s	5755	fs
τ_f (1/e)	14539	fs
Φ_p	146	keV
$n_{e,0}$	$1.74 \cdot 10^{16}$	1/cm ³
ω_{pi}	$1.74 \cdot 10^{11}$	1/s
$ \mathcal{U}_{0,1}/\mathcal{U}_{0,2} $	0.0, (0.7)	1
Parameter	Value	Unit

Table 9.3: Experimental and model parameters used for the calculation of the analytical model curves of Figure 9.18.A.

Model Variables		
I_L	$1 \cdot 10^{18}$	W/cm ²
ϵ_{pump}	1.40	MeV
α_v	0.1	1
$\epsilon_{f,\text{max}}$	1.6	MeV
β_v	0.25	1
γ_v	3	1
Simulation Parameters		
δ_v	0.5	1
\mathcal{E}_c	$5.83 \cdot 10^{11}$	V/m
τ_s	57.55	fs
$l_s(t)$	0.046-0.555	μm
T_e	108	keV
$\lambda_{D,0}$	0.19	μm
c_s	$3.22 \cdot 10^6$	m/s
Φ_p	108	keV
$n_{e,0}$	$1.74 \cdot 10^{20}$	1/cm ³
n_c	$1.74 \cdot 10^{21}$	1/cm ³
ω_{pi}	$1.74 \cdot 10^{13}$	1/s
Δa	800	nm
Parameter	Value	Unit

Table 9.4: Model variables and simulation parameters for the calculation of Figure 9.18.B using the isothermal approximation model.

Figure 9.18.B shows the model result in comparison with the same measurement approximated previously by means of the SPM. The yellow curve shows several peaks on the high energy side of the gap. These peaks are also visible and distinguishable in the smoothed spectrum (red curve), which accounts for the energy resolution of the spectrometer. The model can approximate the experimentally obtained curve (blue line) to a certain extent and provides a better fit than the SPM-result.

It can be shown that various combinations of the proposed model variables and thus ambiguous field configurations can lead to similar redistribution effects. However, a reasonable reproduction of the second high energy peak is only possible if the maximum energy of the proton front $\epsilon_{f,\text{max}}$ is set to a value close to the corresponding energy of this peak ($\epsilon_{f,\text{max}} \approx 1.6$ MeV).

Even if the isothermal approximation model allows for a relatively good match between the experimental and the model spectrum, several points put the applica-

bility of the model into question:

- As explicated in Section 9.3.1 the generation of the two high energy peaks is possible for different settings of ϵ_{pump} . In addition, it was shown that the whole redistribution structure (including the second high energy peak) changes its relative position in the spectrum, according to the setting of ϵ_{pump} or t_{pump} . If only the timing of the pump pulse is changed and not the laser parameters itself, the position of the second high energy peak in the spectrum should not be identical to the value of the maximum front energy $\epsilon_{f,\text{max}}$. This contradicts the model results, where the position of the peak does not change in agreement with ϵ_{pump} , but corresponds with the setting of $\epsilon_{f,\text{max}}$.
- In simulation, the second high energy peak is generated because a specific part of the probing proton beam propagates with the same velocity as the field front which is initiated at the position a of the interaction target. This elongates the effective interaction time between these protons and the expanding field front and leads to additional modulations in the redistributed proton energy spectrum close to $\epsilon_{f,\text{max}}$. However, this effect is restricted to the isothermal approximation and is not generated if the adiabatic approximation model is used. The artificial form of Equation 9.12, which describes the motion of the ion front, is responsible for its creation. As illustrated by Figure 9.12.B, the ion front velocity increases in time until the maximum front velocity $v_{f,\text{max}}$ is reached at the time $t_{f,\text{max}}$. From now on, the front acceleration is zero and the front propagates with $v_{f,\text{max}}$. This leads to the artificial situation that the final front energy $\epsilon_{f,\text{max}}$ is reached, at a time where the field strength of the front (Figure 9.12.A) is still relatively high.

In contrast to the energy redistribution effects of the previous section which could be explained and quantitatively reproduced with analytical model calculations, none of the proposed models provides a satisfactory explanation for the appearance of two high energy peaks in the spectrum.

However, the applied models assume an ideal field geometry. The real situation is much more complex in three dimensions. Therefore, other field components, such as radial electric fields and magnetic fields must also be considered. In principle, these fields may accelerate a part of the probing protons in the direction parallel to the surface of the interaction target, depending on the initial trajectory and probing time of the respective single proton. The induced deflection of the proton beam in combination with the accelerating and decelerating effect of the interaction fields could result in a complex density distribution on the detector which could not have been measured with the applied setup.

Due to the small angle scattering of the probing protons within the relatively thick (800 nm) aluminum foil, the transversal emittance of the proton beam was significantly increased. Therefore, the application of a beam mask for the visualization of transversal force components (cf. Chapter 7) was not possible and the reconstruction of the acting transversal fields was not attainable. For this reason, ultra-thin

foils which allow for the application of a beam mask and thus the investigation of transversal field components will be used in the next chapter.

10 Electromagnetic Fields initiated on Ultra-thin Foils with High-contrast Laser Pulses

This chapter examines the electromagnetic fields, which are generated at plasma vacuum interfaces of laser irradiated ultra-thin foils (30 – 50 nm). For the field generation both femtosecond and picosecond laser pulses with high temporal contrast were used. The field distribution and its evolution were investigated using the method of proton streak deflectometry, whereby two different probing configurations (cf. Chapter 7) were applied. The corresponding deflection measurements can visualize the action of the induced fields. The impact of individual field components on the observed streak deflections depends on the applied probing geometry. Therefore, the combination of both probing configurations provides additional and complementary information about the investigated field distribution.

First, the proton streak deflectometry setup is described, then the experimental results are presented and discussed. Afterwards, several theoretical models are presented, which can describe particular aspects of the laser-induced electromagnetic fields. Based on the respective model, the calculation of electric and magnetic fields is explained with respect to the applied laser and target parameters. In addition the temporal evolution and spatial distribution of particular field components are visualized. In the following sections the results of numerical particle simulations are presented, which can approximate the measurements. First, the general conception of the simulations is explained. Subsequently, simulation results in connection with field effects due to ultra-short laser pulses are discussed, followed by the simulation results concerning picosecond laser pulses. Finally, conclusions are drawn.

10.1 Experimental Setup

The experimental setups in transversal and longitudinal probing geometry are illustrated in Figure 10.1.A and 10.1.B, respectively. The laser irradiation of a 5 μm thick titanium foil and its adherent CH-contamination layer leads to the creation

of a proton beam. The used laser pulse is generated by means of laser arm A (Section 2), which provided a pulse length τ_p (FWHM of intensity) of 30 fs and an ASE background level of $10^{-10} - 10^{-9}$. On their way to the detector the protons propagate perpendicular (Figure 10.1.A) or parallel (Figure 10.1.B) to the surface normal of a plastic foil (CH foil) with a thickness Δa of 30 nm. The plastic foil has the empirical formula $C_5H_7O_2$ and a solid state electron density $n_{\text{eh},0}$ of $3 \cdot 10^{23} \text{ 1/cm}^3$.

The proton beam is used to probe the electromagnetic fields that are created as a result of the interaction between the laser pump pulse and the CH (interaction) target. For the generation of the pump pulse laser arm B (Section 2) was used, which provided a pulse energy from 1 J to 3 J before compression. Taking into account the transmission of the beamline (62%), these values result in an transmitted energy of between 0.62 J and 1.86 J on target. By changing the grating position of the compressor, a pulse length τ_p (FWHM of intensity) from several picoseconds to 50 fs with an ASE background level of $10^{-11} - 10^{-10}$ was realized. The focal intensities of the laser pulses were calculated with respect to the measured focal spot-sizes, pulse energies and pulse durations (Section 2.1). The calculated intensity values of the laser pulse I_{source} are in the range of $7 \cdot 10^{19} - 2 \cdot 10^{20} \text{ W/cm}^2$ and the intensity of the pump pulse I_{pump} was variable depending on the chosen pulse length.

The energy distribution of the probing proton beam was registered with a Thomson slit spectrometer (Chapter 5). The denotations shown in Figure 9.2 are explicated in Section 5.1. For the presented measurements of this chapter, the depicted distances L_1 to L_3 have the values: $L_1 = 477 \text{ mm}$, $L_2 = 228 \text{ mm}$, $L_3 = 515 \text{ mm}$. The applied magnet ($B_x = 0.34 \text{ T}$, $l = 50 \text{ mm}$) is identical as proposed in Section 5.1. The entrance slit has a width s_y of about $288 \mu\text{m}$. This leads to an energy resolution $\Delta\epsilon$ of approximately 45 keV for proton energies of around 2.5 MeV (Section 5.5). In general the relative energy resolution is better than 3% of the relevant kinetic energy values. The target distance a has value of around 35.0 mm. The temporal resolution Δt is around 30 ps if an interaction length of l_I of $100 \mu\text{m}$ is assumed (Section 8.5).

In addition a virtual source distance $z_v(\epsilon)$ of $-0.82 \pm 0.5 \text{ mm}$ could be determined for the proton energy interval between 1 MeV and 3 MeV, as described in Section B.1.

In transversal probing geometry (Figure 10.1.A) two additional Thomson spectrometers were installed opposite the front and rear surface of the CH foil. These were applied to record the energy distribution of the individual ion species that are accelerated in both directions normal to the surface of the interaction target.

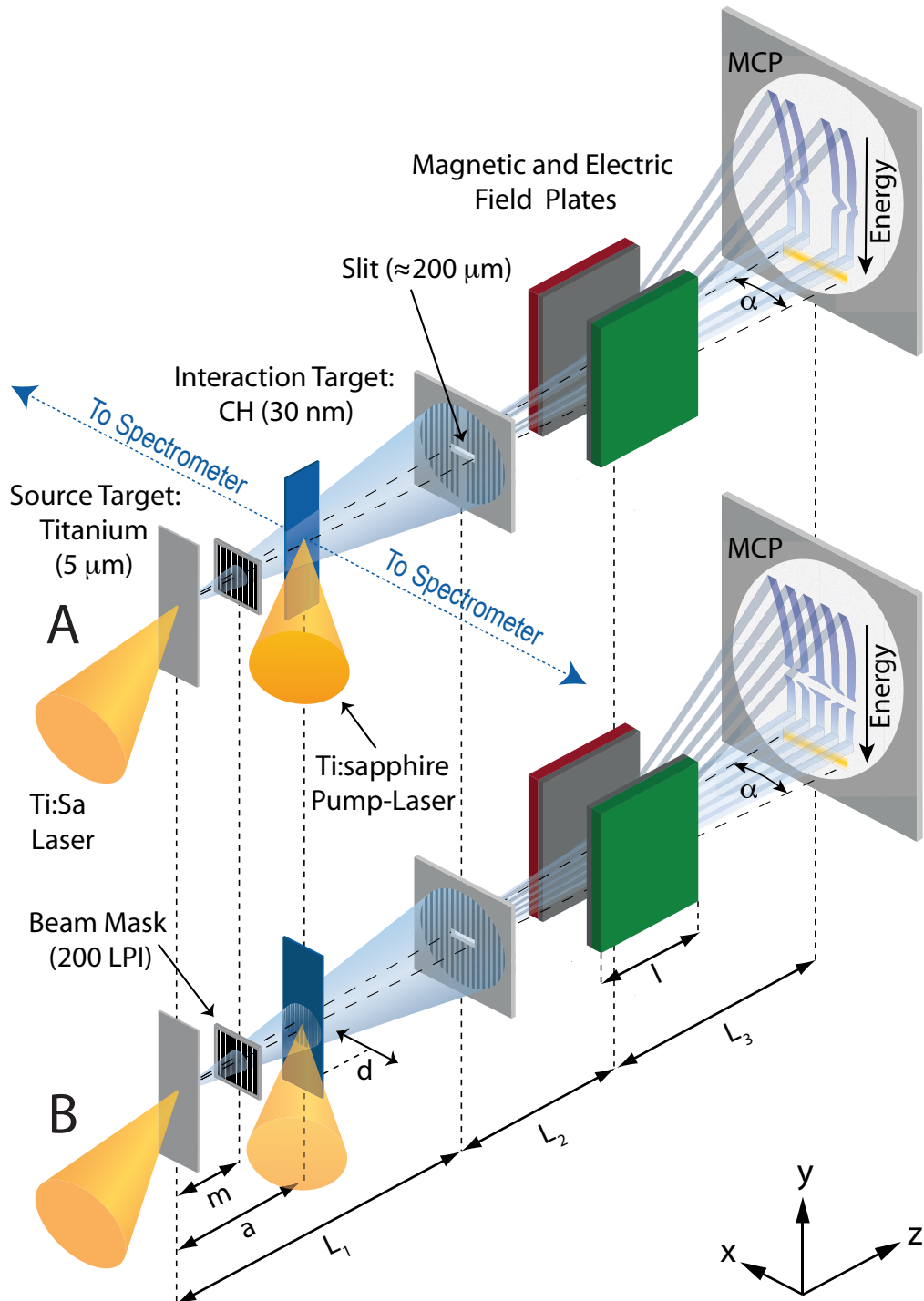


Figure 10.1: Experimental setup. **A** - Transversal Probing Geometry. **B** - Longitudinal Probing Geometry.

10.2 Experimental Results

This section presents the proton deflectometry measurements and discusses the experimental results focussing on the investigation of fields generated with ultra-short laser pulses. The corresponding measurements in longitudinal and transversal probing configuration are presented first. Then, a selected measurement in connection with a picosecond laser pulse is presented. Here, the streak deflections in longitudinal configuration clearly indicate the presence of magnetic fields, which was not observed in the previous case of ultra-short pulses.

10.2.1 Field Effects due to Ultra-short Laser Pulses

In this section the field effects on ultra-thin foils (30 – 50 nm) are investigated, which are initiated by ultra-short laser pulse ($\tau_p = 50$ fs) irradiation with ultra-high temporal contrast ($C = 10^{-11} - 10^{-10}$).

The measurements in transversal direction show a pronounced deflection symmetry between the target front and rear side and make it possible to deduce the expansion velocity of the proton front.

The results in longitudinal configuration exhibit energy redistribution effects in the probing proton beam. These proton redistributions are slightly different in comparison to the observations of Chapter 9, where thicker foils (800 nm) and laser arm A were used for the field generation. In addition the measurements in longitudinal configuration visualize the influence of transversal force components, which are directed perpendicular to the propagation direction of the proton beam. This is possible, because the probing protons propagate through an ultra-thin foil, therefore the effect of small angle scattering is negligible and the initial transversal emittance of the probing proton beam remains low. A beam mask (grating) can thus be used to detect the influence of transversal field components on the intersected proton beam as described in Chapter 7 and Chapter 8.

For the measurements in both probing configuration almost identical laser parameters were used which allowed for a direct comparison of the experimental results.

Transversal Probing Geometry

Figures 10.2 and 10.3 show a selection of processed streak deflectometry measurements in transversal probing geometry. Different regions of the laser-induced fields are probed in consecutive shots using the lateral displacement technique (Section 8.2). The measured proton density distributions $\rho(x, y)$ on the MCP are processed by means of the numerical coordinate transformation, presented in detail in Chapter 5.4 and Chapter 8.3. As a result the distributions $\tilde{\rho}(\beta, t_p)$ are visualized in an orthogonal coordinate system as a function of the initial emission angle β and the probing time t_p , which are represented by the upper abscissa and the left ordinate, respectively. The lower abscissa indicates the corresponding proton en-

ergy for $\beta = 0$. The right ordinate shows the focal distance $x_F(\beta, d)$ (Section 8.2), which depends on β and the lateral displacement parameter d .

In order to visualize the influence of transversal field components (perpendicular to the propagation direction of the probing proton beam) a beam mask in the form of a grating with 300 LPI was used to intersect the proton beam. In the case of Figure 10.3.A the pump laser is blocked. As a result no fields are generated around the interaction target and the probing proton beam is not deflected. The undisturbed proton traces of this image serve as a reference, demonstrating the accuracy of the method.

In view of all measurements, the deflected traces exhibit pronounced deflection symmetry, indicating a highly symmetric field distribution. Protons passing the interaction target on different sides, but with similar energies ϵ_p and similar initial focal distances $|x_F|$, show similar deflection amplitudes.

On both sides the deflection strongly depends on the initial distance to the target surface. Protons passing closer to the foil surface are deflected more strongly than protons which pass at a further distance.

The time t_{pump} defines the arrival time of the pump laser pulse at the interaction target with regard to the creation of the probing proton beam at the source target. In the presented experiments the time t_{pump} is set to 1571 ps which corresponds to the proton t-pump energy $\epsilon_{\text{pump}} = 2.6$ MeV. This means that a proton with the kinetic energy $\epsilon = \epsilon_{\text{pump}}$ needs the time $t_p = t_{\text{pump}}$ to propagate from the source to the interaction target.

With the generation of the electric fields the probing protons are deflected away from the surfaces of the interaction target depending on their relative position, propagation direction and energy. The temporal dependence of the deflection can be divided in several intervals. Protons with energies $\epsilon_p > \epsilon_{\text{pump}}$ reach the second target ($z=a$) even before the laser pump pulse impinges on its surface. These particles are only affected by the initiated fields if their relative distance to the interaction center (pump focus) is smaller than the radial extension of the field distribution in z -direction.

As shown in Figure 10.2.B the deflection becomes visible at the probing time $t_p = t_f = 1410$ ps and can be characterized by a steep increase.

Proton traces with focal distances $|x_F| \lesssim 650 \mu\text{m}$ (for $t_p < t_{\text{pump}}$) show a deflection maximum at the time moment which corresponds exactly to the setting of the pump time $t_{\text{pump}} = 1571$ ps. For traces at higher distances ($|x_F| \gtrsim 650 \mu\text{m}$) the deflection maximum is shifted towards lower proton energies.

After the maximum, the deflection decays relatively quickly for $|x_F| \lesssim 650 \mu\text{m}$, on a time scale of approximately 80 ps. The decay then becomes flatter, and within 250 ps the deflection declines to a quasi-constant value. At higher distances ($|x_F| \gtrsim 400 \mu\text{m}$), the deflected traces show a second local maximum before they drop to constant values in time. At this point the proton deflection becomes relatively independent on the initial ejection angle β .

As explained in Chapter 8.3 (Figure 8.5) the time $t_f \approx 1410$ ps when the deflection

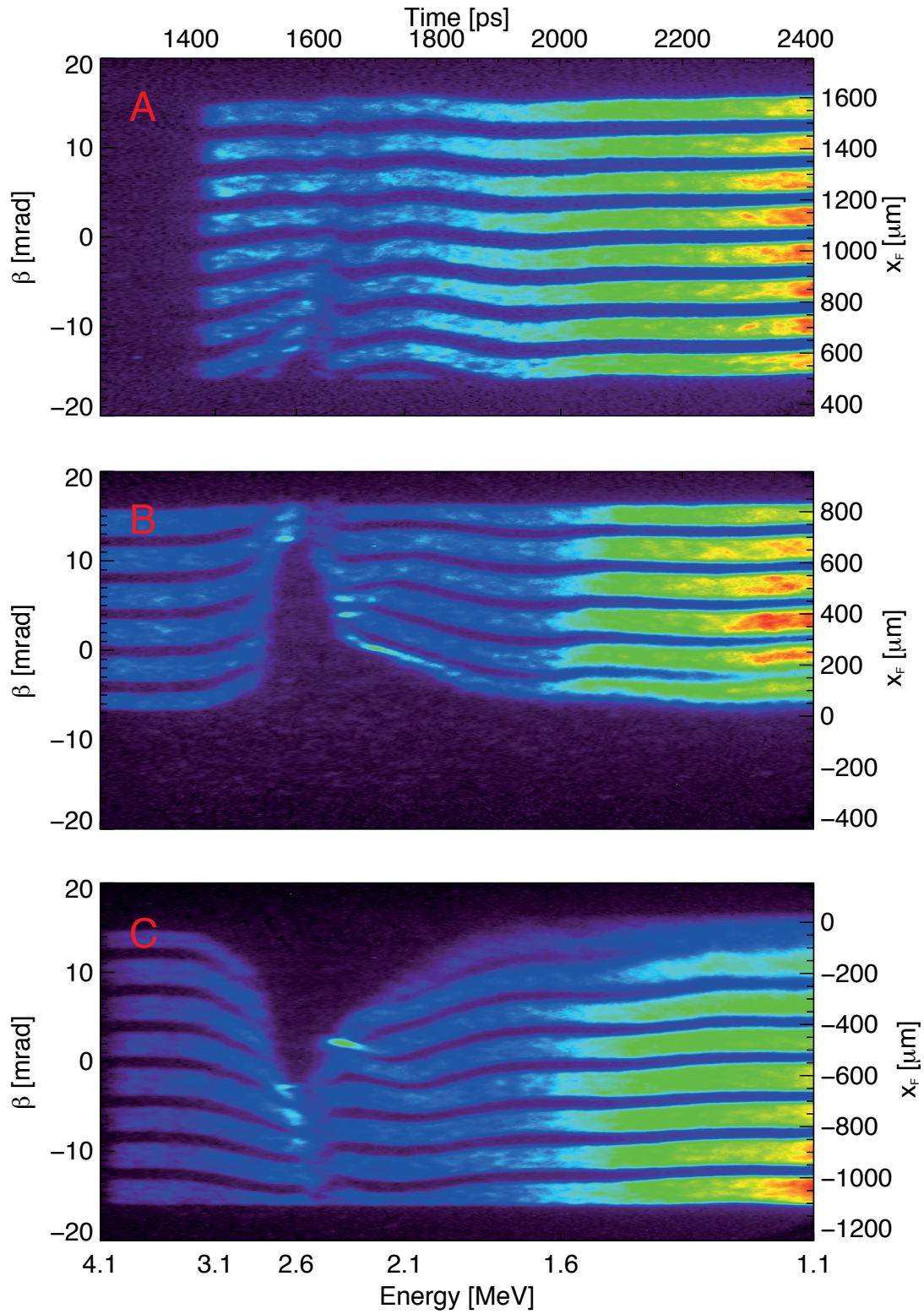


Figure 10.2: Density distribution $\tilde{\rho}(\beta, t_p)$ as a result of streak deflectometry measurements in transversal probing geometry. **A** - $d = -1054 \mu\text{m}$. **B** - $d = -254 \mu\text{m}$. **C** - $d = 545 \mu\text{m}$.

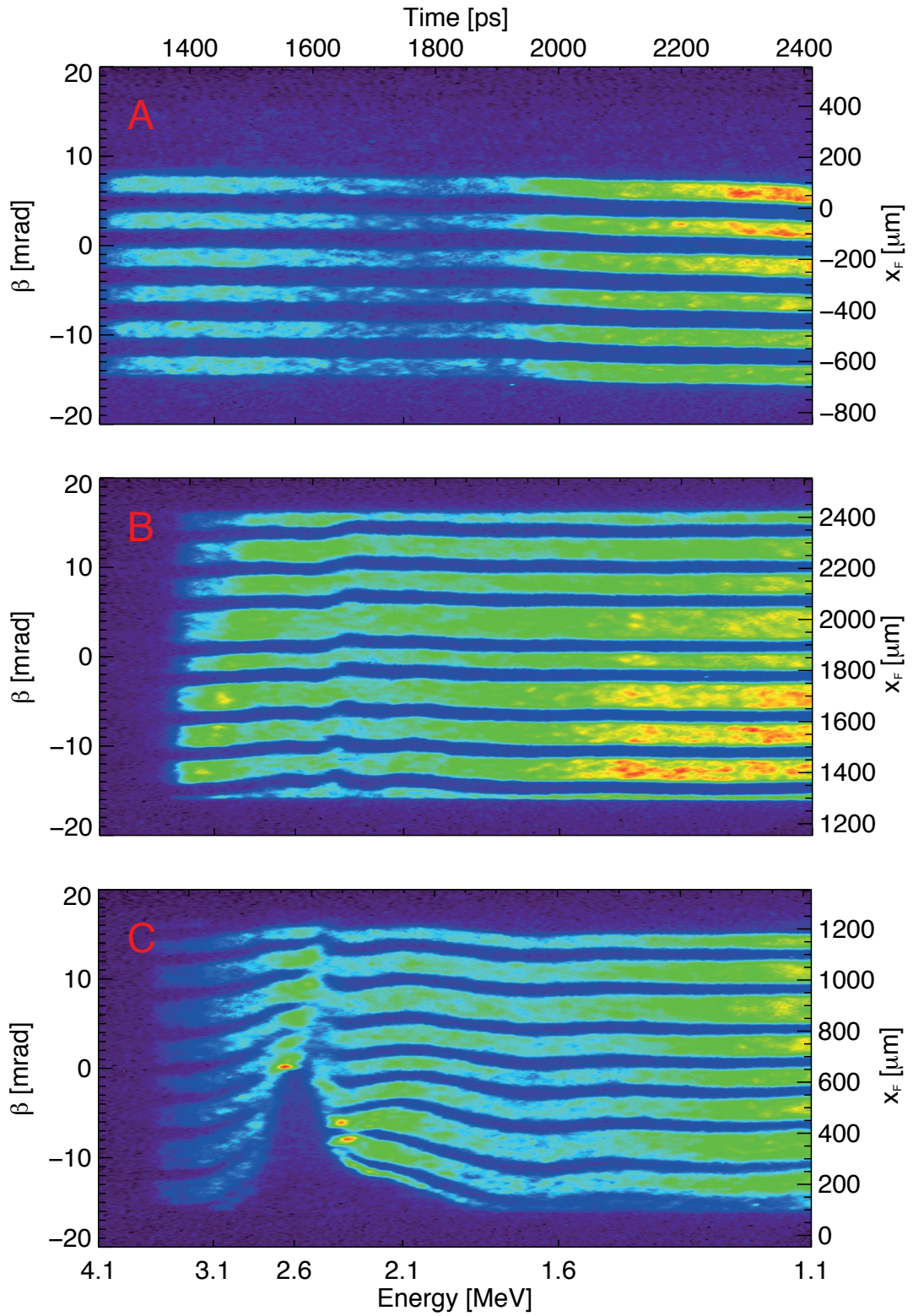


Figure 10.3: Density distribution $\tilde{\rho}(\beta, t_p)$ as a result of streak deflectometry measurements in transversal probing geometry. **A** - $d = 145 \mu\text{m}$. **B** - $d = -1854 \mu\text{m}$. **C** - $d = -654 \mu\text{m}$.

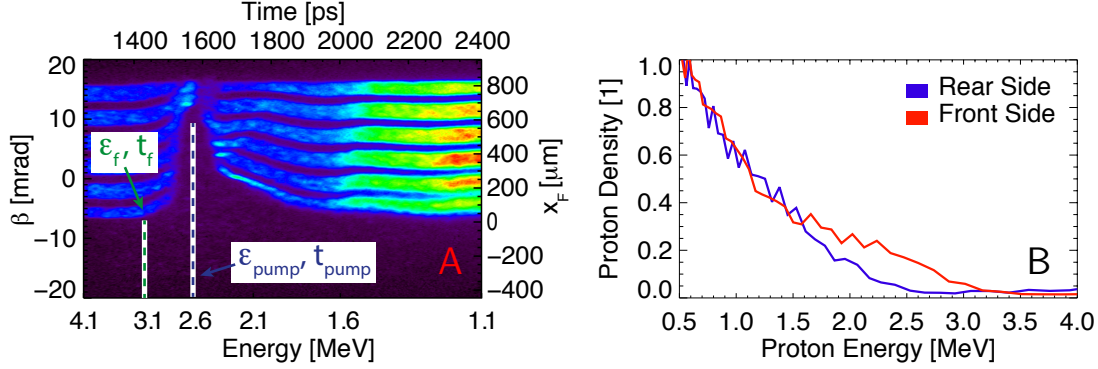


Figure 10.4: **A** - Density distribution $\tilde{\rho}(\beta, t_p)$ of Figure 10.3.B. The dashed green lines shows the start of the deflection and the dashed blue line indicates the (first) deflection maximum. **B** - Proton energy spectra due to the front- and rear-side acceleration on the 30 nm CH foil.

becomes visible is connected with the energy $\epsilon_f = 3.23$ MeV of the fastest influenced protons as illustrated by the green dashed line in Figure 10.4.A. The corresponding velocity value can be used to estimate the extension of the electric field in z -direction under the assumption that the electric field component in z -direction (along the surface) is negligible. In the case of Figure 10.3.B or Figure 10.4.A, respectively an extension radius r_f of 4.3 mm is obtained. Considering that the foil target has a total extension of 5 mm in z -direction and is irradiated in the center, the deduced extension radius is relatively high. This indicates that radial field components along the foil surface (in z -direction) cannot be neglected in the presented case.

Using the extension of the foil in z -direction as an upper limit of the radial field extension, the time resolution of the method can be estimated by means of Formula 8.5. For the probing time $t_p = t_{\text{pump}}$ the time resolution Δt is approximately 250 ps.

In order to obtain complementary information about the acceleration process on the 30 nm CH foil, two Thomson spectrometers were installed opposite its front and rear surfaces. This allowed for the measurement of the composition and energies of the accelerated ion species in combination with the streak deflections of the probing proton beam.

Figures 10.5.A and 10.5.B are photographs of the light emitting phosphor screens showing the ion traces on the MCPs which are caused by the (A) front-side and (B) rear-side acceleration on the 30 nm CH foil. Both figures were recorded simultaneously in one shot and are related to the streak deflectometry measurement of Figure 10.2.B. The corresponding proton traces were evaluated and the resulting energy spectra are illustrated in Figure 10.4.B.

The proton energy spectra, which belong to the streak deflectometry measurements of Figure 10.2.C and 10.3.C are shown in Figure 10.6. Similarly, the proton en-

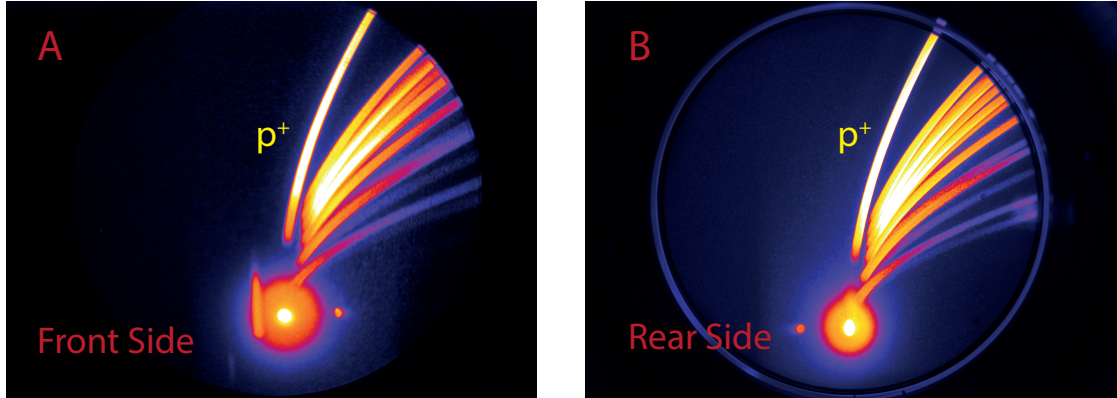


Figure 10.5: Photographs of light emitting phosphor screens. The ion traces on the MCPs are caused by the (A) front-side and (B) rear-side acceleration on the 30 nm CH foil.

ergy spectra that belong to Figure 10.2.A. and Figure 10.3.B. are illustrated in Figure 10.7.

In view of all measurements it becomes clear that the acceleration at the front and rear sides of the CH foil leads to relatively similar ion energy distributions. This is not only valid for the proton signal, but also for all other contributing ion species. The observation is in agreement with the symmetry of the measured streak deflections on the front and rear sides of the CH foil (Figures 10.2.C and 10.2.B). The comparison of all energy spectra shows that the fluctuations of the generated proton (ion) signal are relatively low for consecutive measurements. This proves the repeatability of the laser-induced acceleration process and thus indirectly affirms the comparability of the presented streak deflectometry measurements.

Figures 10.2.A, 10.2.C, 10.3.B and 10.3.C show the proton stripes at greater distances from the foil surface, i.e. for higher values of $|x_F|$. Proton streak deflections

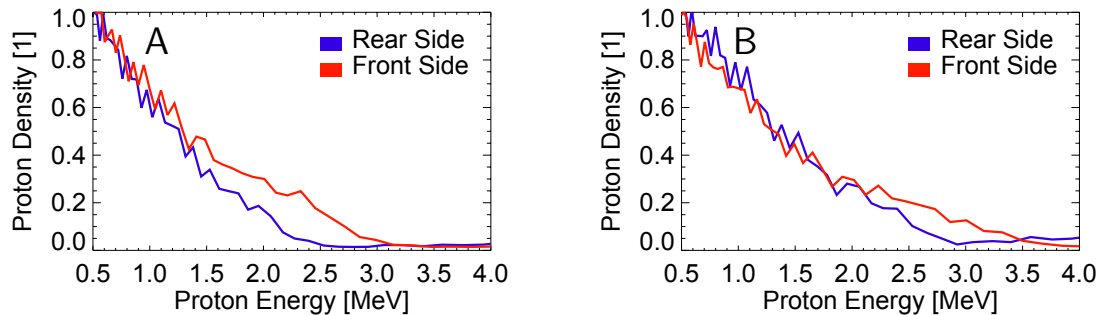


Figure 10.6: Proton energy spectra due to the front- and rear-side acceleration on a 30 nm CH foil. The spectra correspond to the streak deflectometry measurements of Figure 10.2.C. (A) and Figure 10.3.C (B).

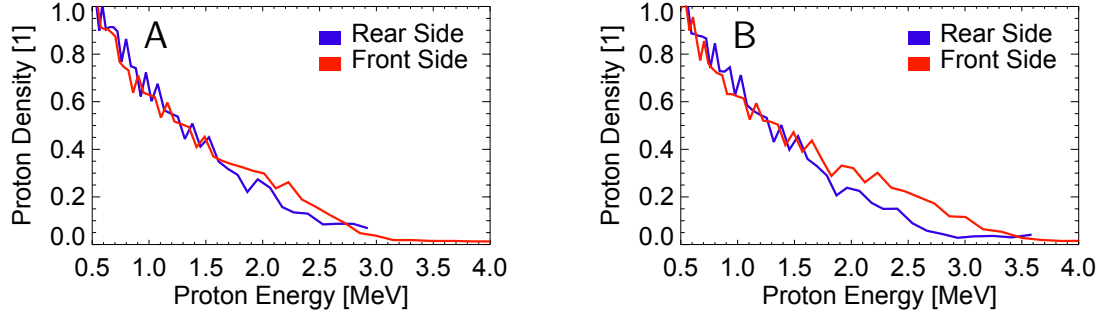


Figure 10.7: Proton energy spectra due to the front- and rear-side acceleration on a 30 nm CH foil. The spectra correspond to the streak deflectometry measurements of Figure 10.2.A. (A) and Figure 10.3.B (B).

are visible up to the maximum recorded value $x_F \approx 2400 \mu\text{m}$, which is a measure of the effective field extension normal to the foil surface. Thus, for the electric field component E_n normal to the target surface an effective extension length $l_{En} \gtrsim 2400 \mu\text{m}$ is found.

For distances $|x_F| \gtrsim 700 \mu\text{m}$ the proton stripes do not overlay and are clearly distinguishable, even at the deflection maximum. For these distances the deflection amplitude is smaller than the width of a proton stripe ($\approx 50 \mu\text{m}$) and decreases at higher values of $|x_F|$. This dependency could be explained by a field gradient $\partial E/\partial x$ which becomes relatively flat for larger distances ($|x_F| \gtrsim 700 \mu\text{m}$). If protons of adjacent stripes are affected by almost the same force, the amplitude of their deflection becomes similar and different stripes cannot overlay on the detector.

A careful analysis of the presented deflection measurements shows that the deflection maximum is shifted to higher probing times t_p with increasing distance $|x_F|$. This property is illustrated for two selected measurements in Figure 10.8. The deflection maxima of each proton stripe is marked by a yellow cross and the

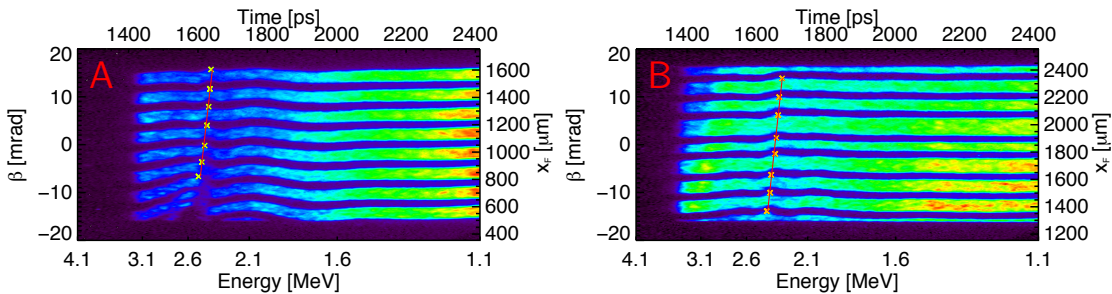


Figure 10.8: Shift of the deflection maximum to higher probing times t_p with increasing distance $|x_F|$. The measurements correspond to Figure 10.2.A (A) and Figure 10.3.B (B).

line of best fit is shown in red. As explained in Section 8.3 the probing time t_p is defined as the time of arrival of a single proton in the x-y-plane of the interaction region at the position $z = a$. The proton density distribution $\tilde{\rho}(\beta, t_p)$ is shown as a function of β and t_p . For small angles β the relation between x_F and β is linear (Equation 8.1). Therefore, the red lines in Figure 10.8 describe a position in the focal plane depending on time, and its slope can be interpreted as a velocity. If the deflection maximum is caused by the field of an expanding ion front, the slope of the red line could represent the expansion velocity of the front. In case of Figure 10.8.A a velocity of $2.34 \cdot 10^7$ m/s is deduced, which corresponds to a proton energy of 2.87 MeV. In case of Figure 10.8.B the velocity $2.39 \cdot 10^7$ m/s is obtained, which results in a proton energy of 3.01 MeV. A comparison with the recorded proton energy spectra (Figure 10.7) shows that these values are in good agreement with the measured cut-off energies.

Longitudinal Probing Geometry

Figure 10.9 shows three selected streak deflectometry measurements in longitudinal probing geometry. All measurements were conducted under almost identical experimental conditions. In addition, the same target and laser parameters as in the previous section for the measurements in transversal probing geometry, were applied. In order to probe different regions of the field distribution, the lateral displacement d (Section 8.2) was changed before each measurement. In case of Figure 10.9.A the pump time t_{pump} was set in agreement with the proton t-pump energy $\epsilon_{\text{pump}} = 2.4$ MeV. For the record of Figures 10.9.B and 10.9.C the t-pump energy $\epsilon_{\text{pump}} = 2.6$ MeV was chosen.

As before, the measured proton density distributions $\rho(x, y)$ on the detector are processed using the numerical coordinate transformation of Chapter 5.4. This time, the proton density distributions $\tilde{\rho}(\beta, \epsilon)$ of Figure 10.9 are not shown depending on the probing time t_p , but as a function of the proton energy ϵ (lower abscissa) and the initial emission angle β (left ordinate). Here, the focal distance $x_F(\beta, d)$ (Section 8.2) is indicated by the right ordinate.

In order to visualize the influence of transversal field components (along the foil surface) a beam mask in the form of a grating with 200 LPI was used to intersect the probing proton beam. The resulting proton stripes (Figure 10.9) on the detector exhibit prominent density dips in the energy range of the selected proton t-pump energy ϵ_{pump} , similar to Chapter 9.

In contrast to the results of that chapter, neither at the low nor the high energy side of the dips a proton density increase in form of a local maximum is detected. The dips are most pronounced near the center of the interaction ($|x_F| = 0$).

A bending of the proton stripes is visible at both sides of the dips, indicating the presence of radial electric field components and/or the influence of magnetic fields (cf. Chapter 7.3). In both cases the bending is directed contrary to the interaction center ($|x_F| = 0 \mu\text{m}$), but the deflection is stronger at the low energy side.

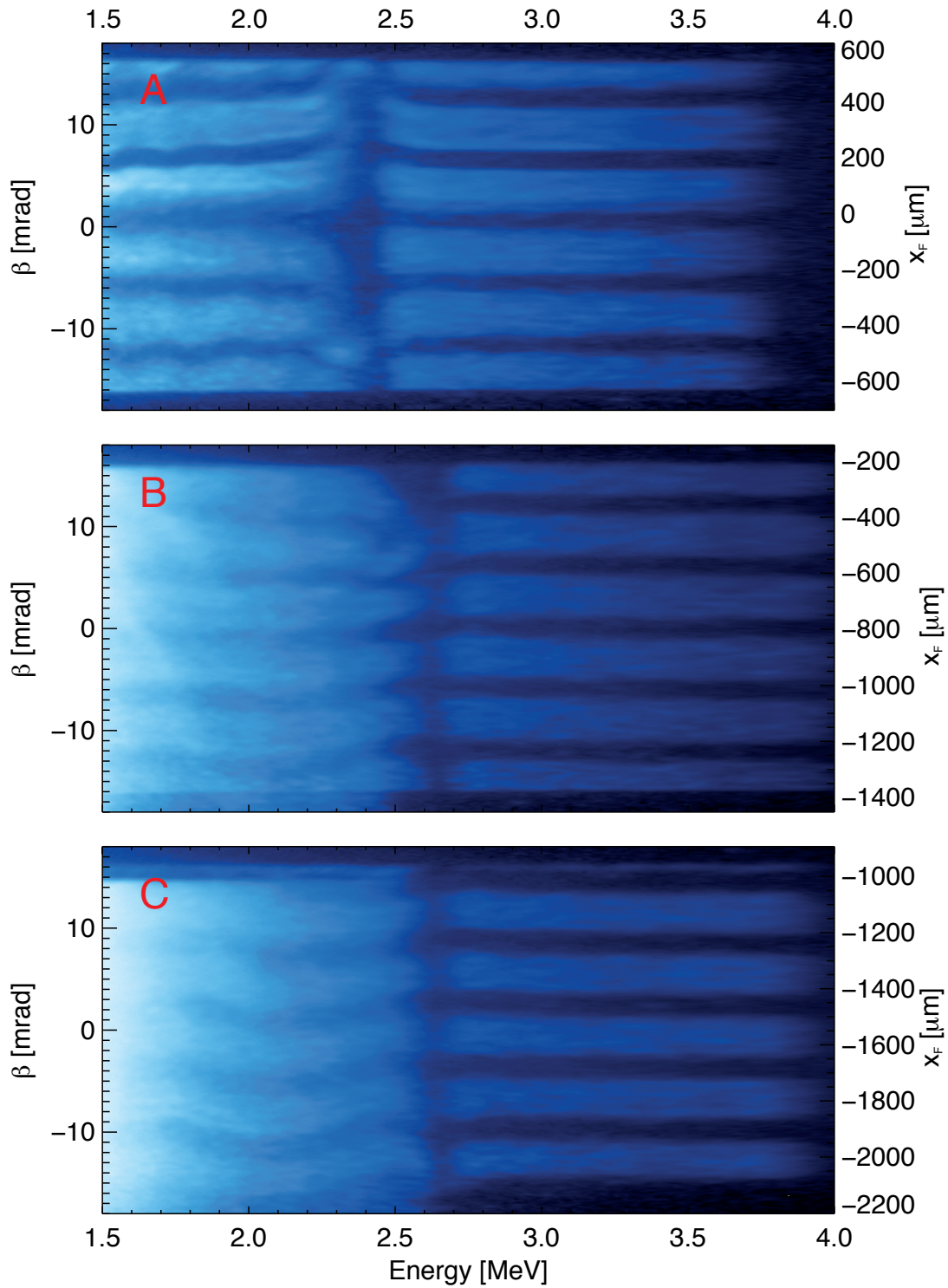


Figure 10.9: Density distribution $\tilde{\rho}(\beta, \epsilon)$ as a result of streak deflectometry measurements in longitudinal probing geometry. **A** - $d = 47 \mu\text{m}$. **B** - $d = 797 \mu\text{m}$. **C** - $d = 1547 \mu\text{m}$.

At greater distances to the interaction center the outward deflection of the protons decreases. As a result no bending of the stripes is detectable for $|x_F| \gtrsim 600 \mu\text{m}$ at the high energy side of the dips.

At the low energy side the bending of the stripes becomes smoother for greater values of $|x_F|$ and the deflection maximum is shifted towards lower energies. Interestingly, the position of the gap remains constant at the energy ϵ_{pump} , even for larger focal distances ($|x_F| \approx 2000 \mu\text{m}$). This indicates that the effect is either caused by a fast evolving process or by an initial field extension which is much larger than the spot size of the laser pulse, or both.

In any case, the deflection measurements allow for an indirect determination of the effective field extension in radial direction. For field components that act in radial direction (E_r, B_φ), an effective extension radius of $r_{\text{Fr}} \lesssim 600 \mu\text{m}$ was found (cf. Chapter 7.3). In contrast, for the normal electric field component E_n an effective radial extension radius $r_{\text{En}} \gtrsim 2000 \mu\text{m}$ can be determined. This interpretation is in agreement with the high value of the estimated field extension radius $r_f \approx 4.3 \text{ mm}$, which was determined in the last section, based on deflection measurements in transversal direction.

Near the focal distance of $x_F \approx \pm 500 \mu\text{m}$ and at the low energy side of the density dips the streak deflections show regions with an increased proton density. This effect might be explained by the overlay of protons that originate from separate (inner) stripes, but are deflected to similar regions on the detector.

10.2.2 Field Effects due to Picosecond Laser Pulses

Figure 10.10 is a photograph of the light emitting phosphor screen and shows the recorded density distribution $\rho(x, y)$ as a function of the x- and y-position in the detector plane, corresponding to the setup in longitudinal probing geometry (cf. Figure 10.1).B. The y-position refers to the proton energy, whereas the x-position visualizes the deflection of the probing protons. The experimental parameters are identical to those of the last section. For the generation of the pump pulse an energy of 1 Joule before compression (0.62 Joule on target) was used. The grating position of the compressor, which provided the shortest pulse length, was changed by a distance of 10 mm. Through this, a pulse length τ_p of approximately 2.7 ps was generated, leading to an intensity of $5.8 \cdot 10^{17} \text{ W/cm}^2$.

Figure 10.11 shows the density distribution $\tilde{\rho}(\beta, \epsilon)$ as a result of the numerical transformation of Image 10.10. Similar to the case of the femtosecond pulse interaction, the generated fields cause prominent density gaps within the proton stripes at the proton energy of approximately 1.24 MeV. This value corresponds well with the applied proton t-pump energy $\epsilon_{\text{pump}} = 1.227 \text{ MeV}$.

In addition a bending of the proton stripes towards the interaction center ($|x_F| = 0$) is visible at the high energy side of the density gaps, which is a clear indication of the presence of a magnetic field. The proton stripes at the low energy side of the gap appear blurred and deformed, which makes a clear interpretation difficult. The

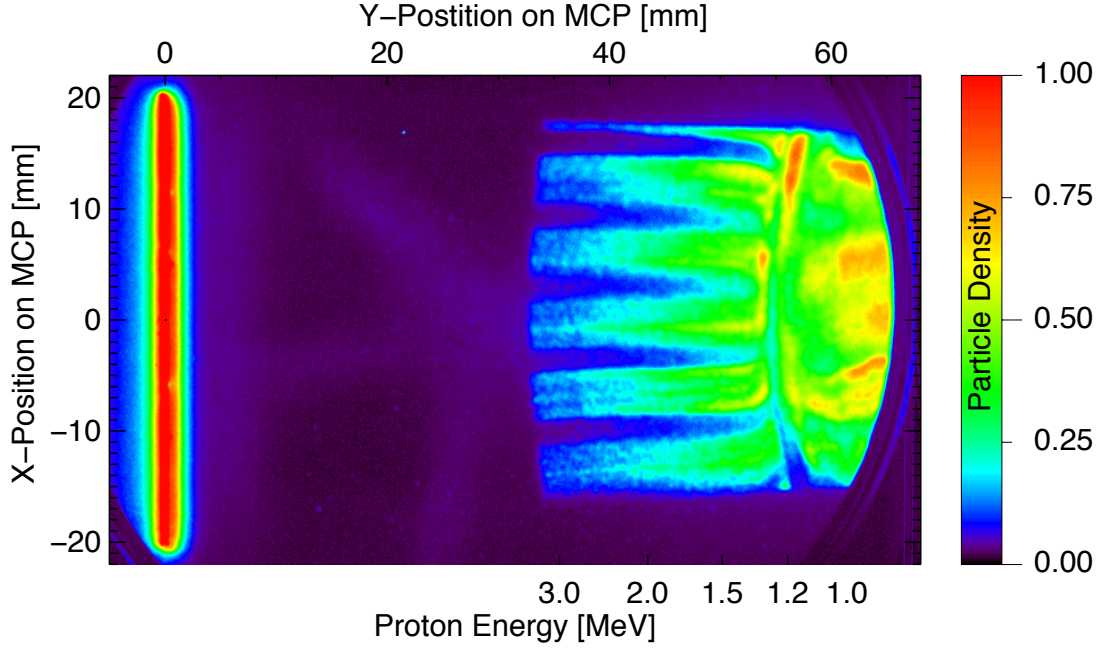


Figure 10.10: Measured density distribution $\rho(x, y)$ on the detector.

width of the stripes are broadened and their mutual distances increased. Near the focal distance of $x_F \approx \pm 400 \mu\text{m}$ at the low energy side of the stripe gaps regions with increased proton density become visible, which indicates an outward deflection of protons.

The shown deflection measurement was conducted under identical experimental conditions to the measurements with ultra-short pulses. Since only the duration of the laser pulse was changed a comparison between these measurements shows the specific influence of this parameter. The streak deflections in longitudinal configuration clearly indicate the presence of magnetic fields, which was not observed in the case of ultra-short pulses. The dominating influence of the magnetic field on the probing proton beam becomes visible in the form of a focussing deflection of the proton stripes. This focussing effect occurs only in a certain energy range ($\epsilon \in M_f$) at the high energy side of a pronounced density dip, which is located around the energy ϵ_{pump} within the energy spectrum.

As explained before, the time t_{pump} defines the arrival time of the pump laser pulse at the interaction target with regard to the creation of the probing proton beam at the source target. In the presented experiment the time t_{pump} is set to 2379 ps which corresponds to the proton t-pump energy $\epsilon_{\text{pump}} = 1.227 \text{ MeV}$. This means that a proton with the kinetic energy $\epsilon = \epsilon_{\text{pump}}$ needs the time $t_p = t_{\text{pump}}$ to propagate from the source ($z=0$) to the interaction target ($z=a$).

Depending on its energy, each probing proton is either before ($z < a$) or behind ($z > a$) the interaction target, when the deflecting fields are initiated at the time

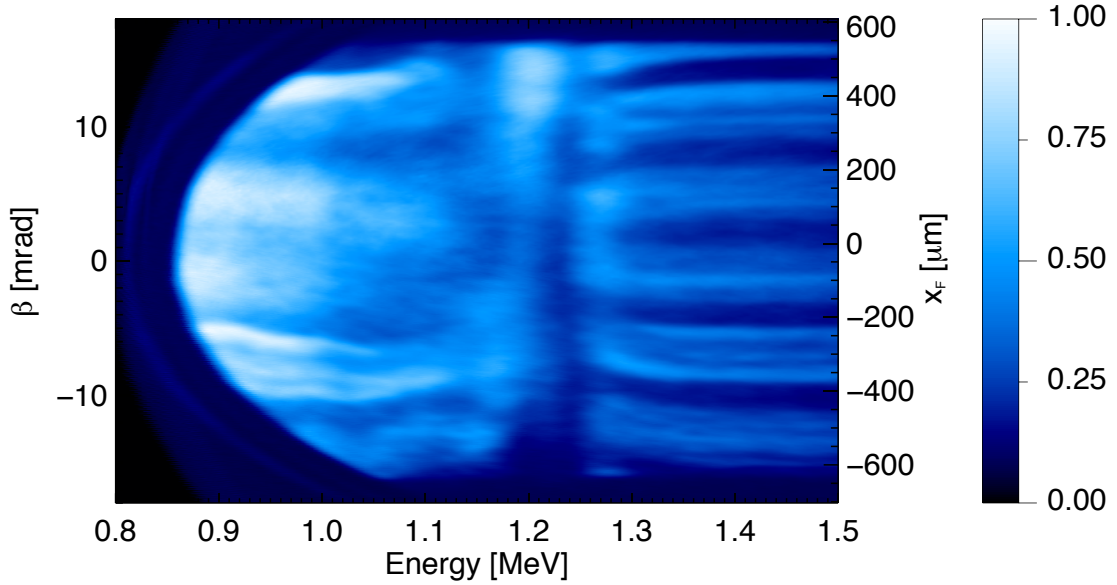


Figure 10.11: Density distribution $\tilde{\rho}(\beta, \epsilon)$ as a result of a streak deflectometry measurement in longitudinal probing geometry. The lateral displacement d is $47 \mu\text{m}$. For the field generation a picosecond laser pulse was used.

$t = t_{\text{pump}}$. Because the focused protons ($\epsilon \in M_f$) have energies $\epsilon > \epsilon_{\text{pump}}$, all of them have already passed the interaction foil ($z > a$) at $t = t_{\text{pump}}$. Therefore, these particles are exclusively influenced by the electromagnetic field distribution which acts on the rear side of the foil. Conversely, this means that none of these particles ($\epsilon \in M_f$) are influenced by the field distribution on the front side of the interaction target. This is a significant experimental observation and has a crucial importance for the interpretation of the acting magnetic fields. Under the assumption that the focussing effect is induced by a magnetic field, the Lorentz force (Equation 7.1) can be used to determine the direction of the acting fields.

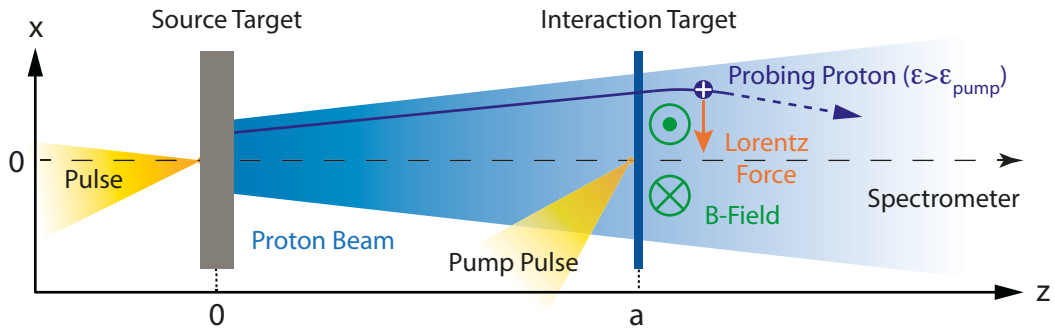


Figure 10.12: Proton propagation in longitudinal probing geometry

Figure 10.12 illustrates the polarity of the magnetic field in reference to the foil surface and indicates the direction of the Lorentz force on a proton with $\epsilon > \epsilon_{\text{pump}}$. In recent investigations [94, 130] of the magnetic field structure generated on thin foils using high intensity lasers ($I_L \approx 10^{19} \text{ W/cm}^2$), a field configuration corresponding to Figure 10.13.A was applied to explain the experimental observations. The experimental results of the last section, in connection with femtosecond laser pulses, did not exhibit a clear signature of a magnetic field. However, the corresponding analytical model description (model A, Section 10.3.1) revealed a magnetic field configuration (cf. Figure 10.15), which is in agreement with field configuration A (Figure 10.13.A). The calculated magnetic field amplitude showed values up to 10^4 T , which is consistent with the findings in reference [130]. However, the influence of the radial electric field on the probing protons was stronger in this case.

In contrast, the polarity of the probed magnetic field on the rear side of the ps-laser irradiated thin foil is exactly the opposite. This corresponds to the situation at the rear side of field configuration B. This phenomenon is observed for the first time in connection with high intensity laser pulses ($I_L > 10^{17} \text{ W/cm}^2$) with high temporal contrast and solid ultra-thin foil targets.

In the case of laser irradiated thin foils, the polarity of the thermoelectric magnetic field generation (cf. Section 10.3.3) corresponds typically to field configuration A (Figure 10.13.A). This is a strong indication that possibly another mechanism for the magnetic field generation is present. Such a magnetic field is possible due to DC currents in steep density gradients, which are driven by temporal variations in the ponderomotive force [85–87]. Another explanation could be the occurrence of fast electron currents which can either be directed into the target [88, 89] or along the target surface [90–92].

So far magnetic fields with opposite orientation as a conventional thermoelectric field were only observed experimentally in the interaction of relativistically intense laser pulses propagating in a preionized plasma [141]. This raises the question if an undercritical plasma could be generated due to the picosecond pulse interaction.

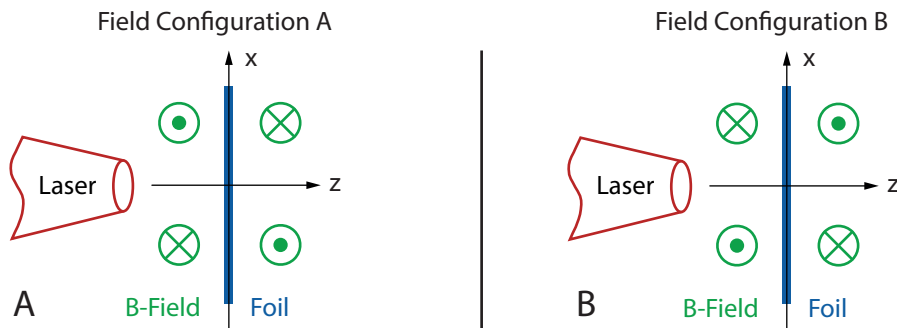


Figure 10.13: Proton propagation in longitudinal probing geometry

10.3 Theoretical Description

In this section several analytical models are proposed which provide different descriptions of laser-induced electric and magnetic fields on thin foils. For convenience these models are referred to as model A, model B and model C. In Section 10.4 these models are used to explain the measured streak deflections and energy redistribution effects of Sections 10.2.1 and 10.2.2. The applicability of the models is tested by means of three-dimensional particle simulations, which can reproduce particular features of the measurements.

If the reader is primarily interested in the modeling of the experimental results and the applicability of the individual models for the explanation of the experimental observations, he should skip this section. Relevant equations and results of this section will be referenced.

10.3.1 Model A - Ultra-short Fields on Ultra-thin Foils

In order to explain the observed proton deflections and redistribution effects, the model of A. Andreev et al. [142] is introduced. This analytical model describes the electric and magnetic field distributions which are generated on a ultra-thin foil (submicrometer) if an ultra-short (< 50 fs) laser pulse irradiates the target surface at an angle of 45° . The model takes into account the motion of the hot electron cloud through the target (along the z -axis) and its transverse expansion along the target surface (x -axis) in a two-dimensional Cartesian geometry.

For convenience the formulas of this section are given in CGS units in agreement with the original publication [142]. In comparison to the typical timescale of the ionic motion, the laser pulse duration is very short [143]. For this reason, it can be assumed that the ion acceleration does not start before the end of the laser-plasma-interaction and that the energy transfer between hot electrons and ions follows the adiabatic law

$$\frac{p_{\text{eh}}}{n_{\text{eh}}^\gamma} = \frac{T_{\text{eh}}}{n_{\text{eh},0}^{\gamma-1}}. \quad (10.1)$$

Here, p_{eh} and n_{eh} represent the pressure and the density of hot electrons, respectively. Their initial temperature is denoted by T_{eh} and their initial density by $n_{\text{eh},0}$. The adiabatic parameter $\gamma = (2 + N)/N$ is defined depending on the number of degrees of freedom N . In comparison to the motion of the hot electrons within the foil, the ion acceleration is a slow process. Therefore, the electron inertia can be neglected in the standard force equation for the density [144]. Hence, the equation of the force in one direction can be written in the reduced form

$$\frac{\partial \varphi}{\partial z} = \frac{1}{e n_{\text{eh}}} \frac{\partial p_{\text{eh}}}{\partial z}, \quad (10.2)$$

whereby φ is the electric potential and e the electron charge. By substituting the adiabatic Equation 10.1 into Equation 10.2 the hot electron density n_{eh} can be expressed as a function of the potential φ of the ambipolar field

$$n_{\text{eh}}(\varphi) = n_{\text{eh},0} \left(1 + \frac{\gamma - 1}{\gamma} \frac{e\varphi}{T_{\text{eh}}} \right)^{\left(\frac{1}{\gamma-1}\right)}. \quad (10.3)$$

By considering a two-dimensional expansion ($\gamma = 2$) the relationship between the hot electron density n_{eh} and the potential φ becomes linear. In this case the normalized hot electron density $\eta_{\text{eh}} = n_{\text{eh}}/n_{\text{eh},0}$ can be written as

$$\eta_{\text{eh}}(\varphi) = 1 + \frac{|e|\varphi}{2T_{\text{eh}}}. \quad (10.4)$$

As a consequence of the laser-matter interaction, hot electrons are accelerated and leave the foil. A positively charged spot is induced on both sides of the target that keeps most of the hot electrons in close proximity. As a result a cloud of hot electrons is formed that circulates through the ultra-thin target while it expands in transverse direction. The net positive charge density $\rho(x, z)$ on the foil is composed of the charge density of cold ions $\rho_{\text{ic}} = eZ_i n_i(x, z)$ and the charge density of cold electrons $\rho_{\text{ec}} = e n_{\text{ec}}$ and can be written as

$$\rho(x, z) = \rho_{\text{ic}} + \rho_{\text{ec}}. \quad (10.5)$$

In the presented model the net positive charge density of Equation 10.5 is approximated by the formula

$$\rho(x, z) = e n_{\text{eh},0} \eta(\xi) \delta(\zeta), \quad (10.6)$$

whereby the coordinates $\xi(x) = x/r_{\text{D}}$ and $\zeta(z) = z/r_{\text{D}}$ are normalized to the Debye radius of hot electrons

$$r_{\text{D}} = \sqrt{\frac{T_{\text{eh}}}{4\pi e^2 n_{\text{eh},0}}}. \quad (10.7)$$

The Dirac-delta function is designated by $\delta(\zeta)$ and the dimensionless function $\eta(\xi)$ describes the transverse profile of the charge density. The given approximation is only valid if the target is thin compared to the Debye radius of hot electrons r_{D} and if the temporal contrast ratio of the laser pulse is sufficiently high [142]. In the latter case any amplified spontaneous emission or pre-pulse-driven plasma dynamics before the pulse peak can be neglected.

In order to describe the dynamics of the charge density $\rho(x, z, t)$, a temporal dependence of the transverse profile $\eta(\xi, t)$ is assumed. The change of the normalized transverse scale of the positively charged spot $l(t) = L(t)/r_{\text{D}}$ is used to mimic the change of the transverse profile $\eta(\xi, t) = \eta(\xi, l(t))$

Using Equation 10.4 and Equation 10.6, the two-dimensional Poisson equation $\Delta\varphi = 4\pi(-\rho(x, z) + en_{\text{eh}}(\varphi))$ can be expressed in terms of the electron density

$$2 \left(\frac{\partial^2}{\partial \xi^2} + \frac{\partial^2}{\partial \zeta^2} \right) \eta_{\text{eh}} = \eta_{\text{eh}} - \eta(\xi, l(t)) \delta(\zeta). \quad (10.8)$$

Using the modified Bessel function of second kind K_0 the known solution of this equation [145] can be expressed as

$$\eta_{\text{eh}}(\xi, \zeta, l(t)) = \frac{1}{4\pi} \int \eta(\tilde{\xi}, l(t)) K_0 \left(\sqrt{\frac{\zeta^2}{2} + \frac{(\xi - \tilde{\xi})^2}{2}} \right) d\tilde{\xi}. \quad (10.9)$$

The Poisson equation does not contain time derivatives. Therefore, the time variable appears as one of the parameters in the solution. Substitution of Equation 10.9 into Equation 10.4 leads to an expression for the electric potential $\varphi(x, z, l(t)) = \tilde{\varphi}(\xi(x), \zeta(z), l(t))$, whereby $\tilde{\varphi}$ is the potential in normalized coordinates

$$\tilde{\varphi}(\xi, \zeta, l(t)) = \frac{T_{\text{eh}}}{2\pi|e|} \int \eta(\tilde{\xi}, l(t)) K_0 \left(\sqrt{\frac{\zeta^2}{2} + \frac{(\xi - \tilde{\xi})^2}{2}} \right) d\tilde{\xi}. \quad (10.10)$$

Therefore, the choice of the transverse profile $\eta(\xi, l(t)) = \eta_0 \cdot \rho_\eta(\xi, l(t))$ determines the electrostatic energy of the hot electrons, whereby $\rho_\eta(\xi, l(t))$ is a normalized distribution. In the following different profiles, such as the Lorentzian distribution

$$\eta(\xi, l(t)) = \eta_0 \cdot \rho_\eta(\xi, l(t)) = \frac{\eta_0}{\pi l(t)} \frac{1}{(1 + \xi^2/l(t)^2)} \quad (10.11)$$

or the Gaussian distribution

$$\eta(\xi, l(t)) = \eta_0 \cdot \rho_\eta(\xi, l(t)) = \frac{\eta_0}{n_g l(t)} \exp \left[- \left(\frac{\xi}{l(t)} \right)^2 \right] \quad (10.12)$$

with $n_g = 1.772$ are used. The amplitude of the transverse profile is determined by the parameter

$$\eta_0 = \frac{4\pi e^2 N_{\text{eh}}}{T_{\text{eh}} D_e}, \quad (10.13)$$

whereby N_{eh} denotes the number and T_{eh} the temperature of hot electrons. The initial electron spot size is named D_e . The number of fast electrons can be estimated [142] by the ratio of the absorbed laser energy and the thermic energy of the electrons

$$N_{\text{eh}} \approx \frac{A_b(l_n) \cdot 10^7 \cdot I_L \cdot \pi r_L^2 \cdot \tau_L}{T_{\text{eh}}}. \quad (10.14)$$

The average energy absorption [143]

$$A_b(l_n) = A_{b0} \frac{\ln(1 + l_n/T_{r0})}{1 + \ln(1 + l_n/T_{r0})} \quad (10.15)$$

depends on the target thickness Δa via the parameter $l_n = \Delta a \cdot \omega_{pe}/c$, whereby A_{b0} is the absorption coefficient and T_{r0} the transmission coefficient. In Equation 10.14 the FWHM of the maximum laser intensity corresponds to $2 \cdot r_L$, whereas I_L is the mean intensity within the enclosed circle πr_L^2 . An estimation for the hot electron density [146] is obtained using the following equation

$$T_{eh} [erg] \approx 10^7 \cdot \left[\left(\frac{A_{b0}(l_n) \cdot I_L \cdot \tau_L}{n_{ec,0}(l_n + 0.2)c/\omega_{pe}} \right) + \left(m_e c^2 \left(\sqrt{1 + \frac{\lambda_L^2 I_L}{1.38 \cdot 10^{10}}} - 1 \right) \right) \right]. \quad (10.16)$$

Here, the left part accounts for the directly absorbed energy per electron and the right part for the ponderomotive potential of hot electrons in the laser focus. The initial cold electron density

$$n_{ec,0} = Z_i n_{i,0} \quad (10.17)$$

is used in Section 10.4.2 as a free model variable in order to approximate the experimental results.

The dynamics of the charged region of the target surface can be described as follows: at the time $t = 0$ the solution of the Poisson equation corresponds to a quasi-neutral solution. The electric field goes to zero for both $\xi \rightarrow \infty$ and $\zeta \rightarrow \infty$. For $t > 0$, the expansion of hot electron leads to a flow of cold electrons from the target periphery in the direction of the charged region. This frustrates the quasi-neutral state and leads to a variation of the width $l(t)$.

The charge conservation law for all particles in the foil at the point $\xi = l$ in its differential form

$$dl \int \eta_{eh}(l, \zeta) d\zeta + d\tau l_f j_c = dl \eta(l), \quad (10.18)$$

allows the transverse dynamics of electron spot size to be deduced. Here, $l_f = \Delta a/r_D$ represents the normalized thickness of the foil and $j_c = j_{cold}/(e n_{eh,0} c)$ describes the dimensionless density of the cold electron current. According to Equation 10.18 the spot expansion is connected to the target conductivity. At first, the electron electrostatic energy is redistributed over a larger area and the spot dimension increases. In this initial stage the solution of Equation 10.18 can be approximated by a diffusion law. Later, when the expansion time is of the order of the effective time of collisions $1/\nu_{ef}$, the expansion decays exponentially and the diffusion law is no longer applicable. An appropriate expression for the expansion of the electron spot size is given by

$$l(t) = \sqrt{l_0^2 + \frac{\kappa}{\nu_{ef}} (1 - e^{-\nu_{ef} t})}. \quad (10.19)$$

Here $l_0 = L(0)/r_D$, $\kappa = a_p(\sigma_{\text{cold}}/\omega_{ph})l_f$ and $a_p \sim 1$ is a constant that depends on the charge density profile. The effective collision time is given by ν_{ef}^{-1} and $\tau = \omega_{ph}t$. The plasma frequency of hot electrons is $\omega_{ph} = \sqrt{4\pi e^2 n_{\text{eh}}/m_e}$. An estimation for the density of hot electrons is given by

$$n_{\text{eh}} \approx \frac{N_{\text{eh}}}{\pi D_e^2 \cdot r_D} \simeq \frac{N_{\text{eh}}^2 e^2}{\pi D_e^4 T_{\text{eh}}}, \quad (10.20)$$

whereby Formulas 10.14 and 10.7 are used to rearrange the equation. The conductivity of the solid plasma target can be estimated by $\sigma_{\text{cold}} \approx \frac{\omega_{pc}}{4\pi}$. In this connection the influence of the magnetic field was neglected. This is possible, because in the presented case the gyro-frequency of the cold electrons is lower than the plasma frequency $\omega_{pc} = \sqrt{4\pi e^2 n_{\text{ec},0}/m_e}$. Using a Taylor expansion to approximate the exponential decay $\exp(-\nu_{\text{ef}}\tau)$, the spot size expansion (Equation 10.19) can be described in first order

$$l(t) = \sqrt{l_0^2 + \kappa\tau} = \sqrt{l_0^2 + v_e t}, \quad (10.21)$$

whereby $v_e = \frac{\Delta a}{r_D} \frac{\omega_{pc}}{4\pi}$. However, in the presented case $v_e = \frac{\Delta a}{r_D} \frac{\omega_{pc}}{0.5}$ was used, which considers a better calibration of the conductivity σ_{cold} , as suggested by A. Andreev in a private communication.

Electric Field Components

The electric field components in normalized coordinates are obtained by means of Equation 10.10 and the equations

$$\tilde{E}_\xi(\xi, \zeta, l(t)) = -\frac{\partial}{\partial \xi} \tilde{\varphi}(\xi, \zeta, l(t)), \quad \tilde{E}_\zeta(\xi, \zeta, l(t)) = -\frac{\partial}{\partial \zeta} \tilde{\varphi}(\xi, \zeta, l(t)). \quad (10.22)$$

Using the modified Bessel function of second kind K_1 allows these components to be written in the form

$$\tilde{E}_\xi(\xi, \zeta, l(t)) = \frac{T_{\text{eh}}}{4\pi|e|} \int \frac{\eta(\tilde{\xi}, l(t)) \cdot (\xi - \tilde{\xi})}{\sqrt{\zeta^2 + (\xi - \tilde{\xi})^2}} K_1 \left(\sqrt{\frac{\zeta^2}{2} + \frac{(\xi - \tilde{\xi})^2}{2}} \right) d\tilde{\xi}, \quad (10.23)$$

$$\tilde{E}_\zeta(\xi, \zeta, l(t)) = \frac{T_{\text{eh}}}{4\pi|e|} \int \frac{\eta(\tilde{\xi}, l(t)) \cdot \zeta}{\sqrt{\zeta^2 + (\xi - \tilde{\xi})^2}} K_1 \left(\sqrt{\frac{\zeta^2}{2} + \frac{(\xi - \tilde{\xi})^2}{2}} \right) d\tilde{\xi}. \quad (10.24)$$

Using these formulas the electric field components in real space can be expressed as

$$E_x(x, z, l(t)) = \frac{1}{r_D} \cdot \tilde{E}_\xi(\xi(x), \zeta(x), l(t)), \quad (10.25)$$

$$E_z(x, z, l(t)) = \frac{1}{r_D} \cdot \tilde{E}_\zeta(\xi(x), \zeta(x), l(t)). \quad (10.26)$$

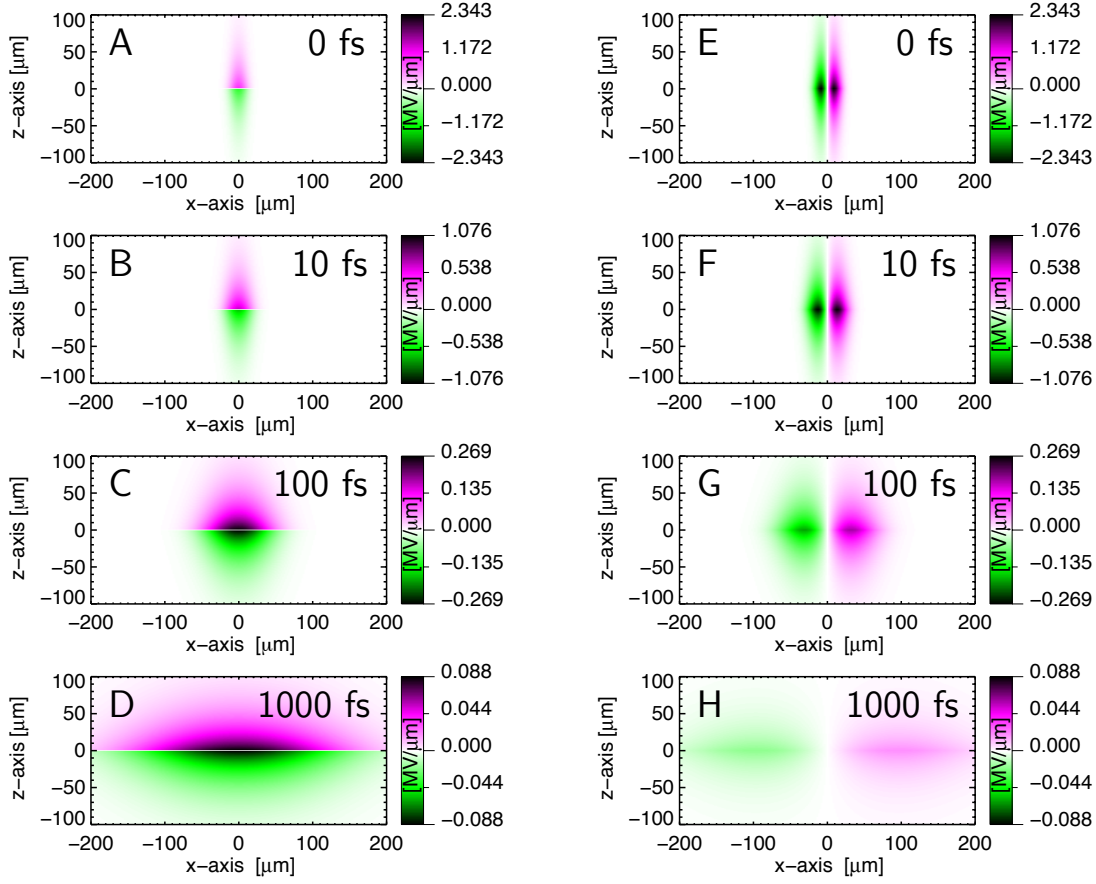


Figure 10.14: Temporal evolution of the normal (A - D) and radial (E - H) electric field components in the x-z-plane ($y=0$).

The numerical computation time of the Expressions 10.23 and 10.24 is relatively long and limits their applicability for numerical particle simulations. For this reason, fast approximations are proposed, which were tested and used in the simulations of Section 10.4. These approximations are given by the formulas

$$\begin{aligned} \tilde{E}_\xi(\xi, \zeta, l(t)) \approx & \frac{-T_{\text{eh}}}{\sqrt{2}|e|} \frac{\partial \eta(\xi, l(t))}{\partial \xi} \left[H \left(\left| \zeta \right| - \frac{l_n c}{2\omega_{pe} r_D} \right) \exp \left(-\frac{1}{\sqrt{2}} \left(\left| \zeta \right| - \frac{l_n c}{2\omega_{pe} r_D} \right) \right) \right. \\ & \left. + H \left(\left| \zeta \right| + \frac{l_n c}{2\omega_{pe} r_D} \right) \right], \end{aligned} \quad (10.27)$$

$$\tilde{E}_\zeta(\xi, \zeta, l(t)) \approx \frac{T_{\text{eh}}}{2|e|} \eta(\xi, l(t)) S(\zeta) H \left(\left| \zeta \right| - \frac{l_n c}{2\omega_{pe} r_D} \right) \exp \left(-\frac{1}{\sqrt{2}} \left(\left| \zeta \right| - \frac{l_n c}{2\omega_{pe} r_D} \right) \right). \quad (10.28)$$

Here, the help functions $H(x)$ and $S(x)$ are defined as follows

$$H(x) = \begin{cases} 1, & \text{if } x > 0, \\ 0, & \text{if } x \leq 0, \end{cases}, \quad S(x) = \begin{cases} 0, & \text{if } x = 0, \\ x/|x|, & \text{if } x \neq 0. \end{cases} \quad (10.29)$$

Figure 10.14 illustrates the spatial distribution of the normal and radial electric field components in the x-z-plane (Equations 10.25 and 10.26) at different moments in time. The model parameters which were used for the shown field calculations are summarized in Table 10.1.

Magnetic Field Component

An approximation for the magnetic field component in normalized coordinates can be written as

$$\begin{aligned} \tilde{B}_\psi(\xi, \zeta, l(t)) \approx & \sqrt{2\pi} \frac{v_B(t)}{c} \frac{T_{eh}}{|e|} \eta(\xi, l(t)) S(\xi) S(\zeta) \\ & \times H\left(|\zeta| - \frac{l_n c}{2\omega_{pe} r_D}\right) \exp\left(-\frac{1}{\sqrt{2}} \left(|\zeta| - \frac{l_n c}{2\omega_{pe} r_D}\right)\right), \end{aligned} \quad (10.30)$$

whereby the function $v_B(t)$ is defined by

$$v_B(t) = \frac{1}{\omega_{eh}} \cdot \frac{\partial}{\partial \xi} l(t) = \frac{1}{\omega_{eh}} \cdot \frac{v_e}{2\sqrt{l_0^2 + v_e t}}. \quad (10.31)$$

The magnetic field component in real coordinates is obtained by

$$B_y(x, z, l(t)) = \frac{1}{r_D} \cdot \tilde{B}_\psi(\xi(x), \zeta(x), l(t)). \quad (10.32)$$

Using this equation and the model parameters of Table 10.1 the magnetic field that points in $(\mathbf{z} \times \mathbf{x})$ -direction is calculated. Figure 10.15 shows its spatial distribution at different moments in time.

10.3.2 Model B - The Electric Field of an Expanding Proton Front

In principle, the presented model is based on the analytical field description of Section 9.4.1 using the isothermal approximation. However, the model is modified for the use in multi-dimensional particle simulations. The description of the electric field is extended to three spatial dimensions [79], by assuming a Gaussian decay of the electric field strength in radial direction

$$E(r, z, t) = E(z, t) \cdot \exp\left[-(r/l_r)^2\right], \quad (10.33)$$

whereby $E(z, t)$ is given by Equation 9.3 and $r = \sqrt{x^2 + y^2}$.

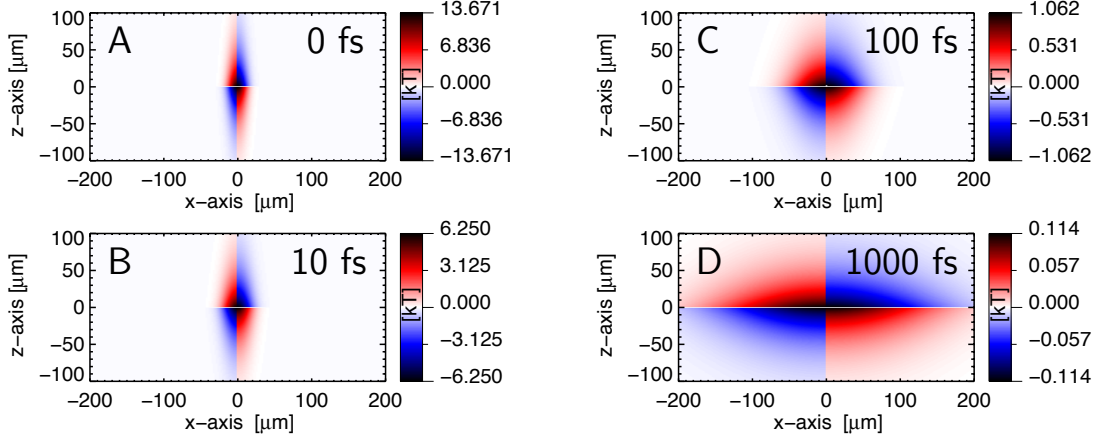


Figure 10.15: Temporal evolution of the magnetic field in the x-z-plane ($y=0$). The field vector points in $(\mathbf{z} \times \mathbf{x})$ -direction.

10.3.3 Model C - Analytic Description of Magnetic Fields on Thin Foil Targets

Model C is a simple approach to describe the laser-induced magnetic field distribution and evolution on thin foil targets. It is used in Section 10.4.3 to reproduce the observed proton deflections in longitudinal probing geometry which are caused by the interaction of a ultra-thin foil with a picosecond laser pulse.

The model is only an analytical field description and not a self-consistent physical model which relies on any plasma and laser parameters. In principle, the model is based exclusively on variables that determine the temporal and spatial dependence of the field itself. These are the constant field amplitude B_0 , the effective temporal field duration t_c as well as the field scale length L_{\parallel} and L_{\perp} which are directed parallel and perpendicular to the foil surface, respectively. However, to allow for a comparison to existing models, such as the thermoelectric magnetic field generation (cf. Section 4.3), the field amplitude B_0 is connected with the electron temperature T_e via equation

$$B_0 = 2 \cdot \left(\frac{T_e}{10^3} \right) \left(\frac{L_{\parallel}}{10^{-6}} \right)^{-1} \left(\frac{L_{\perp}}{10^{-6}} \right)^{-1} \cdot 100 \text{ [Tesla]}, \quad (10.34)$$

which is defined in the style of Equation 4.17. The temporal and spatial distribution of the field is given by

$$B(t, y, z) = B_0 \cdot B_t(t) \cdot B_{\parallel}(r) \cdot B_{\perp}(z), \quad (10.35)$$

whereby the temporal dependence is described by a triangular function

$$B_t(t) = \begin{cases} 0, & \text{if } t < t_0, \\ 0, & \text{if } t > t_2, \\ \begin{cases} \frac{t-t_0}{t_1-t_0}, & \text{if } t \leq t_1, \\ 1 - \frac{t-t_0}{t_2-t_1}, & \text{if } t > t_1, \end{cases} & \text{else.} \end{cases} \quad (10.36)$$

Here, t_0 indicates the begin of the interaction, t_1 the time when the maximum field is reached and t_2 the time when the field drops back to zero. The time duration of the magnetic field t_c is connected with these temporal parameters via the equations $t_0 = t_{\text{pump}}$, $t_1 = t_{\text{pump}} + t_c/2$ and $t_2 = t_0 + t_c$. The radial dependence of the field is described by

$$B_{\parallel}(r) = \begin{cases} \left(\frac{r}{L_{\parallel}}\right)^{2n-1}, & \text{if } 0 \leq |r| \leq L_{\parallel}, \\ \left(\frac{L_{\parallel}}{r}\right)^{1/k}, & \text{if } |r| > L_{\parallel}, \end{cases} \quad (10.37)$$

whereby the exponential parameters n and k describe the field increase and decay. The spatial field distribution along the target normal direction is modeled in a similar way by

$$B_{\perp}(z) = \begin{cases} \left(\frac{z}{L_{\perp}}\right)^{2n-1}, & \text{if } |z| \leq L_{\perp}, \\ \begin{cases} \left(\frac{L_{\perp}}{z}\right)^{1/k}, & \text{if } z > 0 \\ -\left(\frac{L_{\perp}}{z}\right)^{1/k}, & \text{if } z < 0 \end{cases} & \text{if } |z| > L_{\perp}. \end{cases} \quad (10.38)$$

10.4 Modeling of the Experiments and Particle Simulations

In order to draw conclusions on the laser-induced fields, the analytical models of Section 10.3 are applied in order to explain the measured streak deflections and energy redistribution effects of Section 10.2.1 and 10.2.2. The applicability of the individual analytic field description is tested by means of three-dimensional particle simulations, which can reproduce the streak deflectometry measurements to some extent.

10.4.1 Simulation Concept

In principle, the measurements can be reproduced by simulating the proton imaging experiment itself. For this purpose a particle tracer [102] is used to calculate the trajectories of protons that propagate through a simulated streak deflectometry environment (Figure 10.1) in longitudinal or transversal configuration.

At the beginning of the simulation N protons are initiated at the position $z_0 = 0$ and are uniformly distributed within a defined region on the x-y-plane. Each particle starts with a velocity component in x-, y- and z-direction. The initial divergence angles $\beta = \text{atan}(v_x/v_z)$ and $\gamma = \text{atan}(v_y/v_z)$ are set depending on the initial particle position via $x/r_S = \beta/\alpha_v$ and $y/r_S = \gamma/\alpha_v$, with r_S as is the radius of the simulated source size. It is defined by Equation B.2 and has a value of $14 \mu\text{m}$. For its calculation the maximum opening angle $\alpha_v = 17 \text{ mrad}$ and the virtual source distance of $|z_v(\epsilon)| = 0.82 \text{ mm}$ are used, which are determined in Section B.1 of the appendix.

In order to model the characteristic emission of a laser ion source a specific energy distribution could be applied in simulation, for example an isothermal distribution. However, the exact initial distribution is not known for each measurement and must be approximated. Therefore, another approach is used for the presented simulations. In longitudinal configuration the particles start with a uniform energy distribution and in transversal configuration the particles are initiated with energies that lead to a uniform distribution of their arrival time at the interaction target ($x=0, y=0, z=a$). This approach allows for an easy interpretation of the simulated deflections and reduces the computation time.

When the simulation starts, the protons first propagate through an object that simulates the beam mask. Each particle that impinges on a bar of the grating at $z = m$ is removed from the simulation. The remaining particles are further dispersed in space while they propagate in the direction of the interaction region at $z = a$.

At the simulation time $t = t_{\text{pump}}$ the electro-magnetic fields at the interaction zone are calculated according to the applied analytical model. The calculated fields are located around the central interaction point ($x=d, y=0, z=a$) and their direction is adapted to the orientation of the interaction target in longitudinal or transversal probing configuration, respectively. By means of a fifth order Runge-Kutta algorithm with adaptive stepsize control the trajectory change of each particle within the field is calculated. Following this, all particles which do not pass through the opening of the simulated slit at $z = L_1$ are removed from the simulation.

At this point, the influence of the interaction fields is negligible and the assumption that each particle has reached its final velocity and propagation direction is reasonable. In principle these parameters are already sufficient to calculate the simulated proton density distribution $\tilde{\rho}_S$ depending on energy and ejection angle. However, this approach does not account for the influence of the static electro-magnetic fields within the spectrometer. Therefore, the proton density distribution on the detector plane $\rho(x, y)$ cannot be reproduced. In order to visualize the simulated distribution in the same coordinate system as the experimental data $\tilde{\rho}(\beta, \epsilon)$, the coordinate transformation of Chapter 5.4 must be used, which is based on the condition that the initial particle movement is restricted to the x-z-plane.

For this reason, the trajectory of each proton within the spectrometer is calculated. This is possible, because the static electro-magnetic field distribution within the

permanent magnet ($z \approx L_2$) was measured (Section 5.4). This way the point of impact (x_p, y_p) on the detector plane ($z = L_3$) is determined for each particle in the simulation. In a reference simulation, the initial velocity components v_y of all initiated particles are set to zero and the electromagnetic interaction fields are not considered. As described in Section 5.4 this allows for the definition of a bijective relation between the pair (β, ϵ) and the point of impact at the detector (x_p, y_p) , where β is the initial ejection angle in the x-z-plane and the ϵ the initial proton energy. Using the coordinate transformation of Equation 5.12 the simulated proton density distribution $\tilde{\rho}_S(\beta, \epsilon)$ can be described in the same orthogonal coordinate system as the experimental data. In the following sections two different simulation types are applied:

- Type A - The simulated protons possess velocity components v_y in y-direction at $t = 0$ and enter the spectrometer region through a slit opening with a finite extension in y-direction, as in the experiment. Therefore, the energy resolution of the setup is intrinsically considered in the simulation.
- Type B - The initiated particles ($t = 0$) are distributed along the x-axis and have no velocity components v_y in y-direction. Since the force vectors of the electric and magnetic field components also have no components in y-direction at $y = 0$, the particle motion is restricted to the x-z-plane until the spectrometer region is reached. This is valid for all applied analytical field descriptions. For this reason, the simulation results do not account for the resolution of the spectrometer, but can reflect the action of the calculated electromagnetic fields in the x-z plane at $y=0$. In addition the computation time can be reduced significantly in comparison to type A.

10.4.2 Field Effects due to Ultra-short Laser Pulses

In order to draw conclusions on the field effects that are initiated on ultra-thin foils by means of ultra-short laser pulses, the experimental observations of Section 10.2.1 are investigated further. For this purpose, the analytical models of Section 10.3.1 and Section 10.3.2 are used to reproduce the particular features of the measured streak deflections and energy redistribution effects. It will be shown that the measurements in longitudinal and transversal configuration can be explained using different analytical models. The proposed models can describe different properties of the field and do not contradict each other in principle. A combination of both models is partly complementary and allows for a relatively consistent explanation of the experimental observations.

The following section is structured as follows. To begin, model A (Section 10.3.1) is applied to reproduce the redistribution effects and streak deflections that were measured in longitudinal configuration. Following this, model B (Section 10.3.2)

is used to explain the streak deflectometry measurements in transversal configuration. Subsequently it will be discussed why why model B is not applicable to reproduce the measurements in longitudinal configuration and why model A is not suitable to describe the observations of the transversal probing geometry. Then a combination of both models is introduced which allows a more accurate reproduction of the measured effects in both configurations. Finally, the limitations of both models and of their combination are discussed and conclusions are drawn.

Longitudinal Configuration - Model A

In order to reproduce the redistribution effects and streak deflections which were measured in longitudinal configuration the analytical model of Section 10.3.1 (model A) is used to simulate the electro-magnetic field generation on an ultra-thin foil due to the interaction with an ultra-short high intensity laser pulse. The applied model and simulation parameters are summarized in Table 10.1 and are chosen in agreement with the experimental conditions. In order to reproduce the measurements of Figure 10.16 quantitatively, the model variables $n_{ec,0}$ and D_e were adjusted.

Model Variables		
$n_{ec,0}$	$5 \cdot 10^{22}$	$1/\text{cm}^3$
D_e	12.5	μm
Model/Simulation Parameters		
I_L	$3.0 \cdot 10^{19}$	W/cm^2
τ_L	50	fs
r_L	2.5	μm
a	36.5 (35.0)	mm
Δa	30	nm
T_{r0}	0.5	1
A_{b0}	0.4	1
ϵ_{pump}	2.4 (2.6)	MeV
Parameter	Value	Unit

Table 10.1: Model variables and simulation parameters. The values in brackets are used for simulations in transversal configuration.

Calculated Model Parameters		
l_n	1.26	1
$A_b(l_n)$	0.22	1
T_{eh}	13.7	MeV
Φ_p	1.5	MeV
N_{eh}	$3.0 \cdot 10^{10}$	1
$n_{eh,0}$	$1.2 \cdot 10^{18}$	$1/\text{cm}^3$
ω_{pc}	$1.3 \cdot 10^{16}$	1/s
ω_{ph}	$6.3 \cdot 10^{13}$	1/s
r_D	24.5	μm
l_f	$1.3 \cdot 10^{-3}$	1
v_e	$3.1 \cdot 10^{13}$	1/s
η_0	3.2	1
Parameter	Value	Unit

Table 10.2: Calculated model parameters. The shown quantities are obtained using the equations of Section 10.3.1 and the variables and parameters of Table 10.1.

In the presented case an initial electron density $n_{ec,0}$ of $5 \cdot 10^{22} 1/\text{cm}^3$ is assumed. This density is 6 times lower than the solid state electron density ($n_{ec,0} \approx 3 \cdot 10^{23} 1/\text{cm}^3$) of the plastic foil which was used in the experiment. However, simu-

lations with higher initial particle densities ($n_{ec,0} > 5 \cdot 10^{22} \text{ 1/cm}^3$) cannot reproduce the experimental results. As described in Section 10.3.1, the applied model assumes that the ion acceleration does not start before the end of the laser-plasma interaction and that the energy transfer between hot electrons and ions follows the adiabatic law of Equation 10.1. In experiments, the rising edge of the main laser pulse can ionize the target material even before the peak intensity is reached (Section 2). When the matter expands into vacuum, the density declines. For this reason, a lowering of the initial particle density n_i in simulation is reasonable.

The second model variable is the initial electron spot size D_e , which is set to a value of $12.5 \mu\text{m}$ in the presented case. A value $D_e > r_L$ is reasonable [142], because the model does not account for the rising edge of the main laser pulse and the plasma creation process.

Using the proposed model parameters (Table 10.1) and the equations of Section 10.3.1 a variety of characteristic plasma and field parameters are determined (Table 10.2), which are necessary for the calculation of the electromagnetic field distribution. In addition to these parameters the analytical model requires the selection of a function η , which describes the transverse profile of the charge density. For the presented simulations either Gaussian (Equation 10.12) or a Lorentzian (Equation 10.11) distributions are used, as proposed in [142].

Figure 10.14 illustrates the temporal evolution of the normal and radial electric field components, using a Gaussian distribution and the parameters of Table 10.1 and 10.2. The evolution of the magnetic field is shown in Figure 10.15.

In order to include the analytic field description of model A into the particle simulation, the electro-magnetic fields of Equations 10.25, 10.26 and 10.32 are extended to three dimensions by assuming a cylinder symmetric field dependence along the z-axis.

For the simulation results in Figure 10.16 simulation type B (Section 10.4.1) was applied. In the case of Figure 10.16.A a Lorentzian distribution is used to describe transverse profile of the charge density η , whereas in Figure 10.16.B a Gaussian profile is applied. For a direct comparison the corresponding streak deflectometry measurement of Section 10.2.1 is depicted in Figure 10.16.C. In contrast, Figure 10.17 shows the result of simulation type A, which accounts for the energy resolution of the spectrometer. In view of all simulation results, it is apparent that the proposed analytical description of Section 10.3.1 (model A) can qualitatively and quantitatively reproduce the main features of the measurement.

- The simulated proton distributions $\tilde{\rho}_S(\beta, \epsilon)$ exhibit the prominent density dips in the energy range of the selected proton t-pump energy ϵ_{pump} .
- The dips are most pronounced near the center of the interaction ($|x_F| = 0$).
- The outward bending of the proton stripes is clearly visible at the low energy side of the density gaps and is stronger in the vicinity of the interaction center. At the high energy side the bending is only slightly indicated.

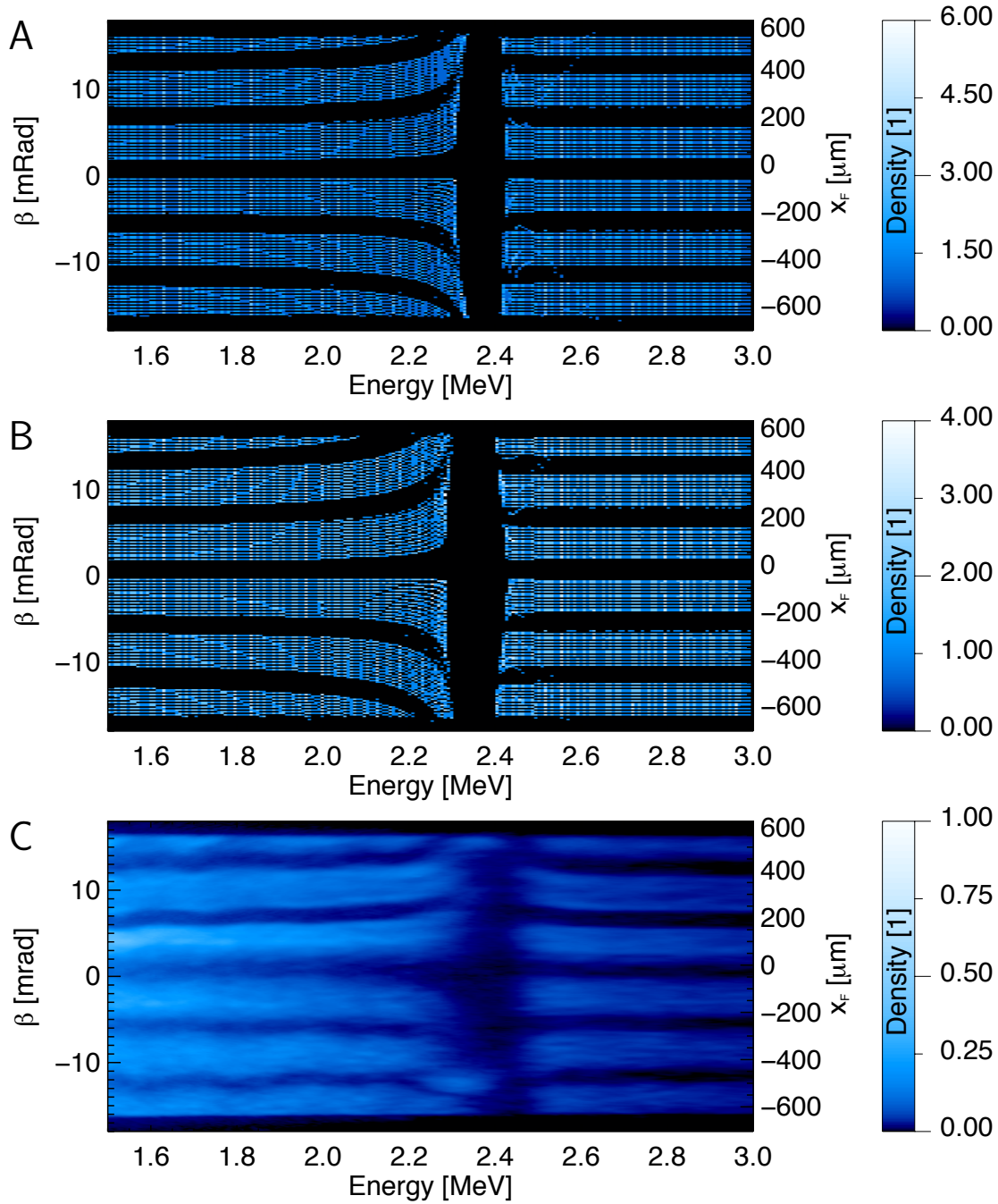


Figure 10.16: Simulated (model A) and experimentally obtained proton density distribution $\tilde{\rho}(\beta, \epsilon)$ in longitudinal configuration. **A** - The simulation result is obtained using a Lorentzian distribution of the charge density η . **B** - The simulation result is obtained using a Gaussian distribution of the charge density η . **C** - Result of the streak deflectometry measurement (Section 10.2.1).

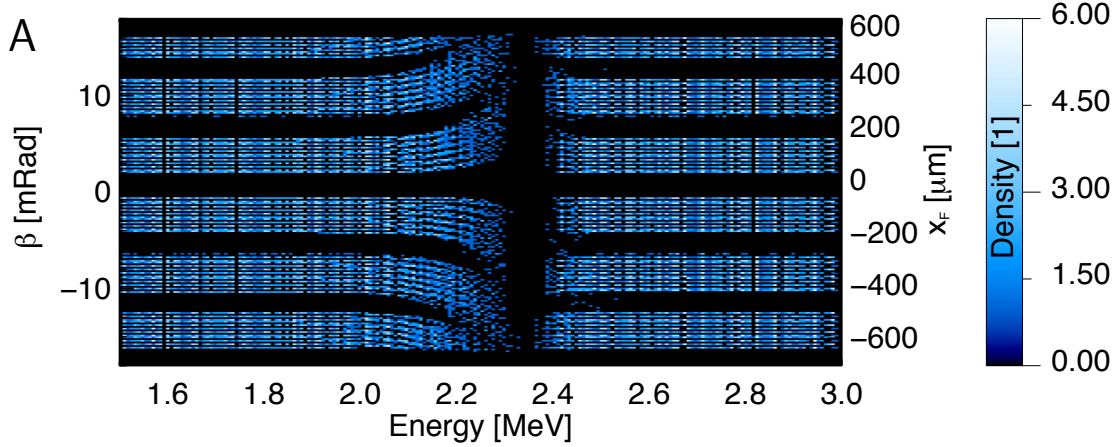


Figure 10.17: Simulated proton density distribution $\tilde{\rho}(\beta, \epsilon)$ in longitudinal configuration. For the simulation Lorentzian distribution of the charge density η was used. In addition the spectrometer resolution was taken into account

- An overlap between different proton stripes at the low energy side of the density gaps is slightly indicated by the simulation.

However, the model cannot explain the occurrence of the density gap for higher values of $|x_F| \gtrsim 700 \mu\text{m}$ (Figure 10.9).

The applied model is intended to describe the electric field configuration at the surface of an ultra-thin foil. Therefore, the model should not only explain the observed streak deflections and energy redistribution effects, but also the proton acceleration on the interaction target itself.

In order to calculate the energy gain of a proton that is accelerated within the proposed field configuration a one-dimensional particle simulation (9.4.2) was conducted. In this simulation the particle is initially at rest and located at the position $(x_0 = 0 \text{ nm}, y_0 = 0 \text{ nm}, z_0 = 30 \text{ nm})$ and the main acceleration field is directed along the z -axis. The electromagnetic field distribution is determined using the same set of parameters as in the shown streak deflectometry simulations (Table 10.1). Using a Gaussian distribution of the charge density η a final proton energy of 2.75 MeV is calculated. After the simulation time of 5 ps the acceleration is almost finished. At this time the particle has gained the energy of 2.66 MeV and is located at $z \approx 90 \mu\text{m}$. The calculated position and velocity of the proton is illustrated in Figure 10.18. Experimentally, the proton spectrum that originates purely from the rear side of the 30 nm CH foil was measured in several different shots. In this connection cut-off energies ranging from 2.4 MeV to 3.0 MeV were found (cf. Figures 10.4.B, 10.6 and 10.7).

In case of the Gaussian distribution η , the numerical result is in good agreement with the experimentally obtained values.

If a Lorentzian distribution is used to describe the charge density η a final proton

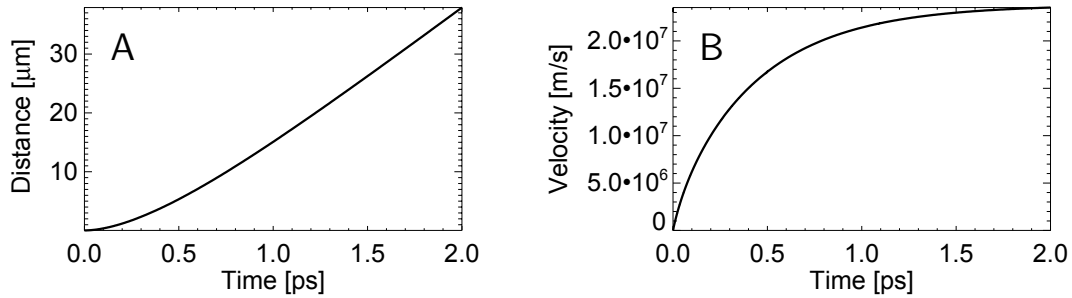


Figure 10.18: Time dependence of the position (**A**) and the velocity (**B**) of a proton. For the numerical calculation of the acceleration process model A was applied. In addition a Gaussian distribution of the charge density η and the model parameters of Table 10.1 and Table 10.2 were used.

energy of 1.3 MeV is calculated. This value is approximately two times smaller than the measured cut-off energies. This is consistent with the simulation result of Figure 10.16.A which exhibits a gap width that is significantly smaller than the experimental result.

In principle, the measurement of the cut-off energy in combination with the numerical determination of the maximum proton energy offers a possibility to eliminate one of the model variables. For instance for a given function of the charge distribution η and a fixed value of n_{eh} , the variable D_e can be varied in order to match the calculated maximum proton energy and the measured cut-off energy.

As illustrated in Figure 10.15 the magnetic field shows values up to 10^4 T, which is in agreement with the findings in reference [130]. All simulations were conducted with consideration of the magnetic field (Formula 10.32). However, it has been found that its influence on the simulated streak deflections is negligible in comparison to the influence of the radial field component (Formula 10.25), which acts in the same direction.

In conclusion model A allows for a good quantitative approximation of the measurements in longitudinal probing geometry. For this reason, it can be applied to conclude about the acting electric and magnetic field evolution and to determine characteristic plasma parameters (Table 10.2).

Transversal Configuration - Model B

In order to reproduce the streak deflectometry measurements which were measured in transversal configuration, the analytical model of Section 10.3.2 (model B) is applied to simulate the electric field of an expanding ion front in three dimensions. The parameters which are required to calculate the field distribution in simulation are summarized in Table 10.3. The maximum front velocity $v_{f,\text{max}} \approx 2.35 \cdot 10^7$ m/s is chosen in agreement with the measured proton energy cut-off, showing values

between 2.5 MeV and 3.0 MeV (cf. Figures 10.4 to 10.7). The electric field amplitude factor \mathcal{E}_c is determined by Equation 4.6 using the hot electron density n_{eh} and temperature T_{eh} of Table 10.2.

Model Parameters		
\mathcal{E}_c	$5.0 \cdot 10^{11}$	MV/ μm
$v_{f,\text{max}}$	$2.35 \cdot 10^7$	m/s
τ_s	300	fs
l_s	0.25	μm
l_r	400	μm
Parameter	Value	Unit

Table 10.3: Model parameters

The remaining model parameters τ_s , l_s and l_r are chosen freely in order to reproduce the experimental results of Figure 10.19.A and 10.19.B. Using model B several numerical simulations were conducted to calculate the deflection of protons that propagate through the field of an expanding proton front in transversal configuration. The outcome of two simulations with the parameters of Table 10.3 is depicted in Figure 10.19.C and Figure 10.19.D

A comparison between the simulation and the measurement shows that model B cannot reproduce the exact distribution of the measured proton streak deflections. However, the model is capable of generating some of the characteristic features

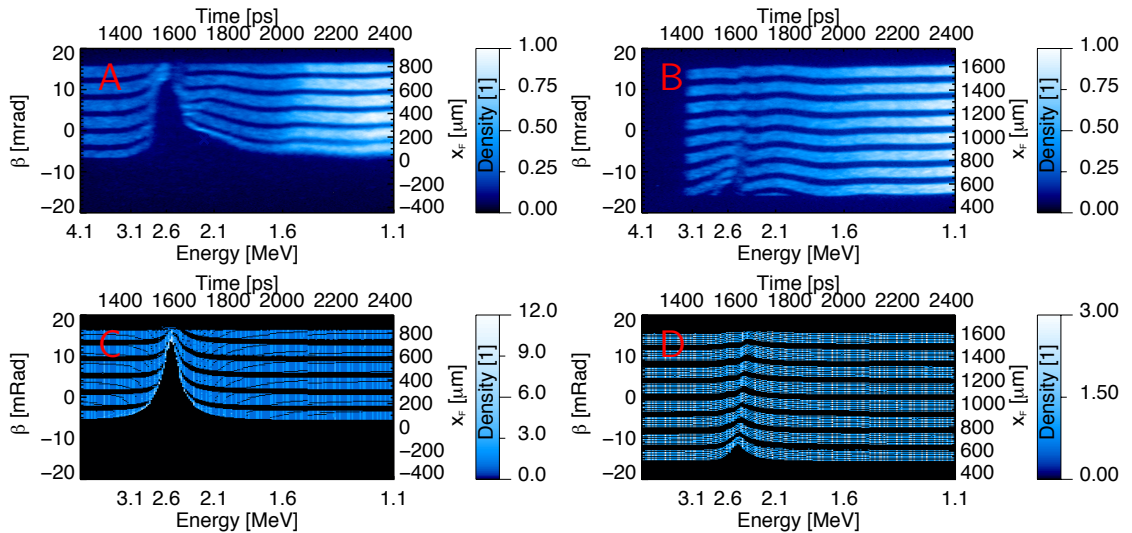


Figure 10.19: Experimentally obtained (A, B) and simulated (C, D) proton density distributions $\tilde{\rho}(\beta, \epsilon)$ in transversal configuration. Here, model B and simulation type B was used.

of the measured field action. The simulated deflection peak at $t_p = t_{\text{pump}}$ has a comparable amplitude but a smaller width than the measured peak. For values $|x_F| \gtrsim 700 \mu\text{m}$, the model can reproduce the experimentally observed shift of the first deflection maximum to higher probing times t_p with increasing distance $|x_F|$ as shown in Figure 10.19.D. This affirms the assumption that the observed deflection pattern in transversal direction is influenced by the field action of an expanding proton front.

Experimentally, a second deflection peak with a relatively small curvature is observed at probing times $t_p \gtrsim 1725 \text{ ps}$, $x_F \gtrsim 400 \mu\text{m}$ as shown in Figure 10.19.B. This peak is not reproduced by the model. This deflection peak may be due to the field effects of a combination of heavier ion species (Figure 10.5.B). These ions are accelerated to much slower velocities in comparison with protons. In addition their beam divergence angle could be relatively high, which might explain the smooth curvature of the second local deflection maximum.

It should be stressed that the proposed model is a very simple approach to describe the field of moving proton front in three dimensions. Naturally, the model cannot reflect all aspects of the complex field distribution, which is generated in reality. In particular, the following points are not considered by the model:

- The divergence of the ion beam
- The energy distribution of the ions depending on the initial ejection angle
- The influence of radial electric field components and magnetic fields
- The change of the source size in time
- The acceleration of multiple ion species

In consideration of these substantial simplifications, it is surprising that the proposed model can reproduce some of the prominent features with the shown accuracy.

As stated, the model variables τ_s , l_s and l_r were chosen freely in order to approximate the measurements. It can be shown that a variety of different combinations can lead to similar deflection patterns, which also resemble the measured density distributions $\tilde{\rho}(\beta, \epsilon)$ of Figures 10.19.A and 10.19.B in appearance. For instance a 10 times smaller extension of the field $l_r = 40 \mu\text{m}$ in radial direction in combination with a higher value of temporal decay parameter $\tau_s = 1000 \text{ fs}$ ($l_s = 0.25 \mu\text{m}$) leads to similar proton streak deflections. However, a good approximation of the measurements can not be maintained if only one parameter is changed. For example, an increment of l_s , which determines the spatial decay of the field front, leads only to similar results if the field amplitude \mathcal{E}_c is decreased at the same time.

In conclusion model B can explain a characteristic property of the measured streak deflections in transversal probing geometry and can identify the responsible field configuration, i.e. the field of an expanding proton front. Though, a conclusion

about characteristic field or plasma parameters is difficult, since the number of free variables is simply too high.

Longitudinal Configuration - Model B

This section will explain why model B is unable to describe either the streak deflections or the observed redistribution effects in longitudinal probing geometry. Figure 10.20.A shows the experimentally obtained proton density distribution $\tilde{\rho}(\beta, \epsilon)$ in longitudinal configuration, which was previously approximated by means of model A (cf. Figure 10.16). For comparison Figure 10.20.B shows the outcome of a par-

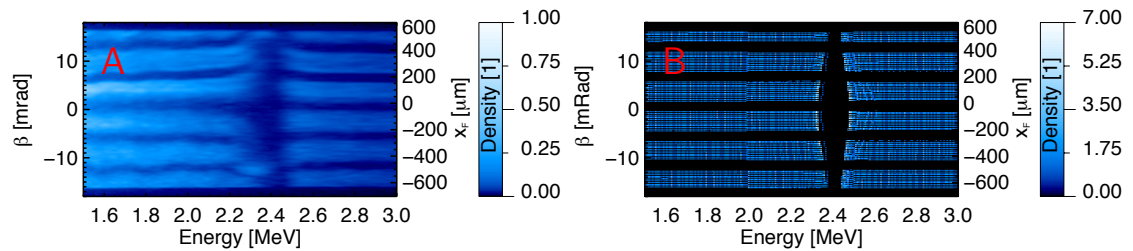


Figure 10.20: Experimentally obtained (A) and simulated (B) proton density distributions $\tilde{\rho}(\beta, \epsilon)$ in longitudinal configuration. Here, simulation type B, model B and the parameters of Table 10.3 were used.

title simulation in which model B was used to simulate the redistribution effects in longitudinal configuration. Here, the same model parameters (Table 10.3) as in the previous section were applied.

Obviously the measured streak deflections are not reproduced at all by the model. This can be explained by the simple fact that the model does not take into account radial electric or magnetic fields.

Similar to the one-dimensional simulations of Chapter 9.5.1 the electric field distribution of model B causes a pronounced gap in the proton energy spectrum. In addition model B leads to the generation of characteristic local density maxima on both sides of the gap, which is in agreement with the findings of Chapter 9 where the field effects on thin foils were investigated using laser arm A. However, these density maxima are not observed in the experiments of this Chapter, where ultra-thin foils were irradiated with laser arm B providing an even higher temporal contrast ($10^{10} - 10^{11}$), than laser arm A. Even if the energy resolution of spectrometer is considered in simulation, the generated maxima do not disappear entirely.

Transversal Configuration - Model A

This section will explicate why model A (Section 10.3.1) is not well suited to describe the deflection measurements in transversal configuration (Section 10.2.1). In order to simulate the streak deflections in transversal probing geometry effected by

model A, additional particle simulations were conducted. Within these simulations the calculated interaction fields of model A were rotated by 90° around the y-axis, according to the orientation of the interaction target.

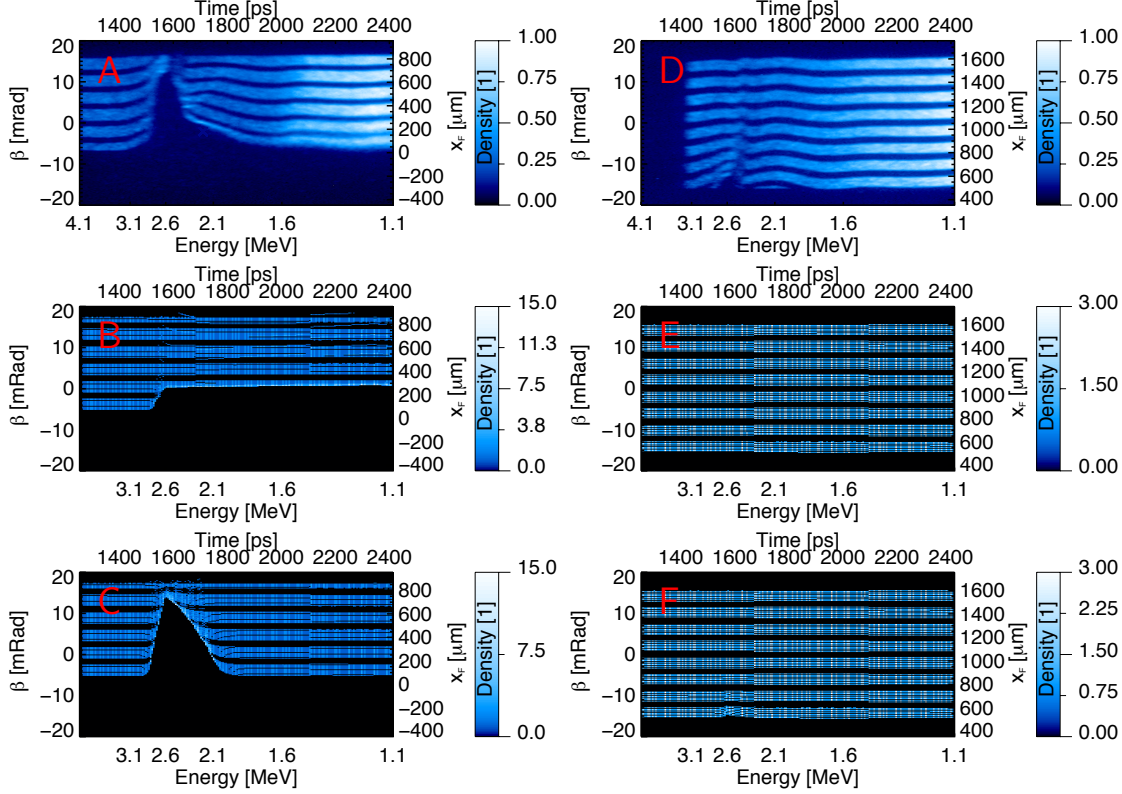


Figure 10.21: Experimentally obtained (A, D) and simulated (B, C, E, F) proton density distributions $\tilde{\rho}(\beta, \epsilon)$ in transversal configuration. For all simulations model A, simulation type B and a Gaussian distribution of the charge density η were applied. B, E - The model parameters of Table 10.1 and 10.2 were used. C, F - The model parameters of Table 10.4 and 10.5 were used. In addition all fields were multiplied with the exponential decay factor $\exp(-t/\tau_l)$.

To allow for a direct comparison with the simulation results, the experimentally obtained proton density distributions $\tilde{\rho}(\beta, \epsilon)$ of two selected measurements in transversal configuration are illustrated in Figure 10.21.A and Figure 10.21.D.

The outcome of two simulations is shown in Figure 10.21.B and Figure 10.21.E, whereby a Gaussian distribution of the charge density η and the parameters of Table 10.1 were used in the simulation. These are the same model parameters which were used in the simulations in longitudinal configuration (cf. Figure 10.16.B). This is possible, since almost identical laser parameters were applied to create the interaction fields, both in longitudinal and in transversal configuration.

By comparing the simulations with the experimental results it becomes apparent that model A cannot explain the observed deflection pattern of the proton stripes.

The model underestimates the spatial extension of the fields and overestimates the temporal duration of the deflection.

In simulation the spatial decay of the electric field normal to the foil surface is so strong that only protons which pass the interaction target at close distances ($|x_F| \lesssim 300 \mu\text{m}$) are significantly deflected by the field.

The reason why the model does not reproduce the time decay of the proton deflection can be explained by the definition of the temporal field evolution. In the analytical model the temporal decay of the fields is connected with the time dependence of the spot size expansion $l(t)$ (Equation 10.21). Due to Equation 10.28 the electric field is directly proportional to the transverse profile of the charge density $\eta(\xi, l(t))$ and because of Equation 10.11 and Equation 10.12 the electric field decays in time while the spot size expands in time. Let us assume that a proton propagates parallel to the foil surface with a certain distance to the foil. Because the transverse profile $\eta(\xi, l(t))$ is normalized in ξ -direction, this is also true for the electric field distribution. For this reason, the integrated force that acts on the proton can be regarded as constant in time, in first approximation. Taking into account that in transversal configuration the fields are rotated and that the protons propagate initially in z -direction, this relationship is reflected by the numerical simulation. After the time t_{pump} the deflection is almost constant in time, which shows the limits of the theoretical model.

In simulation, the proton deflection is visible up to a time of approximately 800 ps after the initiation of the fields. Experimentally, the deflection drops almost back to zero approximately 300 ps after the deflection maximum is reached. Under the assumption that the field description of model A is accurate for small times, the time of 300 ps serves as an upper limit for the validity of the model.

In order to approximate the decay of the observed streak deflections more accurately a simple extension of model A is proposed. Here, the long time evolution of the field is taken into account by introducing the exponential decay factor $\exp(-t/\tau_l)$, with $\tau_l = 50 \text{ ps}$.

However, the reproduction of the observed streak deflections for $|x_F| \gtrsim 300 \mu\text{m}$ is only possible if the effective field extension normal to the target surface is increased. On the basis of model A this is possible by increasing the Debye radius of hot electrons (Equation 10.7). Taking into account the experimental conditions, such as the laser intensity of the pump pulse, this can only be achieved by lowering the initial electron density $n_{\text{ec},0}$ to a value of $1 \cdot 10^{28} \text{ m}^{-3}$.

Additional simulations were conducted using the proposed modification of model A in combination with the decrement of the initial electron density. The results are shown in Figure 10.21.C and Figure 10.21.F and the applied model parameters are summarized in Table 10.4 and 10.5.

As Figure 10.21.A shows the experimentally obtained proton distribution can be approximated to some extent. However, several points indicate that model A in combination with the proposed model parameters (Table 10.4 and 10.5) leads to an artificial field distribution and is not suitable for a consistent explanation of the

Model Variables		
$n_{ec,0}$	$1 \cdot 10^{22}$	$1/\text{cm}^3$
D_e	7.0	μm
Model/Simulation Parameters		
I_L	$3.0 \cdot 10^{19}$	W/cm^2
τ_L	50	fs
r_L	2.5	μm
a	36.5 (35.0)	mm
Δa	30	nm
T_{r0}	0.5	1
A_{b0}	0.4	1
ϵ_{pump}	2.4 (2.6)	MeV
Parameter	Value	Unit

Table 10.4: Model variables and simulation parameters. The values in brackets are used for simulations in transversal configuration.

Calculated Model Parameters		
l_n	0.56	1
$A_b(l_n)$	0.17	1
T_{eh}	42.0	MeV
Φ_p	1.5	MeV
N_{eh}	$7.7 \cdot 10^{10}$	1
$n_{eh,0}$	$2.69 \cdot 10^{17}$	$1/\text{cm}^3$
ω_{pc}	$5.6 \cdot 10^{15}$	1/s
ω_{ph}	$2.9 \cdot 10^{13}$	1/s
r_D	92.8	μm
l_f	$0.32 \cdot 10^{-3}$	1
v_e	$3.6 \cdot 10^{12}$	1/s
η_0	0.47	1
Parameter	Value	Unit

Table 10.5: Calculated model parameters. The shown quantities are obtained using the equations of Section 10.3.1 and the variables and parameters of Table 10.4.

observed proton streak deflections.

- The lowering of the initial electron density $n_{ec,0}$ to a value of $1 \cdot 10^{28} \text{ m}^{-3}$ leads to an unrealistically high electron temperature $T_{eh} = 42.0 \text{ MeV}$ (Equation 10.16).
- Figure 10.22.B shows the outcome of a simulation in longitudinal configuration, in which model A was used in combination with the proposed model parameters of Table 10.4 and 10.5. Apparently the simulated gap width is relatively high in comparison to the experimental result, which is shown for comparison in Figure 10.22.A.
- Using a one-dimensional simulation (cf. Section 9.4.2), the energy gain of a proton is calculated, which is accelerated in the field of model A in connection with the model parameters of Table 10.4 and 10.5. In this simulation the particle is initially at rest and located at the position $(x_0 = 0 \text{ nm}, y_0 = 0 \text{ nm}, z_0 = 30 \text{ nm})$, where the main electric acceleration field is directed along the z-axis. The calculated final proton energy is 1.7 MeV and thus well below the observed proton energy cut-off, which has a value above 2.5 MeV (cf. Figure 10.7.A).
- By comparing Figures 10.21.D, 10.21.E and 10.21.F it becomes apparent that

model A cannot reproduce the observed streak deflection at all for distances $|x_F| \gtrsim 700 \mu\text{m}$. In particular, the model fails to reproduce the observed shift of the deflection maximum to higher probing times t_p with increasing distance $|x_F|$ (cf. Figure 10.8.A). As additional simulations have shown, this inability of model A is independent of the chosen model parameters.

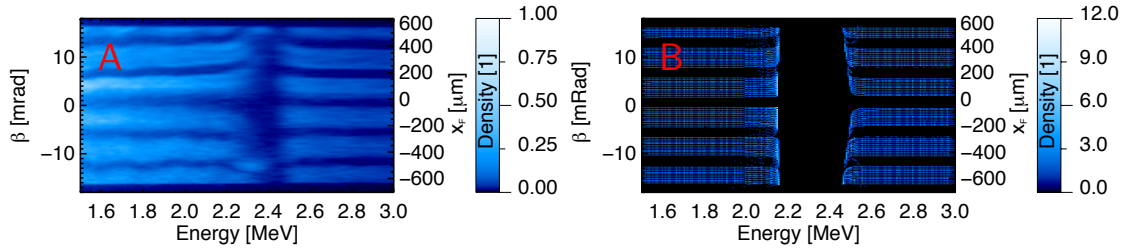


Figure 10.22: Experimentally obtained (A) and simulated (B) and proton density distributions $\tilde{\rho}(\beta, \epsilon)$ in longitudinal configuration. Here, simulation type B, model A and the parameters of Table 10.4 and 10.5 were used.

Combination of both Models

This section discusses the possibility of combining both models for a more accurate description of the experimental results of both probing configurations. Both models can explain different features of the observed streak deflections and both can describe different properties of the field. Model A includes radial electric field components as well as magnetic fields and model B describes the electric field of an expanding proton front.

The simplest approach for combining both models is the superposition of their fields, whereby all field components are simply added.

Figure 10.23 shows the result of particle simulations in which the combined effect of both fields is taken into account. To allow for a direct comparison with the simulation results, the experimentally obtained proton density distributions $\tilde{\rho}(\beta, \epsilon)$ of two selected measurements in longitudinal and transversal configuration are illustrated in Figure 10.21.A and Figure 10.21.D, respectively.

In the simulations the model parameters of Table 10.1, 10.2 and 10.3 are applied. The same parameters were used before to model the observed field effects separately. The transverse profile of the charge density η is described again by a Gaussian distribution. In model A, the long time evolution of the fields is taken into account by introducing the exponential decay factor $\exp(-t/\tau_l)$, with $\tau_l = 100 \text{ ps}$. For the creation of Figures 10.23.B and 10.23.E simulation type B was applied, whereas Figures 10.23.C and 10.23.F are generated using simulation type A, which accounts for the energy resolution of the spectrometer.

In view of the simulation results, it becomes apparent that the combination of both models leads to a complementary field distribution allowing for a relatively

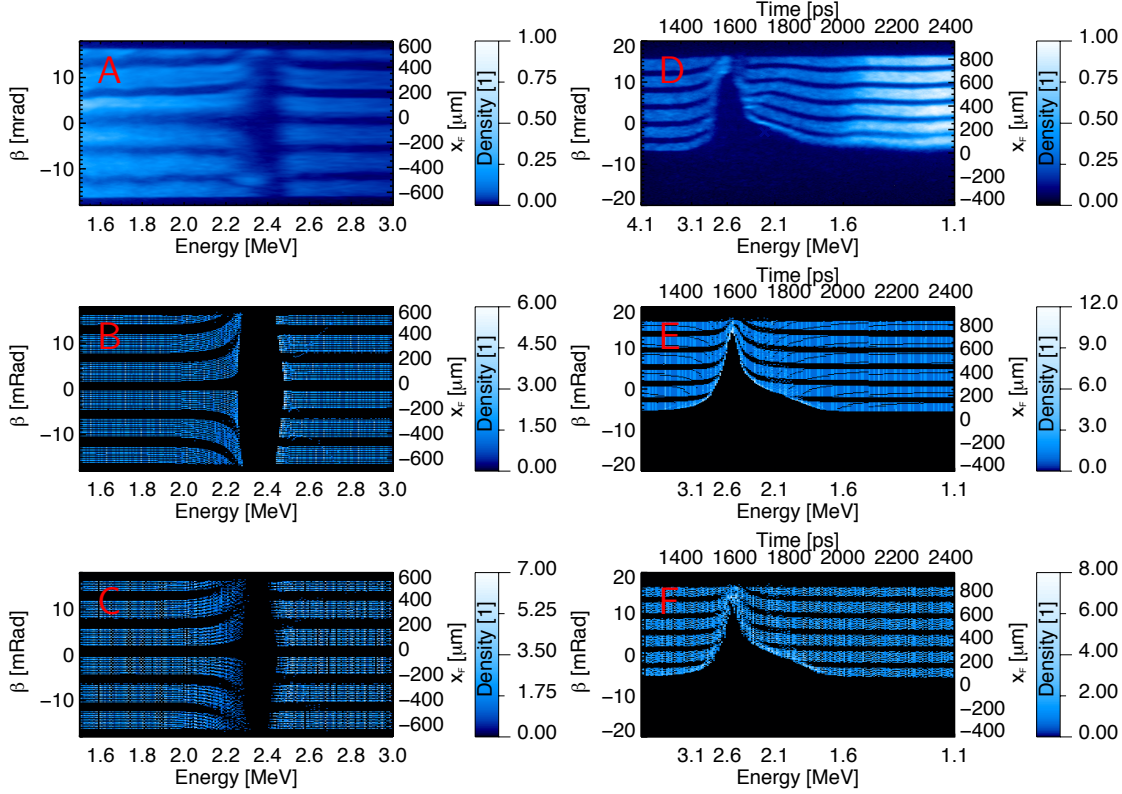


Figure 10.23: Experimentally obtained (A, D) and simulated (B, C, E, F) proton density distributions $\tilde{\rho}(\beta, \epsilon)$ in longitudinal and transversal configuration. For all simulations the fields of model A and model B were added and the model parameters of Table 10.1, 10.2 and 10.3 were used. In model A, the fields are multiplied with the exponential decay factor $\exp(-t/\tau_l)$ ($\tau_l = 100$ ps) and the transverse profile of the charge density η is described by a Gaussian distribution. B, E - Simulation type B. C, F - Simulation type A.

accurate reproduction of the experimentally derived proton distributions $\tilde{\rho}(\beta, \epsilon)$ of both probing configurations.

The use of the exponential decay factor $\exp(-t/\tau_l)$ in model A, with $\tau_l = 100$ ps allows for the reproduction of the flat deflection decay for probing times $t_p \gtrsim 1650$ ps in transversal configuration (Figures 10.23.E and 10.23.F). This additional decay factor is necessary to recreate the transversal streak deflections. For this reason, the term is also used for the simulations in longitudinal configuration. As Figures 10.23.B and 10.23.C show, its application does not significantly affect or deteriorate the simulated streak deflections in longitudinal configuration. However, neither this factor nor the superposition of all fields can explain the creation of the second deflection peak at probing times $t_p \gtrsim 1725$ ps, $x_F \gtrsim 400 \mu\text{m}$ (cf. Figure 10.21.D), which was discussed before.

The proposed combination of both models leads to a complementary field con-

figuration and allows for a relatively consistent explanation of the experimental observations. However, it is necessary to be cautious, since both models provide a description of the electric field component normal to the foil surface. Therefore, both models describe the main acceleration field, which is responsible for the ion acceleration and for the observed redistribution effects in longitudinal configuration. With the proposed combination of both models, all field components are added. As a result, the new acceleration field is the sum of the acceleration fields of both models. Technically this is unproblematic and a particle simulation with the constructed field distribution may even provide a good approximation of the experiment, as in the presented case. Even the field structure itself can be a good approximation of the real situation, but with the given definition of the fields it becomes difficult to reach a conclusion on characteristic plasma properties on the basis of the applied model parameters. Since the model variables are adjusted in order to approximate the experimental results, different values should be determined depending on whether model A alone or the proposed combination of both models is used.

However, in the presented case the model variables were adjusted independently to match the experimental results. Model A was used to match the measurements in longitudinal configuration and model B was applied to approximate the measurements in transversal configuration. Thus, the proposed model parameters (Table 10.1) are derived in a consistent way and can be used to infer characteristic plasma and field parameters on basis of the equations of Section 10.3.1.

Nevertheless the constructed field distribution of the combined models allows for a good approximation of most of the experimentally observed features. Therefore, this field distribution and the presented investigations may be of help for the development of a new analytical model that can describe the observations of both probing configurations in a consistent way.

Finally, the investigations and results of this chapter can be regarded as a proof of principle. The presented method, i.e. the combination of two probing configurations allows for a precise investigation of laser-induced fields. The different probing configurations provide complementary information about the electromagnetic field distribution, which can be used to test the applicability of theoretical models and to derive characteristic field and plasma parameters.

10.4.3 Field Effects due to Picosecond Laser Pulses

In the case of picosecond laser pulses an inward bending of the proton stripes was observed in longitudinal probing geometry (Section 10.2.2) indicating the presence of a magnetic field. In order to find an explanation for this observation, model C (Section 10.3.3) is used to describe the magnetic field distribution in the particle simulation (Section 10.4.1). The applied model parameters are summarized in Table 10.6. The resulting spatial distribution of the simulated magnetic field is illustrated in Figure 10.24.

In order to reproduce the observed redistribution effects, i.e. the occurrence of the density dips in the proton energy spectrum, model B (Section 10.3.2) was also included in the simulation.

Figure 10.25 compares the experimentally obtained proton density distribution $\tilde{\rho}(\beta, \epsilon)$ with the result of the three-dimensional particle simulation. The model causes an outward deflection of the proton stripes at the low energy side of the gap. However, the experimental result is relatively blurred at this position, which makes a clear determination of the streak deflection direction difficult. In contrast, the inward bending of the proton stripes at the high energy side of the density dips is clearly visible in the experimental distribution and is reproduced by the simulation.

Using model C additional simulations with altered model parameters were conducted. The results show that different combinations of the parameters can lead to similar results. For instance a 10 times smaller value of the temporal field duration t_c can be used if other parameters are adapted. However, the inward deflection at the high energy side of the gap can only be reproduced if a field polarity is applied that is in agreement with field configuration B (Figure 10.13.B).

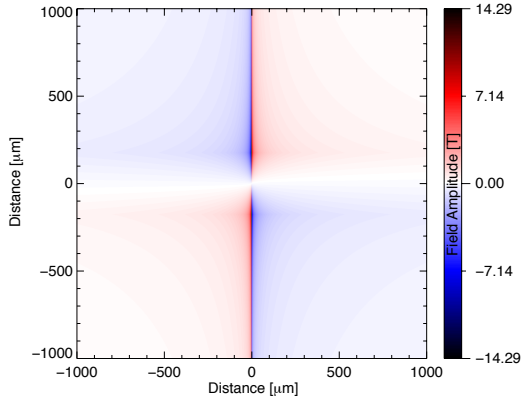


Figure 10.24: Distribution of the azimuthal magnetic field at $t = t_1$.

Model Parameters		
T_e	25	keV
t_c	50	ps
L_{\parallel}	175	μm
L_{\perp}	1	μm
n	1	1
k	2	1
Parameter	Value	Unit

Table 10.6: Model parameters

In contrast a typical thermoelectric magnetic field (Section 4.3) has exactly the opposite polarity, corresponding to field configuration A (Figure 10.13.A). Possible other mechanisms were already proposed in Section 10.2.2.

As stated, the measurements with femtosecond pulses were conducted under identical conditions, with only a change in the duration of the laser pulse. The observed streak deflections differ significantly and can only be explained by means of different mechanisms and acting field components. Thus, the variation of the laser pulse duration allows for the selection of the dominant deflection mechanism. This shows that the variation of certain laser-parameters can be used to manipulate the deflecting fields and even to control the deflection direction of the probing proton

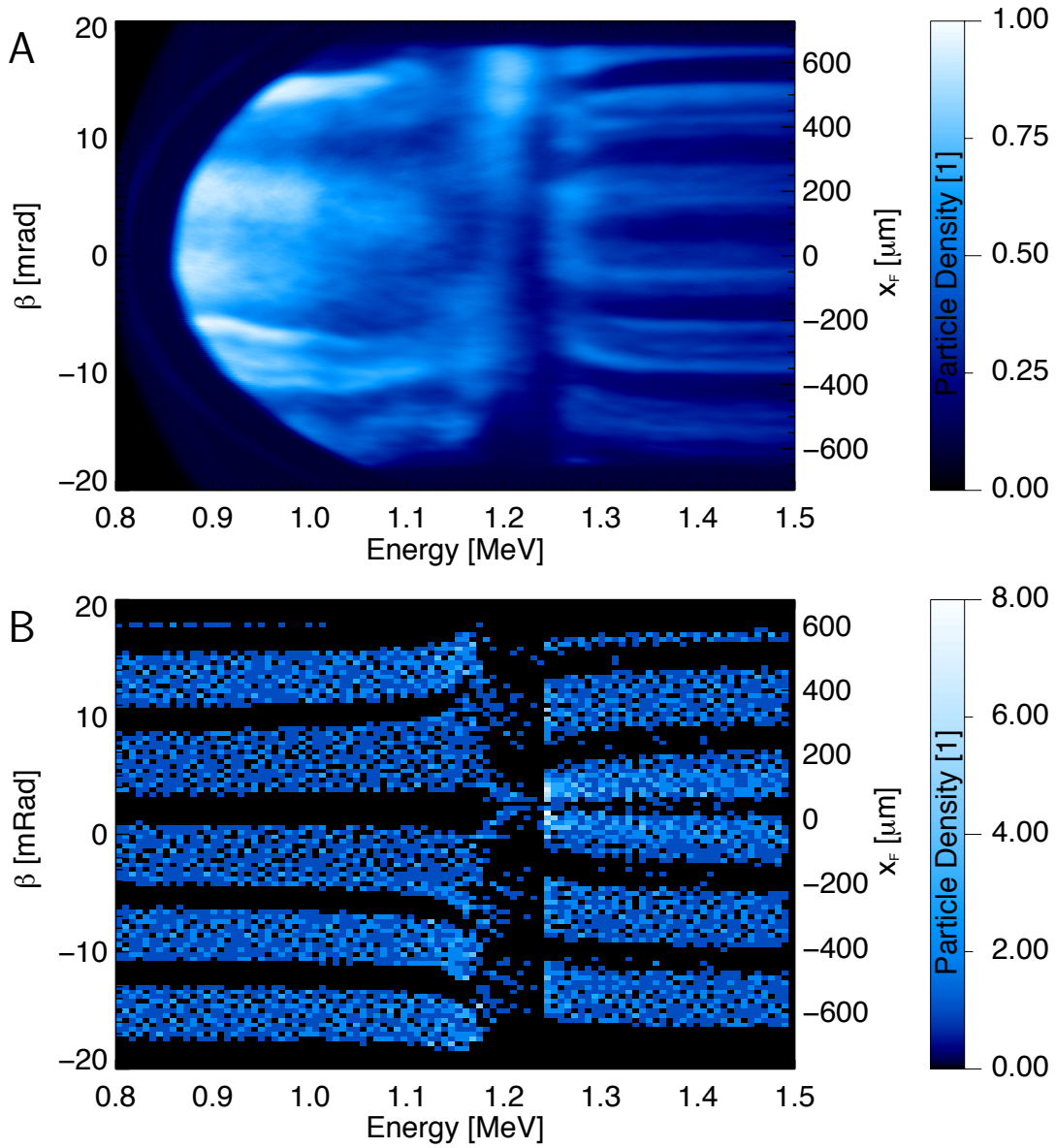


Figure 10.25: Simulated and experimentally obtained proton density distribution $\tilde{\rho}(\beta, \epsilon)$ in longitudinal configuration. **A** - Experiment. **B** - Simulation result, whereby simulation type B was used.

beam for a certain energy interval.

In conclusion, the observed proton deflection pattern at the high energy side of the gap can be quantitatively reproduced using numerical particle simulations. The simulation results confirm the measured polarity of the magnetic field at the rear side of the target. Based on the analytical description of model C, a clear identification of the magnetic field generation mechanism is not possible. For this reason,

further theoretical research is required to find the physical mechanism that leads to the creation of the observed magnetic field.

Summary

This thesis aims for better understanding of the complex dynamics of laser-induced strong fields on thin solid foils which constitutes the basis for laser ion acceleration. Advancing beyond previous work, the application and combination of complementary methods for the field reconstruction was investigated. Changes of the fields could be connected with femtosecond and micrometer scales. For the duration and the extension of the fields, scales in the range of picoseconds and millimeters, respectively, were found. Conclusions on the observed field effects were drawn on the basis of several analytical models. Their applicability was tested using multi-dimensional particle simulations which could reproduce particular features of the experimental observations. As a result, the *proton streak deflectometry* measurements in *longitudinal* and *transversal configuration* could be explained by means of different and partially complementary analytical models.

Within the research of this thesis, the following findings have been identified for the first time:

- Modulations in the proton energy spectrum were detected when intense femtosecond laser pulses with very high temporal contrast ($\sim 10^{10} - 10^{11}$) were applied for the ion acceleration on thin foils. The observed modulations could be connected with the cycle of the driving laser field.
- The imprint of field dynamics at 100 femtosecond timescale on a probing proton beam was measured with the proton deflectometry method in *longitudinal configuration*. The temporal and spatial reconstruction of the various acting field components was possible by comparing the measurements with model calculations.
- An interesting relation between the laser pulse duration and the induced magnetic field configuration on ultra-thin foils was observed. The variation of the pulse duration from several femtoseconds to picoseconds led to an inversion of the field polarity on the rear side of the ultra-thin foil.

In the framework of this thesis the *Thomson slit spectrometer* (Chapter 5) was applied to determine several characteristic properties of a laser-induced ion source and the associated fields. For this reason, a numerical method of coordinate transformation that allows the visualization of the angle dependent proton energy distribution $\tilde{\rho}(\beta, \epsilon)$ in an orthogonal coordinate system was developed. Using a 3D-particle simulation the energy resolution $\Delta\epsilon_S(\beta, \epsilon)$ of the spectrometer as a function of the initial ejection angle β and the initial energy ϵ of a proton was calculated. The result shows that the angle dependence of $\Delta\epsilon_S(\beta, \epsilon)$ is negligible in the presented case (± 15 mrad) and that the resolution can be approximated by an analytic expression that describes the resolution of a conventional Thomson spectrometer.

Faint and regular modulations in the proton energy distribution became detectable (Chapter 6), when intense femtosecond laser pulses with very high temporal contrast ($10^{10} - 10^{11}$) were used for target normal sheath acceleration of ions. The use of a thin and relatively long entrance slit of the spectrometer provided a reasonable energy resolution in combination with a spatial resolution that allowed the observed oscillations to be discriminated from noise. Based on the experimental results the modulations are regarded as a fundamental property of the ion source. Comparison with theoretical analysis including simulation and analytical model calculation gives strong indication that the modulation can be attributed to the pulsing of the acceleration field itself. This effect is explained by the periodical release of electron bunches which is linked to the frequency of the laser pulse. In this regard the modulations reflect the ultra-low longitudinal emittance of the laser-accelerated proton beam.

In order to probe extended field distributions with high magnification and reasonable time resolution, the *proton streak deflectometry* method has been developed further (Chapter 8). A new technique has been introduced which permits the displacement of laser-induced fields with respect to the position of the proton source in consecutive shots. Its applicability has been demonstrated based on a series of field investigations of laser-irradiated thin foils in *transversal configuration*. The field extension in surface normal direction was probed on both sides of the foil in a range from -2.8 mm to 1.8 mm. The acting fields were traced up to ~ 1.5 mm far from the target surface. For the first time, the electric field evolutions at both sides of a thin foil were recorded simultaneously (in one shot). The measurements revealed a high field symmetry between both sides of the foil and allowed for an estimation of the field extension radius along the foil surface $r_f \approx 2.2$ mm under the assumption that radial field components are negligible. By considering this relatively long extension it has been shown that the time resolution of imaging experiments in *transversal configuration* is insufficient to resolve the field evolution of the TNSA process, which takes place on timescales from hundreds of femtoseconds to a few picoseconds.

The investigation of laser-induced strong fields on plasma vacuum interfaces in Chapter 9, demonstrates the capability of *proton imaging in longitudinal configuration*. The principle of the method is based on measuring the energy redistributions within a broad band proton beam with a well-defined kinetic energy chirp. Since these energy redistributions depend on the probed field distribution, a comparison with simulations and model calculations allows conclusions to be made about the laser-induced field, its temporal-spatial change and its dependence on laser pulse and target parameters.

In the presented experiments thin foils were irradiated by ultra-short (70 fs) laser pulses with ultra-high temporal contrast ($10^9 - 10^{10}$). Specific experimental conditions were changed systematically, allowing the redistribution effects in the energy spectrum of the probing proton beam to be modified. As a result, a characteristic dependency of the proton redistribution on the target distance was found, which could be explained and reproduced using analytical model calculations. By varying the experimental parameters the free variables of the model could be confined, which enabled the deduction of characteristic field and plasma parameters. Information about the field symmetry was obtained by irradiating the foil on the opposite side. The radial extension of the field distribution (along the foil surface) was determined by displacing the field generation perpendicular to the propagation direction of the probing proton beam. The results are in good agreement with the findings of Chapter 8, indicating high field symmetry between both sides of the foil and a radial extension radius of approximately 2.0 mm – 2.5 mm. In addition, new and unexpected redistribution effects were observed by means of the lateral displacement technique. These effects could be reproduced experimentally, but could not be explained by one-dimensional models. This motivated the probing of ultra-thin foils in combination with a beam mask that provides additional information about lateral field components acting on the probing proton beam.

This thesis (Chapter 10) attempted to determine and explain the electromagnetic field distribution created on laser irradiated ultra-thin foils (30 – 50 nm thickness). For the field generation both femtosecond and picosecond laser pulses with high temporal contrast ($10^{10} - 10^{11}$) were used. As a diagnostic tool, the method of proton streak deflectometry was applied in two different probing configurations. The corresponding deflection measurements could visualize the action of the induced fields on the probing proton beam, whereby the impact of individual field components on the observed streak deflections was depended on the applied probing geometry. Therefore, the combination of two probing configurations provided additional and complementary information about the investigated field distribution. In the case of ultra-short pulses, the deflection measurements in transversal configuration indicated a high symmetry of the field distribution on both sides of the probed foil. In addition, the measurements allowed for an indirect determination of the effective field extension in target normal direction. For the electric field component E_n normal to the target surface an effective extension length $l_{En} \gtrsim 2400 \mu\text{m}$

was found. Similarly, the streak deflections in longitudinal configuration allowed for an estimation of the effective field extension in radial direction. Field components that act in radial direction (E_r , B_φ) show an effective extension radius of $r_{Fr} \lesssim 600 \mu\text{m}$. In contrast, for the normal electric field component E_n an effective radial extension radius $r_{En} \gtrsim 2000 \mu\text{m}$ was obtained.

For drawing conclusions about the observed field effects initiated on ultra-thin foils, several analytical models [73, 79, 142] were presented. The applicability of the respective models was tested by means of three-dimensional particle simulations, which could reproduce particular features of the measured energy redistribution effects and streak deflections. The measurements in *longitudinal* and *transversal configuration* could be understood with the help of different analytical models. These models can explain different features of the observed streak deflections and can describe different properties of the field. One model includes radial electric field components as well as magnetic fields. The other model describes the electric field of an expanding proton front. A combination of both models is partially complementary and allows for a relatively consistent explanation of the experimental observations.

Based on model calculations, magnetic field values up to 10^4 T were obtained, which is in agreement with the findings in reference [130]. However, it has been found that its influence on the simulated proton deflection is negligible compared to the action of the radial electric field component, which acts in the same direction and has maximum values of the order of $\text{MV}/\mu\text{m}$.

The presented method, i.e. the combination of two probing configurations, allows for a precise investigation of laser-induced fields. The different probing configurations provide complementary information about the electromagnetic field distribution, which can be used to test the applicability of theoretical models and to derive characteristic field and plasma parameters.

In the case of picosecond laser pulses (Chapter 10), the deflection measurements were conducted under almost identical experimental conditions as the measurements with ultra-short pulses, only the duration of the laser pulse was changed. The comparison of these measurements revealed the changed field action on the probing proton beam, which can be attributed to the influence of the changed laser parameter on the initiated field distribution. The streak deflections in *longitudinal configuration* clearly indicate the presence of magnetic fields, which was not observed in the case of ultra-short pulses. The dominating influence of the magnetic field on the probing proton beam becomes visible in form of a collimating deflection of the proton stripes. In the case of femtosecond pulses the deflection is directed in the opposite direction and has a defocussing effect on the proton beam for the same energy interval. Thus, the variation of the laser pulse duration allows for the selection of the dominant deflection mechanism. It can be used to manipulate the deflecting fields and even to control the deflection direction of the probing proton beam for a certain energy interval.

Due to the energy dependent detection method, the observed collimating or defocussing deflection of a certain energy range can be exclusively attributed to the influence of the field distribution located at the rear side of the laser irradiated foil. In the presented case, the experimental setup allowed for the direct observation of the magnetic field polarity, providing an advantage over other proton deflectometry setups. In the case of the laser pulse with femtosecond duration, the calculated magnetic field strength and polarity is in agreement with recent investigations. In contrast, the measured polarity of the magnetic field is exactly the opposite in the case of the picosecond laser pulse. This is surprising, since the measured polarity differs from the results of recent investigations [94] on magnetic fields, where high intensity laser pulses with picosecond durations were used for the field generation. Using numerical particle simulations the observed proton deflection pattern could be quantitatively reproduced in a certain energy range. The simulation results confirm the measured polarity of the magnetic field at the rear side of the target. However, based on the applied analytical description a clear identification of the magnetic field generation mechanism is not unambiguous and further research is required. Especially this last investigation shows that proton streak deflectometry can be advantageously exploited.

Part IV
Appendix

A Basics

A.1 Slowly Varying Envelope Approximation

For the electric field $E(t) = \mathcal{E}(t) \cos(\phi(t))$ the reduced field function $E^+(t)$ has the form

$$E^+(t) = \frac{\mathcal{E}(t)}{2} e^{i\phi(t)}. \quad (\text{A.1})$$

On condition that the spectral amplitude is only not zero in a region around the central frequency ω_0 and $\Delta\omega \ll \omega_0$ is valid, it is reasonable to introduce the carrier frequency ω_0 in the time domain. In this case $E^+(t)$ can be written as

$$E^+(t) = \frac{\mathcal{E}(t)}{2} e^{i\varphi(t)} e^{i\omega_0 t} = \frac{\hat{\mathcal{E}}(t)}{2} e^{i\omega_0 t}, \quad (\text{A.2})$$

whereby $\varphi(t)$ is called temporal phase and $\hat{\mathcal{E}}(t)$ is the complex amplitude or the complex field envelope, respectively. Equivalent to the condition in the frequency domain the condition

$$\left| \frac{d\hat{\mathcal{E}}(t)}{dt} \right| \ll \omega_0 \left| \hat{\mathcal{E}}(t) \right| \quad (\text{A.3})$$

has to be fulfilled in the time domain. A quantity with a periodical phase can be represented in the complex plane as the product of a slowly varying complex amplitude $\hat{\mathcal{E}}$ and the phase factor $e^{i\psi}$ ($\psi(t) = \omega_0 t$). Thus the electric field function can be described by the relation

$$E(\psi) = \frac{1}{2} \left(\hat{\mathcal{E}} e^{i\psi} + \hat{\mathcal{E}}^* e^{-i\psi} \right). \quad (\text{A.4})$$

As a complex quantity the amplitude $\hat{\mathcal{E}}$ can be written as the product of the real quantity \mathcal{E} and the slowly varying phase factor $e^{i\varphi}$:

$$\hat{\mathcal{E}} = \mathcal{E} e^{i\varphi} \quad (\text{A.5})$$

Figure A.1 illustrates the relations between the fast and slowly varying components

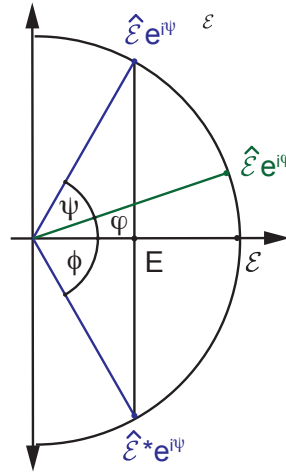


Figure A.1: Amplitude of the electric field in the complex plane

of the electric field

$$E = \text{Re} \left\{ \hat{\mathcal{E}} e^{i\psi} \right\} = \text{Re} \left\{ \mathcal{E} e^{i(\psi+\varphi)} \right\}, \quad (\text{A.6})$$

$$= \mathcal{E} \cos(\psi + \varphi), \quad (\text{A.7})$$

$$= \mathcal{E} \cos(\phi). \quad (\text{A.8})$$

The instantaneous phase $\phi(t)$ is defined as the sum of the fast varying phase term $\psi(t)$ and slowly varying temporal phase $\varphi(t)$

$$\phi(t) = \psi(t) + \varphi(t) = \omega_0 t + \varphi(t), \quad (\text{A.9})$$

whereby ω_0 denotes the angular frequency of the carrier wave.

A.2 Dispersion Parameters

The dispersion parameters can be used to describe the modulation state of a laser pulse. They are obtained by expressing the temporal phase $\varphi(t)$ and the spectral phase $\tilde{\phi}(\omega)$ in a Taylor expansion. The expansion of the temporal phase $\varphi(t)$ has the form

$$\varphi(t) = \sum_{k=0}^{\infty} \frac{\varphi^{(k)}(t_0)}{k!} (t - t_0)^k, \quad \varphi^{(k)} = \left. \frac{d^k}{dt^k} \varphi(t) \right|_{t=t_0}, \quad (\text{A.10})$$

$$\varphi(t) = \varphi^{(0)} + \varphi^{(1)}(t - t_0) + \frac{\varphi^{(2)}}{2}(t - t_0)^2 + \frac{\varphi^{(3)}}{6}(t - t_0)^3 + \dots, \quad (\text{A.11})$$

whereby $\varphi^{(k)}$, ($k = 0, 1, 2, \dots$) are the temporal dispersion parameters. Conventionally t_0 is equal to zero. The so called carrier envelope (CE) Phase is represented

by the coefficient of zeroth order $\varphi^{(0)}$ and defines the position of the carrier wave within the envelope. The coefficient $\varphi^{(1)}$ leads to a shift of the carrier frequency $\omega'_0 = \omega_0 + \varphi^{(1)}$ in the frequency domain but does not affect the group delay in the time domain. Higher orders of the expansion cause a time dependence of the instantaneous frequency

$$\omega(t) = \frac{d\phi(t)}{dt} = \omega_0 + \frac{d\varphi(t)}{dt}. \quad (\text{A.12})$$

The parameter $\varphi^{(2)}$ describes the rate of frequency increase. If $\varphi^{(2)} > 0$, the frequency increases linearly with the pulse duration and the pulse is positive-chirped. In the opposite case ($\varphi^{(2)} < 0$) the frequency decreases linearly with the pulse duration and the pulse is negative-chirped. Due to dispersion pulses can gain higher orders of the temporal phase $\varphi(t)$ if they propagate through material. In this case $\varphi^{(3)}$ causes a quadratic chirp, $\varphi^{(4)}$ a cubic chirp and so forth.

In literature the phase coefficients in the time domain are often related to the instantaneous phase $\phi(t)$ instead of the temporal phase $\varphi(t)$. The coefficients $\phi^{(k)}$ of the instantaneous phase $\phi(t)$ are connected to the coefficients $\varphi^{(k)}$ by Equation A.9 and are identical except for $\phi^{(1)} = \omega_0 + \varphi^{(1)}$. In order to investigate the effect of dissipative media on the pulse it is advantageous to use the frequency domain. Analogue to the temporal phase $\varphi(t)$ the spectral phase $\tilde{\phi}(\omega)$ can be expressed in a Taylor expansion

$$\tilde{\phi}(\omega) = \sum_{n=0}^{\infty} \frac{\tilde{\phi}^{(n)}}{n!} (\omega - \omega_0)^n, \quad \tilde{\phi}^{(n)} = \left. \frac{d^n}{d\omega^n} \tilde{\phi}(\omega) \right|_{\omega=\omega_0}, \quad (\text{A.13})$$

$$\tilde{\phi}(\omega) = \tilde{\phi}^{(0)} + \tilde{\phi}^{(1)}(\omega - \omega_0) + \frac{\tilde{\phi}^{(2)}}{2}(\omega - \omega_0)^2 + \frac{\tilde{\phi}^{(3)}}{6}(\omega - \omega_0)^3 + \dots \quad (\text{A.14})$$

Since the Fourier transform is a linear operation, the constant phase coefficient $\tilde{\phi}^{(0)}$ is equal to the constant phase $\tilde{\varphi}^{(0)}$ in the time domain. The meaning of the term of first order $\tilde{\phi}^{(1)}$ can be explained with the help of the displacement law of the Fourier transformation. A modulation in the frequency domain $|\tilde{E}(\omega)| \exp[i(\omega - \omega_0) \tilde{\phi}^{(1)}]$ leads to displacement leads to a temporal displacement $E(t + \tilde{\phi}^{(1)})$ in the time domain. Since the envelope function is shifted in relation to the carrier frequency ω_0 the coefficient $\tilde{\phi}^{(1)}$ is called group delay. In principle higher orders of the expansion lead to a chirp but their effect on the electric field $E(t)$ in the time domain can not be predicted and has to be investigated by means of the Fourier transformation. The so called group delay dispersion (GDD) $\tilde{\phi}^{(2)}$ leads to a linear chirp. As an example which is analytically simple to handle its influence on a Gaussian pulse is investigated in the appendix (A.3).

A.3 Group Delay Dispersion

An unchirped laser pulse can be described by its reduced electrical field function $E^+(t)$ or the fourier transform $\tilde{E}^+(\omega)$, respectively

$$E^+(t) = \frac{\mathcal{E}_0}{2} \exp\left(-\frac{t^2}{2\sigma_t^2}\right) \exp(i\omega_0 t), \quad (\text{A.15})$$

$$\tilde{E}^+(\omega) = \frac{\mathcal{E}_0}{2} \sqrt{2\pi}\sigma_t \exp\left(-\frac{\sigma_t^2(\omega - \omega_0)^2}{2}\right). \quad (\text{A.16})$$

A reverse fourier transformation of $\tilde{E}^+(\omega)$ with the additional phase $\tilde{\phi}(\omega) = \tilde{\phi}^{(2)}\frac{1}{2}(\omega - \omega_0)^2$ yields

$$E^+(t) = \frac{\mathcal{E}_0}{2\beta^{1/4}} \exp\left(-\frac{t^2}{2\sigma_t^2\beta}\right) \exp(i\varphi(t)) \exp(i\omega_0 t). \quad (\text{A.17})$$

Here, the parameter β is defined by $\beta = 1 + \left(\frac{\tilde{\phi}^{(2)}}{\sigma_t^2}\right)^2$ and the temporal phase of the chirped pulse can be written as

$$\varphi(t) = -\frac{\tilde{\phi}^{(2)}t^2}{2\left(\tilde{\phi}^{(2)2} + \sigma_t^4\right)} - \frac{1}{2} \arctan\left(-\frac{\tilde{\phi}^{(2)}}{\sigma_t^2}\right). \quad (\text{A.18})$$

Figure A.2 illustrates the temporal dependence of Equation A.15 and Equation A.17. The parameter σ_t is a measure for the temporal length of the pulse and is connected to the FWHM τ_p of the intensity by $\tau_p = 2\sigma_t\sqrt{\ln(2)}$. Equation A.17 and A.18 show the effect of the group delay dispersion $\tilde{\phi}_2$ in the time domain. In comparison to the unchirped pulse the pulse is temporally elongated by the factor

$$\sqrt{\beta} = \frac{\sigma_{t, \text{chirp}}}{\sigma_t} = \sqrt{1 + \left(\frac{\tilde{\phi}^{(2)}}{\sigma_t^2}\right)^2}, \quad \varphi^{(2)} = -\frac{\tilde{\phi}^{(2)}}{\tilde{\phi}^{(2)2} + \sigma_t^4}. \quad (\text{A.19})$$

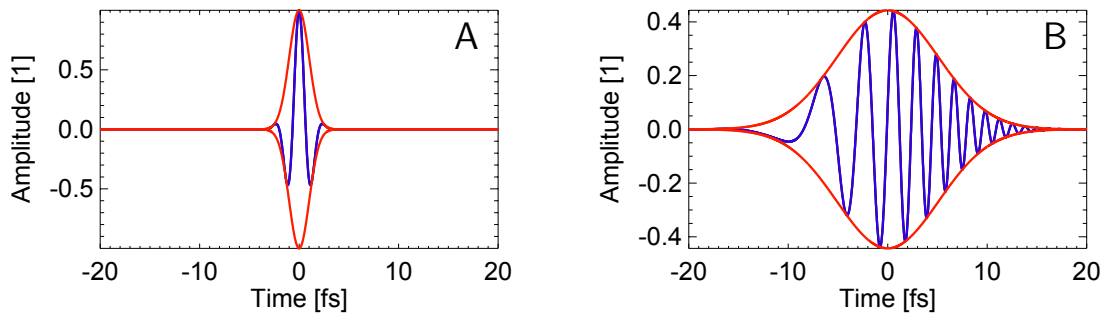


Figure A.2: Amplitude and electric field of a Gaussian pulse. **A** - Bandwidth limited pulse with $\sigma_t = 1$ fs. **B** - Influence of the group delay dispersion $\tilde{\phi}^{(2)} = -5\text{fs}^2$ leads to a linearly chirped Gaussian pulse.

A.4 Change of the Pulse Shape in Dispersive Media

A linear chirped laser pulse can be described by the reduced electrical field function

$$E^+(t) = \frac{\mathcal{E}_0}{2} \exp\left(-\frac{1}{2} \frac{t^2}{\sigma_t^2}\right) \exp\left(i \frac{\varphi^{(2)}}{2} t^2\right) \exp(i\omega_0 t), \quad (\text{A.20})$$

whereby the φ_2 describes the rate of frequency increase. In this case the FWHM of the intensity is given by $\tau_p = 2\sigma_t \sqrt{\ln(2)}$ and the instantaneous frequency by $\omega(t) = \omega_0 + \varphi^{(2)}t$.

The Fourier transform of $E^+(t)$ (Equation A.20) has the form

$$\tilde{E}^+(\omega) = \frac{\mathcal{E}_0 \sqrt{2\pi} \sigma_t}{2(1 + (\varphi^{(2)} \sigma_t^2)^2)^{\frac{1}{4}}} \exp\left[i\tilde{\phi}(\omega) - \frac{(\omega - \omega_0)^2 \sigma_t^2}{2(1 + (\varphi^{(2)} \sigma_t^2)^2)}\right]. \quad (\text{A.21})$$

The spectral phase can be written as

$$\tilde{\phi}(\omega) = -\frac{1}{2} \arctan(\varphi^{(2)} \sigma_t^2) + \frac{\varphi^{(2)} \sigma_t^4}{2(1 + (\varphi^{(2)} \sigma_t^2)^2)} (\omega - \omega_0)^2 \quad (\text{A.22})$$

and the spectral intensity is given by

$$\left|\tilde{E}^+(\omega)\right|^2 = \frac{\mathcal{E}_0^2 2\pi \sigma_t^2}{4(1 + (\varphi^{(2)} \sigma_t^2)^2)^{\frac{1}{2}}} \exp\left[-\frac{(\omega - \omega_0)^2 \sigma_t^2}{(1 + (\varphi^{(2)} \sigma_t^2)^2)}\right]. \quad (\text{A.23})$$

In order to investigate the influence of dispersive media on a Gaussian pulse, the additional phase function (Equation 1.28) is developed to second order

$$\tilde{\phi}_z(\omega) = k^{(0)}z + k^{(1)}z \cdot (\omega - \omega_0) + \frac{k^{(2)}z}{2} \cdot (\omega - \omega_0)^2. \quad (\text{A.24})$$

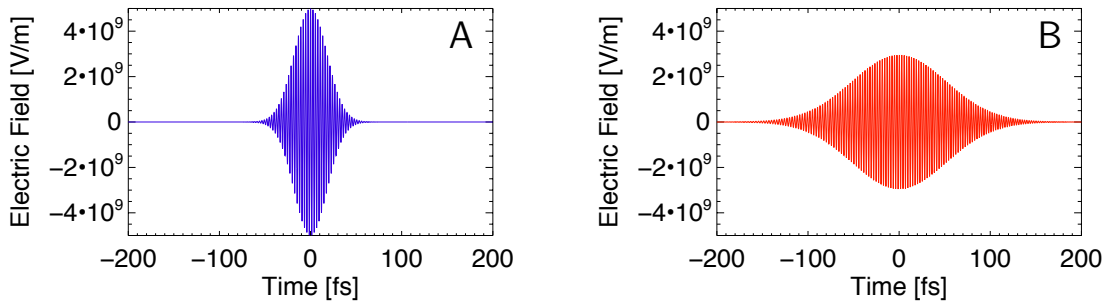


Figure A.3: Influence of a dispersive medium on a Gaussian pulse. **A** - Unchirped input pulse. **B** - Chirped output pulse.

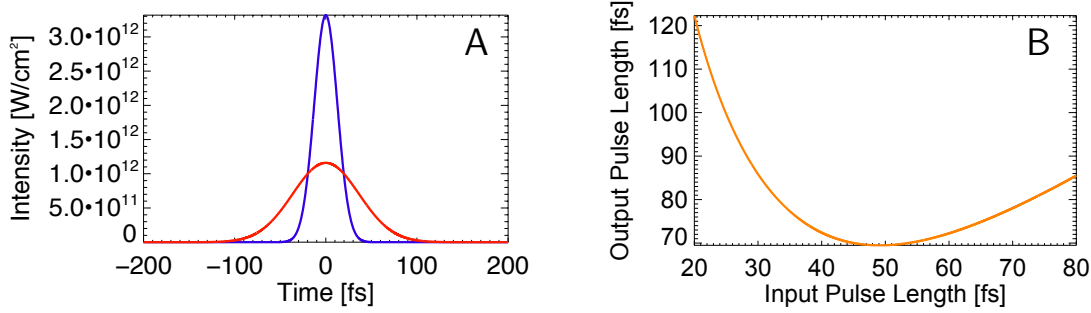


Figure A.4: Influence of a dispersive medium on a Gaussian pulse. **A** - Intensity distribution of input (blue) and output (red) pulse. **B** - Relation between the duration τ_p (FWHM of intensity) of an unchirped input pulse and the output pulse.

The product of $\tilde{E}^+(\omega)$ (Equation A.21) with $\exp(i\tilde{\phi}_z(\omega))$ describes the effect of the dispersive medium on the laser pulse after propagating the length z in the frequency domain. An inverse Fourier transformation yields the reduced field function in the time domain

$$E^+(t) = \frac{\mathcal{E}_0 \sqrt{2} \sigma_t}{4(1 + (\varphi^{(2)} \sigma_t^2)^2)^{1/4}} \frac{\exp\left(i\left(\omega_0 t - k^{(0)} z - \frac{1}{2} \arctan\left(\varphi^{(2)} \sigma_t^2\right)\right)\right)}{\sqrt{\frac{2\sigma_t^2}{4(1 + (\varphi^{(2)} \sigma_t^2)^2)} + i\left(\frac{k^{(2)} z}{2} - \frac{\varphi^{(2)} \sigma_t^4}{2(1 + (\varphi^{(2)} \sigma_t^2)^2)}\right)}} \cdot \exp\left[-\frac{(t - k^{(1)} z)^2}{4\left(\frac{2\sigma_t^2}{4(1 + (\varphi^{(2)} \sigma_t^2)^2)} + i\left(\frac{k^{(2)} z}{2} - \frac{\varphi^{(2)} \sigma_t^4}{2(1 + (\varphi^{(2)} \sigma_t^2)^2)}\right)\right)}\right]. \quad (\text{A.25})$$

The pulse duration after the propagation length z is given by the relation

$$\sigma_t(z) = \sqrt{\frac{8(1 + (\varphi^{(2)} \sigma_t^2)^2)}{2\sigma_t^2} \left(\left[\frac{2\sigma_t^2}{4(1 + (\varphi^{(2)} \sigma_t^2)^2)} \right]^2 + \left[\frac{k^{(2)} z}{2} - \frac{\varphi^{(2)} \sigma_t^4}{2(1 + (\varphi^{(2)} \sigma_t^2)^2)} \right]^2 \right)}, \quad (\text{A.26})$$

whereby the FWHM of the intensity is changed by $\tau_p(z) = 2\sigma_t(z)\sqrt{\ln(2)}$.

The left side of Figure A.3 shows the electric field $E(t) = 2 \cdot \text{Re}(E^+(t))$ of an unchirped $\varphi_2 = 0$ Gaussian pulse having the maximum field amplitude $\mathcal{E}_0 = 5 \cdot 10^9$ V/m, the pulse length $\tau_p = 30$ fs and the central wavelength $\lambda_0 = 800$ nm. The right side of Figure A.3 illustrates the influence of a 20 mm thick quartz substrate on the input pulse. Both the length and the amplitude of the electric output field are modulated.

The intensity change is depicted on the left side of Figure A.4, whereby the unchirped input pulse is shown in blue and the chirped output pulse in red. The right side of Figure A.4 illustrates the relation between the duration τ_p (FWHM of intensity) of an unchirped input pulse and the output pulse which is determined by Equation A.26.

A.5 Wavelength Dependence of the Dispersion Coefficients

The dispersion relation (1.25) connects the angular frequency with the wavelength λ and can be used to calculate the conversion factors between the respective derivations

$$\frac{d}{d\omega} = -\frac{\lambda^2}{2\pi c} \frac{d}{d\lambda}, \quad (\text{A.27})$$

$$\frac{d^2}{d\omega^2} = \frac{\lambda^2}{(2\pi c)^2} \left(\lambda^2 \frac{d^2}{d\lambda^2} + 2\lambda \frac{d}{d\lambda} \right), \quad (\text{A.28})$$

$$\frac{d^3}{d\omega^3} = -\frac{\lambda^3}{(2\pi c)^3} \left(\lambda^3 \frac{d^3}{d\lambda^3} + 6\lambda^2 \frac{d^2}{d\lambda^2} + 6\lambda \frac{d}{d\lambda} \right). \quad (\text{A.29})$$

By means of these equations the additional phase and its derivatives with respect on ω (Equations 1.29) can be described as a function of the wavelength

$$\tilde{\phi}_z(\lambda) = \frac{z2\pi}{\lambda} n(\lambda), \quad \frac{d\tilde{\phi}_z}{d\omega} = \frac{z}{c} \left(n(\lambda) - \lambda \frac{dn}{d\lambda} \right), \quad (\text{A.30})$$

$$\frac{d^2\tilde{\phi}_z}{d\omega^2} = \frac{z\lambda^3}{2\pi c^2} \left(\frac{d^2n}{d\lambda^2} \right), \quad \frac{d^3\tilde{\phi}_z}{d\omega^3} = \frac{z\lambda^4}{4\pi^2 c^3} \left(3 \frac{d^2n}{d\lambda^2} + \lambda \frac{d^3n}{d\lambda^3} \right). \quad (\text{A.31})$$

The dispersion coefficients $\tilde{\phi}_z^{(n)} = d^n \tilde{\phi}_z(\omega) / d\omega^n|_{\omega_0}$ depending on wavelength are obtained by inserting the wavelength $\lambda_0 = 2\pi c / \omega_0$. The respective expressions for $k^{(n)} = d^n k(\omega) / d\omega^n|_{\omega_0}$ are given by means of $\tilde{\phi}_z(\omega) = k(\omega)z$.

A.6 Birefringence

Birefringence is a property of optically anisotropic materials. A ray of light incident on a birefringent crystal is split into two rays taking different path and having different polarizations. One ray is polarized perpendicular to the optical axis and is called ordinary ray. Its refractive index n_o is constant and Snell's law of diffraction is valid.

The refractive index of the so called extraordinary ray $n_{eo}(\Theta)$ depends on the angle Θ , which is defined between the optical axis and the wave vector \mathbf{k} . The direction of \mathbf{k} in which n_e and n_{eo} are equal, defines the optical axis. As illustrated in Figure A.5 the angular dependence of the extraordinary refractive index n_{eo} can be described by the so called index ellipsoid [29]. Its functional dependency is given by

$$\frac{1}{n_{eo}(\Theta)} = \frac{\cos^2(\Theta)}{n_o} + \frac{\sin^2(\Theta)}{n_e}. \quad (\text{A.32})$$

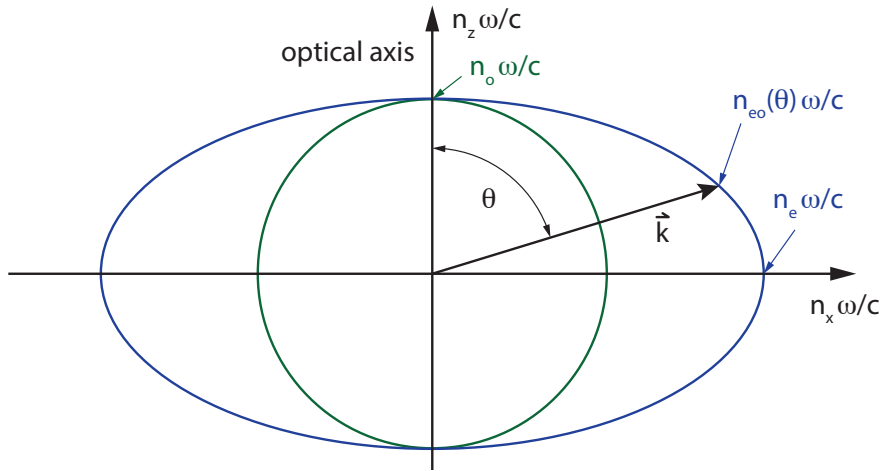


Figure A.5: Index Ellipsoid

The phase velocities of the ordinary ray $v_o = c/n_o$ and the extraordinary ray $v_{eo} = c/n_{eo}$ depend on the corresponding refractive indices. This effect can be used for the generation of phase modulations of a light pulse or to measure the temporal length of ultrashort pulses by means of nonlinear optical processes.

A.7 Nonlinear Optical Processes

Second-harmonic Generation

As an example a simple nonlinear optical processes of second order is discussed. Squaring down of the electric field $E_0(t) = \frac{1}{2}E_\omega \exp(i\omega t) + c.c.$ leads to the equation

$$E_0^2(t) = \underbrace{\frac{1}{2}E_\omega E_\omega^*}_{(1)} + \underbrace{\frac{1}{4}E_\omega^2 \exp(i2\omega t) + \frac{1}{4}E_\omega^{*2} \exp(-i2\omega t)}_{(2)}. \quad (\text{A.33})$$

This leads to the nonlinear polarization $P_{NL}(t) = \epsilon_0 \chi^{(2)} E_0^2(t)$ and the radiation source $S(t) = -\mu_0 \epsilon_0 \chi^{(2)} \frac{\partial^2}{\partial t^2} (E_0^2(t))$. Since Equation A.33 contains terms (2) oscillating with 2ω the radiation source $S(t)$ emits waves with the second harmonic of the input frequency. This process is known as SHG. The first term (1) in Equation A.33 leads to a steady (non-time-varying) polarization density. Because a DC potential difference in the medium is created this phenomena is called electro-optic rectification (EOR).

AC Kerr Effect

If the nonlinear medium is centrosymmetric, the second-order susceptibility ($\chi^{(2)} = 0$) is zero. In this case the material is called a Kerr medium and the dominant nonlinearity is of third order $P_{NL}(t) = \epsilon_0 \chi^{(3)} E_0^3(t)$. The response of Kerr media to optical fields consists in the generation of third harmonics and sums and differences of triplets of frequencies. The cube of the electric field $E_0(t) = \frac{1}{2} E_\omega \exp(i\omega t) + c.c.$ is

$$E_0^3(t) = \frac{3}{8} |E_\omega|^2 E_\omega \exp(i\omega t) + \frac{1}{8} E_\omega^3 \exp(i3\omega t) + c.c.. \quad (\text{A.34})$$

Under consideration of the linear susceptibility the polarization is can be written as

$$P(t) = \left[\epsilon_0 \left(\chi^{(1)} + \frac{3}{4} \chi^{(3)} |E_\omega|^2 \right) \frac{1}{2} E_\omega \exp(i\omega t) + \epsilon_0 \chi^{(3)} \frac{1}{8} E_\omega^3 \exp(i3\omega t) \right] + c.c.. \quad (\text{A.35})$$

Neglecting the part which oscillates with the third harmonic, the total susceptibility can be expressed as the sum of a linear (χ_L) and nonlinear (χ_{NL}) part

$$\chi = \chi_L + \chi_{NL} = \chi^{(1)} + \frac{3\chi^{(3)}}{4} |E_\omega|^2. \quad (\text{A.36})$$

The intensity dependent refractive index n of the medium can be defined by

$$n = (1 + \chi)^{1/2} = (1 + \chi_L + \chi_{NL})^{1/2}, \quad (\text{A.37})$$

whereby $n_0 = (1 + \chi^{(1)})^{1/2}$ denotes the linear refractive index. If $\chi_{NL} \ll n_2$ the equation can be rewritten as a Taylor expansion of first order at the point $\chi = \chi^{(1)}$

$$n(I) \simeq n_0 \left(1 + \frac{1}{2n_0^2} \chi_{NL} \right) = n_0 + \frac{3\chi^{(3)}}{8n_0} |E_\omega|^2 = n_0 + n_2 I, \quad (\text{A.38})$$

whereby n_2 denotes the second-order nonlinear refractive index and I is the intensity of the wave. This effect is know as the AC Kerr effect.

Self-phase Modulation

As a consequence an optical wave propagating through a third-order nonlinear medium undergoes SPMD. The phase shift incurred by an optical beam with intensity I traveling the distance L is given by

$$\varphi = n(I) \frac{2\pi L}{\lambda} = (n_0 + n_2 I) \frac{2\pi L}{\lambda}. \quad (\text{A.39})$$

Thus the intensity dependent change of the phase (phase modulation) is given by

$$\Delta\varphi = n_2 I \frac{2\pi L}{\lambda}. \quad (\text{A.40})$$

A.8 Energy Sensitive Proton Detection

Offline Stack Detectors

Conventionally stacks of CR-39 plates or radiochromic films are used for the proton detection [123]. CR-39 is a plastic polymer which consists of allyl diglycol carbonate (ADC) and can be used as a solid state nuclear track detector (SSNTD). A particle which impinges on the detector penetrates into the material and generates a latent particle trace. Due to ionization radicals are created along this trace. By covering the irradiated CR-39 with a sodium hydroxide solution, the locations of the radicals etch faster than the surrounding material. This way holes are created at the surface of the plates. The number of created holes corresponds to the detected particles and can be determined by means of a microscope. A radiochromic film consists of a single or double layer of radiation-sensitive organic microcrystal monomers which are based on a thin polyester substrate with a transparent coating. The color of the film turns to a shade of blue upon irradiation and its darkness increases with the absorbed dose. For proton detection the film has to be covered by an aluminum filter to prevent signals from photons.

When a proton moves through matter, it ionizes atoms of the material and deposits a dose along its path. As the proton energy decreases the interaction cross section increases. For this reason, the protons deposit energy mainly at the so called Bragg-peak. This peak occurs after a certain penetration length depending on the proton energy. Since the stack detector consist of several layers of radiochromic films or CR-39 plates, the main proton signal of each layer corresponds to a certain energy range. The width of the respective energy range depends on the thickness and material of the layer. For radiochromic films approximately 50 % of the signal in one layer is within an energy range of 0.5 MeV [147]. Since the proton energy corresponds to the probing time of the investigated process, every layer contains information of different times. This way the use of film stack allows for a series of temporal snapshots, whereby the maximum energy of the proton beam determines the number of exposed layers. The temporal resolution is restricted by the width of the energy range of each layer and thus by the thickness of the layer itself. In the presented experiments maximum energies between 2 and 5 MeV were available which allowed for the record of only 2 to 4 temporal snapshots with a single laser pulse.

However, the use of stack detectors has several disadvantages. First of all they have to be replaced after each single shot and in addition the measurement signal is not accessible during the experiment. The replacement can in principle be achieved by a chain of motorized stacks. However, the vacuum experimental chamber provides only space for a few stacks and the opening of the chamber is very time consuming.

Gated Multi-Channel Plates

A replenishing online detection method can be realized by the use of a MCP coupled with a phosphor screen with an attached CCD camera as described in Section 5.2. This method delivers two-dimensional images with a spatial resolution of several micrometer which are accessible during the experiment. If the laser pulse interacts with the source target not only protons are accelerated, but also other energetic ions, electrons and x-rays are generated [148]. Because the MCP is also sensitive to these signals, the recorded images of the phosphor screen would be influenced by them to the extent that the proton signal could not be analyzed any more. As proposed in Section 5.2 the voltage of the phosphor screen can be switched off after the arrival of the protons on the MCP. This way the contribution of heavier ion species to the signal can be suppressed. In a similar way the voltage of the MCP can be switched on after photons and energetic electrons have already reached the MCP. By means of fast high-voltage switchers the MCP and the phosphor screen can be switched on and off on a time scale of several hundreds of picoseconds, which is technically demanding. Since the detector is only sensitive for a this time period (gating time) a pure proton signal can be obtained and the setting of the gating time allows for the selection of a specific energy interval of the proton beam. This gating technique has been successfully applied for imaging the rear side plasmas of thin foils and the probing of irradiated micro water droplets with a time resolution between 400 ps to 23 ps [8]. The drawback of this method is that it allows only a single snapshot of the investigated process in a certain time interval. In order to record the temporal evolution of the process, the experiment must be repeated several times with different gating times.

A more sophisticated diagnostic method is called *proton streak deflectometry* [8, 97]. It allows the continuous record of transient fields on a picosecond time scale. It has already been used to study the electric fields occurring at the rear side of a laser irradiated thin foil [7, 8] and is used for several experiments in this thesis. This method is presented in the Chapter 8.

B Specifics

B.1 Source Properties of the Probing Proton Beam

In order to test the usability of the probing proton beam for streak deflectometry experiments, several source properties of the beam were investigated. These are the composition of the accelerated ion species as well as the energy distribution, pointing and reproducibility of the proton beam.

Of particular interest is the determination of the virtual source distance, since this parameter affects the magnification in proton imaging experiments [8]. The model of the virtual source [104] can describe the laser-induced proton emission after the acceleration process. When the particle interaction is negligible the proton trajectories can be described by straight lines and traced back to a virtual source point in front of the target, as illustrated in Figure B.1.

Therefore, the position z_v of the virtual source point in z-direction and the emission angle determine the initial particle position at the real source in x-direction. For a precise determination of the magnification M in imaging experiments, the distance of the virtual source $|z_v|$ has to be taken into account. The magnification of the

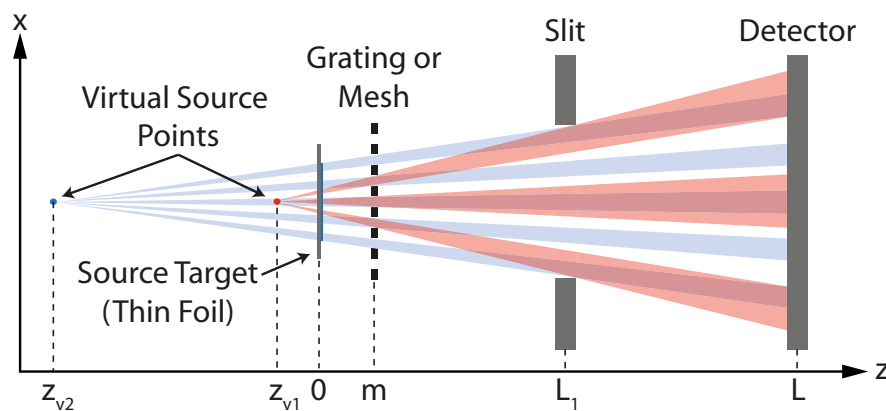


Figure B.1: Concept for the determination of the virtual source distance.

mesh in Figure B.1 is given by

$$M_{\text{mesh}} = \frac{L + |z_v|}{m + |z_v|}. \quad (\text{B.1})$$

In principle the distance of the virtual source can be determined by means of a proton streak deflectometry experiment if the properties of the inserted mesh and the distances of the setup are known. By measuring the magnification M of the proton stripes even the energy dependence of $|z_v(\epsilon)|$ can be investigated [112]. However, it is necessary to be very cautious. The inhomogeneous magnetic field distribution of the permanent magnet (Chapter 5.4) in the spectrometer can lead to a spatial distortion of the detected proton stripes, which might affect the measured magnification M . For this reason, another approach is used in this work. The application of a mesh (or grating) in combination with a slit can be used to measure the number of beamlets which pass through the slit opening (Figure B.1). Because this number is independent from the spectrometer design the exact determination of the virtual source distance $|z_v(\epsilon)|$ depending on proton energy is possible.

Since the laser and focussing parameters were slightly different in Chapters 8 and 9 in comparison to Chapter 10 separate experiments were conducted in order to determine the virtual source distance $|z_v(\epsilon)|$ and its energy dependency. In both cases the principle setup corresponds to Figure 8.1, whereby no interaction target was inserted in the probing proton beam and the pump pulse was switched off. For the generation of the proton beam a $5.0\ \mu\text{m}$ thick titanium foil was irradiated at an angle of incidence of 10° using laser arm A (Section 2).

Figures B.2.A and B.2.B are pictures of the light emitting phosphor screen and show the recorded density distribution $\rho(x, y)$ as a function of the x- and y-position in the detector plane. Both images are recorded with the proton streak deflectometry method. The y-position refers to the proton energy, whereas the x-position visualizes the deflection of the probing protons. The pictures show the undisturbed traces of the intersected proton beam which is dispersed in the Thomson slit spec-

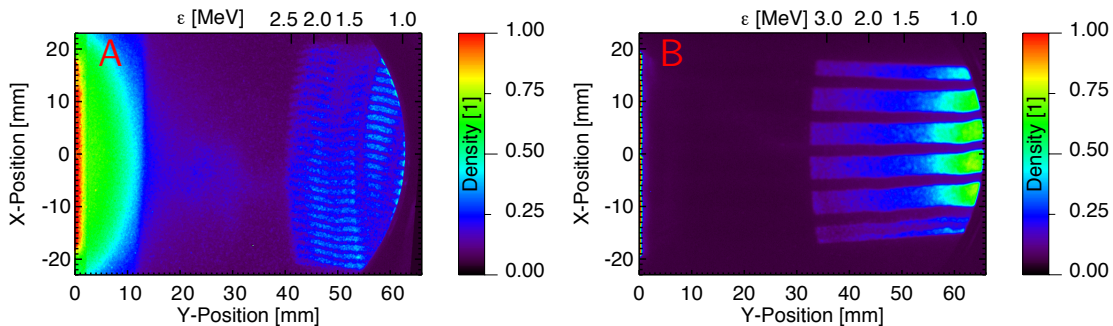


Figure B.2: Proton streak deflectometry measurements (without interaction target) for the determination of the virtual source distance. **A** - Experimental parameters corresponding to Chapter 8. **B** - Experimental parameters of Chapter 10.

trometer. Picture B.2.A was recorded using a mesh with 1000 LPI and with the experimental parameters given in Chapter 8. In contrast a grating with 200 LPI and the parameters of Chapter 10 were used in the case of Picture B.2.B.

The signal of other detected ion species is visible in the background of Image B.2.A. Nevertheless the proton stripes are clearly distinguishable. For the generation of Image B.2.B the MCP was gated (Section 5.2) in order to suppress the signal of heavier ion species. The minimum energy in the measurements is determined by the boundary of the MCP, whereas the energy cut-off of the probing proton beam determines the maximum observable energy.

In both pictures small trace-fluctuations are visible which appear as "wiggly" traces on the detector. Their occurrence can be explained by small movements of the proton source which causes beam pointing variations [8, 109, 133]. Also the density variations of the stripes along the y-direction on the detector can be explained by this effect. A movement of the proton source in y-direction can result in a situation where the line of sight between the source point and the slit is blocked by a horizontal bar of the mesh. This leads to a decrement of the proton signal on the detector for the energy interval in which the source is shifted in the described manner.

However, this effect is not the reason for some small systematic bending of the traces. The inhomogeneous electric and magnetic field distribution within the permanent magnet influences the specific form of the proton traces on the detector. Also the curvature of the energy cut-off and the energy dependent projection of the slit to the MCP is due to this influence. In Section 5.4 this relationship is explicated in greater detail.

Both pictures show clearly that the number of detected stripes remains constant for different energies. This proves that the virtual source distance $|z_v(\epsilon)|$ is independent of the proton energy for the detected energy interval. By evaluating the measured density distributions $\rho(x, y)$ of Figures B.2.A and B.2.B, respectively, the virtual source distances $|z_v(\epsilon)|$ of 1.75 ± 0.5 mm and 0.82 ± 0.5 mm were found.

Neglecting the influence of the virtual source size d_{VS} the maximum opening angle α_v is defined by

$$\alpha_v \approx 2 \cdot \operatorname{atan} \left(\frac{s_x}{L_1 - z_v} \right) = 2 \cdot \operatorname{atan} \left(\frac{r_S}{z_v} \right), \quad (\text{B.2})$$

whereby s_x is the length of the slit in x-direction and r_S the half of its the projection on the plane of the source target. In Chapter 10 r_S will be used to simulate the angle dependent proton emission from an extended source point.

B.2 Redistribution Effects due to Exponentially Decaying Fields

In this section the accelerating field configuration of the TNSA-process is investigated regarding its ability to cause redistribution effects in the energy spectrum of the probing proton beam. For this purpose a PIC-simulation was conducted using a modified 2D-LSP-code [105] with 30 particles in a cell of 4×12 nm and a simulation box of 50×50 μm . The simulation step was 3.3 fs and the total simulation length 200 fs. The irradiation geometry of the model was identical to the experiment. The duration τ_p of the linear polarized laser pulse is 87 fs and its intensity I_L is $5 \cdot 10^{18}$ W/cm². As a target a 0.8 μm thick aluminum foil with 50 nm hydrogen layers attached to its surfaces was used.

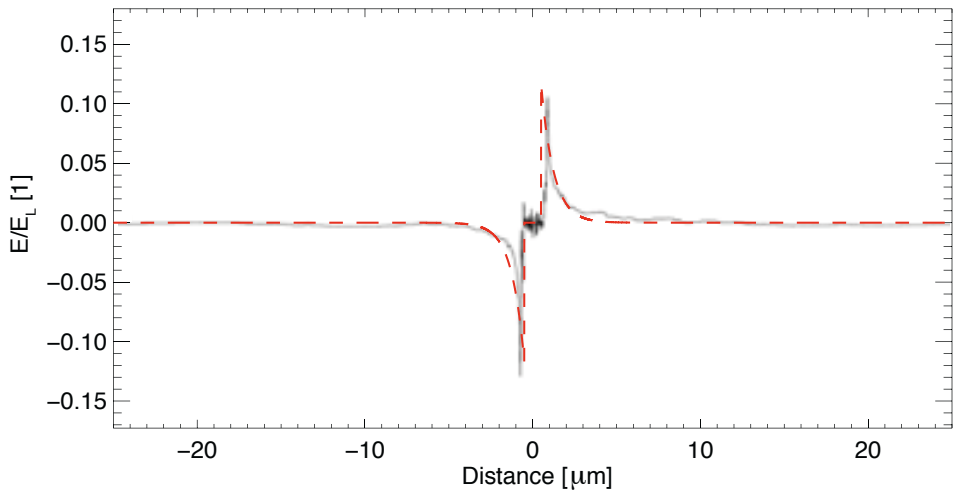


Figure B.3: Result of PIC-simulation. Spatial distribution of the TNSA-field (black curve). Approximation based on Equation B.4 (red curve). Simulation done by A.A. Andreev.

Figure B.3 shows the simulated amplitude of the TNSA-field (black curve) in terms of the incident laser field amplitude E_L . The acceleration field is directed normal to the initial foil surface. Its spatial dependence in this direction is shown at a moment in time, when the laser-plasma interaction of the main pulse is finished. The red dashed line is an exponential approximation of the field, which is based on the formula

$$\mathcal{E}_z = \mathcal{E}_N \exp\left(-\frac{z}{l_s}\right), \quad (\text{B.3})$$

whereby $\mathcal{E}_N = \mathcal{E}_0/E_L = 0.117$ and $l_s = 0.75$ μm .

As shown in Section 6 (Figure 6.5.B) the temporal dependency of the acceleration

field can be approximated by the functions

$$\mathcal{E}_t = \frac{1}{\sqrt{1 + (t/\tau_s)^2}} \quad (\text{A}), \quad \mathcal{E}_z = \frac{1}{1 + (t/\tau_s)} \quad (\text{B}). \quad (\text{B.4})$$

Using these formulas the temporal and spatial dependence of the TNSA-acceleration field can be approximated by

$$E_{\text{TNSA}}(z, t) = E_L \cdot \mathcal{E}_z(z) \cdot \mathcal{E}_t(t). \quad (\text{B.5})$$

Figure B.4.A shows the resulting field distribution at different moments in time, taking into account the ambipolar field geometry and the thickness of the target. In this connection Equation B.4.B is used to describe the time dependence. In the presented case a laser field amplitude E_L of $4.34 \text{ MV}/\mu\text{m}$ was used, which corresponds to the laser intensity $I_L = 5 \cdot 10^{18} \text{ W}/\text{cm}^2$ (Equation 1.19). The spatial scale length l_s was set to $3 \mu\text{m}$, the temporal duration $\tau_s = 150 \text{ fs}$ and $\mathcal{E}_N = 0.2$.

Using the numerical algorithm of Section 9.4.2 the energy change of a proton starting at the source target and having the initial energy ϵ_0 can be calculated when it propagates through field configuration of Figure B.4.A. In this connection both the target distance a and the pump time t_{pump} have to be considered. As a result the function $\epsilon_f(\epsilon_0)$ is obtained, which describes the changed (final) proton energy depending on the initial energy ϵ_0 . Figure B.4.B illustrates this dependency for the target distance $a = 15.14 \text{ mm}$ and the proton t-pump energy $\epsilon_{\text{pump}} = 1.5 \text{ MeV}$ ($t_{\text{pump}} = 775 \text{ ps}$).

The same experimental parameters were used in case of Figure B.5.A which shows a selected experimental result (blue curve) of Section 9.3.1. The black dashed line is a fit to the undisturbed parts of the measured (uncorrected) proton energy spectrum. Using a background correction this fit is used to approximate the initial proton energy distribution function $f(\epsilon_0)$ at a moment in time before it gets disturbed by the initiated fields at the interaction target. In combination with the

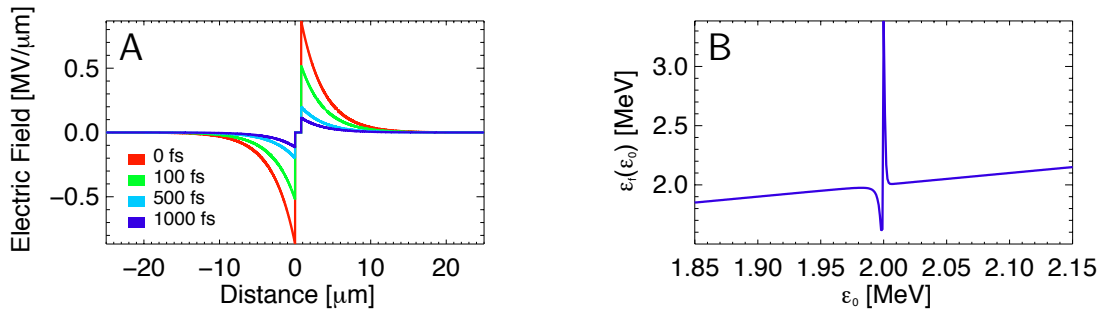


Figure B.4: **A** - Analytical field distribution based on Equations B.4.B and B.5 using the parameters: $I_L = 1 \cdot 10^{18} \text{ W}/\text{cm}^2$, $l_s = 3 \mu\text{m}$ and $\tau_s = 150 \text{ fs}$. **B** - Changed (final) proton energy $\epsilon_f(\epsilon_0)$ as a function of the initial energy ϵ_0 .

calculated energy change $\epsilon_f(\epsilon_0)$ (Figure B.4.B) the function $f(\epsilon_0)$ enables the numerical calculation of the proton energy redistribution $\bar{f}(\epsilon_0)$ (Section 9.4.4). The yellow curve illustrates the calculated proton energy redistribution effect on the undisturbed and uncorrected ion energy distribution (black dashed line). In case of the red curve the instrument function of the spectrometer (≈ 42.5 keV resolution) was taken into account.

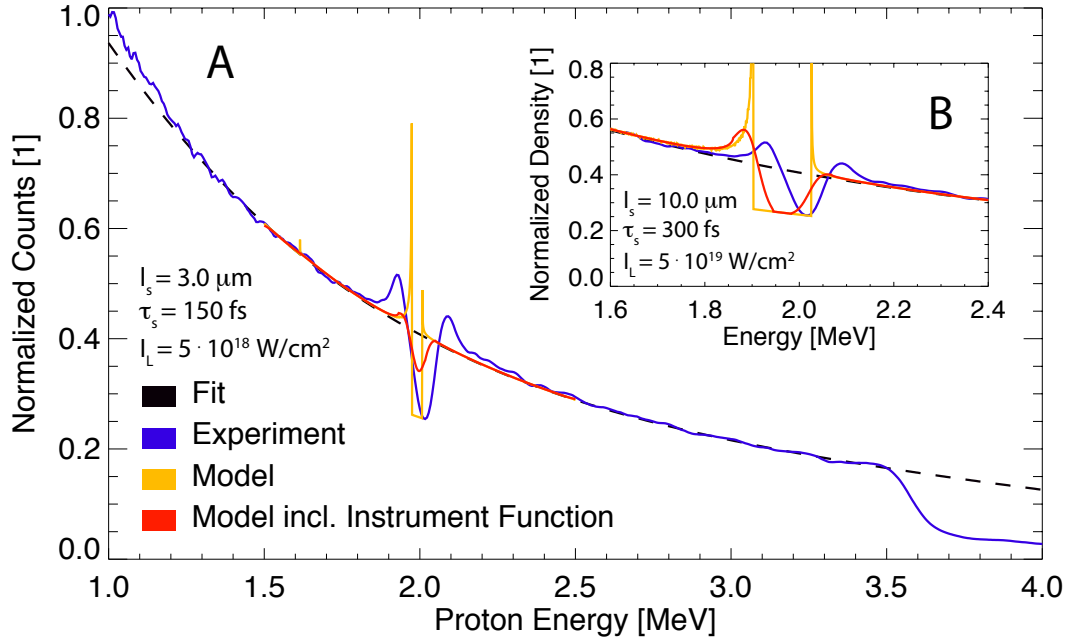


Figure B.5: Simulated and experimentally obtained redistribution effects in the (uncorrected) proton energy spectrum. The simulation is based on Equation B.5 whereby different parameters are used: **A** - $I_L = 1 \cdot 10^{18} \text{ W/cm}^2$, $l_s = 3 \mu\text{m}$, $\tau_s = 150 \text{ fs}$. **B** - $I_L = 5 \cdot 10^{18} \text{ W/cm}^2$, $l_s = 10 \mu\text{m}$, $\tau_s = 300 \text{ fs}$.

In the case of Figure B.5.B a different set of parameters was used for the calculation of the acceleration field (Equation B.5). In this case all parameters are significantly increased: $I_L = 5 \cdot 10^{19} \text{ W/cm}^2$, $l_s = 10 \mu\text{m}$ and $\tau_s = 300 \text{ fs}$.

In both cases the simulated gap width is significantly smaller than the measured width. In addition the experimentally obtained peak on the high energy side of the gap is not reproduced in terms of position and height. Using the approximation of Equation B.5 an adequate reproduction of the high energy peak is generally not possible for small values of $l_s \leq 25 \mu\text{m}$, independent on the setting of E_L or τ_s . Also Formula B.4.A and the functions

$$\mathcal{E}_t = \frac{1}{(1 + (t/\tau_s))^2} \quad (\text{A}), \quad \mathcal{E}_t = \frac{1}{1 + (t/\tau_s)^2} \quad (\text{B}). \quad (\text{B.6})$$

were tested as a description of the time decay $\mathcal{E}_t(t)$ in Equation B.5, but the high energy peak could not be reproduced. Only the use of higher values of $l_s (\geq 25 \mu\text{m})$

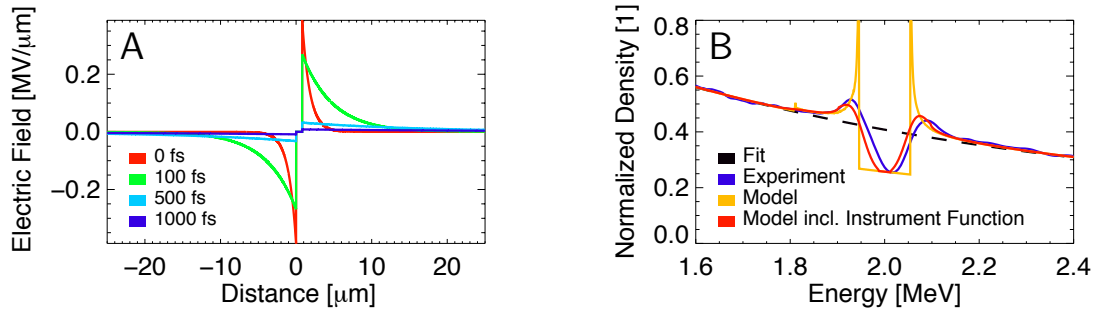


Figure B.6: **A** - Analytical field distribution based on Equations B.5 and B.6 and B.7 using the parameters: $I_L = 1 \cdot 10^{18} \text{ W/cm}^2$, $l_{s0} = 1 \mu\text{m}$, $v_{1s} = 30 \mu\text{m/ps}$ and $\tau_s = 150 \text{ fs}$. **B** - Resulting simulated redistribution effect in comparison with the experimental result.

allows the experimentally obtained redistribution effects to be reproduced to some extent. However, these relatively high extensions are in contradiction to the results of the PIC-simulation, where an initial extension l_s of approximately $1 \mu\text{m}$ was found.

Better results are obtained if the extension $l_s(t)$ of the field increases with time, which is agreement with the PIC-simulation. In first approximation this increase can be described by

$$l_s(t) = l_{s0} + v_{1s}t, \quad (\text{B.7})$$

whereby l_{s0} is the initial extension of the field and v_{1s} a constant.

Figure B.6.A shows the resulting field distribution at different moments in time, whereby Equation B.6.B is used to describe the temporal evolution of the field. The applied parameters are summarized in the figure caption. The resulting simulated redistribution effect is shown in Figure B.6.B and is in good agreement with the experimental result. Also several other experimental results can be reproduced by means of the proposed analytical description. Similar results are obtained if Equation B.6.A is applied. However, in any case the model fails to describe the systematic dependency of the redistribution effect on the target distance a , which was found in Section 9.3.1. In contradiction to the experimental results the local maxima on the low energy side of the density gap does not disappear in simulation if a lower target distance a is used.

This indicates that the proposed approximation of the PIC-simulation (Equation B.5) is possibly too artificial to describe the complex field evolution of the TNSA-process. It is also conceivable that the observed proton redistribution is not only influenced by the high TNSA-fields that act at close distances to the foil, but also by long extended fields which cannot be described by an exponential decay in space. This possibility will be discussed in Section 9.5.1.

B.3 Magnetic Field Components of the Permanent Magnet

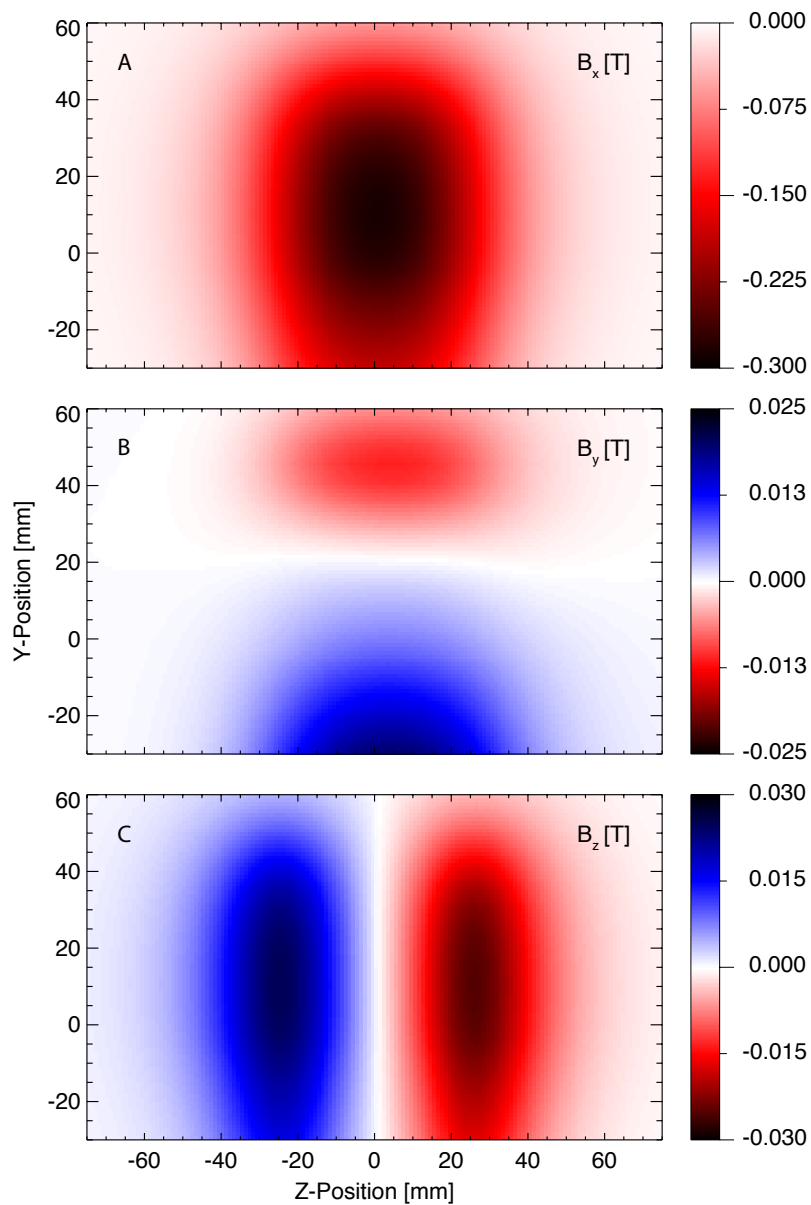


Figure B.7: Magnetic field components in the y-z-plane of the permanent magnet at the position $x = 0$. **A** - B_x , **B** - B_y , **C** - B_z .

B.4 Energy Modulations in Laser Accelerated Ion Beams - Analytical Description

The modulation of the electron density in space and time and its direct relation to oscillations of the ponderomotive pressure is a substantial finding from the PIC simulation (Section 6.3). Based on this result a one-dimensional analytical model [28] was developed by A. Andreev on the basis of a perturbation ansatz. The relativistic energy-momentum relation defines the velocity of an electron $v_e^{(0)}$ within the electric potential φ and can be written in the form

$$\frac{v_e^{(0)}}{c} = \sqrt{1 - \frac{1}{(1 + (\varepsilon_{e0} + e\varphi)/m_e c^2)^2}}, \quad (\text{B.8})$$

whereby c is the velocity of light. The electron charge and mass are denoted by e and m_e and its initial energy by ε_{e0} . By introducing the electron density perturbation n_{1e} the electron density n_e can be expressed as the sum of two terms

$$n_e = n_{e0} \exp\left(\frac{e\varphi}{T_e}\right) \left[1 + \frac{n_{1e}}{n_{e0}} \exp\left(-\frac{t^2}{t_L^2}\right) \cos^2\left(k(z - tv_e^{(0)}(\varphi))\right) \right], \quad (\text{B.9})$$

whereby n_{e0} denotes the initial electron density and T_e the electron temperature. The wave vector of the laser pulse is given by k and its duration by t_L . The propagation-coordinate is z and t is the time. The first term of Equation B.9 describes the undisturbed part of the electron density. The second term models the perturbation of the electron density due to the oscillation of the ponderomotive pressure of the laser radiation. As shown in the numerical simulation (Section 6.3) the ponderomotive action of the laser irradiation leads to the generation of fast electron bunches. The approximated form of the density perturbation is based on the data of these simulations.

The ion motion can be described by means of the continuity equation, the hydrodynamic equation of motion and the Poisson equation

$$\frac{\partial n_i}{\partial t} + \text{div}(n_i v_i) = 0, \quad (\text{B.10})$$

$$\frac{\partial v_i}{\partial t} + (v_i \cdot \nabla) v_i = \frac{Ze}{m_i} \nabla \varphi, \quad (\text{B.11})$$

$$\Delta \varphi = 4\pi e (n_e - Zn_i). \quad (\text{B.12})$$

In zero approximation ($\delta n_{1e} = 0$), e.g. by neglecting the perturbation term in Equation B.9, these equations describe the self-similar motion of an electron-ion plasma in the absence of collisions [67, 73]. In this connection it is assumed that the plasma occupies the half space $z < 0$ at the initial time and at time $t = 0$ begins to expand into a vacuum. By describing the plasma as quasi-neutral $Zn_{i0} = n_{e0}$ a

solution is found and the proton distribution function $f^{(0)}(\varepsilon)$ depending on energy ε is obtained [73]

$$\begin{aligned} v_i^{(0)} &= \frac{z}{t} + c_{s0}, & n_i^{(0)} &= n_{i0} \exp\left(-\left(\frac{z}{c_{s0}t}\right)\right), & e\varphi^{(0)} &= T_e \ln\left(\frac{Zn_i^{(0)}}{n_{e0}}\right), \\ f^{(0)}(\varepsilon) &= \frac{1}{m_i v_i} \frac{dn_i^{(0)}}{dv_i^{(0)}} = \frac{n_{i0}}{\sqrt{2\varepsilon T_e}} \exp\left(1 - \sqrt{\frac{2\varepsilon}{T_e}}\right), & c_{s0} &= \sqrt{\frac{ZT_e}{m_i}}, \end{aligned} \quad (\text{B.13})$$

whereby n_i denotes the fast and n_{i0} the initial ion density. The ion velocity is given by v_i and its charge and mass by Z and m_i , respectively.

A perturbation ansatz is applied to the set of Equations B.8 to B.12 in order to derive a solution, which also includes the second term in Equation B.9. In this connection the electron density perturbation $\delta n_{1e} = n_{1e}/n_{e0} \ll 1$ is assumed to be small. Considering a weak temporal and spatial dependence of the variables in Equation B.13 in comparison to those in Equations B.16 to B.18, the linearization of the hydrodynamic equations leads in first order to the following set of equations:

$$\begin{aligned} \frac{\partial n_i^{(1)}}{\partial t} + n_i^{(0)} \frac{\partial v_i^{(1)}}{\partial x} + v_i^{(0)} \frac{\partial n_i^{(1)}}{\partial x} &= 0, \\ \frac{\partial v_i^{(1)}}{\partial t} + v_i^{(0)} \frac{\partial v_i^{(1)}}{\partial x} &= -\frac{Ze}{m_i} \frac{\partial \varphi^{(1)}}{\partial x}, \\ \frac{\partial^2 \varphi^{(1)}}{\partial x^2} &= 2\pi e n_{1e} \exp\left(\frac{e\varphi^{(0)}}{T_e}\right) \exp\left(-\frac{t^2}{\tau_L^2}\right) \cos\left(2k(z - tv_e^{(0)})\right). \end{aligned} \quad (\text{B.14})$$

The perturbations in this system are connected via the Poisson equation to the perturbation of electron density in Equation B.9. The solution of this inhomogeneous system of linear Equations B.14 consists of a particular solution of the inhomogeneous system and the general one of the homogeneous system.

Formally the general solution (of the homogeneous system) for the ion density perturbation can be expressed as

$$n_{i,\text{hom}}^{(1)} = \sum_{\kappa} C_{\kappa} \cos(\kappa z - \omega(\kappa)t), \quad (\text{B.15})$$

whereby $\omega(\kappa)$ are the natural modes of ion plasma oscillations corresponding to the ion species κ . Naturally the relation $\omega(\kappa) \leq \omega_{pp}$ is valid for the plasma frequency ω_{pp} of accelerated protons. Any initial or boundary conditions for the System B.14 can result in a non-zero coefficient in Equation B.15. In these cases the natural plasma modes will modify the distribution function and its modulation.

However, a modulation of the proton distribution function at an energy of above 0.5 MeV is considered. These protons are accelerated by an electric field which is generated by fast electrons of about the same energy. The hot electron density is

similar or slightly less than the plasma critical density and the accelerated protons have about the same density due to plasma quasi-neutrality. The period of the ion plasma wave at the critical density of the plasma is about 40 times larger than the laser wave period. Therefore, the homogeneous solution (Equations B.15) describes ion density oscillations (also of velocity and potential concerning Equations B.14) with a time period being 40 times larger than the laser period (for the ion sound it is even more). This time scale is about 100 fs and thus comparable to the characteristic time of ion acceleration which corresponds to the simulation time of 250 fs.

As numerical analysis confirms, the relevant initial and boundary conditions favor to omit the eigenmodes of plasma oscillations which take place on a much longer timescale. Therefore, only the particular solution of the inhomogeneous system of differential Equations B.14 is used in the following analysis and the solution of the homogeneous system is neglected. In this case the dependences of all hydro variables in Equations B.14 on space and time are similar to the dependence of the electron density perturbation. Thus, the linear (first) approximations of density, velocity, and the potential functions have the form

$$n_i^{(1)} = n_{10} \cos(2k(z - tv_e^{(0)})), \quad (\text{B.16})$$

$$v_i^{(1)} = v_{10} \cos(2k(z - tv_e^{(0)})), \quad (\text{B.17})$$

$$\varphi^{(1)} = \varphi_{10} \cos(2k(z - tv_e^{(0)})), \quad (\text{B.18})$$

$$\frac{v_e^{(0)}}{c} = \sqrt{1 - \frac{1}{\left(1 + \left(\varepsilon_{e0} + T_e \ln\left(Zn_i^{(0)}/n_{e0}\right)\right)/m_e c^2\right)^2}}. \quad (\text{B.19})$$

Substitution of these functions into Equations B.14 leads to a linear system of algebraic equations for the unknown amplitudes n_{10} , v_{10} and φ_{10} . Its solution is given by

$$n_{10} = -\frac{Z\pi e^2 n_{1e} n_i^{(0)2} \exp(-t^2/t_L^2)}{2k^2 n_{e0} m_i \left(v_e^{(0)} - v_i^{(0)}\right)^2}, \quad (\text{B.20})$$

$$v_{10} = -\frac{Z\pi e^2 n_{1e} n_i^{(0)} \exp(-t^2/t_L^2)}{2k^2 n_{e0} m_i \left(v_e^{(0)} - v_i^{(0)}\right)}, \quad (\text{B.21})$$

$$\varphi_{10} = -\frac{\pi e n_{1e} n_i^{(0)} \exp(-t^2/t_L^2)}{2k^2 n_{e0}}. \quad (\text{B.22})$$

The proton distribution function is determined by $f(\varepsilon) = dn_i/d\varepsilon_i = (1/m_i v_i) \cdot$

dn_i/dv_i and can be expressed by the parametric dependence

$$f(\tau) = \frac{n_{i0}}{ZT_e} \left[\frac{\exp(-\xi/\tau)}{1 + \xi/\tau} \left(1 + \frac{2\beta_e^{(0)}\beta_{10}\sin\left(2k\left(\xi - \tau\beta_e^{(0)}\right)\right)}{\xi/\tau^2} \right) + \frac{2\beta_e^{(0)}N_{10}\sin\left(2k\left(\xi - \tau\beta_e^{(0)}\right)\right)}{(1 + \xi/\tau)\xi/\tau^2} + \frac{\beta_{10}\exp(-\xi/\tau)\cos\left(2k\left(\xi - \tau\beta_e^{(0)}\right)\right)}{(1 + \xi/\tau)} \right] \quad (\text{B.23})$$

$$\varepsilon(\tau) = \frac{ZT_e}{2} \left(1 + \frac{\xi}{\tau} + \beta_{10} \cdot \cos\left(2k\left(\xi - \tau\beta_e^{(0)}\right)\right) \right)^2, \quad \tau \in \left[\frac{\xi T_e}{\varepsilon_{e0}}, \infty \right]. \quad (\text{B.24})$$

whereby $\xi = kz$, $\tau = kc_s t$, $\beta_e^{(0)} = v_e^{(0)}/c_s$, $\beta_{10} = v_{10}/c_s$ and $N_{10} = n_{10}/n_{i0}$. The values for the parameters ε_{e0} , T_e , δn_{1e} are chosen in agreement with simulation and are $14 m_e c^2$, $0.6 m_e c^2$ and 0.02 , respectively.

List of Abbreviations

ADC	allyl diglycol carbonate
AOM	acousto-optic Modulator
ASE	amplified spontaneous emission
BSI	barrier suppression ionization
CCD	charge-coupled device
CE	carrier envelope
CGS	centimetre–gram–second
CPA	chirped pulse amplification
CW	continuous wave
EFM	expanding field model
EOR	electro-optic rectification
FWHM	full width at half maximum
FW	fundamental wave
GDD	group delay dispersion
GPT	general particle tracer
GVD	group velocity dispersion
HFL	high field laser
IR	infra red
KLM	Kerr-lens mode-locking
LPI	lines per inch

MBI Max-Born-Institute

MCP multi-channel plate

NPCPA negatively and positively chirped pulse amplification

PIC particle-in-cell

RPA radiation pressure acceleration

SFG sum-frequency generation

SHG second-harmonic generation

SI système international d'unités

SPMD self-phase modulation

SPM surface potential model

SSNTD solid state nuclear track detector

SVEA slowly varying envelope approximation

Ti:sapphire titanium-sapphire

TNSA target normal sheath acceleration

XPW cross-polarized wave

Bibliography

- [1] D. Habs et al., *WHITEBOOK ELI – Extreme Light Infrastructure; Science and Technology with Ultra-Intense Lasers*, edited by G. A. Mourou, G. Korn, W. Sandner, and J. L. Collier (Andreas Thoss, 2011) (cit. on pp. 1, 2).
- [2] E. O. Lawrence and M. S. Livingston, “The production of high speed light ions without the use of high voltages”, *Physical Review* **40**, 19 (1932) (cit. on p. 1).
- [3] D. Jung, L. Yin, D. C. Gautier, H.-C. Wu, S. Letzring, B. Dromey, R. Shah, S. Palaniyappan, T. Shimada, R. P. Johnson, J. Schreiber, D. Habs, J. C. Fernandez, B. M. Hegelich, and B. J. Albright, “Laser-driven 1 GeV carbon ions from preheated diamond targets in the break-out afterburner regime”, *Physics of Plasmas* **20**, 083103 (2013) (cit. on p. 1).
- [4] T. E. Cowan, J. Fuchs, H. Ruhl, A. Kemp, P. Audebert, M. Roth, R. Stephens, I. Barton, A. Blazevic, E. Brambrink, J. Cobble, J. Fernandez, J. C. Gauthier, M. Geissel, M. Hegelich, J. Kaae, S. Karsch, G. P. Le Sage, S. Letzring, M. Manclossi, S. Meyroneinc, A. Newkirk, H. Pepin, and N. Renard-LeGalloudec, “Ultralow emittance, multi-MeV proton beams from a laser virtual-cathode plasma accelerator”, *Physical Review Letters* **92**, 204801 (2004) (cit. on pp. 2, 93, 111).
- [5] M. Borghesi, A. Schiavi, D. H. Campbell, M. G. Haines, O. Willi, A. J. MacKinnon, L. A. Gizzi, M. Galimberti, R. J. Clarke, and H. Ruhl, “Proton imaging: a diagnostic for inertial confinement fusion/fast ignitor studies”, *Plasma Physics and Controlled Fusion* **43**, A267–A276 (2001) (cit. on pp. 2, 93).
- [6] A. J. Mackinnon, P. K. Patel, R. P. Town, M. J. Edwards, T. Phillips, S. C. Lerner, D. W. Price, D. Hicks, M. H. Key, S. Hatchett, S. C. Wilks, M. Borghesi, L. Romagnani, S. Kar, T. Toncian, G. Pretzler, O. Willi, M. Koenig, E. Martinolli, S. Lepape, A. Benuzzi-Mounaix, P. Audebert, J. C. Gauthier, J. King, R. Snavely, R. R. Freeman, and T. Boehlly, “Proton radiography as an electromagnetic field and density perturbation diagnostic (invited)”, *Review of Scientific Instruments* **75**, 3531–3536 (2004) (cit. on pp. 2, 93).

-
- [7] T. Sokollik, M. Schnürer, S. Ter-Avetisyan, P. V. Nickles, E. Risse, M. Kalashnikov, W. Sandner, G. Priebe, M. Amin, T. Toncian, O. Willi, and A. A. Andreev, “Transient electric fields in laser plasmas observed by proton streak deflectometry”, *Applied Physics Letters* **92**, 091503 (2008) (cit. on pp. 2, 80, 96, 113, 213).
- [8] T. Sokollik, *Investigations of Field Dynamics in Laser Plasmas with Proton Imaging* (Springer, 2011) (cit. on pp. 2, 30, 59, 75, 94, 99, 101, 103, 106, 213, 215, 217).
- [9] P. K. Patel, A. J. Mackinnon, M. H. Key, T. E. Cowan, M. E. Foord, M. Allen, D. F. Price, H. Ruhl, P. T. Springer, and R. Stephens, “Isochoric heating of solid-density matter with an ultrafast proton beam”, *Physical Review Letters* **91**, 125004 (2003) (cit. on p. 2).
- [10] G. M. Dyer, A. C. Bernstein, B. I. Cho, J. Osterholz, W. Grigsby, A. Dalton, R. Shepherd, Y. Ping, H. Chen, K. Widmann, and T. Ditmire, “Equation-of-state measurement of dense plasmas heated with fast protons”, *Physical Review Letters* **101**, 015002 (2008) (cit. on p. 2).
- [11] M. Roth, T. E. Cowan, M. H. Key, S. P. Hatchett, C. Brown, W. Fountain, J. Johnson, D. M. Pennington, R. A. Snavely, S. C. Wilks, K. Yasuike, H. Ruhl, F. Pegoraro, S. V. Bulanov, E. M. Campbell, M. D. Perry, and H. Powell, “Fast ignition by intense laser-accelerated proton beams”, *Physical Review Letters* **86**, 436–439 (2001) (cit. on p. 2).
- [12] V. Y. Bychekov, W. Rozmus, A. Maksimchuk, D. Umstadter, and C. E. Capjack, “Fast ignitor concept with light ions”, *Plasma Physics Reports* **27**, 1017–1020 (2001) (cit. on p. 2).
- [13] K. Krushelnick, E. L. Clark, R. Allott, F. N. Beg, C. N. Danson, A. Machacek, V. Malka, Z. Najmudin, D. Neely, P. A. Norreys, M. R. Salvati, M. I. K. Santala, M. Tatarakis, I. Watts, M. Zepf, and A. E. Dangor, “Ultrahigh-intensity laser-produced plasmas as a compact heavy ion injection source”, *Ieee Transactions On Plasma Science* **28**, 1184–1189 (2000) (cit. on p. 2).
- [14] A. Noda, S. Nakamura, Y. Iwashita, S. Sakabe, M. Hashida, T. Shirai, S. Shimizu, H. Tongu, H. Ito, H. Souda, A. Yamazaki, M. Tanabe, H. Daido, M. Mori, M. Kado, A. Sagisaka, K. Ogura, M. Nishiuchi, S. Orimo, Y. Hayashi, A. Yogo, S. Bulanov, T. Esirkepov, A. Nagashima, T. Kimura, T. Tajima, T. Takeuchi, K. Matsukado, A. Fukumi, and Z. Li, “Phase rotation scheme of laser-produced ions for reduction of the energy spread”, *Laser Physics* **16**, 647–653 (2006) (cit. on p. 2).
- [15] P. Antici, M. Fazi, A. Lombardi, M. Migliorati, L. Palumbo, P. Audebert, and J. Fuchs, “Numerical study of a linear accelerator using laser-generated proton beams as a source”, *Journal of Applied Physics* **104**, 124901 (2008) (cit. on p. 2).

-
- [16] S. V. Bulanov and V. S. Khoroshkov, “Feasibility of using laser ion accelerators in proton therapy”, *Plasma Physics Reports* **28**, 453–456 (2002) (cit. on p. 2).
- [17] S. V. Bulanov, T. Z. Esirkepov, F. F. Kamenets, Y. Kato, A. V. Kuznetsov, K. Nishihara, F. Pegoraro, T. Tajima, and V. S. Khoroshkov, “Generation of high-quality charged particle beams during the acceleration of ions by high-power laser radiation”, *Plasma Physics Reports* **28**, 975–991 (2002) (cit. on p. 2).
- [18] E. Fourkal, J. S. Li, W. Xiong, A. Nahum, and C. M. Ma, “Intensity modulated radiation therapy using laser-accelerated protons: a Monte Carlo dosimetric study”, *Physics in Medicine and Biology* **48**, 3977 (2003) (cit. on p. 2).
- [19] E. Fourkal, J. S. Li, M. Ding, T. Tajima, and C. M. Ma, “Particle selection for laser-accelerated proton therapy feasibility study”, *Medical Physics* **30**, 1660–1670 (2003) (cit. on p. 2).
- [20] V. Malka, S. Fritzler, E. Lefebvre, E. d’Humieres, R. Ferrand, G. Grillon, C. Albaret, S. Meyroneinc, J. P. Chambaret, A. Antonetti, and D. Hulin, “Practicability of protontherapy using compact laser systems”, *Medical Physics* **31**, 1587–1592 (2004) (cit. on p. 2).
- [21] P. R. Bolton, T. Hori, H. Kiriyama, M. Mori, H. Sakaki, K. Sutherland, M. Suzuki, J. Wu, and A. Yogo, “Toward integrated laser-driven ion accelerator systems at the photo-medical research center in Japan”, *Nuclear Instruments and Methods in Physics Research Section A: Accelerators, Spectrometers, Detectors and Associated Equipment* **620**, 71–75 (2010) (cit. on p. 2).
- [22] S. Fritzler, V. Malka, G. Grillon, J. P. Rousseau, F. Burgy, E. Lefebvre, E. d’Humieres, P. McKenna, and K. W. D. Ledingham, “Proton beams generated with high-intensity lasers: applications to medical isotope production”, *Applied Physics Letters* **83**, 3039–3041 (2003) (cit. on p. 2).
- [23] K. W. D. Ledingham, P. McKenna, T. McCanny, S. Shimizu, J. M. Yang, L. Robson, J. Zweit, J. M. Gillies, J. Bailey, G. N. Chimon, R. J. Clarke, D. Neely, P. A. Norreys, J. L. Collier, R. P. Singhal, M. S. Wei, S. P. D. Mangles, P. Nilson, K. Krushelnick, and M. Zepf, “High power laser production of short-lived isotopes for positron emission tomography”, *Journal of Physics D-applied Physics* **37**, 2341 (2004) (cit. on p. 2).
- [24] J. M. Ollinger and J. A. Fessler, “Positron-emission tomography”, *Ieee Signal Processing Magazine* **14**, 43–55 (1997) (cit. on p. 2).
- [25] F. P. Boody, R. Hopel, H. Hora, and J. C. Kelly, “Laser-driven ion source for reduced-cost implantation of metal ions for strong reduction of dry friction and increased durability”, *Laser and Particle Beams* **14**, 443–448 (1996) (cit. on p. 2).

- [26] L. Torrisci, S. Gammino, A. M. Mezzasalma, J. Badziak, P. Parys, J. Wolowski, E. Woryna, J. Krasa, L. Laska, M. Pfeifer, K. Rohlena, and F. P. Boody, “Implantation of ions produced by the use of high power iodine laser”, *Applied Surface Science* **217**, 319–331 (2003) (cit. on p. 2).
- [27] M. Rosinski, J. Badziak, F. P. Boody, S. Gammino, H. Hora, J. Krasa, L. Laska, A. M. Mezzasalma, P. Parys, K. Rohlena, L. Torrisci, J. Ullschmied, J. Wolowski, and E. Woryna, “Application of laser ion source for ion implantation technology”, *Vacuum* **78**, 435–438 (2005) (cit. on p. 2).
- [28] M. Schnürer, A. A. Andreev, F. Abicht, J. Bränzel, C. Koschitzki, K. Y. Platonov, G. Priebe, and W. Sandner, “The beat in laser-accelerated ion beams”, *Physics of Plasmas* **20**, 103102 (2013) (cit. on pp. 3, 77, 81, 86, 223).
- [29] W. Zinth and U. Zinth, *Optik* (Oldenbourg Wissenschaftsverlag, 2009) (cit. on pp. 10, 26, 209).
- [30] B. E. A. Saleh and M. C. Teich, *Fundamentals of Photonics* (John Wiley & Sons, Inc., 2007) (cit. on pp. 12, 13, 25, 26).
- [31] P. F. Moulton, “Spectroscopic and laser characteristics of Ti:Al₂O₃”, *J. Opt. Soc. Am. B* **3**, 125–133 (1986) (cit. on p. 17).
- [32] D. E. Spence, P. N. Kean, and W. Sibbett, “60-fsec pulse generation from a self-mode-locked Ti:sapphire laser”, *Optics Letters* **16**, 42–44 (1991) (cit. on p. 19).
- [33] M. Piché and F. Salin, “Self-mode locking of solid-state lasers without apertures”, *Opt. Lett.* **18**, 1041–1043 (1993) (cit. on p. 19).
- [34] D. Strickland and G. Mourou, “Compression of amplified chirped optical pulses”, *Optics Communications* **56**, 219–221 (1985) (cit. on p. 19).
- [35] F. Träger, *Springer Handbook of Lasers and Optics* (Springer Verlag, 2007) (cit. on p. 20).
- [36] N. V. Didenko, A. V. Konyashchenko, A. P. Lutsenko, and S. Y. Tenyakov, “Contrast degradation in a chirped-pulse amplifier due to generation of prepulses by postpulses”, *Optics Express* **16**, 3178–3190 (2008) (cit. on p. 21).
- [37] P. Gibbon, “High-order harmonic generation in plasmas”, *Quantum Electronics, IEEE Journal of* **33**, 1915–1924 (1997) (cit. on p. 21).
- [38] A. Henig, S. Steinke, M. Schnürer, T. Sokollik, R. Horlein, D. Kiefer, D. Jung, J. Schreiber, B. M. Hegelich, X. Q. Yan, J. Meyer-ter-Vehn, T. Tajima, P. V. Nickles, W. Sandner, and D. Habs, “Radiation-pressure acceleration of ion beams driven by circularly polarized laser pulses”, *Physical Review Letters* **103**, 245003 (2009) (cit. on p. 21).

- [39] C. Ziener, P. S. Foster, E. J. Divall, C. J. Hooker, M. H. R. Hutchinson, A. J. Langley, and D. Neely, “Specular reflectivity of plasma mirrors as a function of intensity, pulse duration, and angle of incidence”, *Journal of Applied Physics* **93**, 768–770 (2003) (cit. on p. 23).
- [40] A. Lévy, T. Ceccotti, P. D’Oliveira, F. Réau, M. Perdrix, F. Quéré, P. Monot, M. Bougeard, H. Lagadec, P. Martin, J.-P. Geindre, and P. Audebert, “Double plasma mirror for ultrahigh temporal contrast ultraintense laser pulses”, *Opt. Lett.* **32**, 310–312 (2007) (cit. on pp. 23, 89).
- [41] S. Steinke, *Entwicklung eines Doppel-Plasmaspiegels zur Erzeugung hochenergetischer Ionen mit ultra-dünnen Targets* (Freie Universität Berlin, 2007) (cit. on pp. 23, 89).
- [42] Y. P. Svirko and N. I. Zheludev, *Polarization of Light in Nonlinear Optics* (2000) (cit. on p. 23).
- [43] N. Minkovski, S. M. Saltiel, G. I. Petrov, O. Albert, and J. Etchepare, “Polarization rotation induced by cascaded third-order processes”, *Opt. Lett.* **27**, 2025–2027 (2002) (cit. on p. 24).
- [44] L. Canova, S. Kourtev, N. Minkovski, A. Jullien, R. Lopez-Martens, O. Albert, and S. M. Saltiel, “Efficient generation of cross-polarized femtosecond pulses in cubic crystals with holographic cut orientation”, *Applied Physics Letters* **92** (2008) (cit. on p. 24).
- [45] M. P. Kalashnikov, K. Osvay, G. Priebe, L. Ehrentraut, S. Steinke, and W. Sandner, “Temporal contrast of high intensity laser systems above 10^{11} with double CPA technique”, *AIP Conf. Proc.* **1462**, 108–111 (2012) (cit. on pp. 24, 30, 77, 78, 80, 89).
- [46] Z. H. Wang, Z. Jin, J. Zheng, P. Wang, Z. Y. Wei, and J. Zhang, “Wavefront correction of high-intensity fs laser beams by using closed-loop adaptive optics system”, *Science In China (Series G) Physics, Mechanics & Astronomy* **48**, 122–128 (2005) (cit. on p. 31).
- [47] P. Gibbon, *Short Pulse Laser Interactions with Matter: An Introduction*. (World Scientific Publishing Company, 2005) (cit. on pp. 35, 36, 43, 44, 49, 54–56, 134).
- [48] J. N. Bardsley, B. M. Penetrante, and M. H. Mittleman, “Relativistic dynamics of electrons in intense laser fields”, *Phys. Rev. A* **40**, 3823–3835 (1989) (cit. on p. 37).
- [49] D. Bauer, *Theory of intense laser-matter interaction* (Max-Planck-Institut für Kernphysik, Heidelberg, 2006) (cit. on p. 40).
- [50] B. Quesnel and P. Mora, “Theory and simulation of the interaction of ultraintense laser pulses with electrons in vacuum”, *Physical Review E* **58**, 3719–3732 (1998) (cit. on p. 42).

-
- [51] C. B. Schaffer, A. Brodeur, and E. Mazur, “Laser-induced breakdown and damage in bulk transparent materials induced by tightly focused femtosecond laser pulses”, *Measurement Science and Technology* **12**, 1784–1794 (2001) (cit. on p. 42).
- [52] L. V. Keldysh, “Ionization in field of a strong electromagnetic wave”, *Soviet physics, JETP* **20**, 1307–1314 (1965) (cit. on p. 43).
- [53] M. Lenzner, J. Krüger, S. Sartania, Z. Cheng, C. Spielmann, G. Mourou, W. Kautek, and F. Krausz, “Femtosecond optical breakdown in dielectrics”, *Physical Review Letters* **80**, 4076–4079 (1998) (cit. on p. 44).
- [54] S. Eliezer, *The Interaction of High-Power Lasers with Plasmas* (Institute of Physics Publishing, 2002) (cit. on pp. 44, 47, 48).
- [55] J. A. Bittencourt, *Fundamentals of Plasma Physics* (Springer-Verlag New York, 2004) (cit. on p. 46).
- [56] E. Lefebvre and G. Bonnaud, “Transparency/Opacity of a solid target illuminated by an ultrahigh-intensity laser pulse”, *Phys. Rev. Lett.* **74**, 2002–2005 (1995) (cit. on p. 46).
- [57] P. Drude, “Zur Elektronentheorie der Metalle”, *Annalen der Physik* **306**, 566–613 (1900) (cit. on p. 47).
- [58] H. Daido, M. Nishiuchi, and A. S. Pirozhkov, “Review of laser-driven ion sources and their applications”, *Reports On Progress In Physics* **75**, 056401 (2012) (cit. on p. 49).
- [59] A. Macchi, M. Borghesi, and M. Passoni, “Ion acceleration by superintense laser-plasma interaction”, *Rev. Mod. Phys.* **85**, 751–793 (2013) (cit. on p. 49).
- [60] S. C. Wilks and W. L. Kruer, “Absorption of ultrashort, ultra-intense laser light by solids and overdense plasmas”, *IEEE Journal of Quantum Electronics* **33**, 1954–1968 (1997) (cit. on pp. 49, 50).
- [61] G. A. Mourou, T. Tajima, and S. V. Bulanov, “Optics in the relativistic regime”, *Reviews of Modern Physics* **78**, 309 (2006) (cit. on p. 49).
- [62] J. R. Davies, “Laser absorption by overdense plasmas in the relativistic regime”, *Plasma Physics and Controlled Fusion* **51**, 014006 (2009) (cit. on p. 49).
- [63] V. F. Diachenko and V. S. Imshennik, “Anomalous interaction of intense light beams with dense plasmas”, *Fizika Plazmy* **5**, 737–744 (1979) (cit. on p. 50).
- [64] F. Brunel, “Not-so-resonant, resonant absorption”, *Physical Review Letters* **59**, 52–55 (1987) (cit. on p. 50).
- [65] W. L. Kruer and K. G. Estabrook, “JxB heating by very intense laser-light”, *Physics of Fluids* **28**, 430–432 (1985) (cit. on p. 50).

- [66] D. R. Bach, D. E. Casperson, D. W. Forslund, S. J. Gitomer, P. D. Goldstone, A. Hauer, J. F. Kephart, J. M. Kindel, R. Kristal, G. A. Kyrala, K. B. Mitchell, D. B. Vanhulsteyn, and A. H. Williams, “Intensity-dependent absorption in 10.6- μm laser-illuminated spheres”, *Physical Review Letters* **50**, 2082–2085 (1983) (cit. on p. 50).
- [67] A. V. Gurevich, L. V. Pariiskaya, and L. P. Pitaevskii, “Self-similar motion or rarefied plasma”, *Soviet physics, JETP* **22**, 449–454 (1966) (cit. on pp. 50, 223).
- [68] A. V. Gurevich, L. V. Pariiskaya, and L. P. Pitaevskii, “Ion acceleration on expansion of a rarefied plasma”, *Zh. Eksp. Teor. Fiz.* **63**, 516–531 (1972) (cit. on p. 50).
- [69] J. E. Crow, P. L. Auer, and J. E. Allen, “Expansion of a plasma into a vacuum”, *Journal of Plasma Physics* **14**, 65–76 (1975) (cit. on p. 50).
- [70] A. V. Gurevich and A. P. Meshcherkin, “Ion acceleration in an expanding plasma”, *Zh. Eksp. Teor. Fiz.* **80**, 1810–1826 (1981) (cit. on p. 50).
- [71] D. S. Dorozhkina and V. E. Semenov, “Exact solution of vlasov equations for quasineutral expansion of plasma bunch into vacuum”, *Physical Review Letters* **81**, 2691–2694 (1998) (cit. on p. 50).
- [72] V. F. Kovalev and V. Y. Bychenkov, “Analytic solutions to the vlasov equations for expanding plasmas”, *Physical Review Letters* **90**, 185004 (2003) (cit. on p. 50).
- [73] P. Mora, “Plasma expansion into a vacuum”, *Physical Review Letters* **90**, 185002 (2003) (cit. on pp. 50, 52–54, 88, 124, 134, 198, 223, 224).
- [74] P. Mora, “Thin-foil expansion into a vacuum”, *Physical Review E* **72**, 056401 (2005) (cit. on pp. 50, 52, 126, 127, 134, 140, 141).
- [75] M. Lontano and M. Passoni, “Electrostatic field distribution at the sharp interface between high density matter and vacuum”, *Physics of Plasmas* **13**, 042102 (2006) (cit. on p. 50).
- [76] M. Nishiuchi, A. Fukumi, H. Daido, Z. Li, A. Sagisaka, K. Ogura, S. Orimo, M. Kado, Y. Hayashi, M. Mori, S. V. Bulanov, T. Esirkepov, K. Nemoto, Y. Oishi, T. Nayuki, T. Fujii, A. Noda, Y. Iwashita, T. Shirai, and S. Nakamura, “The laser proton acceleration in the strong charge separation regime”, *Physics Letters A* **357**, 339–344 (2006) (cit. on p. 50).
- [77] J. Schreiber, F. Bell, F. Grüner, U. Schramm, M. Geissler, M. Schnürer, S. Ter-Avetisyan, B. M. Hegelich, J. Cobble, E. Brambrink, J. Fuchs, P. Audebert, and D. Habs, “Analytical model for ion acceleration by high-intensity laser pulses”, *Physical Review Letters* **97**, 045005 (2006) (cit. on p. 50).

- [78] J. Fuchs, P. Antici, E. d’Humières, E. Lefebvre, M. Borghesi, E. Brambrink, C. A. Cecchetti, M. Kaluza, V. Malka, M. Manclossi, S. Meyroneinc, P. Mora, J. Schreiber, T. Toncian, H. Pépin, and P. Audebert, “Laser-driven proton scaling laws and new paths towards energy increase”, *Nature Physics* **2**, 48–54 (2006) (cit. on p. 52).
- [79] M. Amin, *Experimental control of the beam properties of laser-accelerated protons and carbon ions* (Heinrich-Heine-Universität Düsseldorf, 2008) (cit. on pp. 52, 173, 198).
- [80] P. Mora, “Collisionless expansion of a gaussian plasma into a vacuum”, *Physics of Plasmas* **12**, 112102, 112102 (2005) (cit. on p. 52).
- [81] J. A. Stamper, K. Papadopo, R. N. Sudan, S. O. Dean, E. A. Mclean, and J. M. Dawson, “Spontaneous magnetic fields in laser-produced plasmas”, *Physical Review Letters* **26**, 1012 (1971) (cit. on p. 54).
- [82] A. R. Bell, F. N. Beg, Z. Chang, A. E. Dangor, C. N. Danson, C. B. Edwards, A. P. Fews, M. H. R. Hutchinson, S. Luan, P. Lee, P. A. Norreys, R. A. Smith, P. F. Taday, and F. Zhou, “Observation of plasma-confinement in picosecond laser-plasma interactions”, *Physical Review E* **48**, 2087–2093 (1993) (cit. on p. 54).
- [83] F. N. Beg, A. R. Bell, A. E. Dangor, C. N. Danson, A. P. Fews, M. E. Glinsky, B. A. Hammel, P. Lee, P. A. Norreys, and M. Tatarakis, “A study of picosecond laser-solid interactions up to 10^{19} W/cm²”, *Physics of Plasmas* **4**, 447–457 (1997) (cit. on p. 54).
- [84] C. A. Cecchetti, M. Borghesi, J. Fuchs, G. Schurtz, S. Kar, A. Macchi, L. Romagnani, P. A. Wilson, P. Antici, R. Jung, J. Osterholtz, C. A. Pipahl, O. Willi, A. Schiavi, M. Notley, and D. Neely, “Magnetic field measurements in laser-produced plasmas via proton deflectometry”, *Physics of Plasmas* **16**, 043102 (2009) (cit. on pp. 54, 93, 97).
- [85] R. N. Sudan, “Mechanism for the generation of 10^9 G magnetic fields in the interaction of ultraintense short laser-pulse with an overdense plasma target”, *Physical Review Letters* **70**, 3075–3078 (1993) (cit. on pp. 55, 166).
- [86] V. K. Tripathi and C. S. Liu, “Self-generated magnetic-field in an amplitude-modulated laser filament in a plasma”, *Physics of Plasmas* **1**, 990–992 (1994) (cit. on pp. 55, 166).
- [87] R. J. Mason and M. Tabak, “Magnetic field generation in high-intensity-laser-matter interactions”, *Physical Review Letters* **80**, 524–527 (1998) (cit. on pp. 55, 166).
- [88] A. Pukhov and J. MeyerTerVehn, “Laser hole boring into overdense plasma and relativistic electron currents for fast ignition of ICF targets”, *Physical Review Letters* **79**, 2686–2689 (1997) (cit. on pp. 56, 166).

-
- [89] A. R. Bell and R. J. Kingham, “Resistive collimation of electron beams in laser-produced plasmas”, *Physical Review Letters* **91**, 035003 (2003) (cit. on pp. 56, 166).
- [90] F. Brunel, “Anomalous absorption of high-intensity subpicosecond laser-pulses”, *Physics of Fluids* **31**, 2714–2719 (1988) (cit. on pp. 56, 166).
- [91] P. Gibbon, “Efficient production of fast electrons from femtosecond laser interaction with solid targets”, *Physical Review Letters* **73**, 664–667 (1994) (cit. on pp. 56, 166).
- [92] H. Ruhl and P. Mulser, “Relativistic Vlasov simulation of intense fs laser pulse-matter interaction”, *Physics Letters A* **205**, 388–392 (1995) (cit. on pp. 56, 166).
- [93] Y. Sakagami, H. Kawakami, S. Nagao, and C. Yamanaka, “Two-dimensional distribution of self-generated magnetic fields near the laser-plasma resonant-interaction region”, *Phys. Rev. Lett.* **42**, 839–842 (1979) (cit. on p. 56).
- [94] G. Sarri, A. Macchi, C. A. Cecchetti, S. Kar, T. V. Liseykina, X. H. Yang, M. E. Dieckmann, J. Fuchs, M. Galimberti, L. A. Gizzi, R. Jung, I. Kourakis, J. Osterholz, F. Pegoraro, A. P. L. Robinson, L. Romagnani, O. Willi, and M. Borghesi, “Dynamics of self-generated, large amplitude magnetic fields following high-intensity laser matter interaction”, *Phys. Rev. Lett.* **109**, 205002 (2012) (cit. on pp. 56, 97, 166, 199).
- [95] U. Wagner, M. Tatarakis, A. Gopal, F. Beg, E. Clark, A. Dangor, R. Evans, M. Haines, S. Mangles, P. Norreys, M.-S. Wei, M. Zepf, and K. Krushelnick, “Laboratory measurements of 0.7 GG magnetic fields generated during high-intensity laser interactions with dense plasmas”, *Phys. Rev. E* **70**, 026401 (2004) (cit. on p. 56).
- [96] F. Califano, R. Prandi, F. Pegoraro, and S. Bulanov, “Nonlinear filamentation instability driven by an inhomogeneous current in a collisionless plasma”, *Phys. Rev. E* **58**, 7837–7845 (1998) (cit. on p. 56).
- [97] S. Ter-Avetisyan, M. Schnürer, P. V. Nickles, T. Sokollik, E. Risse, M. Kalashnikov, W. Sandner, and G. Priebe, “The Thomson deflectometer: a novel use of the Thomson spectrometer as a transient field and plasma diagnostic”, *Review of Scientific Instruments* **79**, 033303 (2008) (cit. on pp. 59, 213).
- [98] S. Sakabe, T. Mochizuki, T. Yamanaka, and C. Yamanaka, “Modified Thomson parabola ion spectrometer of wide dynamic-range”, *Review of Scientific Instruments* **51**, 1314–1315 (1980) (cit. on p. 59).
- [99] S. Ter-Avetisyan, M. Schnürer, and P. V. Nickles, “Time resolved corpuscular diagnostics of plasmas produced with high-intensity femtosecond laser pulses”, *Journal of Physics D-applied Physics* **38**, 863–867 (2005) (cit. on p. 61).

- [100] S. J. Gitomer, R. D. Jones, F. Begay, A. W. Ehler, J. F. Kephart, and R. Kristal, “Fast ions and hot-electrons in the laser-plasma interaction”, *Physics of Fluids* **29**, 2679–2688 (1986) (cit. on p. 62).
- [101] M. Hegelich, S. Karsch, G. Pretzler, D. Habs, K. Witte, W. Guenther, M. Allen, A. Blazevic, J. Fuchs, J. C. Gauthier, M. Geissel, P. Audebert, T. Cowan, and M. Roth, “MeV ion jets from short-pulse-laser interaction with thin foils”, *Physical Review Letters* **89**, 085002 (2002) (cit. on p. 62).
- [102] S. B. van der Geer and M. J. de Loos, *General Particle Tracer (GPT)*, <http://www.pulsar.nl/gpt/> (cit. on pp. 64, 72, 175).
- [103] R. F. Schneider, C. M. Luo, and M. J. Rhee, “Resolution of the Thomson spectrometer”, *Journal of Applied Physics* **57**, 1–5 (1985) (cit. on p. 69).
- [104] M. Borghesi, A. J. Mackinnon, D. H. Campbell, D. G. Hicks, S. Kar, P. K. Patel, D. Price, L. Romagnani, A. Schiavi, and O. Willi, “Multi-MeV proton source investigations in ultraintense laser-foil interactions”, *Physical Review Letters* **92**, 055003 (2004) (cit. on pp. 75, 93, 101, 111, 215).
- [105] H. Ruhl, “3D kinetic simulation of super-intense laser-induced anomalous transport”, *Plasma Sources Science and Technology* **11**, pages (2002) (cit. on pp. 81, 218).
- [106] L. Romagnani, J. Fuchs, M. Borghesi, P. Antici, P. Audebert, F. Ceccherini, T. Cowan, T. Grismayer, S. Kar, A. Macchi, P. Mora, G. Pretzler, A. Schiavi, T. Toncian, and O. Willi, “Dynamics of electric fields driving the laser acceleration of multi-MeV protons”, *Physical Review Letters* **95**, 195001 (2005) (cit. on pp. 88, 93, 96, 111, 113, 123, 127, 128, 134).
- [107] A. P. L. Robinson, R. M. G. M. Trines, J. Polz, and M. Kaluza, “Absorption of circularly polarized laser pulses in near-critical plasmas”, *Plasma Physics and Controlled Fusion* **53**, 065019 (2011) (cit. on p. 89).
- [108] M. Shirozhan, M. Moshkelgosha, and R. Sadighi-Bonabi, “The effects of circularly polarized laser pulse on generated electron nano-bunches in oscillating mirror model”, *Laser and Particle Beams* **32**, 285–293 (2014) (cit. on p. 89).
- [109] J. Schreiber, S. Ter-Avetisyan, E. Risse, M. P. Kalachnikov, P. V. Nickles, W. Sandner, U. Schramm, D. Habs, J. Witte, and M. Schnürer, “Pointing of laser-accelerated proton beams”, *Physics of Plasmas* **13**, 033111 (2006) (cit. on pp. 93, 103, 111, 217).
- [110] M. Borghesi, S. Kar, L. Romagnani, T. Toncian, P. Antici, P. Audebert, E. Brambrink, F. Ceccherini, C. A. Cecchetti, J. Fuchs, M. Galimberti, L. A. Gizzi, T. Grismayer, T. Lyseikina, R. Jung, A. Macchi, P. Mora, J. Osterholtz, A. Schiavi, and O. Willi, “Impulsive electric fields driven by high-intensity laser matter interactions”, *Laser and Particle Beams* **25**, 161–167 (2007) (cit. on pp. 93, 111).

-
- [111] S. Ter-Avetisyan, M. Schnürer, P. V. Nickles, W. Sandner, T. Nakamura, and K. Mima, “Correlation of spectral, spatial, and angular characteristics of an ultrashort laser driven proton source”, *Physics of Plasmas* **16**, 043108 (2009) (cit. on p. 93).
- [112] S. Ter-Avetisyan, M. Borghesi, M. Schnürer, P. V. Nickles, W. Sandner, A. A. Andreev, T. Nakamura, and K. Mima, “Characterization and control of ion sources from ultra-short high-intensity laser-foil interaction”, *Plasma Physics and Controlled Fusion* **51**, 124046 (2009) (cit. on pp. 93, 216).
- [113] L. Romagnani, S. V. Bulanov, M. Borghesi, P. Audebert, J. C. Gauthier, K. Loewenbrueck, A. J. Mackinnon, P. Patel, G. Pretzler, T. Toncian, and O. Willi, “Observation of collisionless shocks in laser-plasma experiments”, *Physical Review Letters* **101**, 025004 (2008) (cit. on p. 93).
- [114] A. Ravasio, L. Romagnani, S. Le Pape, A. Benuzzi-Mounaix, C. Cecchetti, D. Batani, T. Boehly, M. Borghesi, R. Dezulian, L. Gremillet, E. Henry, D. Hicks, B. Loupias, A. MacKinnon, N. Ozaki, H. S. Park, P. Patel, A. Schiavi, T. Vinci, R. Clarke, M. Notley, S. Bandyopadhyay, and M. Koenig, “Proton radiography of a shock-compressed target”, *Physical Review E* **82**, 016407 (2010) (cit. on p. 93).
- [115] M. Borghesi, S. Bulanov, D. H. Campbell, R. J. Clarke, T. Z. Esirkepov, M. Galimberti, L. A. Gizzi, A. J. MacKinnon, N. M. Naumova, F. Pegoraro, H. Ruhl, A. Schiavi, and O. Willi, “Macroscopic evidence of soliton formation in multiterawatt laser-plasma interaction”, *Physical Review Letters* **88**, 135002 (2002) (cit. on p. 93).
- [116] M. Borghesi, D. H. Campbell, A. Schiavi, M. G. Haines, O. Willi, A. J. MacKinnon, P. Patel, L. A. Gizzi, M. Galimberti, R. J. Clarke, F. Pegoraro, H. Ruhl, and S. Bulanov, “Electric field detection in laser-plasma interaction experiments via the proton imaging technique”, *Physics of Plasmas* **9**, 2214–2220 (2002) (cit. on pp. 93, 113).
- [117] M. Borghesi, L. Romagnani, A. Schiavi, D. H. Campbell, M. G. Haines, O. Willi, A. J. Mackinnon, M. Galimberti, L. Gizzi, R. J. Clarke, and S. Hawkes, “Measurement of highly transient electrical charging following high-intensity laser-solid interaction”, *Applied Physics Letters* **82**, 1529–1531 (2003) (cit. on p. 93).
- [118] M. Borghesi, S. V. Bulanov, T. Z. Esirkepov, S. Fritzler, S. Kar, T. V. Liseikina, V. Malka, F. Pegoraro, L. Romagnani, J. P. Rousseau, A. Schiavi, O. Willi, and A. V. Zayats, “Plasma ion evolution in the wake of a high-intensity ultrashort laser pulse”, *Physical Review Letters* **94**, 195003 (2005) (cit. on p. 93).

- [119] A. J. Mackinnon, P. K. Patel, M. Borghesi, R. C. Clarke, R. R. Freeman, H. Habara, S. P. Hatchett, D. Hey, D. G. Hicks, S. Kar, M. H. Key, J. A. King, K. Lancaster, D. Neely, A. Nikkro, P. A. Norreys, M. M. Notley, T. W. Phillips, L. Romagnani, R. A. Snavely, R. B. Stephens, and R. P. J. Town, “Proton radiography of a laser-driven implosion”, *Physical Review Letters* **97**, 045001 (2006) (cit. on p. 93).
- [120] P. M. Nilson, L. Willingale, M. C. Kaluza, C. Kamperidis, S. Minardi, M. S. Wei, P. Fernandes, M. Notley, S. Bandyopadhyay, M. Sherlock, R. J. Kingham, M. Tatarakis, Z. Najmudin, W. Rozmus, R. G. Evans, M. G. Haines, A. E. Dangor, and K. Krushelnick, “Magnetic reconnection and plasma dynamics in two-beam laser-solid interactions”, *Physical Review Letters* **97**, 255001 (2006) (cit. on pp. 93, 97).
- [121] S. Kar, M. Borghesi, C. A. Cecchetti, L. Romagnani, F. Ceccherini, T. V. Liseykina, A. Macchi, R. Jung, J. Osterholz, O. Willi, L. A. Gizzi, A. Schiavi, M. Galimberti, and R. Heathcote, “Dynamics of charge-displacement channeling in intense laser-plasma interactions”, *New Journal of Physics* **9**, 402 (2007) (cit. on p. 93).
- [122] N. L. Kugland, D. D. Ryutov, C. Plechaty, J. S. Ross, and H.-S. Park, “Invited article: relation between electric and magnetic field structures and their proton-beam images”, *Review of Scientific Instruments* **83**, 101301 (2012) (cit. on pp. 95, 97).
- [123] S. Gaillard, J. Fuchs, N. Renard-Le Galloudec, and T. E. Cowan, “Study of saturation of CR39 nuclear track detectors at high ion fluence and of associated artifact patterns”, *Review of Scientific Instruments* **78**, 013304 (2007) (cit. on pp. 95, 212).
- [124] C. K. Li, F. H. Séguin, J. A. Frenje, J. R. Rygg, R. D. Petrasso, R. P. J. Town, P. A. Amendt, S. P. Hatchett, O. L. Landen, A. J. Mackinnon, P. K. Patel, V. A. Smalyuk, T. C. Sangster, and J. P. Knauer, “Measuring E and B fields in laser-produced plasmas with monoenergetic proton radiography”, *Physical Review Letters* **97**, 135003 (2006) (cit. on p. 97).
- [125] A. Gopal, M. Tatarakis, F. N. Beg, E. L. Clark, A. E. Dangor, R. G. Evans, P. A. Norreys, M. S. Wei, M. Zepf, and K. Krushelnick, “Temporally and spatially resolved measurements of multi-megagauss magnetic fields in high intensity laser-produced plasmas”, *Physics of Plasmas* **15**, 122701 (2008) (cit. on p. 97).
- [126] R. D. Petrasso, C. K. Li, F. H. Seguin, J. R. Rygg, J. A. Frenje, R. Betti, J. P. Knauer, D. D. Meyerhofer, P. A. Amendt, D. H. Froula, O. L. Landen, P. K. Patel, J. S. Ross, and R. P. J. Town, “Lorentz mapping of magnetic fields in hot dense plasmas”, *Physical Review Letters* **103**, 085001 (2009) (cit. on p. 97).

- [127] S. le Pape, P. Patel, S. Chen, R. Town, and A. Mackinnon, “Proton radiography of magnetic field in laser produced plasma”, *European Physical Journal-Special Topics* **175**, 61–64 (2009) (cit. on p. 97).
- [128] A. P. L. Robinson, P. Foster, D. Adams, D. C. Carroll, B. Dromey, S. Hawkes, S. Kar, Y. T. Li, K. Markey, P. McKenna, C. Spindloe, M. Streeter, C. G. Wahlstrom, M. H. Xu, M. Zepf, and D. Neely, “Spectral modification of laser-accelerated proton beams by self-generated magnetic fields”, *New Journal of Physics* **11**, 083018 (2009) (cit. on p. 97).
- [129] L. Willingale, P. M. Nilson, M. C. Kaluza, A. E. Dangor, R. G. Evans, P. Fernandes, M. G. Haines, C. Kamperidis, R. J. Kingham, C. P. Ridgers, M. Sherlock, A. G. R. Thomas, M. S. Wei, Z. Najmudin, K. Krushelnick, S. Bandyopadhyay, M. Notley, S. Minardi, M. Tatarakis, and W. Rozmus, “Proton deflectometry of a magnetic reconnection geometry”, *Physics of Plasmas* **17**, 043104 (2010) (cit. on p. 97).
- [130] W. Schumaker, N. Nakanii, C. McGuffey, C. Zulick, V. Chyvkov, F. Dollar, H. Habara, G. Kalintchenko, A. Maksimchuk, K. A. Tanaka, A. G. R. Thomas, V. Yanovsky, and K. Krushelnick, “Ultrafast electron radiography of magnetic fields in high-intensity laser-solid interactions”, *Phys. Rev. Lett.* **110**, 015003 (2013) (cit. on pp. 97, 166, 182, 198).
- [131] A. A. Andreev, R. Sonobe, S. Kawata, S. Miyazaki, K. Sakai, K. Miyauchi, T. Kikuchi, K. Platonov, and K. Nemoto, “Effect of a laser prepulse on fast ion generation in the interaction of ultra-short intense laser pulses with a limited-mass foil target”, *Plasma Physics and Controlled Fusion* **48**, 1605–1619 (2006) (cit. on p. 97).
- [132] S. M. Pfotenhauer, O. Jäckel, J. Polz, S. Steinke, H.-P. Schlenvoigt, J. Heymann, A. P. L. Robinson, and M. C. Kaluza, “A cascaded laser acceleration scheme for the generation of spectrally controlled proton beams”, *New Journal of Physics* **12**, 103009 (2010) (cit. on pp. 97, 122).
- [133] S. Ter-Avetisyan, M. Schnürer, T. Sokollik, P. V. Nickles, W. Sandner, H. R. Reiss, J. Stein, D. Habs, T. Nakamura, and K. Mima, “Proton acceleration in the electrostatic sheaths of hot electrons governed by strongly relativistic laser-absorption processes”, *Physical Review E* **77**, 016403 (2008) (cit. on pp. 103, 217).
- [134] F. Abicht, M. Schnürer, J. Bränzel, G. Priebe, A. A. Andreev, C. Koschitzki, S. Steinke, T. Toncian, O. Willi, and W. Sandner, “Coaction of strong electrical fields in laser irradiated thin foils and its relation to field dynamics at the plasma-vacuum interface”, *SPIE Proceedings* **8779**, 87790V (2013) (cit. on pp. 113, 130, 133, 144).

- [135] T. Ceccotti, A. Levy, H. Popescu, F. Reau, P. D'Oliveira, P. Monot, J. P. Geindre, E. Lefebvre, and P. Martin, "Proton acceleration with high-intensity ultrahigh-contrast laser pulses", *Physical Review Letters* **99**, 185002 (2007) (cit. on p. 113).
- [136] M. Schnürer, A. A. Andreev, S. Steinke, T. Sokollik, T. Paasch-Colberg, P. V. Nickles, A. Henig, D. Jung, D. Kiefer, R. Hörlein, J. Schreiber, T. Tajima, D. Habs, and W. Sandner, "Comparison of femtosecond laser-driven proton acceleration using nanometer and micrometer thick target foils", *Laser and Particle Beams* **29**, 437–446 (2011) (cit. on p. 113).
- [137] S. C. Wilks, W. L. Kruer, M. Tabak, and A. B. Langdon, "Absorption of ultra-intense laser-pulses", *Physical Review Letters* **69**, 1383–1386 (1992) (cit. on p. 134).
- [138] M. Schnürer, R. Nolte, A. Rousse, G. Grillon, G. Cheriaux, M. P. Kalachnikov, P. V. Nickles, and W. Sandner, "Dosimetric measurements of electron and photon yields from solid targets irradiated with 30 fs pulses from a 14 TW laser", *Physical Review E* **61**, 4394–4401 (2000) (cit. on p. 134).
- [139] G. Pretzler, T. Schlegel, E. Fill, and D. Eder, "Hot-electron generation in copper and photopumping of cobalt", *Physical Review E* **62**, 5618–5623 (2000) (cit. on p. 134).
- [140] S. Betti, F. Ceccherini, F. Cornolti, and F. Pegoraro, "Expansion of a finite-size plasma in vacuum", *Plasma Physics and Controlled Fusion* **47**, 521–529 (2005) (cit. on p. 141).
- [141] M. Borghesi, A. J. Mackinnon, R. Gaillard, O. Willi, A. Pukhov, and J. Meyer-ter-Vehn, "Large quasistatic magnetic fields generated by a relativistically intense laser pulse propagating in a preionized plasma", *Physical Review Letters* **80**, 5137–5140 (1998) (cit. on p. 166).
- [142] A. Andreev, T. Ceccotti, A. Levy, K. Platonov, and P. Martin, "Divergence of fast ions generated by interaction of intense ultra-high contrast laser pulses with thin foils", *New Journal of Physics* **12**, 045007 (2010) (cit. on pp. 167–169, 179, 198).
- [143] A. Andreev, A. Lévy, T. Ceccotti, C. Thauray, K. Platonov, R. Loch, and P. Martin, "Fast-ion energy-flux enhancement from ultrathin foils irradiated by intense and high-contrast short laser pulses", *Phys. Rev. Lett.* **101**, 155002 (2008) (cit. on pp. 167, 170).
- [144] W. L. Kruer, *The Physics Of Laser Plasma Interactions*, edited by D. A. Jaroszynski, R. Bingham, and R. A. Cairns (Reading, MA (US); Addison-Wesley Publishing Co., 1988) (cit. on p. 167).
- [145] A. Andreev, *Generation and Application of Super-Strong Laser Fields* (Nova Publishing, 2001) (cit. on p. 169).

-
- [146] A. A. Andreev, K. Y. Platonov, M. Schnürer, R. Prasad, and S. Ter-Avetisyan, “Hybrid proton acceleration scheme using relativistic intense laser light”, *Physics of Plasmas* **20**, 033110 (2013) (cit. on p. 170).
- [147] M. Borghesi, A. Schiavi, D. H. Campbell, M. G. Haines, O. Willi, A. J. Mackinnon, P. Patel, M. Galimberti, and L. A. Gizzi, “Proton imaging detection of transient electromagnetic fields in laser-plasma interactions (invited)”, *Review of Scientific Instruments* **74**, 1688–1693 (2003) (cit. on p. 212).
- [148] S. P. Hatchett, C. G. Brown, T. E. Cowan, E. A. Henry, J. S. Johnson, M. H. Key, J. A. Koch, A. B. Langdon, B. F. Lasinski, R. W. Lee, A. J. Mackinnon, D. M. Pennington, M. D. Perry, T. W. Phillips, M. Roth, T. C. Sangster, M. S. Singh, R. A. Snavely, M. A. Stoyer, S. C. Wilks, and K. Yasuike, “Electron, photon, and ion beams from the relativistic interaction of petawatt laser pulses with solid targets”, *Physics of Plasmas* **7**, 2076–2082 (2000) (cit. on p. 213).

Acknowledgments

I am using this opportunity to express my gratitude to everyone who contributed to this work and supported me during my time as a Ph.D. student. Without their help, enthusiasm and fruitful discussions this thesis would not have been possible. In particular, I would like to thank the following people:

- Prof. Dr. W. Sandner for giving me the opportunity to be part of his excellent group at the MBI, his commitment in the Ph.D. seminar and for reviewing this work
- Prof. Dr. J. Schreiber for being the second referee of this thesis
- Dr. M. Schnürer for his extraordinary dedication, outstanding competence, mentoring and help
- Prof. Dr. A.A. Andreev for patiently answering all my questions concerning theoretical issues
- J. Bränzel for her friendly support and help in countless hours in the lab
- Dr. G. Priebe for keeping the laser running and his extraordinary support
- Prof. Dr. P.V. Nickles for reviewing an early version of this manuscript
- C. Koschitzki, L. Ehrentraut, Dr. S. Steinke, Dr. Ter-Avetisian, Dr. R. Prasad, Dr. T. Toncian, Dr. H. Stiel, D. Sommer and D. Brete
- All other administrative and technical employers: P. Friedrich, S. Szlapka, B. Becker, G. Kommol, J. Meißner, J. Gläsel and D. Rohloff.
- Last but not least, my family for their personal support during all the years and especially Hélène for being there for me all the time